Spectroscopy of Twisted Bilayer Graphene Correlated Insulators

Dumitru Călugăru,[1] Nicolas Regnault,[1] Myungchul Oh,[1] Kevin P. Nuckolls,[1] Dillon Wong,[1] Ryan L. Lee,[1] Ali Yazdani,[1] Oskar Vafek,[2,3] and Andrei B. Bernevig[1,4,5]

[1]*Department of Physics, Princeton University, Princeton, New Jersey 08544, USA*
[2]*National High Magnetic Field Laboratory, Tallahassee, Florida, 32310, USA*
[3]*Department of Physics, Florida State University, Tallahassee, Florida 32306, USA*
[4]*Donostia International Physics Center, P. Manuel de Lardizabal 4, 20018 Donostia-San Sebastian, Spain*
[5]*IKERBASQUE, Basque Foundation for Science, Bilbao, Spain*

We calculate STM signatures of correlated ground-states at integer filling of the magic angle twisted bilayer graphene narrow bands. First, we compute the fully-interacting TBG spectral function at ± 4 electrons/moiré unit cell and show that it can be used to experimentally validate the strong-coupling approach. Although variation exists in the data, we find experimental evidence for the strong-coupling regime. For all other integer fillings of the flat bands, we consider the spatial features of the corresponding spectral functions of many states in the large degenerate ground-state manifold, and assess the possibility of Kekulé distortion (KD) emerging at the graphene lattice scale. Remarkably, we find that coupling the two opposite graphene valleys in the intervalley-coherent (IVC) TBG insulators does not always result in KD. As an example, we show that the K-IVC state and its nonchiral U (4) rotations do not exhibit any KD, while T-IVC does. We analyze 14 different many-body correlated states and show that their combined STM/Chern number signal can be used to uniquely determine the nature of the many-body ground-state. Their STM signal and features are obtained over a large range of energies and model parameters.

Introduction. Near the first magic angle [1–3], twisted bilayer graphene (TBG) features a wealth of superconducting and correlated insulating phases, as seen in both transport [4–18] and spectroscopy [19–28] experiments, sparking considerable theoretical effort towards their understanding [29–73]. Owing to nearly dispersionless active bands, the physics of the system near an integer filling ν was argued to be in the strong coupling regime *i.e.* dictated by the interaction-only Hamiltonian projected onto the almost-flat bands [42, 43, 58, 63, 68]. In strong coupling, the enlarged continuous spin-valley symmetries [U (4) and U (4) $\times$ U (4)] [42, 43, 58, 74] have rendered a low-energy manifold of its many-body eigenstates exactly solvable at integer fillings with $-4 \leq \nu \leq 4$ electrons per moiré unit cell [42, 43, 58, 63, 68]. Following analytical arguments [42, 58, 68, 74], which were numerically validated [55, 58, 69], the resulting eigenstates of the projected TBG interaction Hamiltonian were shown to be energetically-competitive candidates for the TBG ground states, if not the actual ground states of the system, for a large range of parameters. In addition, Refs. [63, 75] have shown that the *exact* many-body excitations with n additional particles on top of the integer-filled exact eigenstates can be computed in the strong-coupling limit as an $(n-1)$-body problem.

The goal of this paper is to identify spectroscopic signatures of the various competing states by building upon the mentioned theoretical advances. With the many-body electron and hole excitations at hand [63, 75], the exact spectral functions for the various integer-filled TBG insulators can be computed analytically for relatively large system sizes (*i.e.* much larger than achievable with exact diagonalization [30, 51, 69, 76]). The differential conductance measured in scanning tunneling microscopy (STM) experiments is in turn proportional to the spectral function [77]. We find that the STM features of the proposed correlated states – particularly the presence or absence of a Kekulé distortion (KD) at the graphene lattice scale (*i.e.* the modulation of the STM signal at wavevectors connecting the two graphene valleys) – together with the knowledge of their Chern number, can distinguish among the candidate many-body states. The ability to use the STM to directly visualize broken symmetry states, including valley-polarized or Kekule order due to many-body interactions in a low-density flat band system, has recently been demonstrated in probing such states forming in the zeroth Landau level of monolayer graphene [78–80]. These findings and the techniques developed for directly measuring the order parameters of various phases using local phase-sensitive analysis of Fourier-transformed STM conductance maps can also be used to verify the nature of many-body ground states we examine here for TBG.

The competing correlated states of TBG at an integer filling ν can be characterized by their Chern number $\mathcal{C}$ and valley polarization, in that they can be valley polarized (VP) or inter-valley coherent (IVC). Furthermore, even for $C = 0$, IVC states may either spontaneously break time reversal symmetry (K-IVC) or preserve it (T-IVC) [42, 43, 58, 74]. Some of these states can be stabilized by magnetic field [12, 15, 17, 25, 26, 81]. In this paper, we show, analytically and confirm numerically, that: a) all VP states at any filling and $\mathcal{C}$ do not exhibit a KD; b) $\nu = -1$, $\mathcal{C} = 1$ (a state with two occupied IVC bands and one valley polarized Chern band), $\nu = -2, 0$, $\mathcal{C} = 0$ K-IVC states, and $\nu = -4$, $\mathcal{C} = 0$ (correlated band insulator) do not exhibit a KD; c) $\nu = -3$, $\mathcal{C} = 1$ IVC, $\nu = -2$, $\mathcal{C} = 0$ T-IVC, and $\nu = -2$, $\mathcal{C} = 2$ IVC, exhibit a KD. At positive fillings, the same conclusions apply, by particle-hole symmetry [74]. Furthermore, we show

that the strong versus weak coupling nature of the system can be uniquely inferred from the spectral function at the band insulator filling $\nu = \pm 4$: while the weak coupling approach gives an almost symmetric peak structure, the strong coupling approach, whose excitations [63, 75] are strongly particle-hole asymmetric around fixed filling, gives a markedly different peak structure, which, moreover varies dramatically as the STM tip moves from the AA to AB moiré region. While the experimental data experiences large sample-to-sample and STM tip position variation, some data sets are uniquely compatible with strong coupling, which shows large variations in the local density of states (LDOS) from the AA to AB regions of the same sample. We furthermore provide analytic expressions for the LDOS, exactly and in different approximations, and analyze numerically the LDOS over a wide range of parameter regimes of the Bistritzer-MacDonald model [1] at both AA and AB regions.

Model. Near the first magic twist angle, the kinetic energy of the two active bands of TBG (per spin and per valley) is quenched [1–3], and hence neglected in a strong-coupling description. The physics of the system is dominated by the repulsive Coulomb interaction Hamiltonian projected in the almost-flat bands near charge neutrality [42, 58, 74] (see Appendix [A 2])

$$H_I = \frac{1}{2\Omega_{\mathrm{TBG}}} \sum_{\mathbf{q}\in \mathrm{MBZ}} \sum_{\mathbf{G}\in\mathcal{Q}_0} O_{-\mathbf{q}-\mathbf{G}} O_{\mathbf{q}+\mathbf{G}}. \tag{1}$$

where Ω_{TBG} is the area of the TBG sample, MBZ and $\mathcal{Q}_0$ respectively denote the moiré Brillouin zone (MBZ) and reciprocal lattice, while

$$O_{\mathbf{q}+\mathbf{G}} = \sum_{\substack{\mathbf{k},\eta,s \\ n,m=\pm 1}} \sqrt{V(\mathbf{q}+\mathbf{G})} M^{\eta}_{mn}(\mathbf{k},\mathbf{q}+\mathbf{G}) \times \left(\hat{c}^{\dagger}_{\mathbf{k}+\mathbf{q},m,\eta,s} \hat{c}_{\mathbf{k},n,\eta,s} - \frac{1}{2}\delta_{\mathbf{q},\mathbf{0}}\delta_{m,n} \right) \tag{2}$$

are proportional to the flat-band-projected density operators. In particular, $\hat{c}^{\dagger}_{\mathbf{k},n,\eta,s}$ is the electron creation operator for the TBG conduction ($n = +1$) and valence ($n = -1$) flat bands from valley $\eta = \pm$ and spin $s = \uparrow, \downarrow$, while $M^{\eta}_{mn}(\mathbf{k},\mathbf{q}+\mathbf{G})$ are the TBG form factors. The Fourier-transformed screened Coulomb potential is $V(\mathbf{q}) = 2\pi U_\xi \xi^2 \left(1 - e^{-2\xi q}\right)/(\xi q)$, where we take $U_\xi = 8\,\mathrm{meV}$ and $\xi = 30\,\mathrm{nm}$ (unless mentioned otherwise), corresponding to the typical single-gate arrangement of the TBG sample in an STM experiment [25].

At the single-particle level, the TBG Hamiltonian features a series of discrete symmetries (see Appendix [A 1]): the C_{2z}, C_{3z}, T, and C_{2x} *commuting* symmetries, as well as an approximate unitary particle-hole P *anti-commuting* symmetry [74, 82–85]. The latter enlarges the valley-spin-charge $\mathrm{U}(2) \times \mathrm{U}(2)$ rotation symmetry of H_I to the so-called nonchiral-flat $\mathrm{U}(4)$ symmetry [42, 43, 58, 74], henceforth denoted by $\mathrm{U_{nc}}(4)$. Additionally, when the inter-layer tunneling amplitude at the AA stacking centers (w_0) is neglected compared to the one at AB stacking centers (w_1) – in the so-called chiral limit ($w_0/w_1 = 0$) – the single-particle Hamiltonian enjoys an additional *anti-commuting* chiral C symmetry [74, 86], which further enlarges the symmetry group of H_I to the chiral-flat $\mathrm{U}(4) \times \mathrm{U}(4)$ group [58, 74]. Recombining the active TBG bands into Chern-number e_Y bands with operators $\hat{d}^{\dagger}_{\mathbf{k},e_Y,\eta,s} = \frac{1}{\sqrt{2}}\left(\hat{c}^{\dagger}_{\mathbf{k},+1,\eta,s} + i e_Y \hat{c}^{\dagger}_{\mathbf{k},-1,\eta,s}\right)$, the 32 generators the chiral-flat $\mathrm{U}(4) \times \mathrm{U}(4)$ group correspond to independent valley-spin rotations within each Chern sector. Away from the chiral limit the $\mathrm{U}(4) \times \mathrm{U}(4)$ generators get combined into the 16 $\mathrm{U_{nc}}(4)$ generators such that $\mathrm{U_{nc}}(4)$ intervalley (intravalley) rotations act on the two Chern sectors in the same (opposite) way [74].

The presence of enlarged symmetries renders some of the eigenstates of H_I exactly solvable at integer fillings with ν additional electrons per moiré unit cell ($-4 \leq \nu \leq +4$). Both analytical and numerical works have shown that, up to rotations $\hat{U}$ belonging to the symmetry group of H_I, the TBG ground states are Slater determinants obtained by populating the active TBG bands one Chern-valley-spin sector $\left(e_{Y_j}, \eta_j, s_j\right)$ at a time [42, 55, 58, 68, 69, 74, 75]

$$|\varphi\rangle = \hat{U} \prod_{\mathbf{k}} \prod_{j=1}^{\nu} \hat{d}^{\dagger}_{\mathbf{k},e_{Y_j},\eta_j,s_j} |0\rangle . \tag{3}$$

In the chiral limit, $|\varphi\rangle$ is an *exact* eigenstate of H_I for any choice of the filled Chern-valley-spin sectors and $\hat{U} \in \mathrm{U}(4) \times \mathrm{U}(4)$ [68]. Away from the chiral limit, only the insulators from Eq. (3) with fully-filled or fully-empty valley-spin flavors and $\hat{U} \in \mathrm{U_{nc}}(4)$ are *exact*, with the rest being *perturbative* eigenstates of H_I [68].

Spectral function. For a given state $|\varphi\rangle$ from Eq. (3), an STM experiment allows for the direct measurement of its spectral function [77]

$$A(\mathbf{r},\omega) = \sum_{\xi,s} \Big[\left| \left\langle \xi \middle| \hat{\psi}^{\dagger}_s(\mathbf{r}) \middle| \varphi \right\rangle \right|^2 \delta(\omega - E_\xi + E_\varphi) + \left| \left\langle \xi \middle| \hat{\psi}_s(\mathbf{r}) \middle| \varphi \right\rangle \right|^2 \delta(\omega + E_\xi - E_\varphi) \Big] . \tag{4}$$

where $\psi_s(\mathbf{r})$ denotes the electron field annihilation operator corresponding to spin $s = \uparrow, \downarrow$, and a summation is performed over all the *many-body* eigenstates $|\xi\rangle$ of H_I with energy E_ξ (see Appendix [C]). The two contributions to $A(\mathbf{r},\omega)$ correspond respectively to electron and hole excitations. Expressing the field operators in the TBG energy-band basis $\hat{\psi}^{\dagger}_s(\mathbf{r}) = \sum_{\eta,n} V_{\mathbf{r},\mathbf{k}n\eta} \hat{c}^{\dagger}_{\mathbf{k},n,\eta,s}$ (where the factors $V_{\mathbf{r},\mathbf{k}n\eta}$ depend on the carbon p_z orbitals and the TBG flat band wave-functions), we find that

$$A(\mathbf{r},\omega) = \sum_{\substack{\mathbf{k}\in\mathrm{MBZ}, \\ n,\eta,n',\eta' \\ c=\pm}} \left[\mathcal{M}^{c}_{\varphi}(\omega)\right]_{\mathbf{k}n\eta,\mathbf{k}n'\eta'} \left[\mathcal{B}(\mathbf{r})\right]_{\mathbf{k}n\eta,\mathbf{k}n'\eta'} . \tag{5}$$

In Eq. (5), we have introduced the spatial factor matrix $\left[\mathcal{B}(\mathbf{r})\right]_{\mathbf{k}n\eta,\mathbf{k}'n'\eta'} = V_{\mathbf{r},\mathbf{k}n\eta} V^{*}_{\mathbf{r},\mathbf{k}'n'\eta'}$ (which depends only on

the TBG single-particle Hamiltonian) and the spectral function matrices (which depend on the state $|\varphi\rangle$)

$$\begin{aligned}\left[\mathcal{M}^{c}_{\varphi}(\omega)\right]_{\mathbf{k}n\eta,\mathbf{k}n'\eta'} &= \sum_{\lambda_{-c},s} \langle\lambda_{+}|\hat{c}_{\mathbf{k},n',\eta',s}|\lambda_{-}\rangle \\ &\times \left\langle\lambda_{-}\middle|\hat{c}^{\dagger}_{\mathbf{k},n,\eta,s}\middle|\lambda_{+}\right\rangle \delta\left(\omega - E_{\lambda_{-}} + E_{\lambda_{+}}\right),\end{aligned} \tag{6}$$

where $|\lambda_c\rangle = |\varphi\rangle$ and we assumed no breaking of the moiré translation symmetry. Since a $\hat{c}^{\dagger}_{\mathbf{k},n,\eta,s}$ operator acts in *one* single-layer graphene (SLG) valley, $[\mathcal{B}(\mathbf{r})]_{\mathbf{k}n\eta,\mathbf{k}n'\eta}$ is only modulated at the level of the SLG and TBG lattices. In contrast, $[\mathcal{B}(\mathbf{r})]_{\mathbf{k}n\eta,\mathbf{k}n'(-\eta)}$ contains an additional modulation corresponding to wave-vectors linking the two Dirac points of the same graphene layer, which manifests in real space as a KD of the SLG.

As shown in Eqs. (5) and (6), computing the TBG spectral function requires exact eigenstates of H_I containing an extra electron/hole compared to $|\varphi\rangle$ (*i.e.* the charge-one excitations). Despite H_I being a quartic Hamiltonian, the exact charge-($\pm$)one excitations on top of $|\varphi\rangle$ can be computed as a zero-body problem using the *charge-one commutation relations* [63, 75]. The electron commutation relation reads as

$$\left[H_I - \mu\hat{N}, \hat{c}^{\dagger}_{\mathbf{k},n,\eta,s}\right]|\varphi\rangle = \sum_{m} R^{\eta}_{mn}(\mathbf{k})\,\hat{c}^{\dagger}_{\mathbf{k},m,\eta,s}|\varphi\rangle \tag{7}$$

where μ denotes the chemical potential, $\hat{N}$ is the total fermion number operator and the matrix $R(\mathbf{k})$ depends on ν, the active TBG wave-functions and the Coulomb repulsion potential (see Appendix [B]). A similar expression holds for the hole commutation relation. As such, the $\hat{c}^{\dagger}_{\mathbf{k},n,\eta,s}$ and the $\hat{c}_{\mathbf{k},n,\eta,s}$ operators can be recombined into exact electron and hole excitations, allowing for the exact calculation of the spectral function of $|\varphi\rangle$ (see Appendix [D]).

Signatures of strong correlation. We first analyze the spectral function of the $\nu = -4$ ($\nu = +4$) TBG insulator from Eq. (3), for which the active TBG bands are fully-empty (fully-filled). Because these states are invariant under *any* $\mathrm{U}(4) \times \mathrm{U}(4)$ rotations, no ambiguity in the choice of ground-state arises at these fillings. Moreover, unlike at other integer fillings, at $\nu = \pm 4$, the insulators Eq. (3) are exact eigenstates of the *full* projected TBG Hamiltonian *including* the kinetic energy term. As shown in Fig. 1, the strong coupling and weak coupling spectral functions at $\nu = \pm 4$ are markedly different. This difference stems from large interaction induced dispersion of single particle excitations in the strong coupling regime[63, 75] (see the insets from Fig. 1 b and e) as compared to a small (flat band) dispersion in the weak coupling regime, as well as from different van-Hove singularities and Dirac points.

In what follows, we will discuss the $\nu = -4$ insulator (shown in Fig. 1a-c), with the $\nu = +4$ insulator (depicted in Fig. 1d and e) following analogously from the many-body charge-conjugation symmetry of TBG [74]. Details about the experimental measurements are provided in Appendix [F]. For $\nu = -4$, we focus on positive-energy biases ($\omega - \mu \geq 0$), such that the electrons tunnel from the STM tip into the fermion states corresponding to the active TBG bands, which are combined into the charge-one excitations computed according to Eq. (7). The signal normalization based on tip height is explained in Appendix [C]. The electron excitation energies ($E^{p}_{\mathbf{k}}$ for $1 \leq p \leq 8$, see inset of Fig. 1 b) are comprised of four sets of two-fold [spin $\mathrm{SU}(2)$] degenerate bands, which are further paired by the approximate $C_{2z}P$ symmetry of H_I into two sets of almost four-fold degenerate bands [63, 75, 82, 84]. For both the AA and AB regions and small bias, the electrons start tunnelling into the regions at the bottom of the excitation bands away from any high-symmetry points (*e.g.* halfway between the Γ_M and M_M points of the MBZ), giving rise to the peak near $\omega - \mu \approx 0\,\mathrm{meV}$ in the spectral function. Upon increasing the bias to about $\omega - \mu \approx 20\,\mathrm{meV}$, the electrons tunnel into the almost-flat regions near the boundary of the MBZ, giving rise to two close peaks in the theoretical spectral function, which merge into one in the experimental STM signal. For larger biases, the spectral function decreases as the electron tunnel in the strongly-dispersive bands near Γ_M.

The variation of the spatial factor $[\mathcal{B}(\mathbf{r})]_{\mathbf{k}n\eta,\mathbf{k}n'\eta'}$ across the MBZ at the AA and AB sites (depicted in Fig. 1f) explains the change in the STM signal between the two stacking centers: at the AA site, the spatial factor has roughly the same magnitude in the MBZ for the two almost-flat regions of the excitation bands, resulting in similar magnitudes for the LDOS peaks at $\omega - \mu \approx 0\,\mathrm{meV}, 20\,\mathrm{meV}$. At the AB site, the spatial factor has a larger amplitude on the boundary of the MBZ, diminishing the intensity of the peak at $\omega - \mu \approx 0\,\mathrm{meV}$ compared to the one at $\omega - \mu \approx 20\,\mathrm{meV}$. A similar decrease is also present in the experimental data from Fig. 1a, while clearly absent in the weak-coupling LDOS Fig. 1c, which is computed by neglecting the Coulomb repulsion, and assuming only the single-particle TBG Hamiltonian. Moreover, the width ($\Delta\omega$) of the spectral function is much narrower in the non-interacting case ($\Delta\omega \sim 4\,\mathrm{meV}$, comparable the the active TBG bandwidth) than in the experiment and the strong-coupling prediction ($\Delta\omega \sim 45\,\mathrm{meV}$ comparable to U_ξ). While the STM signal is sample dependent and may vary from different AA or AB sites (see Appendix [F]), this data set indicates evidence of strong correlations governing the physics of TBG near charge-neutrality.

Discriminating correlated insulating phases. We now investigate the LDOS of the integer $-4 < \nu < 4$ correlated insulator states of different Chern numbers and valley polarization/coherence. We first consider the effects of inter-valley coherence in the state $|\varphi\rangle$ on the *spatial* variation of $A(\mathbf{r}, \omega)$. Intuitively, in an IVC state, coupling the two valleys of a graphene layer should lead to the appearence of KD in the STM signal. Mathematically, to obtain the electron (hole) excited states neces-

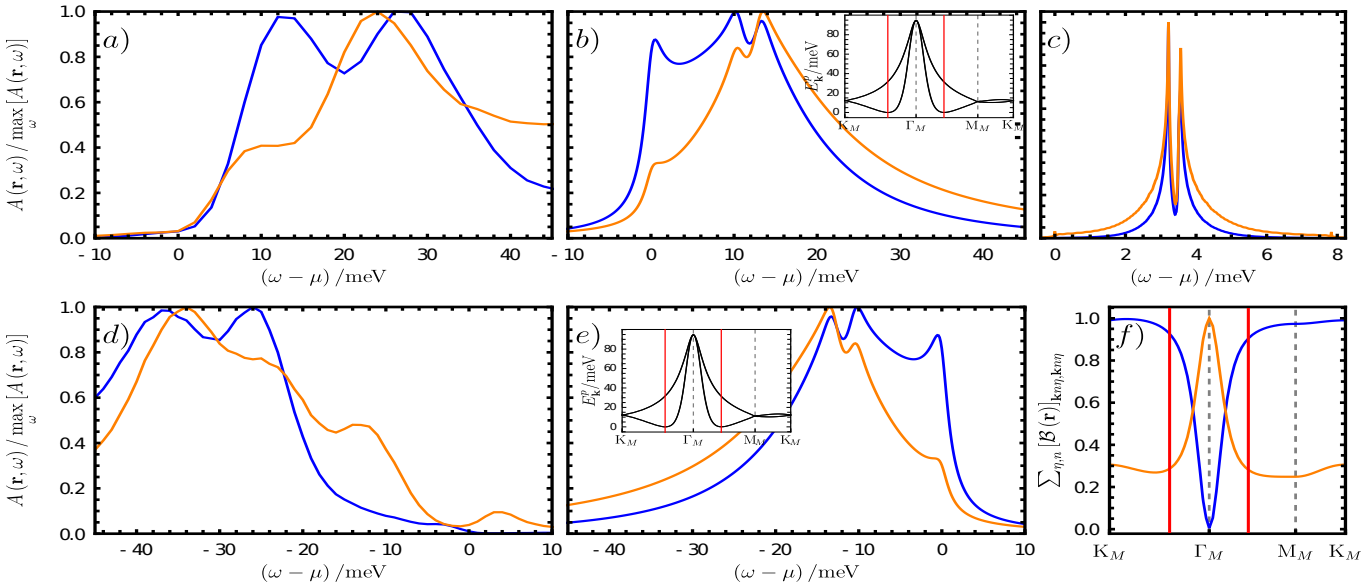

FIG. 1. The TBG spectral function for the $\nu = \pm 4$ insulator. For $\nu = -4$ ($\nu = +4$), we compare the experimentally-measured STM signal in a) [d)] with the spectral function computed from the charge-one excitation of H_I in b) [e)]]. For reference, the TBG spectral function at $\nu = -4$ derived from the single-particle TBG Hamiltonian is given in c). The signal at the center of the AA (AB) site is shown in blue (orange). All signals are normalized by their maxima in the energy range at that particular location. The theoretically-computed spectral function is averaged over three SLG unit cells. The inset in b) [e)] shows the electron [hole] excitation dispersion $E^p_{\mathbf{k}}$ ($\tilde{E}^p_{\mathbf{k}}$) computed from Eq. (7) (the red vertical lines are a guide for eye pointing the minima of the dispersion). f) provides the spatial factor at the AA and AB sites along the high symmetry line. The red lines indicate the position of dispersion minima. Note that we have used $U_\xi = 24\,\text{meV}$ for b) and e).

sary for the evaluation of $\mathcal{M}^{\pm}_{\varphi}$ from Eq. (6), the charge-one excitation matrices from Eq. (7), must be diagonalized in the subspace of empty (occupied) bands of $|\varphi\rangle$. Assuming that $|\varphi\rangle$ is IVC, the charge-one excitation operators must themselves be IVC. In turn, this implies from Eq. (6) that $\mathcal{M}^{\pm}_{\varphi}$ have non-vanishing valley off-diagonal terms. As the valley-off-diagonal elements of the spatial factor $\mathcal{B}(\mathbf{r})$ are modulated by wave-vectors connecting the two Dirac points of a graphene layer, KD is expected to appear in the STM signal of $|\varphi\rangle$.

Our detailed analytical calculations in Appendix [E] show that breaking valley U (1) symmetry does *not* guarantee the emergence of KD in the STM patterns, as a result of discrete symmetries of TBG. For instance, Fig. 2 shows the simulated STM patterns for two *fully* IVC TBG insulators at $\nu = -2$, the Kramers IVC (K-IVC) state and the T-symmetric invervalley-coherent (T-IVC) state [58, 68]

$$\begin{aligned} |\text{K-IVC}\rangle &= \prod_{\mathbf{k}} \prod_{e_Y=\pm 1} \frac{\hat{d}^\dagger_{\mathbf{k},e_Y,+,\uparrow} + e_Y \hat{d}^\dagger_{\mathbf{k},e_Y,-,\uparrow}}{\sqrt{2}} |0\rangle \\ |\text{T-IVC}\rangle &= \prod_{\mathbf{k}} \prod_{e_Y=\pm 1} \frac{\hat{d}^\dagger_{\mathbf{k},e_Y,+,\uparrow} + \hat{d}^\dagger_{\mathbf{k},e_Y,-,\uparrow}}{\sqrt{2}} |0\rangle \end{aligned} \tag{8}$$

The K-IVC (T-IVC) state is obtained by starting from a fully-filled valley-spin flavor and rotating the two Chern bands in the xz valley plane in opposite (identical) directions, as depicted by the valley Bloch spheres in Figs. 2c) and f). Remarkably, while the STM patterns of the T-IVC state show clear signs of KD, no KD emerges for the K-IVC state.

The counter-intuitive absence of KD in the $\nu = -2$ K-IVC state is part of a more general *exact* result (see Appendix [E 1]), relying on the C_{2z}, T, and P symmetries of TBG: a VP even-ν insulator with only fully-filled and fully-empty valley-spin flavors and all its $\text{U}_{\text{nc}}(4)$ rotations have *identical* spectral functions, without exhibiting KD. Note that these are precisely the theoretically-proposed exact ground states of H_I at even filling and away from the chiral limit [42, 58, 68, 69]. Moreover, even when the P symmetry is broken, we find that the C_{2z} and T symmetries of TBG are enough to guarantee the *exact* absence of KD in the K-IVC state, although not necessarily in its general $\text{U}_{\text{nc}}(4)$ rotations (see Appendix [E 4]).

When $|\varphi\rangle$ is *not* a $\text{U}_{\text{nc}}(4)$ rotation of an insulator with only fully-filled or fully-empty valley-spin flavors, intervalley-coherence *can* lead to the emergence of KD, but fine-tuned counter examples do exist. While a complete treatment of *all* states $|\varphi\rangle$ for general $\text{U}(4) \times \text{U}(4)$ rotations is beyond the scope of this work, we can derive simple rules for the maximally-spin polarized states (see Appendix [E 3 b]): 1) Filling a single IVC Chern band will give rise to KD; 2) An exact cancellation of the KD signal occurs upon filling a pair of Chern bands with *opposite* Chern numbers whose valley polarization projections in the valley xy plane of the Bloch sphere

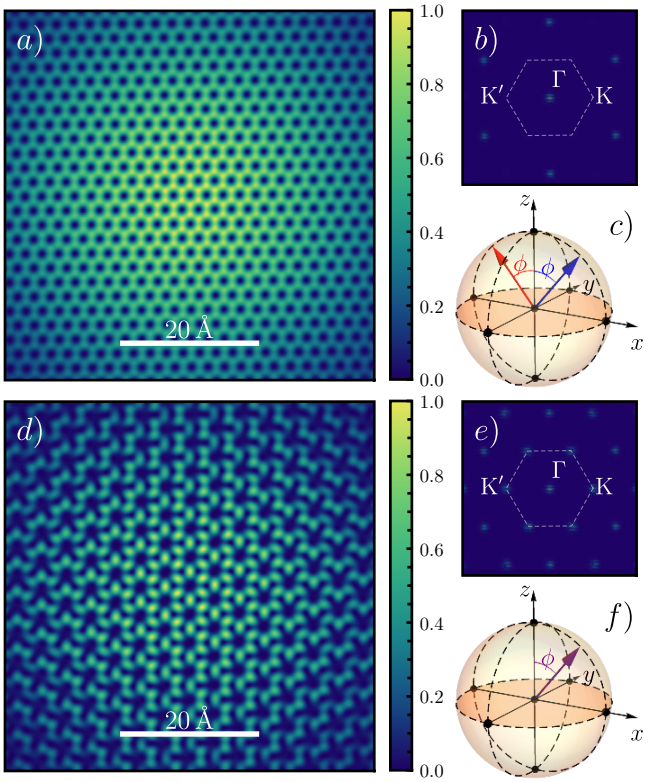

FIG. 2. Kekulé distortion and intervalley-coherence. (a) and (b) [(d) and (e)] respectively illustrate the real-space spectral function and its Fourier transform for the $\nu = -2$ K-IVC (T-IVC) TBG insulator. The presence of KD in the K-IVC state appears as three-fold enlargement of the SLG unit cell and as a signal at the K and K' points of the SLG Brillouin zone. In the valley Bloch sphere from (c) [(f)] the valley polarizations of the two Chern bands of the K-IVC (T-IVC) state shown in red and blue have are rotated in opposite (identical) direction in the xz plane by an angle $\phi = \pi/2$.

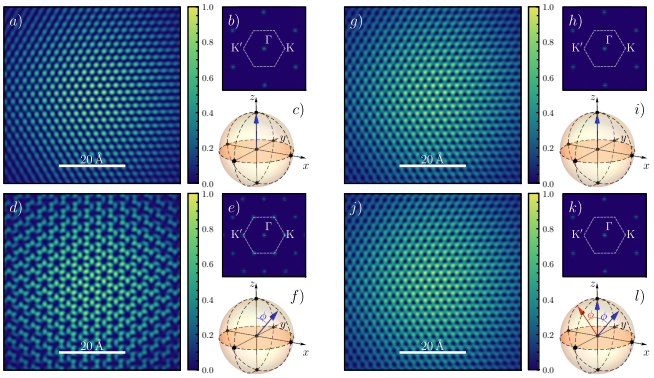

FIG. 3. Real-space spectral function, its Fourier transform and the valley Bloch sphere for four TBG insulators. We use the same conventions as in Fig. 2. a), b) and c) $\nu = -2$ VP $C = 2$ Chern insulator. d), e) and f) $\nu = -2$ IVC $C = 2$ Chern insulator. g), h) and i) $\nu = -1$ fully VP $C = 3$ Chern insulator. j), k) and l) $\nu = -1$ partially IVC $C = 1$ Chern insulator.

are nonzero and cancel out (as shown for the K-IVC in Fig. 2 c). In Fig. 3, we provide four additional examples of insulators as an illustration of these rules for Chern number states, which at odd filling are the theoretical ground-states, while at even filling are the ground-states in-field [12, 15, 17, 25, 26, 81]. The $\nu = -2$ valley polarized $C = 2$ Chern insulator and the $\nu = -1$ fully valley polarized $C = 3$ Chern insulator trivially have no KD. The $\nu = -2$ IVC $C = 2$ Chern insulator does exhibit KD since the valley polarizations of the two bands projected in the xy plane of the valley Bloch sphere do not cancel out. Finally, the $\nu = -1$ partially valley-coherent $C = 1$ Chern insulator has one VP filled Chern band and a pair of filled IVC Chern bands, satisfying rule 2 and therefore it does not display any KD. Between states showing no KD, further LDOS differences exist because the Chern band operators $\hat{d}^{\dagger}_{\mathbf{k},e_Y,\eta,s}$ are primarily located on a single SLG sublattice, depending on $e_Y\eta = \pm 1$. In the $\nu = -2$, $C = 2$ state, two Chern bands with $e_Y = +1$ are occupied in the same valley $\eta = +$ (and two spin sectors), leading to the appearance of a triangular lattice in the STM signal from Fig. 3 a). To obtain the VP $\nu = -1$, $C = 3$ (IVC $\nu = -1$, $C = 1$) state, a Chern band with $\eta = -$, $e_Y = +1$ ($\eta = +$, $e_Y = -1$) is added, which is polarized primarily on the other graphene sublattice. Hence two inter-penetrating triangular lattices of weight $2:1$ appear in the LDOS patterns from Fig. 3 g) and j).

Conclusion. In the current letter we analyzed the spectroscopic signal of a multitude of the predicted candidates for the correlated insulators in TBG. We showed that, surprisingly, the Chern zero celebrated KIVC state at $\nu = \pm 2$, along with other KIVC states at $\nu = 0$ do not exhibit a KD pattern, while other IVC states, including the TIVC and the Chern 2 state at $\nu = \pm 2$ do exhibit KD. We analytically obtain the LDOS signal for a large number of correlated insulator states, and show which IVC states do not/do have KD patterns. We identify the LDOS signal from the correlated insulators and show how it can be used to differentiate between the ground-states. Furthermore we show that at band-insulator filling $\nu = \pm 4$, where the ground-state is known without ambiguity, the strong coupling LDOS differs dramatically from the weak coupling one due to the fundamentally different nature of the quasiparticle dispersion. We identified several additional signatures of strong coupling regime, including a specific variation of the LDOS signal from AA to AB sites. Although experimental data varies from sample to sample, we present STM data which fits the overall aspects of the predicted signal while being in contradiction with a weak-coupling picture.

Acknowledgments. We thank Fang Xie for fruitful discussions. During the later stages of preparation of our manuscript, we became aware of a similar work, to be posted on the same date, by JP Hong, T. Soejima, M. Zaletel, which also computes the STM signal of various TBG states. B.A.B. and N.R. were supported by the

Office of Naval Research (ONR Grant No. N00014-20-1-2303), U.S. Department of Energy (Grant No. DE-SC0016239), and were partially supported by the National Science Foundation (EAGER Grant No. DMR 1643312), a Simons Investigator grant (No. 404513), the Packard Foundation, the Schmidt Fund for Innovative Research, the BSF Israel US foundation (Grant No. 2018226), the Gordon and Betty Moore Foundation through Grant No. GBMF8685 towards the Princeton theory program, and a Guggenheim Fellowship from the John Simon Guggenheim Memorial Foundation. B.A.B. and N.R. were supported by the NSF-MRSEC (Grant No. DMR-2011750). B.A.B. and N.R. gratefully acknowledge financial support from the Schmidt DataX Fund at Princeton University made possible through a major gift from the Schmidt Futures Foundation. This work is also partly supported by a project that has received funding from the European Research Council (ERC) under the European Union's Horizon 2020 research and innovation programme (grant agreement no. 101020833). O. V. is supported by NSF DMR-1916958 and partially by the National High Magnetic Field Laboratory through NSF Grant No. DMR-1157490 and the State of Florida. This work was also supported by the Gordon and Betty Moore Foundation's EPiQS initiative grants GBMF9469 and DOE-BES grant DE-FG02-07ER46419 to A.Y. Other support for the experimental work was provided by NSF-MRSEC through the Princeton Center for Complex Materials NSF-DMR- 2011750, NSF-DMR-1904442, ExxonMobil through the Andlinger Center for Energy and the Environment at Princeton, and the Princeton Catalysis Initiative. A.Y. acknowledge the hospitality of the Aspen Center for Physics, which is supported by National Science Foundation grant PHY-1607611, and Trinity College, Cambridge UK where part of this work was carried in with the support of in part by a QuantEmX grant from ICAM and the Gordon and Betty Moore Foundation through Grant GBMF9616.

[1] R. Bistritzer and A. H. MacDonald, PNAS **108**, 12233 (2011).
[2] J. M. B. Lopes dos Santos, N. M. R. Peres, and A. H. Castro Neto, Phys. Rev. Lett. **99**, 256802 (2007).
[3] E. Suárez Morell, J. D. Correa, P. Vargas, M. Pacheco, and Z. Barticevic, Phys. Rev. B **82**, 121407 (2010).
[4] Y. Cao, V. Fatemi, A. Demir, S. Fang, S. L. Tomarken, J. Y. Luo, J. D. Sanchez-Yamagishi, K. Watanabe, T. Taniguchi, E. Kaxiras, R. C. Ashoori, and P. Jarillo-Herrero, Nature **556**, 80 (2018).
[5] M. Yankowitz, S. Chen, H. Polshyn, Y. Zhang, K. Watanabe, T. Taniguchi, D. Graf, A. F. Young, and C. R. Dean, Science **363**, 1059 (2019).
[6] X. Lu, P. Stepanov, W. Yang, M. Xie, M. A. Aamir, I. Das, C. Urgell, K. Watanabe, T. Taniguchi, G. Zhang, A. Bachtold, A. H. MacDonald, and D. K. Efetov, Nature **574**, 653 (2019).
[7] H. Polshyn, M. Yankowitz, S. Chen, Y. Zhang, K. Watanabe, T. Taniguchi, C. R. Dean, and A. F. Young, Nat. Phys. **15**, 1011 (2019).
[8] Y. Cao, D. Chowdhury, D. Rodan-Legrain, O. Rubies-Bigorda, K. Watanabe, T. Taniguchi, T. Senthil, and P. Jarillo-Herrero, Phys. Rev. Lett. **124**, 076801 (2020).
[9] M. Serlin, C. L. Tschirhart, H. Polshyn, Y. Zhang, J. Zhu, K. Watanabe, T. Taniguchi, L. Balents, and A. F. Young, Science **367**, 900 (2020).
[10] G. Chen, A. L. Sharpe, E. J. Fox, Y.-H. Zhang, S. Wang, L. Jiang, B. Lyu, H. Li, K. Watanabe, T. Taniguchi, Z. Shi, T. Senthil, D. Goldhaber-Gordon, Y. Zhang, and F. Wang, Nature **579**, 56 (2020).
[11] P. Stepanov, I. Das, X. Lu, A. Fahimniya, K. Watanabe, T. Taniguchi, F. H. L. Koppens, J. Lischner, L. Levitov, and D. K. Efetov, Nature **583**, 375 (2020).
[12] X. Liu, Z. Wang, K. Watanabe, T. Taniguchi, O. Vafek, and J. I. A. Li, arXiv:2003.11072 [cond-mat] (2020), arXiv:2003.11072 [cond-mat].
[13] J. M. Park, Y. Cao, K. Watanabe, T. Taniguchi, and P. Jarillo-Herrero, arXiv:2008.12296 [cond-mat] (2020), arXiv:2008.12296 [cond-mat].
[14] Y. Saito, J. Ge, K. Watanabe, T. Taniguchi, and A. F. Young, Nat. Phys. **16**, 926 (2020).
[15] S. Wu, Z. Zhang, K. Watanabe, T. Taniguchi, and E. Y. Andrei, arXiv:2007.03735 [cond-mat] (2020), arXiv:2007.03735 [cond-mat].
[16] X. Lu, B. Lian, G. Chaudhary, B. A. Piot, G. Romagnoli, K. Watanabe, T. Taniguchi, M. Poggio, A. H. MacDonald, B. A. Bernevig, and D. K. Efetov, arXiv:2006.13963 [cond-mat] (2020), arXiv:2006.13963 [cond-mat].
[17] Y. Saito, J. Ge, L. Rademaker, K. Watanabe, T. Taniguchi, D. A. Abanin, and A. F. Young, Nat. Phys. , 1 (2021).
[18] Y. Cao, D. Rodan-Legrain, J. M. Park, N. F. Q. Yuan, K. Watanabe, T. Taniguchi, R. M. Fernandes, L. Fu, and P. Jarillo-Herrero, Science **372**, 264 (2021).
[19] A. Kerelsky, L. J. McGilly, D. M. Kennes, L. Xian, M. Yankowitz, S. Chen, K. Watanabe, T. Taniguchi, J. Hone, C. Dean, A. Rubio, and A. N. Pasupathy, Nature **572**, 95 (2019).
[20] Y. Xie, B. Lian, B. Jäck, X. Liu, C.-L. Chiu, K. Watanabe, T. Taniguchi, B. A. Bernevig, and A. Yazdani, Nature **572**, 101 (2019).
[21] Y. Jiang, X. Lai, K. Watanabe, T. Taniguchi, K. Haule, J. Mao, and E. Y. Andrei, Nature **573**, 91 (2019).
[22] Y. Choi, J. Kemmer, Y. Peng, A. Thomson, H. Arora, R. Polski, Y. Zhang, H. Ren, J. Alicea, G. Refael, F. von Oppen, K. Watanabe, T. Taniguchi, and S. Nadj-Perge, Nat. Phys. **15**, 1174 (2019).
[23] D. Wong, K. P. Nuckolls, M. Oh, B. Lian, Y. Xie, S. Jeon, K. Watanabe, T. Taniguchi, B. A. Bernevig, and A. Yazdani, Nature **582**, 198 (2020).
[24] Y. Choi, H. Kim, Y. Peng, A. Thomson, C. Lewandowski, R. Polski, Y. Zhang, H. S. Arora, K. Watanabe, T. Taniguchi, J. Alicea, and S. Nadj-Perge, arXiv:2008.11746 [cond-mat] (2020), arXiv:2008.11746 [cond-mat].
[25] K. P. Nuckolls, M. Oh, D. Wong, B. Lian, K. Watanabe, T. Taniguchi, B. A. Bernevig, and A. Yazdani, Nature

588, 610 (2020).
[26] Y. Choi, H. Kim, Y. Peng, A. Thomson, C. Lewandowski, R. Polski, Y. Zhang, H. S. Arora, K. Watanabe, T. Taniguchi, J. Alicea, and S. Nadj-Perge, Nature **589**, 536 (2021).
[27] Y. Choi, H. Kim, C. Lewandowski, Y. Peng, A. Thomson, R. Polski, Y. Zhang, K. Watanabe, T. Taniguchi, J. Alicea, and S. Nadj-Perge, arXiv:2102.02209 [cond-mat] (2021), arXiv:2102.02209 [cond-mat].
[28] C. L. Tschirhart, M. Serlin, H. Polshyn, A. Shragai, Z. Xia, J. Zhu, Y. Zhang, K. Watanabe, T. Taniguchi, M. E. Huber, and A. F. Young, Science **372**, 1323 (2021).
[29] N. F. Q. Yuan and L. Fu, Phys. Rev. B **98**, 045103 (2018).
[30] M. Ochi, M. Koshino, and K. Kuroki, Phys. Rev. B **98**, 081102 (2018).
[31] A. Thomson, S. Chatterjee, S. Sachdev, and M. S. Scheurer, Phys. Rev. B **98**, 075109 (2018).
[32] J. F. Dodaro, S. A. Kivelson, Y. Schattner, X. Q. Sun, and C. Wang, Phys. Rev. B **98**, 075154 (2018).
[33] X. Y. Xu, K. T. Law, and P. A. Lee, Phys. Rev. B **98**, 121406 (2018).
[34] M. Koshino, N. F. Q. Yuan, T. Koretsune, M. Ochi, K. Kuroki, and L. Fu, Phys. Rev. X **8**, 031087 (2018).
[35] H. C. Po, L. Zou, A. Vishwanath, and T. Senthil, Phys. Rev. X **8**, 031089 (2018).
[36] J. W. F. Venderbos and R. M. Fernandes, Phys. Rev. B **98**, 245103 (2018).
[37] D. M. Kennes, J. Lischner, and C. Karrasch, Phys. Rev. B **98**, 241407 (2018).
[38] T. Huang, L. Zhang, and T. Ma, Science Bulletin **64**, 310 (2019).
[39] J. Liu, J. Liu, and X. Dai, Phys. Rev. B **99**, 155415 (2019).
[40] X.-C. Wu, C.-M. Jian, and C. Xu, Phys. Rev. B **99**, 161405 (2019).
[41] L. Classen, C. Honerkamp, and M. M. Scherer, Phys. Rev. B **99**, 195120 (2019).
[42] J. Kang and O. Vafek, Phys. Rev. Lett. **122**, 246401 (2019).
[43] K. Seo, V. N. Kotov, and B. Uchoa, Phys. Rev. Lett. **122**, 246402 (2019).
[44] Y. Da Liao, Z. Y. Meng, and X. Y. Xu, Phys. Rev. Lett. **123**, 157601 (2019).
[45] F. Wu and S. Das Sarma, Phys. Rev. Lett. **124**, 046403 (2020).
[46] M. Xie and A. H. MacDonald, Phys. Rev. Lett. **124**, 097601 (2020).
[47] N. Bultinck, S. Chatterjee, and M. P. Zaletel, Phys. Rev. Lett. **124**, 166601 (2020).
[48] A. Davydov, K. Choo, M. H. Fischer, and T. Neupert, arXiv:2012.12942 [cond-mat] (2020), arXiv:2012.12942 [cond-mat].
[49] D. V. Chichinadze, L. Classen, and A. V. Chubukov, Phys. Rev. B **102**, 125120 (2020).
[50] S. Chatterjee, N. Bultinck, and M. P. Zaletel, Phys. Rev. B **101**, 165141 (2020).
[51] C. Repellin, Z. Dong, Y.-H. Zhang, and T. Senthil, Phys. Rev. Lett. **124**, 187601 (2020).
[52] K. Hejazi, X. Chen, and L. Balents, arXiv:2007.00134 [cond-mat] (2020), arXiv:2007.00134 [cond-mat].
[53] T. Cea and F. Guinea, Phys. Rev. B **102**, 045107 (2020).
[54] Y. Zhang, K. Jiang, Z. Wang, and F. Zhang, Phys. Rev. B **102**, 035136 (2020).
[55] J. Kang and O. Vafek, Phys. Rev. B **102**, 035161 (2020).
[56] R. M. Fernandes and J. W. F. Venderbos, Science Advances **6**, eaba8834 (2020).
[57] E. Brillaux, D. Carpentier, A. A. Fedorenko, and L. Savary, arXiv:2008.05041 [cond-mat] (2020), arXiv:2008.05041 [cond-mat].
[58] N. Bultinck, E. Khalaf, S. Liu, S. Chatterjee, A. Vishwanath, and M. P. Zaletel, Phys. Rev. X **10**, 031034 (2020).
[59] M. Xie and A. H. MacDonald, arXiv:2010.07928 [cond-mat] (2020), arXiv:2010.07928 [cond-mat].
[60] T. Soejima, D. E. Parker, N. Bultinck, J. Hauschild, and M. P. Zaletel, Phys. Rev. B **102**, 205111 (2020).
[61] M. Christos, S. Sachdev, and M. S. Scheurer, PNAS **117**, 29543 (2020).
[62] P. Eugenio and C. Dag, SciPost Physics Core **3**, 015 (2020).
[63] O. Vafek and J. Kang, Phys. Rev. Lett. **125**, 257602 (2020).
[64] S. Liu, E. Khalaf, J. Y. Lee, and A. Vishwanath, Phys. Rev. Research **3**, 013033 (2021).
[65] Y. Da Liao, J. Kang, C. N. Breiø, X. Y. Xu, H.-Q. Wu, B. M. Andersen, R. M. Fernandes, and Z. Y. Meng, Phys. Rev. X **11**, 011014 (2021).
[66] J. Liu and X. Dai, Phys. Rev. B **103**, 035427 (2021).
[67] J. Kang, B. A. Bernevig, and O. Vafek, arXiv:2104.01145 [cond-mat] (2021), arXiv:2104.01145 [cond-mat].
[68] B. Lian, Z.-D. Song, N. Regnault, D. K. Efetov, A. Yazdani, and B. A. Bernevig, Phys. Rev. B **103**, 205414 (2021).
[69] F. Xie, A. Cowsik, Z.-D. Song, B. Lian, B. A. Bernevig, and N. Regnault, Phys. Rev. B **103**, 205416 (2021).
[70] D. E. Parker, T. Soejima, J. Hauschild, M. P. Zaletel, and N. Bultinck, Phys. Rev. Lett. **127**, 027601 (2021).
[71] Y. H. Kwan, G. Wagner, T. Soejima, M. P. Zaletel, S. H. Simon, S. A. Parameswaran, and N. Bultinck, arXiv:2105.05857 [cond-mat] (2021), arXiv:2105.05857 [cond-mat].
[72] B.-B. Chen, Y. D. Liao, Z. Chen, O. Vafek, J. Kang, W. Li, and Z. Y. Meng, Nat Commun **12**, 5480 (2021).
[73] G. Wagner, Y. H. Kwan, N. Bultinck, S. H. Simon, and S. A. Parameswaran, arXiv:2109.09749 [cond-mat] (2021), arXiv:2109.09749 [cond-mat].
[74] B. A. Bernevig, Z.-D. Song, N. Regnault, and B. Lian, Phys. Rev. B **103**, 205413 (2021).
[75] B. A. Bernevig, B. Lian, A. Cowsik, F. Xie, N. Regnault, and Z.-D. Song, Phys. Rev. B **103**, 205415 (2021).
[76] P. Potasz, M. Xie, and A. H. MacDonald, arXiv:2102.02256 [cond-mat] (2021), arXiv:2102.02256 [cond-mat].
[77] P. Coleman, *Introduction to Many-Body Physics* (Cambridge University Press, Cambridge, 2015).
[78] X. Liu, G. Farahi, C.-L. Chiu, Z. Papic, K. Watanabe, T. Taniguchi, M. P. Zaletel, and A. Yazdani, arXiv:2109.11555 [cond-mat] (2021), arXiv:2109.11555 [cond-mat].
[79] A. Coissard, D. Wander, H. Vignaud, A. G. Grushin, C. Repellin, K. Watanabe, T. Taniguchi, F. Gay, C. Winkelmann, H. Courtois, H. Sellier, and B. Sacépé, arXiv:2110.02811 [cond-mat] (2021), arXiv:2110.02811 [cond-mat].
[80] X. Li, F. Wu, and A. H. MacDonald, arXiv:1907.12338

[cond-mat] (2019), arXiv:1907.12338 [cond-mat].
[81] I. Das, X. Lu, J. Herzog-Arbeitman, Z.-D. Song, K. Watanabe, T. Taniguchi, B. A. Bernevig, and D. K. Efetov, arXiv:2007.13390 [cond-mat] (2020), arXiv:2007.13390 [cond-mat].
[82] Z. Song, Z. Wang, W. Shi, G. Li, C. Fang, and B. A. Bernevig, Phys. Rev. Lett. **123**, 036401 (2019).
[83] J. Kang and O. Vafek, Phys. Rev. X **8**, 031088 (2018).
[84] Z.-D. Song, B. Lian, N. Regnault, and B. A. Bernevig, Phys. Rev. B **103**, 205412 (2021).
[85] H. C. Po, L. Zou, T. Senthil, and A. Vishwanath, Phys. Rev. B **99**, 195455 (2019).
[86] G. Tarnopolsky, A. J. Kruchkov, and A. Vishwanath, Phys. Rev. Lett. **122**, 106405 (2019).
[87] B. A. Bernevig, Z.-D. Song, N. Regnault, and B. Lian, Phys. Rev. B **103**, 205411 (2021).
[88] K. Uchida, S. Furuya, J.-I. Iwata, and A. Oshiyama, Phys. Rev. B **90**, 155451 (2014).
[89] M. M. van Wijk, A. Schuring, M. I. Katsnelson, and A. Fasolino, 2D Mater. **2**, 034010 (2015).
[90] S. Dai, Y. Xiang, and D. J. Srolovitz, Nano Lett. **16**, 5923 (2016).
[91] S. K. Jain, V. Juričić, and G. T. Barkema, 2D Mater. **4**, 015018 (2016).
[92] J. Wang, Y. Zheng, A. J. Millis, and J. Cano, arXiv:2010.03589 [cond-mat] (2020), arXiv:2010.03589 [cond-mat].
[93] J. Ahn, S. Park, and B.-J. Yang, Phys. Rev. X **9**, 021013 (2019).
[94] A. A. Radzig and B. M. Smirnov, *Reference Data on Atoms, Molecules, and Ions*, Springer Series in Chemical Physics (Springer-Verlag, Berlin Heidelberg, 1985).
[95] M. Ijäs, M. Ervasti, A. Uppstu, P. Liljeroth, J. van der Lit, I. Swart, and A. Harju, Phys. Rev. B **88**, 075429 (2013).
[96] N. M. R. Peres, L. Yang, and S.-W. Tsai, New J. Phys. **11**, 095007 (2009).
[97] M. M. Ervasti, F. Schulz, P. Liljeroth, and A. Harju, J. Electron Spectrosc. Relat. Phenom. SI: The Electronic Structure of 2D and Layered Materials, **219**, 63 (2017).
[98] A. H. Barnett, J. Magland, and L. af Klinteberg, SIAM J. Sci. Comput. **41**, C479 (2019).
[99] A. H. Barnett, Appl. Comput. Harmon. Anal. **51**, 1 (2021).
[100] J. R. Yates, X. Wang, D. Vanderbilt, and I. Souza, Phys. Rev. B **75**, 195121 (2007).
[101] C. Gutiérrez, C.-J. Kim, L. Brown, T. Schiros, D. Nordlund, E. B. Lochocki, K. M. Shen, J. Park, and A. N. Pasupathy, Nat. Phys. **12**, 950 (2016).
[102] C. Bao, H. Zhang, T. Zhang, X. Wu, L. Luo, S. Zhou, Q. Li, Y. Hou, W. Yao, L. Liu, P. Yu, J. Li, W. Duan, H. Yao, Y. Wang, and S. Zhou, Phys. Rev. Lett. **126**, 206804 (2021).
[103] D. Wong, S. Jeon, K. P. Nuckolls, M. Oh, S. C. J. Kingsley, and A. Yazdani, Review of Scientific Instruments **91**, 023703 (2020).
[104] K. Kim, M. Yankowitz, B. Fallahazad, S. Kang, H. C. P. Movva, S. Huang, S. Larentis, C. M. Corbet, T. Taniguchi, K. Watanabe, S. K. Banerjee, B. J. LeRoy, and E. Tutuc, Nano Lett. **16**, 1989 (2016).

CONTENTS

Appendix A: Review of notation

This appendix provides a short review of the single-particle and interacting twisted bilayer graphene (TBG) Hamiltonians. We will follow the same conventions as those employed in Refs. [68, 69, 74, 75, 84, 87], to which the interested reader is referred for more details. After briefly discussing the Bistritzer-MacDonald model of the single-particle Hamiltonian [1], we outline the discrete symmetries of TBG, which were extensively discussed in Refs. [74, 82, 84–86], as well as the gauge-fixing procedure used throughout this work [74]. We then review the TBG interaction Hamiltonian [42, 43, 58, 74] and its enlarged continuous symmetries arising under various limits [42, 43, 58, 63, 74]. These will be used extensively in our analytical proofs of the LDOS signal.

1. Single-particle Hamiltonian

a. Fermion operators on the moiré lattice

TBG consists of two graphene layers rotated at an angle θ relative to one another. We define $\mathcal{R}_{\theta,l}$ to be the matrix implementing the rotation transformation corresponding to the graphene layer $l = \pm$ (where $l = +$ denotes the top layer, while $l = -$ denotes the bottom layer) relative to a *reference* (*i.e.* unrotated) coordinate system

$$\mathcal{R}_{\theta,l} = \begin{pmatrix} \cos\left(\frac{\theta l}{2}\right) & -\sin\left(\frac{\theta l}{2}\right) \\ \sin\left(\frac{\theta l}{2}\right) & \cos\left(\frac{\theta l}{2}\right) \end{pmatrix}. \tag{A1}$$

Within layer l, we define $\hat{a}^\dagger_{\mathbf{R},\alpha,s,l}$ to be the microscopic fermion operator creating an electron of spin $s =\uparrow,\downarrow$ in the unit cell indexed by $\mathbf{R}$ (but located at $\mathcal{R}_{\theta,l}\mathbf{R}$) and graphene sublattice $\alpha = A, B$. $\mathbf{R}$ belongs to the reference single layer graphene (SLG) lattice, *i.e.* $\mathbf{R} \in \mathbb{Z}\mathbf{a}_1 + \mathbb{Z}\mathbf{a}_2$, where

$$\mathbf{a}_1 = a_0 \left(\frac{1}{3}, \frac{1}{\sqrt{3}}\right)^T, \qquad \mathbf{a}_2 = a_0 \left(\frac{1}{3}, -\frac{1}{\sqrt{3}}\right)^T \tag{A2}$$

are the primitive SLG lattice vectors, with a_0 being the length of a carbon-carbon bond, as shown in Fig. 4. We also define the displacement vectors for the two graphene sublattices relative to the SLG unit cell origin according to

$$\mathbf{t}_A = \frac{2}{3}\mathbf{a}_1 + \frac{1}{3}\mathbf{a}_2, \qquad \mathbf{t}_B = \frac{1}{3}\mathbf{a}_1 + \frac{2}{3}\mathbf{a}_2. \tag{A3}$$

Using Eqs. (A1) to (A3), we can write the Fourier transformation of the $\hat{a}^\dagger_{\mathbf{R},\alpha,s,l}$ operators over the SLG Brillouin Zone BZ_l corresponding to layer l as

$$\hat{a}^\dagger_{\mathbf{R},\alpha,s,l} = \frac{1}{\sqrt{N_0}} \sum_{\mathbf{p}\in \mathrm{BZ}_l} \hat{a}^\dagger_{\mathbf{p},\alpha,s,l} e^{-i\mathbf{p}\cdot\mathcal{R}_{\theta,l}(\mathbf{R}+\mathbf{t}_\alpha)}. \tag{A4}$$

In Eq. (A4), N_0 represents the number of unit cells in each graphene layer, and the momentum $\mathbf{p}$ is measured from the Γ point of BZ_l. It is also useful to introduce the reciprocal lattices corresponding to the two graphene layers. More precisely, we let $\mathcal{G}_l = \mathbb{Z}\mathbf{g}_{l,1} + \mathbb{Z}\mathbf{g}_{l,2}$ be the reciprocal lattice corresponding to layer l, generated by the reciprocal vectors $\mathbf{g}_{l,i} = \mathcal{R}_{\theta,l}\mathbf{g}_i$, where the reference or unrotated reciprocal lattice vectors $\mathbf{g}_i$ are given by

$$\mathbf{g}_1 = \frac{2\pi}{a_0}\left(\frac{3}{2}, \frac{\sqrt{3}}{2}\right)^T, \qquad \mathbf{g}_2 = \frac{2\pi}{a_0}\left(\frac{3}{2}, -\frac{\sqrt{3}}{2}\right)^T. \tag{A5}$$

Focusing on TBG, we define $\mathbf{K}_l = \frac{1}{3}(\mathbf{g}_{l,1} + \mathbf{g}_{l,2})$ as the K point of the SLG Brillouin Zone BZ_l. $\mathbf{K}_+$ and $\mathbf{K}_-$ differ by a twist angle θ. We take $\mathbf{K}_\pm$ to be along the direction with an angle $\pm\theta/2$ to the $\hat{\mathbf{x}}$ axis. Each graphene layer contains two valleys K and K', labeled by $\eta = \pm$ and located at momenta $\eta\mathbf{K}_\pm$, corresponding to the two (decoupled) valleys of the moiré single-particle Hamiltonian.

Introducing the two-dimensional momenta

$$\mathbf{q}_1 = (\mathbf{K}_+ - \mathbf{K}_-) = k_\theta (0,1)^T, \qquad \mathbf{q}_2 = C_{3z}\mathbf{q}_1 = k_\theta \left(-\frac{\sqrt{3}}{2}, -\frac{1}{2}\right)^T, \qquad \mathbf{q}_3 = C_{3z}^2\mathbf{q}_1 = k_\theta \left(\frac{\sqrt{3}}{2}, -\frac{1}{2}\right)^T, \tag{A6}$$

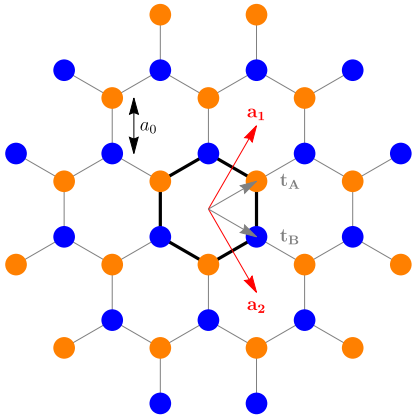

FIG. 4. The reference single layer graphene (SLG) lattice. The corresponding triangular lattice is generated by the lattice vectors $\mathbf{a}_1$ and $\mathbf{a}_2$. Within each unit cell, we denote the carbon atoms belonging to the two sublattices A and B by orange and blue circles, respectively. The nearest-neighbor distance between two carbon atoms is given by a_0. Additionally, $\mathbf{t}_A$ and $\mathbf{t}_B$ respectively denote the displacements corresponding to sublattices A and B. The top ($l = +1$) and bottom ($l = -1$) graphene layers of TBG are obtained by rotating the reference lattice by an angle $l\theta/2$.

where $k_\theta = |\mathbf{K}_- - \mathbf{K}_+| = 2|\mathbf{K}_+|\sin(\theta/2)$, we can define the moiré Brillouin Zone (MBZ) for the (triangular) TBG moiré lattice $\mathcal{Q}_0 = \mathbb{Z}\mathbf{b}_{M1} + \mathbb{Z}\mathbf{b}_{M2}$, which is generated by the reciprocal vectors

$$\mathbf{b}_{M1} = \mathbf{q}_3 - \mathbf{q}_1 \ , \qquad \mathbf{b}_{M2} = \mathbf{q}_3 - \mathbf{q}_2. \tag{A7}$$

Additionally, we introduce two shifted momentum lattices $\mathcal{Q}_+ = \mathbf{q}_1 + \mathcal{Q}_0$ and $\mathcal{Q}_- = -\mathbf{q}_1 + \mathcal{Q}_0$, which together form a honeycomb lattice. This allows us to define the low-energy TBG fermion operators as

$$\hat{c}^\dagger_{\mathbf{k},\mathbf{Q},\eta,\alpha,s} \equiv \hat{a}^\dagger_{\eta\mathbf{K}_l+\mathbf{k}-\mathbf{Q},\alpha,s,l}, \qquad \text{for} \qquad \mathbf{Q} \in \mathcal{Q}_{\eta l}, \tag{A8}$$

with $\mathbf{k} \in$ MBZ and $\mathbf{k} = \mathbf{0}$ representing the Γ_M point (*i.e.* the Γ point of the MBZ).

b. Hamiltonian and the energy band basis

The Bistrizer-MacDonald model [1] for the single-particle TBG Hamiltonian reads as [74, 84, 87]

$$\hat{H}_0 = \sum_{\mathbf{k}\in\text{MBZ}} \sum_{\eta,\alpha,\beta,s} \sum_{\mathbf{Q},\mathbf{Q}'\in\mathcal{Q}_\pm} \left[h^{(\eta)}_{\mathbf{Q},\mathbf{Q}'}(\mathbf{k})\right]_{\alpha\beta} \hat{c}^\dagger_{\mathbf{k},\mathbf{Q},\eta,\alpha,s}\hat{c}_{\mathbf{k},\mathbf{Q}',\eta,\beta,s}, \tag{A9}$$

where the first-quantized TBG Hamiltonian in valley η, $h^{(\eta)}_{\mathbf{Q},\mathbf{Q}'}(\mathbf{k})$, is independent on spin as a consequence of the absence of spin-orbit coupling in SLG. In valley $\eta = +$, it takes the form

$$h^{(+)}_{\mathbf{Q},\mathbf{Q}'}(\mathbf{k}) = v_F\delta_{\mathbf{Q},\mathbf{Q}'}(\mathbf{k}-\mathbf{Q})\cdot\boldsymbol{\sigma} - \lambda v_F\frac{\theta}{2}\zeta_{\mathbf{Q}}\delta_{\mathbf{Q},\mathbf{Q}'}(\mathbf{k}-\mathbf{Q})\times\boldsymbol{\sigma} + \sum_{j=1}^{3} T_j\delta_{\mathbf{Q},\mathbf{Q}'\pm\mathbf{q}_j}, \tag{A10}$$

where v_F is SLG Fermi velocity, θ is the twist angle, $\boldsymbol{\sigma} = (\sigma_x, \sigma_y)$, $\zeta_{\mathbf{Q}}$ is the sublattice factor

$$\zeta_{\mathbf{Q}} = \begin{cases} +1 & \text{if} \quad \mathbf{Q} \in \mathcal{Q}_+ \\ -1 & \text{if} \quad \mathbf{Q} \in \mathcal{Q}_- \end{cases}, \tag{A11}$$

and the T_j's represent the inter-layer tunneling matrices defined according to

$$T_j = w_0\sigma_0 + w_1\left[\sigma_x\cos\frac{2\pi\,(j-1)}{3} + \sigma_y\sin\frac{2\pi\,(j-1)}{3}\right], \quad \text{for} \quad j = 1,2,3 \tag{A12}$$

For small angles θ, the second term in Eq. (A10) is suppressed in magnitude with respect to the first one and is usually neglected [82, 84]. We will investigate its effects through the parameter $\lambda = 0, 1$. For $\lambda = 0$ the TBG Hamiltonian

features a unitary particle-hole symmetry, which is only slightly broken in the case $\lambda = 1$ [82, 84]. The tunneling matrices T_j ($1 \leq j \leq 3$) depend on two parameters, $w_0 \geq 0$ and $w_1 \geq 0$, which are the inter-layer hoppings at the AA and AB stacking centers of the two graphene sheets, respectively. Generically, in realistic systems $w_0 < w_1$ due to lattice relaxation and corrugation effects [84, 88–91]. For the numerical calculations in this paper, we will use $\theta = 1.05^\circ$, $w_1 = 110\,\text{meV}$, $v_F = 5.944\,\text{eV}\,\text{Å}$, $|\mathbf{K}_+| = 1.703\,\text{Å}^{-1}$, and explore multiple values of the ratio $w_0/w_1 \leq 1$. Finally, we note that the first-quantized Hamiltonian in valley $\eta = -$ is obtained through

$$h^{(-)}_{\mathbf{Q},\mathbf{Q}'}(\mathbf{k}) = \sigma_x h^{(+)}_{-\mathbf{Q},-\mathbf{Q}'}(-\mathbf{k})\,\sigma_x. \tag{A13}$$

The TBG Hamiltonian in Eq. (A9) can be diagonalized as follows

$$\hat{H}_0 = \sum_{\mathbf{k}\in\text{MBZ}} \sum_{\eta,n,s} \epsilon_{n,\eta}(\mathbf{k})\,\hat{c}^\dagger_{\mathbf{k},n,\eta,s}\hat{c}_{\mathbf{k},n,\eta,s}, \tag{A14}$$

where

$$\hat{c}^\dagger_{\mathbf{k},n,\eta,s} = \sum_{\mathbf{Q}\in\mathcal{Q}_\pm,\alpha} u_{\mathbf{Q}\alpha;n\eta}(\mathbf{k})\,\hat{c}^\dagger_{\mathbf{k},\mathbf{Q},\eta,\alpha,s}, \tag{A15}$$

are the energy band operators. We define $u_{\mathbf{Q}\alpha;n\eta}(\mathbf{k})$ to be the eigenstate wave functions of energy band n of the first quantized single-particle TBG Hamiltonian [74]

$$\sum_\beta \sum_{\mathbf{Q}'\in\mathcal{Q}_\pm} \left[h^{(\eta)}_{\mathbf{Q},\mathbf{Q}'}\right]_{\alpha\beta} u_{\mathbf{Q}'\beta;n\eta}(\mathbf{k}) = \epsilon_{n,\eta} u_{\mathbf{Q}\alpha;n\eta}(\mathbf{k}). \tag{A16}$$

For each valley and spin, we will use the integer $n > 0$ to denote the n-th conduction band and use the integer $n < 0$ to label the $|n|$-th valence band. Throughout this paper, we will be concerned exclusively with the active TBG bands (corresponding to $n = \pm 1$). Finally, we note that the completeness of the TBG eigenstate wave functions allows us to express the moiré lattice operators from Eq. (A8) in the energy band basis as

$$\hat{c}^\dagger_{\mathbf{k},\mathbf{Q},\eta,\alpha,s} = \sum_n u^*_{\mathbf{Q}\alpha;n\eta}(\mathbf{k})\,\hat{c}^\dagger_{\mathbf{k},n,\eta,s}. \tag{A17}$$

c. *Discrete symmetries of TBG*

We now briefly review the discrete symmetries of TBG which have been derived and extensively discussed in Refs. [74, 82, 84–86]. Since graphene has zero spin-orbit coupling, we can define a set of spinless symmetry transformations for TBG: the spinless unitary discrete symmetries C_{2z}, C_{3z}, C_{2x}, and the spinless anti-unitary time-reversal symmetry T. In addition to the above symmetry operators which commute with the many-body projected Hamiltonian of TBG (H), one can also define a unitary particle-hole transformation P [82, 84], as well as a chiral transformation C [86]. The particle-hole transformation is an anticommuting symmetry of the single-particle TBG Hamiltonian from Eq. (A9) for $\lambda = 0$, and remains an approximate symmetry of the model for $\lambda = 1$ [82, 84]. In the first chiral limit, when the inter-layer AA-hopping w_0 can be neglected ($w_0 = 0$), the chiral transformation C also denotes an anticommuting symmetry of $\hat{H}_0$ [74, 86]. It is worth noting, that the first chiral limit *always* implies the presence of particle-hole symmetry, as the second term in Eq. (A10) can be gauged away [86, 92].

We denote the action of any symmetry transformation operator g on the moiré lattice fermions to be

$$g\hat{c}^\dagger_{\mathbf{k},\mathbf{Q},\eta,\alpha,s}g^{-1} = \sum_{\mathbf{Q}',\eta',\beta} [D(g)]_{\mathbf{Q}'\eta'\beta,\mathbf{Q}\eta\alpha}\,\hat{c}^\dagger_{g\mathbf{k},\mathbf{Q}',\eta',\beta,s}, \tag{A18}$$

where $D(g)$ is the representation matrix of the symmetry operator g in the space of indices $\{\mathbf{Q},\eta,\alpha\}$ of the $\hat{c}^\dagger_{\mathbf{k},\mathbf{Q},\eta,\alpha,s}$ fermion operators. We denote $g\mathbf{k}$ to be the momentum obtained after acting the transformation g on momentum $\mathbf{k}$. In particular $T\mathbf{k} = P\mathbf{k} = -\mathbf{k}$, while $C\mathbf{k} = \mathbf{k}$. The representation matrices for the discrete symmetries of TBG are given by [74, 82, 84]

$$[D(C_{2z})]_{\mathbf{Q}'\eta'\beta,\mathbf{Q}\eta\alpha} = \delta_{\mathbf{Q}',-\mathbf{Q}}\delta_{\eta',-\eta}(\sigma_x)_{\beta\alpha}, \tag{A19}$$

$$[D(C_{3z})]_{\mathbf{Q}'\eta'\beta,\mathbf{Q}\eta\alpha} = \delta_{\mathbf{Q}',C_{3z}\mathbf{Q}}\delta_{\eta',\eta}\left(e^{i\eta\frac{2\pi}{3}\sigma_z}\right)_{\beta\alpha}, \tag{A20}$$

$$[D(C_{2x})]_{\mathbf{Q}'\eta'\beta,\mathbf{Q}\eta\alpha} = \delta_{\mathbf{Q}',C_{2x}\mathbf{Q}}\delta_{\eta',\eta}(\sigma_x)_{\beta\alpha}, \tag{A21}$$

$$[D(T)]_{\mathbf{Q}'\eta'\beta,\mathbf{Q}\eta\alpha} = \delta_{\mathbf{Q}',-\mathbf{Q}}\delta_{\eta',-\eta}\delta_{\beta,\alpha}, \tag{A22}$$

$$[D(P)]_{\mathbf{Q}'\eta'\beta,\mathbf{Q}\eta\alpha} = \delta_{\mathbf{Q}',-\mathbf{Q}}\delta_{\eta',\eta}\delta_{\beta,\alpha}\zeta_{\mathbf{Q}}, \tag{A23}$$

$$[D(C)]_{\mathbf{Q}'\eta'\beta,\mathbf{Q}\eta\alpha} = \delta_{\mathbf{Q}',\mathbf{Q}}\delta_{\eta',\eta}(\sigma_z)_{\beta\alpha}, \tag{A24}$$

where in Eq. (A23), we have employed the sublattice factor $\zeta_{\mathbf{Q}}$ defined in Eq. (A11).

d. Gauge-fixing the single-particle spectrum

The symmetries presented in Appendix [A 1 c] yield certain relations between single-particle TBG eigenstates, which will prove instrumental in deriving the properties of the TBG spectral function. Here, we briefly review the gauge-fixing conditions for the TBG single-particle eigenstates defined in Eq. (A15) which were introduced in Refs. [74, 84].

For brevity, we will consider the wave function $u_{\mathbf{Q}\alpha;n\eta}(\mathbf{k})$ as a column vector $u_{n\eta}(\mathbf{k})$ in the space of indices $\{\mathbf{Q},\alpha\}$. Furthermore, when a representation matrix $D(g)$ of an operation g defined in Eq. (A18) acts on a wave function $u_{n\eta'}(\mathbf{k})$, we denote the resulting wave function in valley η for short as $\sum_{\eta'}[D(g)]_{\eta\eta'}u_{n\eta'}(\mathbf{k})$, the components of which are given by $\sum_{\mathbf{Q}'\beta\eta'}[D(g)]_{\mathbf{Q}\alpha\eta,\mathbf{Q}'\beta\eta'}u_{\mathbf{Q}'\beta;n\eta'}(\mathbf{k})$. Namely, we suppress the indices $\{\mathbf{Q},\alpha\}$ of the representation matrix $D(g)$ to streamline notation.

When g is a commuting (anticommuting) symmetry operator of the single-particle TBG Hamiltonian, if $u_{n\eta'}(\mathbf{k})$ is an eigenstate wave function at momentum $\mathbf{k}$, the wave function $\sum_{\eta}[D(g)]_{\eta\eta'}u_{n\eta'}(\mathbf{k})$ (an additional complex conjugation is needed if g is anti-unitary) must also be an eigenstate wave function at momentum $g\mathbf{k}$ at the same (opposite) single-particle energy. This allows us to define a sewing matrix corresponding to the symmetry operator g and the eigenstates $u_{n\eta'}(\mathbf{k})$

$$[D(g)]_{\eta\eta'}u_{n\eta'}(\mathbf{k}) = \sum_m [B^g(\mathbf{k})]_{m\eta,n\eta'}u_{m\eta}(g\mathbf{k}). \tag{A25}$$

In the energy band basis defined in Eq. (A15), a symmetry g acts as

$$g\hat{c}^\dagger_{\mathbf{k},n,\eta',s}g^{-1} = \sum_{m,\eta}[B^g(\mathbf{k})]_{m\eta,n\eta'}\hat{c}^\dagger_{g\mathbf{k},m,\eta,s}. \tag{A26}$$

The gauge-fixing of the TBG energy band operators was discussed at length in Refs. [74, 84]. We will first consider the particle-hole symmetric case ($\lambda = 0$). We will only summarize the results here and refer the reader to Refs. [74, 84] for complete proofs. All sewing matrices are closed within the pair of bands $n = \pm 1$. Therefore, for the bands with band index $n = \pm 1$, we will use ζ^a and τ^a ($a = 0, x, y, z$) to denote the identity and Pauli matrices in the energy band $n = \pm 1$ and the valley spaces, respectively. For all the symmetries that leave $\mathbf{k}$ invariant, the following $\mathbf{k}$-independent gauge-fixings will be adopted in this paper

$$B^{C_{2z}T}(\mathbf{k}) = \zeta^0\tau^0, \qquad B^{C_{2z}P}(\mathbf{k}) = \zeta^y\tau^y, \qquad B^C(\mathbf{k}) = \zeta^y\tau^z, \tag{A27}$$

where the sewing matrix corresponding to the chiral symmetry operator C is only applicable in the first chiral limit ($w_0/w_1 = 0$) [74, 86]. Additionally, we will further fix the relative gauge between wave functions at momenta $\mathbf{k}$ and $-\mathbf{k}$ by fixing the sewing matrices of C_{2z} and P.

$$B^{C_{2z}}(\mathbf{k}) = \begin{cases}\zeta^0\tau^x & \mathbf{k}\neq\mathbf{k}_{M_M}\\ -\zeta^0\tau^x & \mathbf{k}=\mathbf{k}_{M_M}\end{cases} \quad B^T(\mathbf{k}) = \begin{cases}\zeta^0\tau^x & \mathbf{k}\neq\mathbf{k}_{M_M}\\ -\zeta^0\tau^x & \mathbf{k}=\mathbf{k}_{M_M}\end{cases} \quad B^P(\mathbf{k}) = \begin{cases}-i\zeta^y\tau^z & \mathbf{k}\neq\mathbf{k}_{M_M}\\ i\zeta^y\tau^z & \mathbf{k}=\mathbf{k}_{M_M}\end{cases}, \tag{A28}$$

where $\mathbf{k}_{M_M}$ denotes any one of the three equivalent M_M points in the MBZ

$$\mathbf{k}_{M_M} \in \left\{\frac{1}{2}\mathbf{b}_{M1}, \frac{1}{2}\mathbf{b}_{M2}, \frac{1}{2}\mathbf{b}_{M1}+\frac{1}{2}\mathbf{b}_{M2}\right\}. \tag{A29}$$

The reason for the additional minus sign of the sewing matrix $B^P(\mathbf{k})$ at $\mathbf{k} = \mathbf{k}_{M_M}$ was explained in Ref. [74]. In addition to the gauge-fixing conditions given in Eqs. (A27) and (A28), we fix the relative sign between the single-particle wave functions $u_{+,\eta}(\mathbf{k})$ and $u_{-,\eta}(\mathbf{k})$ imposing [87]

$$\lim_{\mathbf{q}\to\mathbf{0}}\left|u^\dagger_{n\eta}(\mathbf{k}+\mathbf{q})u_{n\eta}(\mathbf{k}) - u^\dagger_{-n\eta}(\mathbf{k}+\mathbf{q})u_{-n\eta}(\mathbf{k})\right| = 0. \tag{A30}$$

By fixing the sewing matrix of the $C_{2z}T$ transformation according to Eq. (A28), as well as the continuous gauge condition from Eq. (A30), we can introduce the Chern band basis [74, 84, 93] within the two active bands in each valley-spin flavor

$$\hat{d}^{\dagger}_{\mathbf{k},e_Y,\eta,s} = \frac{1}{\sqrt{2}}\left(\hat{c}^{\dagger}_{\mathbf{k},+1,\eta,s} + ie_Y\hat{c}^{\dagger}_{\mathbf{k},-1,\eta,s}\right) = \sum_n W_{e_Y,n}\hat{c}^{\dagger}_{\mathbf{k},n,\eta,s}, \tag{A31}$$

where $e_Y = \pm 1$ and the unitary matrix W is given by

$$W = \frac{1}{\sqrt{2}}\begin{pmatrix} 1 & i \\ 1 & -i \end{pmatrix} \tag{A32}$$

As proven in Refs. [74, 84], the operator $\hat{d}^{\dagger}_{\mathbf{k},e_Y,\eta,s}$ for $\mathbf{k} \in \mathrm{MBZ}$ and fixed e_Y, η, and s corresponds to a Chern band carrying Chern number e_Y. To numerically determine the gauge-fixed TBG wave functions, we follow the procedure employed in Ref. [69].

In the case $\lambda = 1$, P is no longer an exact symmetry of $\hat{H}_0$ in Eq. (A10), and a different approach is needed. We start by diagonalizing the first-quantized TBG Hamiltonian from Eq. (A10) in valley $\eta = +$, fix the sewing matrix of $C_{2z}T$ according to Eq. (A27), and impose the continuous gauge condition from Eq. (A30). These conditions are enough to guarantee the existence of the Chern band basis as defined in Eq. (A31) [84] for valley $\eta = +$. At the same time, for each $\mathbf{k}$, we are free to transform the wave functions according to

$$u_{n+}(\mathbf{k}) = \sum_{m=\pm 1} U_{nm}(\mathbf{k})\, u_{m+}(\mathbf{k}), \tag{A33}$$

where the 2×2, momentum-dependent matrix $U(\mathbf{k})$ obeys

$$\begin{aligned} &U(\mathbf{k}) = \pm\mathbb{1} \quad \text{if} \quad \epsilon_{+1,\eta}(\mathbf{k}) \neq \epsilon_{-1,\eta}(\mathbf{k}), \\ &U(\mathbf{k}) \in \mathrm{SO}(2) \quad \text{if} \quad \epsilon_{+1,\eta}(\mathbf{k}) = \epsilon_{-1,\eta}(\mathbf{k}) \end{aligned}. \tag{A34}$$

Ref. [84] showed that *even* when $\lambda = 1$, one still has

$$1 - \left| u^{\dagger}_{-n\eta}(-\mathbf{k}) \left[D(P)\right]_{\eta\eta} u_{n\eta}(\mathbf{k}) \right|^2 \lesssim 0.04, \tag{A35}$$

meaning that the particle-hole symmetry breaking is small *even* when $\lambda = 1$. We choose $U(\mathbf{k})$ in such a way as to ensure that

$$\left\| \left[D(P)\right]_{++} u_{n+}(\mathbf{k}) - \left[B^P(\mathbf{k})\right]_{-n+,n+} u_{-n+}(\mathbf{k}) \right\| \quad \text{is minimized.} \tag{A36}$$

To find the wave functions in the $\eta = -$ valley, we then use the C_{2z} symmetry of TBG and impose the corresponding sewing matrix from Eq. (A28). By *approximately* fixing the sewing matrix of the particle-hole transformation in the $\lambda = 1$ case according to Eq. (A36), we ensure that this case is smoothly connected to the $\lambda = 0$ one. At the same time, Eq. (A36) guarantees that even when $\lambda = 1$, Eq. (A26) still holds *approximately* for $g = P$.

2. Interaction Hamiltonian

a. *Form factor matrices*

After discussing the single-particle wave functions of TBG, we now briefly review the Coulomb interaction Hamiltonian, which has been derived and discussed at length in Refs. [68, 74]. We let $V(\mathbf{r})$ denote the interaction potential between two electrons within the TBG sample, and define $V(\mathbf{q})$ as its Fourier transformation. For the time being, we will keep $V(\mathbf{r})$ generic and only require that it denotes a repulsive interaction ($V(\mathbf{q}) \geq 0$). It was shown in Ref. [42, 58, 74] that the interaction Hamiltonian *projected* in the active TBG bands is a positive semi-definite operator and reads as

$$H_I = \frac{1}{2\Omega_{\mathrm{TBG}}} \sum_{\mathbf{q}\in\mathrm{MBZ}} \sum_{\mathbf{G}\in\mathcal{Q}_0} O_{-\mathbf{q}-\mathbf{G}} O_{\mathbf{q}+\mathbf{G}}, \tag{A37}$$

where Ω_{TBG} is the area of the TBG sample, and we have introduced the operators

$$O_{\mathbf{q}+\mathbf{G}} = \sum_{\mathbf{k},\eta,s} \sum_{n,m=\pm 1} \sqrt{V(\mathbf{q}+\mathbf{G})} M^{\eta}_{mn}(\mathbf{k},\mathbf{q}+\mathbf{G}) \left(\hat{c}^{\dagger}_{\mathbf{k}+\mathbf{q},m,\eta,s} \hat{c}_{\mathbf{k},n,\eta,s} - \frac{1}{2}\delta_{\mathbf{q},\mathbf{0}}\delta_{m,n} \right). \tag{A38}$$

In Eq. (A38) we have employed the wave function overlap matrix (also known as the form factor matrix) which is defined in terms of the active TBG wave functions as [74]

$$M^{\eta}_{mn}(\mathbf{k},\mathbf{q}+\mathbf{G}) = \sum_{\alpha} \sum_{\mathbf{Q}\in\mathcal{Q}_{\pm}} u^{*}_{\mathbf{Q}-\mathbf{G}\alpha;m\eta}(\mathbf{k}+\mathbf{q})\, u_{\mathbf{Q}\alpha;n\eta}(\mathbf{k}). \tag{A39}$$

The symmetries of the single-particle TBG Hamiltonian impose a series of constraints on the form factors matrices, through the gauge-fixing conditions from Appendix [A 1 d] [74]. Letting g be a symmetry of $\hat{H}_0$ as defined in Appendix [A 1 c], Eq. (A25) implies that

$$\begin{aligned}
&\sum_{\eta,n',m'} [B^{g}(\mathbf{k})]_{n'\eta',n\eta} [B^{g}(\mathbf{k}+\mathbf{q})]^{*}_{m'\eta',m\eta} M^{\eta'}_{m'n'}(g\mathbf{k}, g\mathbf{q}+g\mathbf{G}) \\
=&\sum_{\eta,n',m'} \sum_{\alpha} \sum_{\mathbf{Q}\in\mathcal{Q}_{\pm}} [B^{g}(\mathbf{k}+\mathbf{q})]^{*}_{m'\eta',m\eta} u^{*}_{g\mathbf{Q}-g\mathbf{G}\alpha;m'\eta'}(g\mathbf{k}+g\mathbf{q}) [B^{g}(\mathbf{k})]_{n'\eta',n\eta} u_{g\mathbf{Q}\alpha;n'\eta'}(g\mathbf{k}) \\
=&\sum_{\eta} \sum_{\alpha} \sum_{\mathbf{Q}\in\mathcal{Q}_{\pm}} \Big[[D(g)]_{\eta'\eta} u_{m\eta}(\mathbf{k}+\mathbf{q}) \Big]^{*}_{\mathbf{Q}-\mathbf{G}\alpha} \Big[[D(g)]_{\eta'\eta} u_{n\eta}(\mathbf{k}) \Big]_{\mathbf{Q}\alpha} \\
=&\sum_{\alpha} \sum_{\mathbf{Q}\in\mathcal{Q}_{\pm}} u^{*}_{\mathbf{Q}-\mathbf{G}\alpha;m\eta}(\mathbf{k}+\mathbf{q})\, u_{\mathbf{Q}\alpha;n\eta}(\mathbf{k}),
\end{aligned} \tag{A40}$$

with an additional complex conjugation when g is anti-unitary. Written in matrix form, Eq. (A40) reads as

$$B^{\dagger g}(\mathbf{k}+\mathbf{q}) M^{(*)}(g\mathbf{k}, g\mathbf{q}+g\mathbf{G})\, B^{g}(\mathbf{k}) = M(\mathbf{k},\mathbf{q}+\mathbf{G}), \tag{A41}$$

where $^{(*)}$ denotes an additional complex conjugation when g is anti-unitary. Additionally, the form factor matrix obeys the following Hermiticity condition

$$M^{*\eta}_{mn}(\mathbf{k},\mathbf{q}+\mathbf{G}) = M^{\eta}_{nm}(\mathbf{k}+\mathbf{q}, -\mathbf{q}-\mathbf{G}), \tag{A42}$$

which can be readily checked from its definition from Eq. (A39).

Under the gauge-fixing conditions outlined in Appendix [A 1 d] and as a consequence of Eq. (A41), the $C_{2z}T$ symmetry imposes a reality condition for both the $\lambda = 0$ and $\lambda = 1$ cases [74]. As such, the form factor matrix can be generically parameterized as

$$\begin{aligned}
M(\mathbf{k},\mathbf{q}+\mathbf{G}) =& \zeta^{0}\tau^{0}\alpha_0(\mathbf{k},\mathbf{q}+\mathbf{G}) + \zeta^{x}\tau^{z}\alpha_1(\mathbf{k},\mathbf{q}+\mathbf{G}) + i\zeta^{y}\tau^{0}\alpha_2(\mathbf{k},\mathbf{q}+\mathbf{G}) + \zeta^{z}\tau^{z}\alpha_3(\mathbf{k},\mathbf{q}+\mathbf{G}) \\
&+\zeta^{0}\tau^{z}\alpha_4(\mathbf{k},\mathbf{q}+\mathbf{G}) + \zeta^{x}\tau^{0}\alpha_5(\mathbf{k},\mathbf{q}+\mathbf{G}) + i\zeta^{y}\tau^{z}\alpha_6(\mathbf{k},\mathbf{q}+\mathbf{G}) + \zeta^{z}\tau^{0}\alpha_7(\mathbf{k},\mathbf{q}+\mathbf{G}).
\end{aligned} \tag{A43}$$

When $\lambda = 0$, the presence of the anti-commuting $C_{2z}P$ symmetry enforces $\alpha_i(\mathbf{k},\mathbf{q}+\mathbf{G}) = 0$ for all $4 \le i \le 7$, leading to the following parameterization in the band and valley subspaces [74]

$$M(\mathbf{k},\mathbf{q}+\mathbf{G}) = \zeta^{0}\tau^{0}\alpha_0(\mathbf{k},\mathbf{q}+\mathbf{G}) + \zeta^{x}\tau^{z}\alpha_1(\mathbf{k},\mathbf{q}+\mathbf{G}) + i\zeta^{y}\tau^{0}\alpha_2(\mathbf{k},\mathbf{q}+\mathbf{G}) + \zeta^{z}\tau^{z}\alpha_3(\mathbf{k},\mathbf{q}+\mathbf{G}). \tag{A44}$$

It is worth noting that, because the P anti-commuting symmetry (and hence the $C_{2z}P$ anti-commuting symmetry) is only slightly broken even in the $\lambda = 1$ case [84], we generically find that in Eq. (A43)

$$|\alpha_i(\mathbf{k},\mathbf{q}+\mathbf{G})| \ll |\alpha_j(\mathbf{k},\mathbf{q}+\mathbf{G})|, \quad \text{for} \quad 0 \le i \le 3 \quad \text{and} \quad 4 \le j \le 7, \tag{A45}$$

provided that Eq. (A36) is imposed. Finally, we note that in the first chiral limit ($w_0 = 0$), the single-particle wave functions at a given momentum are additionally constrained by the chiral symmetry operator C. As shown in Ref. [74], this implies that the form factors are further restricted to the parameterization

$$M(\mathbf{k},\mathbf{q}+\mathbf{G}) = \zeta^{0}\tau^{0}\alpha_0(\mathbf{k},\mathbf{q}+\mathbf{G}) + i\zeta^{y}\tau^{0}\alpha_2(\mathbf{k},\mathbf{q}+\mathbf{G}). \tag{A46}$$

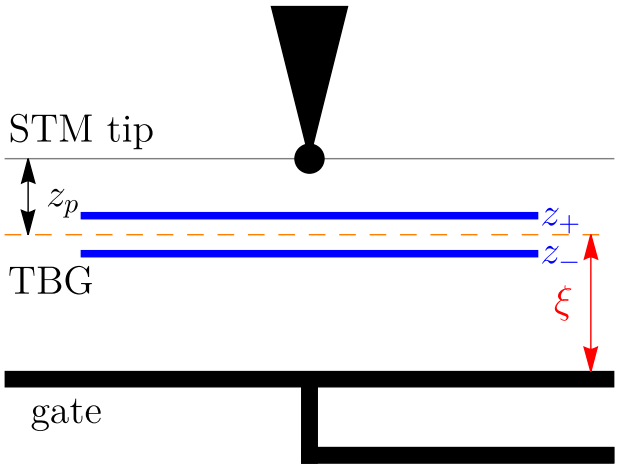

FIG. 5. Schematic of the typical experimental setup considered. The TBG sample is is located in between a gate plate and the scanning tunneling microscopy (STM) tip, with ξ denoting the distance between the gate and the sample and z_p being the height of the STM tip. The two graphene monolayers are located at heights z_l ($l = \pm$) with the inter-layer TBG separation obeying $|z_+ - z_-| \ll \xi$.

b. *Coulomb interaction potential*

With the general form of the projected interaction TBG Hamiltonian at hand, we now turn to the electron-electron repulsion potential. We consider the experimental setup shown schematically in Fig. 5, corresponding to a single-gate arrangement for scanning tunneling microscopy (STM) experiments. The potential between two electrons separated by $\mathbf{r}$ in the plane of the TBG sample includes a contribution from the image charge formed on the gate located at a distance ξ below the sample

$$V(\mathbf{r}) = \frac{e^2}{\epsilon}\left(\frac{1}{r} - \frac{1}{\sqrt{r^2 + (2\xi)^2}}\right). \tag{A47}$$

Using the identity

$$\int \frac{\mathrm{d}^2 q}{(2\pi)^2} \frac{e^{-\alpha q + i\mathbf{q}\cdot\mathbf{r}}}{q} = \frac{1}{2\pi}\frac{1}{\sqrt{r^2+\alpha^2}}, \tag{A48}$$

we find that the Fourier transformation of the single-gate potential reads

$$V(\mathbf{q}) = \frac{2\pi e^2}{\epsilon}\frac{1-e^{-2\xi q}}{q} = 2\pi U_\xi \xi^2 \frac{1-e^{-2\xi q}}{\xi q}. \tag{A49}$$

In Eq. (A49), e represents the electron charge, ϵ is the dielectric constant, $q = |\mathbf{q}|$, and $U_\xi = e^2/(\epsilon\xi)$. In this work and unless stated otherwise, we use $U_\xi = 8\,\mathrm{meV}$ and $\xi = 30\,\mathrm{nm}$.

c. *Continuous symmetries of the projected interaction Hamiltonian*

Throughout this paper, we will work exclusively in the flat limit, as defined by Refs. [68, 74], implying that the TBG Hamiltonian H is given solely by the projected interaction Hamiltonian from Eq. (A37), *i.e.* $H = H_I$. Refs. [68, 69] have found that owing to its enlarged continuous symmetries (which will be discussed below), H_I features a large manifold of degenerate ground states. This degeneracy is broken by the finite dispersion of the single-particle Hamiltonian which acts perturbatively within the ground state manifold [68, 69]. Instead of focusing on a single ground state at each integer filling as predicted by perturbation theory [58, 68], we will instead explore the properties of the degenerate manifold in an effort to identify the experimentally-relevant ground state.

We will now briefly review the symmetries of the interaction Hamiltonian H_I, which were derived and extensively discussed in Refs. [42, 43, 58, 74]. Following the notation of Ref. [74], we shall use ζ^a, τ^a, and s^a to denote the identity matrix ($a = 0$), and Pauli matrices ($a = x, y, z$) in the band ($n = \pm 1$), valley ($\eta = \pm$), and spin ($s = \uparrow, \downarrow$) subspaces, respectively.

- $\mathrm{U}(2)\times\mathrm{U}(2)$ *symmetry in the non-particle-hole-symmetric case ($\lambda = 1$).* Due to the absence of spin-orbit coupling in TBG, as well as the suppression of intervalley scattering processes in Eq. (A37), H_I, enjoys a $\mathrm{U}(2)\times\mathrm{U}(2)$ rotation symmetry corresponding to independent spin-charge rotation within each valley. The corresponding generators are given by

$$S^{ab} = \sum_{\mathbf{k}} \sum_{\substack{n,\eta,s \\ n',\eta',s'}} \left[s^{ab}\right]_{n\eta s,n'\eta's'} \hat{c}^{\dagger}_{\mathbf{k},n,\eta,s}\hat{c}_{\mathbf{k},n',\eta',s'}, \quad \text{for} \quad a=0,z \quad b=0,x,y,z, \tag{A50}$$

where the matrices s^{ab} read as

$$s^{0b} = \zeta^0\tau^0 s^b, \quad s^{zb} = \zeta^0\tau^z s^b. \tag{A51}$$

- $\mathrm{U}(4)$ *symmetry in the particle-hole-symmetric case ($\lambda = 0$).* The presence of the anticommuting particle-hole symmetry restricts the parameterization of the form factors, as shown in Eq. (A44). In turn, this enlarges the $\mathrm{U}(2)\times\mathrm{U}(2)$ symmetry of H_I to the $\mathrm{U}(4)$ group [42, 43, 58, 74] (corresponding to the so-called *nonchiral-flat* limit, as defined by Ref. [74]). In what follows, we will always denote the nonchiral-flat $\mathrm{U}(4)$ group as $\mathrm{U_{nc}}(4)$ to distinguish it from other $\mathrm{U}(4)$ groups. The generators of $\mathrm{U_{nc}}(4)$ read as

$$S^{ab} = \sum_{\mathbf{k}} \sum_{\substack{n,\eta,s \\ n',\eta',s'}} \left[s^{ab}\right]_{n\eta s,n'\eta's'} \hat{c}^{\dagger}_{\mathbf{k},n,\eta,s}\hat{c}_{\mathbf{k},n',\eta',s'}, \quad \text{for} \quad a,b=0,x,y,z, \tag{A52}$$

with the matrices s^{ab} being given by

$$s^{0b} = \zeta^0\tau^0 s^b, \quad s^{xb} = \zeta^y\tau^x s^b, \quad s^{yb} = \zeta^y\tau^y s^b, \quad s^{zb} = \zeta^0\tau^z s^b. \tag{A53}$$

For future reference, we also define the set

$$\mathcal{N}_{\mathrm{U_{nc}}(4)} = \left\{ \sum_{a,b\in\{0,x,y,z\}} \phi^{ab}s^{ab} \;\middle|\; \phi^{ab}\in\mathbb{C}, \phi^{00}=0 \right\}, \tag{A54}$$

which contains all eight-dimensional matrices which can be expressed as a linear combinations of the generators s^{ab} from Eq. (A53) for $a,b\in\{0,x,y,z\}$ and $ab\neq 0$. For any $M\in\mathcal{N}_{\mathrm{U_{nc}}(4)}$, $\left[M,s^{ab}\right]\in\mathcal{N}_{\mathrm{U_{nc}}(4)}$, implying that the set $\mathcal{N}_{\mathrm{U_{nc}}(4)}$ is closed under any $\mathrm{U_{nc}}(4)$ group transformation.

- $\mathrm{U}(4)\times\mathrm{U}(4)$ *symmetry in the first chiral limit.* Finally, in the first chiral limit ($w_0 = 0$) [74, 86], the anticommuting C symmetry further restricts the parameterization of the form factors, given in Eq. (A46). As a consequence, the projected interaction Hamiltonian enjoys a large $\mathrm{U}(4)\times\mathrm{U}(4)$ symmetry [58, 74] (corresponding to the *chiral-flat* limit, as defined in Ref. [74]) which is generated by the 32 operators

$$S^{ab}_{\pm} = \sum_{\mathbf{k}} \sum_{\substack{n,\eta,s \\ n',\eta',s'}} \left[s^{ab}_{\pm}\right]_{n\eta s,n'\eta's'} \hat{c}^{\dagger}_{\mathbf{k},n,\eta,s}\hat{c}_{\mathbf{k},n',\eta',s'}, \quad \text{for} \quad a,b=0,x,y,z, \tag{A55}$$

with the matrices $s^{ab}_{\pm}$ being given by

$$s^{ab}_{\pm} = \frac{1}{2}\left(\zeta^0 \pm \zeta^y\right)\tau^a s^b. \tag{A56}$$

In analogy with Eq. (A54), we also introduce the set

$$\mathcal{N}_{\mathrm{U}(4)\times\mathrm{U}(4)} = \left\{ \sum_{a,b\in\{0,x,y,z\}} \left(\phi^{ab}_{+}s^{ab}_{+} + \phi^{ab}_{-}s^{ab}_{-}\right) \;\middle|\; \phi^{ab}_{\pm}\in\mathbb{C}, \phi^{00}_{+}=\phi^{00}_{-}=0 \right\}, \tag{A57}$$

which is closed under any $\mathrm{U}(4)\times\mathrm{U}(4)$ transformation.

The $\mathrm{U_{nc}}(4)$ group in the nonchiral-flat limit is a subgroup of the $\mathrm{U}(4)\times\mathrm{U}(4)$ group in the chiral-flat limit, but is not one of the tensor-producted $\mathrm{U}(4)$ subgroups of the later [74]. To better understand the group-subgroup relation between the two groups, is is instructive to recast the generators from Eqs. (A52) and (A55) in the Chern band basis

defined in Eq. (A31). In the Chern band basis, the chiral-flat generators from Eq. (A55) correspond to independent $\mathrm{U}(4)$ charge-valley-spin rotations within each Chern sector

$$S_{\pm}^{ab}=\sum_{\mathbf{k}}\sum_{\eta,s,\eta',s'}\left[\tau^{a}s^{b}\right]_{\eta s,\eta' s'}\hat{d}_{\mathbf{k},\pm1,\eta,s}^{\dagger}\hat{d}_{\mathbf{k},\pm1,\eta',s'},\quad\text{for}\quad a,b=0,x,y,z. \tag{A58}$$

When the chiral anticommuting symmetry is broken, the generators of the $\mathrm{U}(4)\times\mathrm{U}(4)$ group get combined into the generators of the $\mathrm{U}_{\mathrm{nc}}(4)$ group from Eq. (A52)

$$S^{ab}=\begin{cases}S_{+}^{ab}+S_{-}^{ab}, & \text{if}\quad a=0,z\\ S_{+}^{ab}-S_{-}^{ab}, & \text{if}\quad a=x,y\end{cases},\quad\text{for}\quad a,b=0,x,y,z. \tag{A59}$$

As such, we find that away from the chiral limit, the fermions belonging to the two Chern sectors can no longer be rotated independently in the charge-valley-spin space. Instead, the $\mathrm{U}_{\mathrm{nc}}(4)$ rotations which do not mix the two valleys rotate the two Chern sectors in the same directions, while the generators corresponding to valley rotations in the xz and yz planes rotate the two Chern sectors in in opposite directions.

Appendix B: Charge-one excitations at integer fillings

The spectral function of the TBG insulators which is measured by STM experiments depends on the eigenstates of the TBG Hamiltonian obtained by adding or removing one electron from the ground state – the charge-one excitations. The latter constitute the main focus of this appendix. We start with a brief review of the method devised by Ref. [75] for obtaining the charge-one excitations above the ground states of TBG obtained in Ref. [68]: the charge-one excitation can be found by diagonalizing the so-called charge-one excitation matrices. We then investigate the consequences of the various discrete symmetries of TBG from Appendix [A 1 c] on the charge-one excitation matrices and obtain their parameterizations under different limits. Finally, by focusing on a specific state from the approximately degenerate ground state manifold of TBG derived in Ref. [68], we explicitly work out the charge-one excitation spectrum.

1. Charge-one excitation matrices

Ref. [75] has shown that for the different ground states of the TBG Hamiltonian at integer fillings derived in Ref. [68], the charge-one excitations can be computed directly as a zero-body problem. Here, we will briefly review the procedure introduced in Ref. [75] for obtaining them.

Let $|\varphi\rangle$ be one of the exact eigenstates of H_I at filling ν introduced in Ref. [68] (which will be specified in detail below). The energies and wave functions of the charge-one excitations can be determined using the following commutation relations [75]

$$\left[H_I-\mu\hat{N},\hat{c}_{\mathbf{k},n,\eta,s}^{\dagger}\right]|\varphi\rangle=\sum_{m}R_{mn}^{\eta}\left(\mathbf{k}\right)\hat{c}_{\mathbf{k},m,\eta,s}^{\dagger}\left|\varphi\right\rangle, \tag{B1}$$

$$\left[H_I-\mu\hat{N},\hat{c}_{\mathbf{k},n,\eta,s}\right]|\varphi\rangle=\sum_{m}\tilde{R}_{mn}^{\eta}\left(\mathbf{k}\right)\hat{c}_{\mathbf{k},m,\eta,s}\left|\varphi\right\rangle, \tag{B2}$$

where μ denotes the chemical potential and $\hat{N}$ is the total fermion number operator

$$\hat{N}=\sum_{\mathbf{k},n,\eta,s}\hat{c}_{\mathbf{k},n,\eta,s}^{\dagger}\hat{c}_{\mathbf{k},n,\eta,s}. \tag{B3}$$

The charge-one excitation matrices $R_{mn}^{\eta}\left(\mathbf{k}\right)$ and $\tilde{R}_{mn}^{\eta}\left(\mathbf{k}\right)$ depend only on the filling ν of the ground state $|\varphi\rangle$ and are given in terms of the form factors introduced in Eq. (A39)

$$\begin{aligned}R_{mn}^{\eta}\left(\mathbf{k}\right)=\frac{1}{2\Omega_{\mathrm{TBG}}}\sum_{\mathbf{G}\in\mathcal{Q}_{0}}\Bigg[&\left(\sum_{\mathbf{q}\in\mathrm{MBZ},m'}V\left(\mathbf{q}+\mathbf{G}\right)M_{m'm}^{*\eta}\left(\mathbf{k},\mathbf{q}+\mathbf{G}\right)M_{m'n}^{\eta}\left(\mathbf{k},\mathbf{q}+\mathbf{G}\right)\right)\\&+2A_{-\mathbf{G}}\sqrt{V\left(\mathbf{G}\right)}M_{mn}^{\eta}\left(\mathbf{k},\mathbf{G}\right)\Bigg]-\mu\delta_{mn},\end{aligned} \tag{B4}$$

$$\tilde{R}^{\eta}_{mn}(\mathbf{k}) = \frac{1}{2\Omega_{\mathrm{TBG}}} \sum_{\mathbf{G}\in\mathcal{Q}_0} \left[\left(\sum_{\mathbf{q}\in\mathrm{MBZ},m'} V(\mathbf{q}+\mathbf{G}) M^{\eta}_{m'm}(\mathbf{k},\mathbf{q}+\mathbf{G}) M^{*\eta}_{m'n}(\mathbf{k},\mathbf{q}+\mathbf{G}) \right) \right.$$
$$\left. -2A_{-\mathbf{G}}\sqrt{V(\mathbf{G})} M^{*\eta}_{mn}(\mathbf{k},\mathbf{G}) \right] + \mu\delta_{mn}, \tag{B5}$$

with the factor $A_{\mathbf{G}}$ depending on the filling ν according to [75]

$$A_{\mathbf{G}} = \sqrt{V(\mathbf{G})} \sum_{\substack{\mathbf{k}\in\mathrm{MBZ}\\ n,\eta}} \frac{\nu}{4} M^{\eta}_{nn}(\mathbf{k},\mathbf{G}) = \sqrt{V(\mathbf{G})} \sum_{\mathbf{k}\in\mathrm{MBZ}} \frac{\nu}{4} \mathrm{Tr}\left[M(\mathbf{k},\mathbf{G})\right]. \tag{B6}$$

The charge-one excitation matrices defined in Eq. (B4) are valid for any gauge choice. Under the gauge-fixing conditions defined in Appendix [A 1 d], the form factors are real, so the complex-conjugation can be dropped.

Refs. [63, 75] derived the charge-one commutation relations from Eqs. (B1) and (B2) in the particle-hole symmetric case ($\lambda = 0$), for $|\varphi\rangle$ being one of the ground states [1] of H_I derived in Ref. [68]. Away from the first chiral limit ($w_0 \neq 0$), Eqs. (B1) and (B2) are valid provided $|\varphi\rangle$ is one of ground states $|\Psi_\nu\rangle$ of H_I at even filling ν defined by [68]

$$|\Psi_\nu\rangle = \prod_{\mathbf{k}} \left(\prod_{j=1}^{(\nu+4)/2} \hat{c}^{\dagger}_{\mathbf{k},+1,\eta_j,s_j} \hat{c}^{\dagger}_{\mathbf{k},-1,\eta_j,s_j} \right) |0\rangle, \quad \text{for} \quad \nu = 0, \pm 2, \pm 4, \tag{B7}$$

as well as any $\mathrm{U_{nc}}(4)$ rotation thereof given by the generators from Eq. (A52). In Eq. (B7), $\{\eta_j, s_j\}$ denote the occupied valley-spin flavors of $|\Psi_\nu\rangle$ and the "vacuum state" $|0\rangle$ corresponds to filling $\nu = -4$ (*i.e.* unoccupied TBG active bands). The states $|\Psi_\nu\rangle$ and their $\mathrm{U_{nc}}(4)$ rotations carry zero Chern number.

In the first chiral limit ($w_0 = 0$), Eqs. (B1) and (B2) are valid for any of the Chern number $\mathcal{C}$ ground states $\left|\Psi_\nu^{\nu_+,\nu_-}\right\rangle$ of H_I at integer filling ν defined by [68]

$$|\Psi_\nu^{\nu_+,\nu_-}\rangle = \prod_{\mathbf{k}} \left(\prod_{j_1=1}^{\nu_+} \hat{d}^{\dagger}_{\mathbf{k},+1,\eta_{j_1},s_{j_1}} \prod_{j_2=1}^{\nu_-} \hat{d}^{\dagger}_{\mathbf{k},-1,\eta_{j_2},s_{j_2}} \right) |0\rangle, \quad \text{for} \quad -4 \leq \nu \leq 4 \tag{B8}$$

and any of their $\mathrm{U}(4) \times \mathrm{U}(4)$ rotations generated by the operators from Eq. (A55). In Eq. (B8), the occupancies of the two Chern sectors are given by

$$\nu_+ = \frac{\nu + 4 + \mathcal{C}}{2} \quad \text{and} \quad \nu_- = \frac{\nu + 4 - \mathcal{C}}{2}, \tag{B9}$$

with $\{\eta_{j_1}, s_{j_1}\}$ and $\{\eta_{j_2}, s_{j_2}\}$ denoting the (arbitrarily chosen) occupied valley-spin flavors of the two Chern sectors.

Additionally, the charge-one commutation relations from Eqs. (B1) and (B2) are also valid in the $\lambda = 1$ case for any of the ground states of H_I from Eq. (B7), along with any $\mathrm{U}(2) \times \mathrm{U}(2)$ rotation thereof. In what follows, we will assume the charge-one commutation relations to hold for any $\mathrm{U}(4) \times \mathrm{U}(4)$ rotation of the integer filling states from Eq. (B8), even *away* from the first chiral limit ($w_0 \neq 0$) *and* in the *absence* of exact particle-hole symmetry ($\lambda = 1$). To see why this approximation is justified, we first note that in moving away from the chiral limit ($w_0 = 0$ and $\lambda = 0$) to the nonchiral, but particle-hole symmetric case ($w_0 \neq 0$ and $\lambda = 0$), the states of the form in Eq. (B8) are still perturbatively the ground states of the TBG Hamiltonian, even at odd integer fillings [68, 69]. Moreover, through a renormalization group approach, Ref. [63] has shown that by successively integrating the remote TBG bands in the nonchiral case ($w_0 \neq 0$), the system flows towards the chiral limit, thus approaching the $\mathrm{U}(4) \times \mathrm{U}(4)$-symmetric case. It is therefore justified to use the same charge-one commutation relation away from the chiral limit for $\mathrm{U}(4) \times \mathrm{U}(4)$ rotations of the states in Eq. (B8). Finally, moving away from the case with *exact* particle-hole symmetry can be justified by noting that even in the $\lambda = 1$ case, particle-hole is still and excellent *approximate* symmetry [84].

2. Symmetry properties of the charge-one excitation matrices

Under the gauge-fixing conditions outlined in Appendix [A 1 d], the symmetries of the single-particle TBG Hamiltonian impose a series of constraints on the charge-one excitation matrices. This appendix aims to derive these

[1] Strictly speaking, Ref. [68] showed that in the nonchiral- and chiral-flat cases, respectively, the states from Eq. (B7) and Eq. (B8) are *eigenstates* of H_I. Additionally, they were shown to be the *ground states* of H_I only for $\nu = 0$, or for $\nu \neq 0$ assuming that the flat metric condition holds [68, 87]. However, Ref. [69] proved the validity of the flat metric approximation by offering compelling numerical evidence that the states from Eq. (B7) and Eq. (B8) are indeed the ground states of H_I in the corresponding limits.

constraints with the goal of parameterizing the $R(\mathbf{k})$ and $\tilde{R}(\mathbf{k})$ matrices within the band and valley subspaces. This will then used for analytic approximations of the LDOS. Part of this parametrization was first derived in [67].

Let g be one of the symmetries of the single-particle TBG Hamiltonian from Appendix [A 1 c]. Using the symmetry properties of the form factor matrix from Eq. (A41), Eq. (B6) implies that

$$\begin{aligned} A_{\mathbf{G}} =& \sqrt{V(\mathbf{G})} \sum_{\mathbf{k}\in \mathrm{MBZ}} \frac{\nu}{4} \operatorname{Tr}\left[M(\mathbf{k},\mathbf{G})\right] = \sqrt{V(\mathbf{G})} \sum_{\mathbf{k}\in \mathrm{MBZ}} \frac{\nu}{4} \operatorname{Tr}\left[B^{\dagger g}(\mathbf{k}) M(g\mathbf{k}, g\mathbf{G}) B^{g}(\mathbf{k})\right] \\ =& \sqrt{V(g\mathbf{G})} \sum_{\mathbf{k}\in \mathrm{MBZ}} \frac{\nu}{4} \operatorname{Tr}\left[M(g\mathbf{k}, g\mathbf{G})\right] = A_{g\mathbf{G}}, \end{aligned} \tag{B10}$$

where we have used the reality of the form factor matrix, the invariance of the interaction potential under two-dimensional spatial rotations, as well as the unitarity of the sewing matrices. Applying Eqs. (A41) and (B10) in the definition from Eq. (B4), we find that

$$\begin{aligned} R^{\eta}_{mn}(\mathbf{k}) =& \frac{1}{2\Omega_{\mathrm{TBG}}} \sum_{\mathbf{G}\in\mathcal{Q}_0} \Bigg[\Bigg(\sum_{\mathbf{q}\in\mathrm{MBZ},m'} V(g\mathbf{q}+g\mathbf{G}) \left[B^{\dagger g}(\mathbf{k}+\mathbf{q}) M(g\mathbf{k}, g\mathbf{q}+g\mathbf{G}) B^{g}(\mathbf{k})\right]^{*\eta}_{m'm} \\ & \times \left[B^{\dagger g}(\mathbf{k}+\mathbf{q}) M(g\mathbf{k}, g\mathbf{q}+g\mathbf{G}) B^{g}(\mathbf{k})\right]^{\eta}_{m'n} \Bigg) \\ & + 2A_{-g\mathbf{G}} \sqrt{V(g\mathbf{G})} \left[B^{\dagger g}(\mathbf{k}) M(g\mathbf{k}, g\mathbf{G}) B^{g}(\mathbf{k})\right]^{\eta}_{mn} \Bigg] - \mu\delta_{mn} \\ =& \frac{1}{2\Omega_{\mathrm{TBG}}} \sum_{\mathbf{G}\in\mathcal{Q}_0} \Bigg[\Bigg(\sum_{\mathbf{q}\in\mathrm{MBZ},m'} V(\mathbf{q}+\mathbf{G}) \left[B^{\dagger g}(\mathbf{k}+\mathbf{q}) M(g\mathbf{k}, \mathbf{q}+\mathbf{G}) B^{g}(\mathbf{k})\right]^{*\eta}_{m'm} \\ & \times \left[B^{\dagger g}(\mathbf{k}+\mathbf{q}) M(g\mathbf{k}, \mathbf{q}+\mathbf{G}) B^{g}(\mathbf{k})\right]^{\eta}_{m'n} \Bigg) + 2A_{-\mathbf{G}} \sqrt{V(\mathbf{G})} \left[B^{\dagger g}(\mathbf{k}) M(g\mathbf{k}, \mathbf{G}) B^{g}(\mathbf{k})\right]^{\eta}_{mn} \Bigg] - \mu\delta_{mn}. \end{aligned} \tag{B11}$$

We now proceed to simplify the first term in Eq. (B11),

$$\begin{aligned} & \sum_{m'} \left[B^{\dagger g}(\mathbf{k}+\mathbf{q}) M(g\mathbf{k}, \mathbf{q}+\mathbf{G}) B^{g}(\mathbf{k})\right]^{*\eta}_{m'm} \left[B^{\dagger g}(\mathbf{k}+\mathbf{q}) M(g\mathbf{k}, \mathbf{q}+\mathbf{G}) B^{g}(\mathbf{k})\right]^{\eta}_{m'n} \\ =& \sum_{m'} \sum_{\substack{\eta_1,n_1,m_1 \\ \eta_2,n_2,m_2}} \left[B^{g}(\mathbf{k})\right]^{*}_{n_1\eta_1,m\eta} \left[B^{g}(\mathbf{k}+\mathbf{q})\right]_{m_1\eta_1,m'\eta} M^{*\eta_1}_{m_1 n_1}(g\mathbf{k}, \mathbf{q}+\mathbf{G}) \\ & \times \left[B^{g}(\mathbf{k})\right]_{n_2\eta_2,n\eta} \left[B^{g}(\mathbf{k}+\mathbf{q})\right]^{*}_{m_2\eta_2,m'\eta} M^{\eta_2}_{m_2 n_2}(g\mathbf{k}, \mathbf{q}+\mathbf{G}) \\ =& \sum_{\substack{\eta_1,n_1,m_1 \\ \eta_2,n_2,m_2}} \left[B^{g}(\mathbf{k})\right]^{*}_{n_1\eta_1,m\eta} M^{*\eta_1}_{m_1 n_1}(g\mathbf{k}, \mathbf{q}+\mathbf{G}) \left[B^{g}(\mathbf{k})\right]_{n_2\eta_2,n\eta} M^{\eta_2}_{m_2 n_2}(g\mathbf{k}, \mathbf{q}+\mathbf{G}) \delta_{m_1 m_2} \delta_{\eta_1\eta_2} \\ =& \sum_{\substack{\eta',m' \\ n_1,n_2}} \left[B^{g}(\mathbf{k})\right]^{*}_{n_1\eta',m\eta} M^{*\eta'}_{m' n_1}(g\mathbf{k}, \mathbf{q}+\mathbf{G}) \left[B^{g}(\mathbf{k})\right]_{n_2\eta',n\eta} M^{\eta'}_{m' n_2}(g\mathbf{k}, \mathbf{q}+\mathbf{G}). \end{aligned} \tag{B12}$$

Finally, combining Eqs. (B11) and (B12), it is straightforward to show that

$$R^{\eta}_{mn}(\mathbf{k}) = \sum_{\eta',n_1,n_2} \left[B^{g}(\mathbf{k})\right]^{*}_{n_1\eta',m\eta} \left[B^{g}(\mathbf{k})\right]_{n_2\eta',n\eta} R^{\eta'}_{n_1 n_2}(g\mathbf{k}), \tag{B13}$$

or alternatively, in matrix notation

$$R(\mathbf{k}) = B^{\dagger g}(\mathbf{k}) R(g\mathbf{k}) B^{g}(\mathbf{k}). \tag{B14}$$

Note that the $C_{2z}T$ symmetry of TBG, through the gauge-fixing conditions from Appendix [A 1 d], imposes a reality condition on the form-factor matrix, and consequently on the matrix $R(\mathbf{k})$. As such, we have not included a complex conjugation when g is anti-unitary. Strictly speaking, for a different gauge choice (*i.e.* when the charge-excitation matrices are *not* real), an additional complex conjugation could be required in Eq. (B14) when g is anti-unitary.

Obtaining the symmetry transformation of the $\tilde{R}(\mathbf{k})$ matrix proceeds analogously with the derivation of Eq. (B14), as $R(\mathbf{k})$ and $\tilde{R}(\mathbf{k})$ only differ by the sign of the second term and of the chemical potential

$$\tilde{R}(\mathbf{k}) = B^{Tg}(\mathbf{k}) \tilde{R}(g\mathbf{k}) B^{*g}(\mathbf{k}). \tag{B15}$$

Under the gauge-fixing conditions from Appendix [A 1 d], all sewing matrices are real, Eqs. (B14) and (B15) can be written equivalently as

$$R\left(\mathbf{k}\right)=B^{\dagger g}(\mathbf{k})R\left(g\mathbf{k}\right)B^{g}(\mathbf{k}), \tag{B16}$$

$$\tilde{R}\left(\mathbf{k}\right)=B^{\dagger g}(\mathbf{k})\tilde{R}\left(g\mathbf{k}\right)B^{g}(\mathbf{k}). \tag{B17}$$

Finally, we note that the charge-one excitation matrices are Hermitian

$$R^{\dagger}\left(\mathbf{k}\right)=R\left(\mathbf{k}\right) \tag{B18}$$

$$\tilde{R}^{\dagger}\left(\mathbf{k}\right)=\tilde{R}\left(\mathbf{k}\right) \tag{B19}$$

We will prove this for $R\left(\mathbf{k}\right)$ using the definition from Eq. (B14), as well as the Hermiticity of the form factor matrix from Eq. (A42)

$$\begin{aligned}
R^{*\eta}_{nm}\left(\mathbf{k}\right)&=\frac{1}{2\Omega_{\mathrm{TBG}}}\sum_{\mathbf{G}\in\mathcal{Q}_0}\left[\left(\sum_{\mathbf{q}\in\mathrm{MBZ},m'}V\left(\mathbf{q}+\mathbf{G}\right)M^{\eta}_{m'n}\left(\mathbf{k},\mathbf{q}+\mathbf{G}\right)M^{*\eta}_{m'm}\left(\mathbf{k},\mathbf{q}+\mathbf{G}\right)\right)\right.\\
&\left.+2A^{*}_{-\mathbf{G}}\sqrt{V\left(\mathbf{G}\right)}M^{*\eta}_{nm}\left(\mathbf{k},\mathbf{G}\right)\right]-\mu\delta_{mn}\\
&=\frac{1}{2\Omega_{\mathrm{TBG}}}\sum_{\mathbf{G}\in\mathcal{Q}_0}\left[\left(\sum_{\mathbf{q}\in\mathrm{MBZ},m'}V\left(\mathbf{q}+\mathbf{G}\right)M^{*\eta}_{m'm}\left(\mathbf{k},\mathbf{q}+\mathbf{G}\right)M^{\eta}_{m'n}\left(\mathbf{k},\mathbf{q}+\mathbf{G}\right)\right)\right.\\
&\left.+2A_{\mathbf{G}}\sqrt{V\left(\mathbf{G}\right)}M^{\eta}_{mn}\left(\mathbf{k},-\mathbf{G}\right)\right]-\mu\delta_{mn}\\
&=R^{\eta}_{mn}\left(\mathbf{k}\right),
\end{aligned} \tag{B20}$$

with the Hermiticity of $\tilde{R}\left(\mathbf{k}\right)$ following analogously.

3. Parameterization of the charge-one excitation matrices

With the transformation properties of the charge-one excitation matrices at hand, we now analyze the consequence of each discrete symmetry of TBG from Appendix [A 2 c].

Firstly, as shown in Appendix [B 2], the charge-one excitation matrices are Hermitian and diagonal in valley space. Moreover, as a consequence of the $C_{2z}T$ symmetry, they are real, and hence symmetric. In the most general case, they can be parameterized as

$$R\left(\mathbf{k}\right)=\zeta^{0}\tau^{z}d_1\left(\mathbf{k}\right)+\zeta^{0}\tau^{0}d_2\left(\mathbf{k}\right)+\zeta^{x}\tau^{z}d_3\left(\mathbf{k}\right)+\zeta^{x}\tau^{0}d_4\left(\mathbf{k}\right)+\zeta^{z}\tau^{z}d_5\left(\mathbf{k}\right)+\zeta^{z}\tau^{0}d_6\left(\mathbf{k}\right), \tag{B21}$$

$$\tilde{R}\left(\mathbf{k}\right)=\zeta^{0}\tau^{z}\tilde{d}_1\left(\mathbf{k}\right)+\zeta^{0}\tau^{0}\tilde{d}_2\left(\mathbf{k}\right)+\zeta^{x}\tau^{z}\tilde{d}_3\left(\mathbf{k}\right)+\zeta^{x}\tau^{0}\tilde{d}_4\left(\mathbf{k}\right)+\zeta^{z}\tau^{z}\tilde{d}_5\left(\mathbf{k}\right)+\zeta^{z}\tau^{0}\tilde{d}_6\left(\mathbf{k}\right), \tag{B22}$$

where $d_i\left(\mathbf{k}\right)$ and $\tilde{d}_i\left(\mathbf{k}\right)$ $(1\leq i\leq 6)$ are real functions of the crystalline momentum $\mathbf{k}$. Moreover, as a consequence of Eqs. (B16) and (B17) for $g=C_{2z}$, we find that the parity of $d_i\left(\mathbf{k}\right)$ and $\tilde{d}_i\left(\mathbf{k}\right)$ $(1\leq i\leq 6)$ with respect to $\mathbf{k}$ is given by the parity of i, *i.e.*

$$d_i\left(-\mathbf{k}\right)=(-1)^{i}d_i\left(\mathbf{k}\right),\qquad \tilde{d}_i\left(-\mathbf{k}\right)=(-1)^{i}\tilde{d}_i\left(\mathbf{k}\right),\quad \text{for}\quad 1\leq i\leq 6. \tag{B23}$$

No additional restrictions are imposed by the time-reversal symmetry T.

In the particle-hole symmetric case ($\lambda=0$), we find that the particle-hole transformation P additionally imposes

$$d_i\left(-\mathbf{k}\right)=\begin{cases}d_i\left(\mathbf{k}\right) & \text{if}\quad 1\leq i\leq 2\\ -d_i\left(\mathbf{k}\right) & \text{if}\quad 3\leq i\leq 6\end{cases},\qquad \tilde{d}_i\left(-\mathbf{k}\right)=\begin{cases}\tilde{d}_i\left(\mathbf{k}\right) & \text{if}\quad 1\leq i\leq 2\\ -\tilde{d}_i\left(\mathbf{k}\right) & \text{if}\quad 3\leq i\leq 6\end{cases}, \tag{B24}$$

which together with Eq. (B23) requires that $d_i\left(\mathbf{k}\right)=\tilde{d}_i\left(\mathbf{k}\right)=0$ for $i=1,4,6$. In the particle-hole symmetric case ($\lambda=0$), the parameterization of the charge-one excitation matrices reads as

$$R\left(\mathbf{k}\right)=\zeta^{0}\tau^{0}d_2\left(\mathbf{k}\right)+\zeta^{x}\tau^{z}d_3\left(\mathbf{k}\right)+\zeta^{z}\tau^{z}d_5\left(\mathbf{k}\right), \tag{B25}$$

$$\tilde{R}\left(\mathbf{k}\right)=\zeta^{0}\tau^{0}\tilde{d}_2\left(\mathbf{k}\right)+\zeta^{x}\tau^{z}\tilde{d}_3\left(\mathbf{k}\right)+\zeta^{z}\tau^{z}\tilde{d}_5\left(\mathbf{k}\right), \tag{B26}$$

where the momentum parity of the functions $d_i(\mathbf{k})$ and $\tilde{d}_i(\mathbf{k})$ for $i = 2, 3, 5$ is given by Eq. (B23).

In the $\lambda = 1$ case, although not exact, the particle-hole transformation P is an an excellent *approximate* symmetry [84]. Provided the gauge-fixing condition from Eq. (A36) is imposed, we find that the parameterization of the charge-one excitation matrices from Eqs. (B21) and (B22) obeys

$$|d_i(\mathbf{k})| \ll |d_j(\mathbf{k})| \quad \text{and} \quad \left|\tilde{d}_i(\mathbf{k})\right| \ll \left|\tilde{d}_j(\mathbf{k})\right|, \quad \text{for } i = 1, 4, 6 \text{ and } j = 2, 3, 5, \tag{B27}$$

meaning that Eqs. (B25) and (B26) still hold *approximately*. Nevertheless, in the absence of *exact* particle-hole symmetry, we will employ the exact parameterizations from Eqs. (B21) and (B22) and only then explore the consequences of Eq. (B27).

Finally, in the first chiral limit ($w_0 = 0$), the presence of the anti-commuting C symmetry implies that the charge-one excitation matrices are diagonal

$$R(\mathbf{k}) = \zeta^0 \tau^0 d_2(\mathbf{k}), \tag{B28}$$

$$\tilde{R}(\mathbf{k}) = \zeta^0 \tau^0 \tilde{d}_2(\mathbf{k}), \tag{B29}$$

where the real functions $d_2(\mathbf{k})$ and $\tilde{d}_2(\mathbf{k})$ are even with respect to momentum inversion.

4. Charge-one excitation above specific ground states

As written in Eqs. (B1) and (B2), the charge-one commutation relations are cumbersome to apply for any choice of TBG ground states apart from the states $|\Psi_\nu\rangle$ defined in Eq. (B7). This is because for a generic $\mathrm{U}(4) \times \mathrm{U}(4)$ rotation of the state $\left|\Psi_\nu^{\nu_+,\nu_-}\right\rangle$ introduced in Eq. (B8) and for a given momentum $\mathbf{k}$, the states $\hat{c}^\dagger_{\mathbf{k},n,\eta,s}\left|\Psi_\nu^{\nu_+,\nu_-}\right\rangle$ ($\hat{c}_{\mathbf{k},n,\eta,s}\left|\Psi_\nu^{\nu_+,\nu_-}\right\rangle$) are not necessarily linearly independent, and therefore provide a redundant basis for the electron (hole) excitations above the ground state. As a simple example, consider the $\nu = -3$ valley-polarized ground state with $\mathcal{C} = 1$

$$|\varphi\rangle = \prod_{\mathbf{k}} \hat{d}^\dagger_{\mathbf{k},+1,+,\uparrow}|0\rangle = \prod_{\mathbf{k}} \frac{1}{\sqrt{2}}\left(\hat{c}^\dagger_{\mathbf{k},+1,+,\uparrow} + i\hat{c}^\dagger_{\mathbf{k},-1,+,\uparrow}\right)|0\rangle. \tag{B30}$$

With only one occupied Chern band, the state $|\varphi\rangle$ admits a single hole excitation with momentum $\mathbf{k}$. On the other hand, both $\hat{c}_{\mathbf{k},+1,+,\uparrow}|\varphi\rangle$ and $\hat{c}_{\mathbf{k},-1,+,\uparrow}|\varphi\rangle$ are non-vanishing. The solution to this apparent contradiction is that $\hat{c}_{\mathbf{k},+1,+,\uparrow}|\varphi\rangle = i\hat{c}_{\mathbf{k},-1,+,\uparrow}|\varphi\rangle$, meaning that the two hole excitations are in fact one and the same. The situation becomes even worse when considering generic rotations of the state $|\varphi\rangle$, where a coherent superposition of potentially *all* the TBG active bands is filled: despite having only *one* filled band and hence a single hole excitation for a given momentum, acting with *any* of the energy band operators $\hat{c}_{\mathbf{k},n,\eta,s}$ leads to a non-vanishing state.

Since the states $\left|\Psi_\nu^{\nu_+,\nu_-}\right\rangle$ from Eq. (B8) are obtained by filling Chern bands of different valley-spin flavors, we will find it useful perform a basis change and recast Eqs. (B1) and (B2) in terms of the Chern band operators from Eq. (A31) as

$$\left[H_I - \mu\hat{N}, \hat{d}^\dagger_{\mathbf{k},e_{Y_1},\eta,s}\right]|\varphi\rangle = \sum_{e_{Y_2}} R'^{\eta}_{e_{Y_2}e_{Y_1}}(\mathbf{k})\,\hat{d}^\dagger_{\mathbf{k},e_{Y_2},\eta,s}|\varphi\rangle, \tag{B31}$$

$$\left[H_I - \mu\hat{N}, \hat{d}_{\mathbf{k},e_{Y_1},\eta,s}\right]|\varphi\rangle = \sum_{e_{Y_2}} \tilde{R}'^{\eta}_{e_{Y_2}e_{Y_1}}(\mathbf{k})\,\hat{d}_{\mathbf{k},e_{Y_2},\eta,s}|\varphi\rangle, \tag{B32}$$

where the charge-one excitation matrices expressed in the Chern-band basis are given by

$$\begin{aligned} R'^{\eta}_{e_{Y_2}e_{Y_1}}(\mathbf{k}) &= \sum_{m,n} W^*_{e_{Y_2},m} W_{e_{Y_1},n} R^{\eta}_{mn}(\mathbf{k}), \\ \tilde{R}'^{\eta}_{e_{Y_2}e_{Y_1}}(\mathbf{k}) &= \sum_{m,n} W_{e_{Y_2},m} W^*_{e_{Y_1},n} \tilde{R}^{\eta}_{mn}(\mathbf{k}). \end{aligned} \tag{B33}$$

Here and in what follows, we will use the same symbol to represent a matrix or a vector in both the Chern ($e_Y = \pm 1$) and energy band ($n = \pm 1$) bases. To avoid confusion, we will employ a "prime" ($'$) symbol to denote that a matrix or vector is expressed in the Chern band basis, rather than the energy band basis. For generic $\mathrm{U}(4) \times \mathrm{U}(4)$ rotations of the states $\left|\Psi_\nu^{\nu_+,\nu_-}\right\rangle$, we will also define *rotated* Chern and energy band fermion operators. By doing so, we avoid the problems associated with redundant bases for the charge-one excitations.

a. Rotated fermion operators

Consider a specific $\mathrm{U}(4) \times \mathrm{U}(4)$ rotation (henceforth denoted by $\hat{U}$) of the state from Eq. (B8)

$$|\varphi\rangle = \hat{U} \left|\Psi_{\nu}^{\nu_+,\nu_-}\right\rangle . \tag{B34}$$

We employ $\rho_{e_Y,\eta,s} = 0, 1$ to explicitly show which Chern-valley-spin flavors are occupied in the unrotated state $\left|\Psi_{\nu}^{\nu_+,\nu_-}\right\rangle$, such that

$$\rho_{e_Y,\eta,s} = \begin{cases} 1, & \text{if the Chern-valley-spin flavor } \{e_Y,\eta,s\} \text{ band is occupied in } \left|\Psi_{\nu}^{\nu_+,\nu_-}\right\rangle \\ 0, & \text{if the Chern-valley-spin flavor } \{e_Y,\eta,s\} \text{ band is empty in } \left|\Psi_{\nu}^{\nu_+,\nu_-}\right\rangle \end{cases} . \tag{B35}$$

We are interested in explicitly deriving the charge-one excitation states above $|\varphi\rangle$, by particularizing Eqs. (B1) and (B2). To find a non-redundant basis for the charge-one excitations, we define the *rotated* Chern band basis

$$\hat{g}^{\dagger}_{\mathbf{k},e_Y,\eta,s} \equiv \hat{U} \hat{d}^{\dagger}_{\mathbf{k},e_Y,\eta,s} \hat{U}^{\dagger} = \sum_{e'_Y,\eta',s'} U'_{e_Y\eta s,e'_Y\eta's'} \hat{d}^{\dagger}_{\mathbf{k},e'_Y,\eta',s'}, \tag{B36}$$

as well as the *rotated* energy band basis

$$\hat{f}^{\dagger}_{\mathbf{k},n,\eta,s} \equiv \hat{U} \hat{c}^{\dagger}_{\mathbf{k},n,\eta,s} \hat{U}^{\dagger} = \sum_{n',\eta',s'} U_{n\eta s,n'\eta's'} \hat{c}^{\dagger}_{\mathbf{k},n',\eta',s'}. \tag{B37}$$

In Eq. (B36) and Eq. (B37), $U'_{e_Y\eta s,e'_Y\eta's'}$ and $U_{n\eta s,n'\eta's'}$ respectively denote eight-dimensional unitary matrices implementing the rotation $\hat{U}$ within the original Chern band ($\hat{d}^{\dagger}_{\mathbf{k},e_Y,\eta,s}$) and energy band ($\hat{c}^{\dagger}_{\mathbf{k},n,\eta,s}$) bases. The rotated Chern band operator $\hat{g}^{\dagger}_{\mathbf{k},e_Y,\eta,s}$ creates a fermion with a Chern number $e_Y = \pm 1$, as the $\mathrm{U}(4) \times \mathrm{U}(4)$ rotations generated by Eq. (A55) do not mix the different Chern sectors. On the other hand, $\hat{g}^{\dagger}_{\mathbf{k},e_Y,\eta,s}$ generally denotes a coherent superposition of fermions at momentum $\mathbf{k}$ from *all* valley and spin sectors, with the indices η and s merely indicating that $\hat{g}^{\dagger}_{\mathbf{k},e_Y,\eta,s}$ is obtained from $\hat{d}^{\dagger}_{\mathbf{k},e_Y,\eta,s}$ by acting with the transformation $\hat{U}$. For the rotated energy band fermion $\hat{f}^{\dagger}_{\mathbf{k},n,\eta,s}$, the band ($n$), valley ($\eta$), and spin ($s$) indices are simply an indication that it was obtained by rotating the original energy band fermion $\hat{c}^{\dagger}_{\mathbf{k},n,\eta,s}$ according to the transformation $\hat{U}$.

The main benefit of using the rotated Chern basis from Eq. (B36) is that the ground state $|\varphi\rangle$ of Eq. (B34) has a particularly simple expression

$$|\varphi\rangle = \prod_{\mathbf{k}} \left(\prod_{\substack{e_Y,\eta,s \\ \rho_{e_Y,\eta,s}=1}} \hat{g}^{\dagger}_{\mathbf{k},e_Y,\eta,s} \right) |0\rangle , \tag{B38}$$

where the product runs over those values $\{e_Y,\eta,s\}$ for which $\rho_{e_Y,\eta,s} = 1$. When written in this form, it becomes clear that a non-redundant basis for the electron excitations above $|\varphi\rangle$ with a definite momentum $\mathbf{k}$ is given by the $4-\nu$ operators $\hat{g}^{\dagger}_{\mathbf{k},e_Y,\eta,s}$ for which $\rho_{e_Y,\eta,s} = 0$. Similarly, a linearly-independent basis for the hole excitations is given by the $4+\nu$ operators $\hat{g}_{\mathbf{k},e_Y,\eta,s}$ for which $\rho_{e_Y,\eta,s} = 0$. We illustrate this schematically for a generic $\mathrm{U}(4) \times \mathrm{U}(4)$ rotation of the state $\left|\Psi_{-1}^{1,2}\right\rangle$ in Fig. 6.

b. Rotated charge-one excitation matrices

As discussed in Appendix [B 4 a] and shown schematically in Fig. 6, the Chern band operators $\hat{d}^{\dagger}_{\mathbf{k},e_Y,\eta,s}$ represent coherent superpositions of the occupied bands in $|\varphi\rangle$. As such, we will rewrite Eqs. (B31) and (B32) in terms of the rotated Chern band basis defined in Eq. (B36)

$$\left[H_I - \mu\hat{N}, \hat{g}^{\dagger}_{\mathbf{k},e_{Y_1},\eta_1,s_1}\right] |\varphi\rangle = \sum_{\substack{e_{Y_2},\eta_2,s_2 \\ \rho_{e_{Y_2},\eta_2,s_2}=0}} \left[R'^{\hat{U}}(\mathbf{k})\right]_{e_{Y_2}\eta_2 s_2, e_{Y_1}\eta_1 s_1} \hat{g}^{\dagger}_{\mathbf{k},e_{Y_2},\eta_2,s_2} |\varphi\rangle , \quad \text{for} \quad \rho_{e_{Y_1},\eta_1,s_1} = 0, \tag{B39}$$

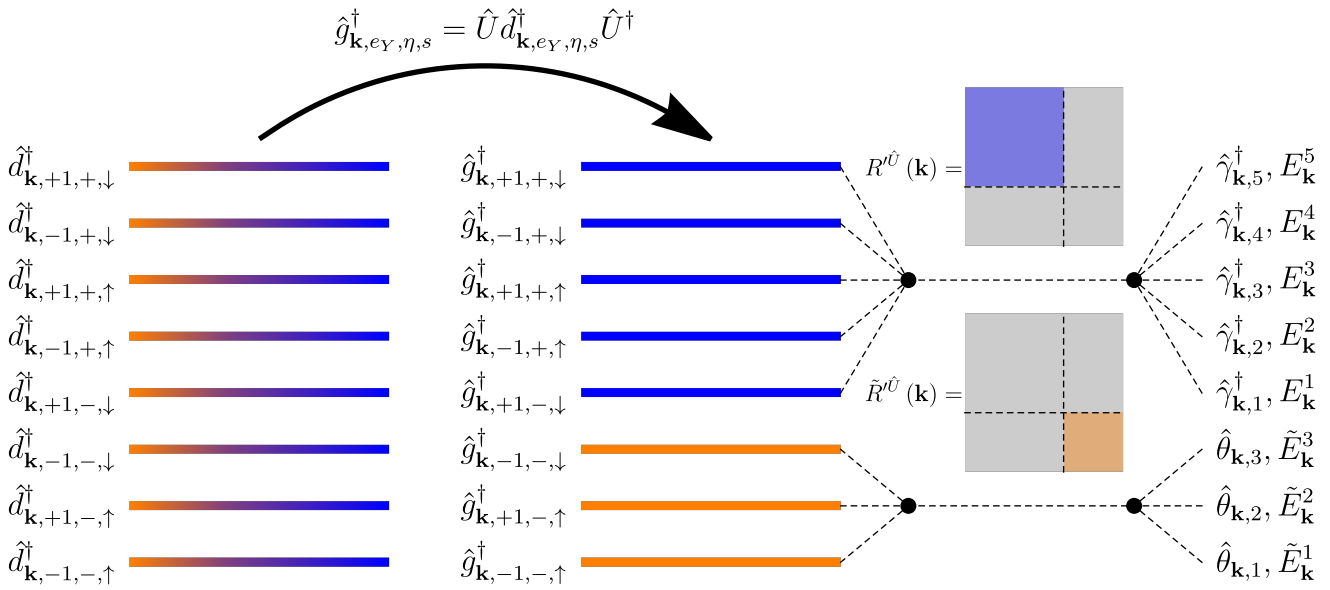

FIG. 6. Defining a non-redundant basis for the charge-one excitations. We consider the state $|\varphi\rangle = \hat{U}\left|\Psi^{1,2}_{-1}\right\rangle$, where $\hat{U}$ denotes a $\mathrm{U}(4)\times\mathrm{U}(4)$ rotation. For generic rotations $\hat{U}$ the three occupied bands of $|\varphi\rangle$ represent coherent superpositions of the original TBG Chern bands, implying that the operators $\hat{d}^\dagger_{\mathbf{k},e_Y,\eta,s}$ ($\hat{d}_{\mathbf{k},e_Y,\eta,s}$) acting on the state $|\varphi\rangle$ constitute a redundant basis for the electron (hole) excitations. By defining a *rotated* Chern band basis according to Eq. (B36), the state $|\varphi\rangle$ can be rewritten simply as $\prod_{\mathbf{k}}\left(\hat{g}^\dagger_{\mathbf{k},-1,-,\uparrow}\hat{g}^\dagger_{\mathbf{k},+1,-,\uparrow}\hat{g}^\dagger_{\mathbf{k},-1,-,\downarrow}\right)|0\rangle$. The rotated operators $\hat{g}^\dagger_{\mathbf{k},e_Y,\eta,s}$ ($\hat{g}_{\mathbf{k},e_Y,\eta,s}$) corresponding to the empty (filled) bands in $|\varphi\rangle$ provide a linearly independent basis for *all* the electron (hole) excitations on top of $|\varphi\rangle$. The rotated charge-one excitation matrices $R'^{\hat{U}}(\mathbf{k})$ and $\tilde{R}'^{\hat{U}}(\mathbf{k})$ defined in Eqs. (B41) and (B42) are then diagonalized in the space of empty and filled bands of $|\varphi\rangle$, respectively. For a given momentum $\mathbf{k}$, the rotated operators $\hat{g}^\dagger_{\mathbf{k},e_Y,\eta,s}$ ($\hat{g}_{\mathbf{k},e_Y,\eta,s}$) corresponding to the empty (filled) bands in $|\varphi\rangle$ can be recombined into the operators $\hat{\gamma}^\dagger_{\mathbf{k},p}$ for $1\le p\le 4-\nu$ ($\hat{\theta}_{\mathbf{k},p}$ for $1\le p\le 4+\nu$), which create an electron (hole) excitation above $|\varphi\rangle$ with energy $E^p_{\mathbf{k}}$ ($\tilde{E}^p_{\mathbf{k}}$).

$$\left[H_I-\mu\hat{N},\hat{g}_{\mathbf{k},e_{Y_1},\eta_1,s_1}\right]|\varphi\rangle = \sum_{\substack{e_{Y_2},\eta_2,s_2\\ \rho_{e_{Y_2},\eta_2,s_2}=1}}\left[\tilde{R}'^{\hat{U}}(\mathbf{k})\right]_{e_{Y_2}\eta_2 s_2,e_{Y_1}\eta_1 s_1}\hat{g}_{\mathbf{k},e_{Y_2},\eta_2,s_2}|\varphi\rangle\,,\quad \text{for}\quad \rho_{e_{Y_1},\eta_1,s_1}=1. \tag{B40}$$

where we have also introduced the *rotated* charge-one excitation matrices given by

$$\left[R'^{\hat{U}}(\mathbf{k})\right]_{e_{Y_2}\eta_2 s_2,e_{Y_1}\eta_1 s_1} = \sum_{\substack{e_{Y_3},\eta_3,s_3\\ e_{Y_4},\eta_4,s_4}} U'_{e_{Y_1}\eta_1 s_1,e_{Y_3}\eta_3 s_3}R'^{\eta_3}_{e_{Y_4},e_{Y_3}}(\mathbf{k})\,\delta_{\eta_3\eta_4}\delta_{s_3 s_4}U'^{*}_{e_{Y_2}\eta_2 s_2,e_{Y_4}\eta_4 s_4}, \tag{B41}$$

$$\left[\tilde{R}'^{\hat{U}}(\mathbf{k})\right]_{e_{Y_2}\eta_2 s_2,e_{Y_1}\eta_1 s_1} = \sum_{\substack{e_{Y_3},\eta_3,s_3\\ e_{Y_4},\eta_4,s_4}} U'^{*}_{e_{Y_1}\eta_1 s_1,e_{Y_3}\eta_3 s_3}\tilde{R}'^{\eta_3}_{e_{Y_4},e_{Y_3}}(\mathbf{k})\,\delta_{\eta_3\eta_4}\delta_{s_3 s_4}U'_{e_{Y_2}\eta_2 s_2,e_{Y_4}\eta_4 s_4}, \tag{B42}$$

or equivalently, in matrix form, by

$$R'^{\hat{U}}(\mathbf{k}) = U'^{*}\left(R'(\mathbf{k})\otimes s^0\right)U'^{T}, \tag{B43}$$

$$\tilde{R}'^{\hat{U}}(\mathbf{k}) = U'\left(\tilde{R}'(\mathbf{k})\otimes s^0\right)U'^{\dagger}. \tag{B44}$$

Note that in the electron (hole) commutation relation, we have restricted to only those operators $\hat{g}^\dagger_{\mathbf{k},e_Y,\eta,s}$ ($\hat{g}_{\mathbf{k},e_Y,\eta,s}$) which create (destroy) fermions belonging to the empty (filled) rotated Chern bands of $|\varphi\rangle$. In the chiral limit ($w_0=0$), Eqs. (B28) and (B29) imply that the charge-one excitation matrices $R(\mathbf{k})$ and $\tilde{R}(\mathbf{k})$, and hence the rotated charge-one excitation matrices are proportional to identity. As such, they do not include any off-diagonal elements between the fermions belonging to the empty and filled rotated Chern bands in $|\varphi\rangle$. Away from the chiral limit ($w_0\neq 0$), without exact particle-hole symmetry ($\lambda=1$), and for general $\mathrm{U}(4)\times\mathrm{U}(4)$ rotations, the $R'^{\hat{U}}(\mathbf{k})$ and $\tilde{R}'^{\hat{U}}(\mathbf{k})$ matrices will

generically contain non-vanishing off-diagonal elements between the fermions belonging to the empty and filled bands of $|\varphi\rangle$. This is a consequence of $|\varphi\rangle$ being a perturbative rather than exact eigenstate of H_I.

The charge commutation relations from Eqs. (B39) and (B40) written in the rotated Chern band basis allow us to find the electron and hole excitation states above the ground state $|\varphi\rangle$. To see this, we first note that $R'^{\hat{U}}(\mathbf{k})$ and $\tilde{R}'^{\hat{U}}(\mathbf{k})$ are Hermitian, being related by a unitary transformations to the Hermitian matrices $R(\mathbf{k})\otimes s^0$ and $\tilde{R}(\mathbf{k})\otimes s^0$, respectively. Therefore, their restrictions into the filled or empty rotated Chern bands from Eqs. (B39) and (B40) are Hermitian and can be diagonalized. We define the electron ($\Xi'^{p}_{\mathbf{k},e_Y\eta s}$ for $1\leq p\leq 4-\nu$) and hole ($\tilde{\Xi}'^{p}_{\mathbf{k},e_Y\eta s}$ for $1\leq p\leq 4+\nu$) excitation wave functions in the rotated Chern basis from Eq. (B36) (where p indexes the excitation), with support only on the empty and occupied rotated Chern bands, respectively, *i.e.*

$$\Xi^{p}_{\mathbf{k},e_Y\eta s}=0,\quad \text{if}\quad \rho_{e_Y,\eta,s}=1, \tag{B45}$$

$$\tilde{\Xi}^{p}_{\mathbf{k},e_Y\eta s}=0,\quad \text{if}\quad \rho_{e_Y,\eta,s}=0. \tag{B46}$$

The charge excitation wave functions diagonalize the restriction of $R'^{\hat{U}}(\mathbf{k})$ $[\tilde{R}'^{\hat{U}}(\mathbf{k})]$ in the empty (occupied) rotated Chern bands

$$\sum_{\substack{e_{Y_1},\eta_1,s_1\\ \rho_{e_{Y_1},\eta_1,s_1}=0}}\left[R'^{\hat{U}}(\mathbf{k})\right]_{e_{Y_2}\eta_2 s_2,e_{Y_1}\eta_1 s_1}\Xi'^{p}_{\mathbf{k},e_{Y_1}\eta_1 s_1}=E^{p}_{\mathbf{k}}\Xi'^{p}_{\mathbf{k},e_{Y_2}\eta_2 s_2},\ \text{for } 1\leq p\leq 4-\nu,\ \text{if } \rho_{e_{Y_2},\eta_2,s_2}=0 \tag{B47}$$

$$\sum_{\substack{e_{Y_1},\eta_1,s_1\\ \rho_{e_{Y_1},\eta_1,s_1}=1}}\left[\tilde{R}'^{\hat{U}}(\mathbf{k})\right]_{e_{Y_2}\eta_2 s_2,e_{Y_1}\eta_1 s_1}\tilde{\Xi}'^{p}_{\mathbf{k},e_{Y_1}\eta_1 s_1}=\tilde{E}^{p}_{\mathbf{k}}\tilde{\Xi}'^{p}_{\mathbf{k},e_{Y_2}\eta_2 s_2},\ \text{for } 1\leq p\leq 4+\nu,\ \text{if } \rho_{e_{Y_2},\eta_2,s_2}=1, \tag{B48}$$

where $E^{p}_{\mathbf{k}}$ and $\tilde{E}^{p}_{\mathbf{k}}$ denote the electron and hole excitation energies [2], respectively. Assuming that $|\varphi\rangle$ is a ground state of the TBG interaction Hamiltonian, the excitation energies must be positive $E^{p}_{\mathbf{k}},\tilde{E}^{p}_{\mathbf{k}}\geq 0$ [75]. Defining the charge-one excitation operators

$$\hat{\gamma}^{\dagger}_{\mathbf{k},p}=\sum_{e_Y,\eta,s}\Xi'^{p}_{\mathbf{k},e_Y\eta s}\hat{g}^{\dagger}_{\mathbf{k},e_Y,\eta,s}=\sum_{n,\eta,s}\Xi^{p}_{\mathbf{k},n\eta s}\hat{f}^{\dagger}_{\mathbf{k},n,\eta,s},\ \text{for } 1\leq p\leq 4-\nu, \tag{B49}$$

$$\hat{\theta}_{\mathbf{k},p}=\sum_{e_Y,\eta,s}\tilde{\Xi}'^{p}_{\mathbf{k},e_Y\eta s}\hat{g}_{\mathbf{k},e_Y,\eta,s}=\sum_{n,\eta,s}\tilde{\Xi}^{p}_{\mathbf{k},n\eta s}\hat{f}_{\mathbf{k},n,\eta,s},\ \text{for } 1\leq p\leq 4+\nu, \tag{B50}$$

corresponding respectively to the electron and hole excitations above the $|\varphi\rangle$ state, we find that

$$\left[H_I-\mu\hat{N},\hat{\gamma}^{\dagger}_{\mathbf{k},p}\right]|\varphi\rangle=E^{p}_{\mathbf{k}}\hat{\gamma}^{\dagger}_{\mathbf{k},p}|\varphi\rangle,\ \text{for } 1\leq p\leq 4-\nu, \tag{B51}$$

$$\left[H_I-\mu\hat{N},\hat{\theta}_{\mathbf{k},p}\right]|\varphi\rangle=\tilde{E}^{p}_{\mathbf{k}}\hat{\theta}_{\mathbf{k},p}|\varphi\rangle,\ \text{for } 1\leq p\leq 4+\nu, \tag{B52}$$

implying that $\hat{\gamma}^{\dagger}_{\mathbf{k},p}|\varphi\rangle$ ($\hat{\theta}_{\mathbf{k},p}|\varphi\rangle$) is an electron (hole) excited eigenstate of H_I above the ground state $|\varphi\rangle$ with eigenvalue $E_\varphi+E^{p}_{\mathbf{k}}+\mu$ ($E_\varphi+\tilde{E}^{p}_{\mathbf{k}}-\mu$), where E_φ is the energy of $|\varphi\rangle$, *i.e.* $H_I|\varphi\rangle=E_\varphi|\varphi\rangle$. In Eqs. (B49) and (B50), we have also introduced the charge-one excitation wave functions in the rotated energy band basis

$$\Xi^{p}_{\mathbf{k},n\eta s}=\sum_{e_Y}W_{e_Y,n}\Xi'^{p}_{\mathbf{k},e_Y\eta s} \tag{B53}$$

$$\tilde{\Xi}^{p}_{\mathbf{k},n\eta s}=\sum_{e_Y}W^{*}_{e_Y,n}\tilde{\Xi}'^{p}_{\mathbf{k},e_Y\eta s} \tag{B54}$$

Having obtained the charge-one excitation operators from Eqs. (B49) and (B50), we now perform one last basis transformation to express the corresponding wave functions in the original TBG fermion basis. Defining

$$Z'^{p}_{\mathbf{k},e_Y\eta s}=\sum_{e'_Y,\eta',s'}U'_{e'_Y\eta' s',e_Y\eta s}\Xi'^{p}_{\mathbf{k},e'_Y\eta' s'},\ \text{for } 1\leq p\leq 4-\nu, \tag{B55}$$

[2] The excitation energies are defined with respect to the grand canonical Hamiltonian $H_I-\mu\hat{N}$.

$$\tilde{Z}'^{p}_{\mathbf{k},e_Y\eta s}=\sum_{e'_Y,\eta',s'}U'^{*}_{e'_Y\eta's',e_Y\eta s}\tilde{\Xi}'^{p}_{\mathbf{k},e'_Y\eta's'},\ \text{for}\ 1\leq p\leq 4+\nu, \tag{B56}$$

we can rewrite the charge-one excitation operators as

$$\hat{\gamma}^{\dagger}_{\mathbf{k},p}=\sum_{e_Y,\eta,s}Z'^{p}_{\mathbf{k},e_Y\eta s}\hat{d}^{\dagger}_{\mathbf{k},e_Y,\eta,s}=\sum_{n,\eta,s}Z^{p}_{\mathbf{k},n\eta s}\hat{c}^{\dagger}_{\mathbf{k},n,\eta,s},\ \text{for}\ 1\leq p\leq 4-\nu, \tag{B57}$$

$$\hat{\theta}_{\mathbf{k},p}=\sum_{e_Y,\eta,s}\tilde{Z}'^{p}_{\mathbf{k},e_Y\eta s}\hat{d}_{\mathbf{k},e_Y,\eta,s}=\sum_{n,\eta,s}\tilde{Z}^{p}_{\mathbf{k},n\eta s}\hat{c}_{\mathbf{k},n,\eta,s},\ \text{for}\ 1\leq p\leq 4+\nu, \tag{B58}$$

where we have also defined the charge-one excitation wave functions $Z^{p}_{\mathbf{k},n\eta s}$ and $\tilde{Z}^{p}_{\mathbf{k},n\eta s}$ in the TBG energy band basis. Finally, we can define two projector matrices which project in the empty and occupied Chern bands of the unrotated state $\left|\Psi^{\nu_+,\nu_-}_{\nu}\right\rangle$, whose components in the Chern band basis read as

$$\Pi'_{e_{Y_1}\eta_1 s_1,e_{Y_2}\eta_2 s_2}=\delta_{e_{Y_1},e_{Y_2}}\delta_{\eta_1,\eta_2}\delta_{s_1,s_2}-\rho_{e_{Y_1},\eta_1,s_1}\rho_{e_{Y_2},\eta_2,s_2}, \tag{B59}$$

$$\tilde{\Pi}'_{e_{Y_1}\eta_1 s_1,e_{Y_2}\eta_2 s_2}=\rho_{e_{Y_1},\eta_1,s_1}\rho_{e_{Y_2},\eta_2,s_2}, \tag{B60}$$

respectively. Eqs. (B59) and (B60) can be employed to obtain a set of important relations which relate the $\mathrm{U}(4)\times\mathrm{U}(4)$ transformation $\hat{U}$, the occupied bands of the unrotated state $\left|\Psi^{\nu_+,\nu_-}_{\nu}\right\rangle$, the charge-one excitation matrices from Eqs. (B1) and (B2), and the charge-one excitation spectra for $|\varphi\rangle$

$$\sum_{p=1}^{4-\nu}E^{p}_{\mathbf{k}}\Xi^{*p}_{\mathbf{k},n\eta s}\Xi^{p}_{\mathbf{k},n'\eta's'}=\left[\Pi R^{*\hat{U}}(\mathbf{k})\Pi\right]_{n\eta s,n'\eta's'}=\left[\Pi U\left(R(\mathbf{k})\otimes s^{0}\right)U^{\dagger}\Pi\right]_{n\eta s,n'\eta's'}, \tag{B61}$$

$$\sum_{p=1}^{4+\nu}\tilde{E}^{p}_{\mathbf{k}}\tilde{\Xi}^{p}_{\mathbf{k},n\eta s}\tilde{\Xi}^{*p}_{\mathbf{k},n'\eta's'}=\left[\tilde{\Pi}\tilde{R}^{\hat{U}}(\mathbf{k})\tilde{\Pi}\right]_{n\eta s,n'\eta's'}=\left[\tilde{\Pi}U\left(\tilde{R}(\mathbf{k})\otimes s^{0}\right)U^{\dagger}\tilde{\Pi}\right]_{n\eta s,n'\eta's'}, \tag{B62}$$

$$\sum_{p=1}^{4-\nu}E^{p}_{\mathbf{k}}Z^{*p}_{\mathbf{k},n\eta s}Z^{p}_{\mathbf{k},n'\eta's'}=\left[U^{\dagger}\Pi R^{*\hat{U}}(\mathbf{k})\Pi U\right]_{n\eta s,n'\eta's'}=\left[U^{\dagger}\Pi U\left(R(\mathbf{k})\otimes s^{0}\right)U^{\dagger}\Pi U\right]_{n\eta s,n'\eta's'}, \tag{B63}$$

$$\sum_{p=1}^{4+\nu}\tilde{E}^{p}_{\mathbf{k}}\tilde{Z}^{p}_{\mathbf{k},n\eta s}\tilde{Z}^{*p}_{\mathbf{k},n'\eta's'}=\left[U^{\dagger}\tilde{\Pi}\tilde{R}^{\hat{U}}(\mathbf{k})\tilde{\Pi}U\right]_{n\eta s,n'\eta's'}=\left[U^{\dagger}\tilde{\Pi}U\left(\tilde{R}(\mathbf{k})\otimes s^{0}\right)U^{\dagger}\tilde{\Pi}U\right]_{n\eta s,n'\eta's'}. \tag{B64}$$

In Appendix [E], we will employ these relations in order to provide an analytical understanding of the symmetry properties of the spectral function of the TBG ground states.

Appendix C: Spectral function

An STM experiment allows for the indirect determination of the spectral function $A(\mathbf{r},\omega)$ of a certain quantum system. This appendix is dedicated to defining and then deriving the spectral function for a TBG sample. We show that the TBG spectral function can be written as a contraction between two (gauge-dependent) tensors: the spectral function matrix (which depends on the specific ground state that we consider and on the many-body TBG Hamiltonian), and the spatial factor (which depends on the active band TBG wave functions). We then investigate the properties of the spatial factor arising from the single-particle symmetries of the single-particle TBG Hamiltonian outlined in Appendix [A 1 c], as well as on the gauge-fixing conditions from Appendix [A 1 d]. Finally, we will provide an approximation to the spatial factor and compute it at key momenta within the SLG Brillouin zone.

1. Derivation

a. Fermionic field operators

We start by introducing the fermionic field operator $\hat{\Psi}_s(\mathbf{r})$ which annihilates an electron of spin s at position $\mathbf{r}$. Letting $\phi(\mathbf{r})$ denote the carbon p_z orbital wave function, we can obtain the following anti-commutation relation between the field operator $\hat{\Psi}_s(\mathbf{r})$ and the microscopic fermion operators $\hat{a}^{\dagger}_{\mathbf{R},\alpha,s,l}$ introduced in Appendix [A 1 a]

$$\left\{\hat{\Psi}_s(\mathbf{r}),\hat{a}^{\dagger}_{\mathbf{R},\alpha,s,l}\right\}=\langle 0|\hat{\Psi}_s(\mathbf{r})\hat{a}^{\dagger}_{\mathbf{R},\alpha,s,l}|0\rangle=\phi\left[\mathbf{r}-\mathcal{R}_{\theta,l}(\mathbf{R}+\mathbf{t}_{\alpha})-\mathbf{z}_l\right], \tag{C1}$$

i	ξ_i	C_i	N_i
1	0.9807	0.2824	1.100
2	1.4436	0.5470	2.891
3	2.6005	0.2320	12.59
4	6.5100	0.0103	124.9

TABLE I. Parameters of the valence electron wave function of the carbon atom p_z orbital from Eq. (C2). These parameters were tabulated by Ref. [94], and were obtained by a series expansion in the basis set of atomic Slater orbitals.

with $\mathbf{z}_l = z_l \hat{\mathbf{z}}$, where z_l is the height of the layer l (see Fig. 5). Note that $\hat{a}^\dagger_{\mathbf{R},\alpha,s,l}$ creates an electron of spin s in a carbon p_z orbital located at position $\mathcal{R}_{\theta,l}\left(\mathbf{R}+\mathbf{t}_\alpha\right)$. Throughout this work, we take the p_z orbital wave function to be given by an analytic approximation of the carbon atom p_z orbital [94, 95]

$$\phi\left(\mathbf{r}\right) = \frac{1}{2}\sqrt{\frac{3}{\pi a_B^5}} z \sum_{i=1}^{4} C_i N_i e^{-\frac{\xi_i r}{a_B}}, \tag{C2}$$

where $\mathbf{r} = x\hat{\mathbf{x}} + y\hat{\mathbf{y}} + z\hat{\mathbf{z}}$, a_B is the Bohr radius, and the dimensionless parameters C_i, N_i and ξ_i (for $1 \leq i \leq 4$) were defined and tabulated by Ref. [94] and are also provided in Table I. In what follows, we will assume p_z orbitals belonging to different carbon atoms to be orthogonal and thus

$$\left\{\hat{a}^\dagger_{\mathbf{R},\alpha,s,l}, \hat{a}_{\mathbf{R}',\beta,s',l'}\right\} = \delta_{\mathbf{R},\mathbf{R}'}\delta_{\alpha,\beta}\delta_{s,s'}\delta_{l,l'}. \tag{C3}$$

Strictly speaking, this is not true, as we are assuming atomic orbitals as opposed to Wannier ones. Nevertheless, for visualizing STM patterns, Eq. (C2) provides a good enough approximation [95]. Using the anti-commutation relations from Eqs. (C1) and (C3) we can express the fermionic field operator at the STM tip position in terms of the microscopic graphene orbitals as

$$\hat{\Psi}^\dagger_s\left(\mathbf{r}+\mathbf{z}_p\right) = \sum_{\alpha,l}\sum_{\mathbf{R}} \phi\left[\mathbf{r}+\mathbf{z}_p - R_{\theta,l}\left(\mathbf{R}+\mathbf{t}_\alpha\right) - \mathbf{z}_l\right] \hat{a}^\dagger_{\mathbf{R},\alpha,s,l} + \ldots, \tag{C4}$$

where $\mathbf{z}_p = z_p\hat{\mathbf{z}}$, with z_p being the height of the STM tip (see Fig. 5). The dots at the end imply that Eq. (C4) does not provide a full expansion of the fermionic field, as the p_z Carbon atoms of the TBG sample do not form a complete basis set. For Eq. (C4) to be complete, one would need to include the all the (infinitely many) orbitals *orthogonal* to the ones created by the set of operators $\hat{a}^\dagger_{\mathbf{R},\alpha,s,l}$. As they are not relevant for the physics of TBG near charge neutrality, we leave them unspecified in the expansion from Eq. (C4) and omit them completely henceforth.

We assume the height of the STM tip to remain constant throughout an experiment [3]. As such, we will employ a convention in which $\mathbf{r}$ denotes a strictly two-dimensional vectors in the plane of the TBG sample, and use the shorthand notation where

$$\hat{\psi}^\dagger_s\left(\mathbf{r}\right) \equiv \hat{\Psi}^\dagger_s\left(\mathbf{r}+\mathbf{z}_p\right) \tag{C5}$$

denotes the Fermionic field operator corresponding to the STM tip position and

$$\phi_l\left(\mathbf{r}\right) \equiv \phi\left(\mathbf{r}+\mathbf{z}_p-\mathbf{z}_l\right). \tag{C6}$$

is the orbital wave function for a p_z orbital located at the origin, within layer l.

Using the notation in Eqs. (C5) and (C6), Eq. (C4) becomes

$$\hat{\psi}^\dagger_s\left(\mathbf{r}\right) = \sum_{\alpha,l}\sum_{\mathbf{R}} \phi_l\left[\mathbf{r} - R_{\theta,l}\left(\mathbf{R}+\mathbf{t}_\alpha\right)\right] \hat{a}^\dagger_{\mathbf{R},\alpha,s,l}. \tag{C7}$$

We will now relate the Fermion field operator to the TBG energy band operators introduced in Eq. (A15). We start by introducing the two-dimensional Fourier transformation of the p_z orbital wave function over the SLG Brillouin Zone BZ_l

$$\phi_l\left(\mathbf{r}\right) = \frac{1}{N_0\Omega_{\mathrm{SLG}}} \sum_{\substack{\mathbf{p}\in\mathrm{BZ}_l \\ \mathbf{G}\in\mathcal{G}_l}} \phi_l\left(\mathbf{p}+\mathbf{G}\right) e^{-i(\mathbf{p}+\mathbf{G})\cdot\mathbf{r}}, \tag{C8}$$

[3] For the theoretically predicted STM signal, we assume the height of the STM tip to remain constant, whereas for experiments, its height changes so as to keep the tunneling current constant. As such, we normalize the experimentally-measured STM signals and the theoretically-predicted spectral functions in Fig. 1 according to their maxima.

where $\mathcal{G}_l$ is the reciprocal lattice of the graphene layer l, as defined in the text surrounding Eq. (A5), $\Omega_{\rm SLG}$ denotes the surface area of the SLG unit cell, and N_0 denotes the number of SLG unit cells. The total area of the TBG sample is thus given by $\Omega_{\rm TBG} = N_0\Omega_{\rm SLG}$. Owing to the rotational symmetry of the p_z orbital around the $\hat{\mathbf{z}}$ axis, we have that

$$\phi_l\left(\mathbf{p}+\mathbf{G}\right) = \phi_l\left(\left|\mathbf{p}+\mathbf{G}\right|\right) \tag{C9}$$

and $\phi_l\left(\mathbf{p}+\mathbf{G}\right)$ is also real, *i.e.*

$$\phi_l\left(\mathbf{p}+\mathbf{G}\right) = \phi_l^*\left(\mathbf{p}+\mathbf{G}\right). \tag{C10}$$

Employing the Fourier transformations introduced in Eqs. (A4) and (C8), we can express the Fermionic field operators $\hat{\psi}_s^\dagger\left(\mathbf{r}\right)$ in terms of the moiré lattice low-energy operators defined in Eq. (A8)

$$\begin{aligned}\hat{\psi}_s^\dagger\left(\mathbf{r}\right) &= \frac{1}{N_0\Omega_{\rm SLG}\sqrt{N_0}}\sum_{\alpha,l}\sum_{\mathbf{R}}\sum_{\substack{\mathbf{p}_1,\mathbf{p}_2\in{\rm BZ}_l\\ \mathbf{G}\in\mathcal{G}_l}}\phi_l\left(\mathbf{p}_1+\mathbf{G}\right)\hat{a}^\dagger_{\mathbf{p}_2,\alpha,s,l}e^{-i(\mathbf{p}_1+\mathbf{G})\cdot\mathbf{r}}e^{i(\mathbf{p}_1-\mathbf{p}_2)\cdot R_{\theta,l}(\mathbf{R}+\mathbf{t}_\alpha)}e^{i\mathbf{G}\cdot R_{\theta,l}\mathbf{t}_\alpha}\\ &= \frac{1}{\Omega_{\rm SLG}\sqrt{N_0}}\sum_{\alpha,l}\sum_{\substack{\mathbf{p}\in{\rm BZ}_l\\ \mathbf{G}\in\mathcal{G}_l}}\phi_l\left(\mathbf{p}+\mathbf{G}\right)\hat{a}^\dagger_{\mathbf{p},\alpha,s,l}e^{i\mathbf{G}\cdot R_{\theta,l}\mathbf{t}_\alpha}e^{-i(\mathbf{p}+\mathbf{G})\cdot\mathbf{r}}\\ &= \frac{1}{\Omega_{\rm SLG}\sqrt{N_0}}\sum_{\alpha,l,\eta}\sum_{\substack{\mathbf{k}\in{\rm MBZ}_l\\ \mathbf{Q}\in\mathcal{Q}_{\eta l}\\ \mathbf{G}\in\mathcal{G}_l}}\phi_l\left(\eta\mathbf{K}_l+\mathbf{k}-\mathbf{Q}+\mathbf{G}\right)e^{i\mathbf{G}\cdot R_{\theta,l}\mathbf{t}_\alpha}e^{-i(\eta\mathbf{K}_l+\mathbf{k}-\mathbf{Q}+\mathbf{G})\cdot\mathbf{r}}\hat{c}^\dagger_{\mathbf{k},\mathbf{Q},\eta,\alpha,s}.\end{aligned} \tag{C11}$$

Using Eq. (A17), we can also write Eq. (C11) in the energy band basis as

$$\hat{\psi}_s^\dagger\left(\mathbf{r}\right) = \sum_{\eta,n}V_{\mathbf{r},\mathbf{k}n\eta}\hat{c}^\dagger_{\mathbf{k},n,\eta,s}, \tag{C12}$$

where we have defined

$$V_{\mathbf{r},\mathbf{k}n\eta} = \frac{1}{\Omega_{\rm SLG}\sqrt{N_0}}\sum_{\alpha,l}\sum_{\substack{\mathbf{Q}\in\mathcal{Q}_{\eta l}\\ \mathbf{G}\in\mathcal{G}_l}}\phi_l\left(\eta\mathbf{K}_l+\mathbf{k}-\mathbf{Q}+\mathbf{G}\right)e^{i\mathbf{G}\cdot R_{\theta,l}\mathbf{t}_\alpha}e^{-i(\eta\mathbf{K}_l+\mathbf{k}-\mathbf{Q}+\mathbf{G})\cdot\mathbf{r}}u^*_{\mathbf{Q}\alpha;n\eta}\left(\mathbf{k}\right). \tag{C13}$$

b. The TBG spectral function

As mentioned previously, the key quantity which is measured in an STM experiment is the real-space spectral function $A\left(\mathbf{r},\omega\right)$ which can be written as [77, 96, 97]

$$A\left(\mathbf{r},\omega\right) = \sum_{\lambda,\xi}\sum_s P_\lambda\left[\left|\left\langle\xi\middle|\hat{\psi}_s^\dagger\left(\mathbf{r}\right)\middle|\lambda\right\rangle\right|^2\delta\left(\omega-E_\xi+E_\lambda\right)+\left|\left\langle\xi\middle|\hat{\psi}_s\left(\mathbf{r}\right)\middle|\lambda\right\rangle\right|^2\delta\left(\omega+E_\xi-E_\lambda\right)\right], \tag{C14}$$

where $\left|\lambda\right\rangle$ and $\left|\xi\right\rangle$ denote the exact many-body eigenstates of TBG, with the corresponding energies being given by E_ξ and E_λ, respectively. In Eq. (C14) P_λ represents the thermodynamic probability of the system being in state λ. In what follows, we will focus on low-temperature measurements, and so we will assume that $P_\lambda = 1$ if $\left|\lambda\right\rangle$ is one of the ground-states of TBG, and zero otherwise [42, 58, 68]. In Eq. (C14), the state $\hat{\psi}_s^\dagger\left(\mathbf{r}\right)\left|\lambda\right\rangle$ ($\hat{\psi}_s\left(\mathbf{r}\right)\left|\lambda\right\rangle$) is formed by creating (destroying) an electron from the TBG many-body ground state, and thus represents a superposition of charge-one excitations [75]. It follows that the only states $\left|\xi\right\rangle$ which give a non-zero contribution to the spectral function in Eq. (C14) are the charge-one excitations above the many-body ground states of TBG, whose properties were analytically derived in Ref. [75] and summarized and extended in Appendix [B].

As discussed in Appendix [B], Ref. [75] has shown that the low-energy charge-one excitation above a given TBG ground state at integer fillings $-4\leq\nu\leq 4$ [68] are obtained by acting with the energy band operators from Eq. (A15) with $n=\pm1$, or alternatively, with the Chern band basis operators from Eq. (A31) on the many-body ground states of TBG. As such, we can employ Eq. (C12) to write the real-space spectral function in terms of the energy-band operators as

$$A\left(\mathbf{r},\omega\right) = \sum_{\mathbf{k}',\mathbf{k}\in{\rm MBZ}}\sum_{\substack{n,\eta\\ n',\eta'}}\left\{\left[\mathcal{M}^+\left(\omega\right)\right]_{\mathbf{k}n\eta,\mathbf{k}'n'\eta'}V_{\mathbf{r},\mathbf{k}n\eta}V^*_{\mathbf{r},\mathbf{k}'n'\eta'}+\left[\mathcal{M}^-\left(\omega\right)\right]_{\mathbf{k}n\eta,\mathbf{k}'n'\eta'}V_{\mathbf{r},\mathbf{k}n\eta}V^*_{\mathbf{r},\mathbf{k}'n'\eta'}\right\} = \tag{C15}$$

$$= \sum_{\mathbf{k}',\mathbf{k}\in\mathrm{MBZ}} \sum_{\substack{n,\eta \\ n',\eta'}} \left[\mathcal{M}^{+}(\omega) + \mathcal{M}^{-}(\omega)\right]_{\mathbf{k}n\eta,\mathbf{k}'n'\eta'} \left[\mathcal{B}(\mathbf{r})\right]_{\mathbf{k}n\eta,\mathbf{k}'n'\eta'} \tag{C15}$$

where here, and in what follows, all summations over the TBG energy bands will be restricted to the *active* TBG bands (*i.e.* $n, n' = \pm 1$). Eq. (C15) represents the central result of this appendix: the spectral function of TBG is the tensor contraction between the spectral function matrices $\left[\mathcal{M}^{\pm}(\omega)\right]_{\mathbf{k}n\eta,\mathbf{k}'n'\eta'}$, which depend on the particular TBG ground state that we consider and whose elements are given by

$$\left[\mathcal{M}^{+}(\omega)\right]_{\mathbf{k}n\eta,\mathbf{k}'n'\eta'} = \sum_{\lambda,\xi} \sum_{s,s'} P_{\lambda} \langle\lambda|\hat{c}_{\mathbf{k}',n',\eta',s'}|\xi\rangle \left\langle \xi \middle| \hat{c}^{\dagger}_{\mathbf{k},n,\eta,s} \middle| \lambda \right\rangle \delta_{s,s'} \delta\left(\omega - E_{\xi} + E_{\lambda}\right), \tag{C16}$$

$$\left[\mathcal{M}^{-}(\omega)\right]_{\mathbf{k}n\eta,\mathbf{k}'n'\eta'} = \sum_{\lambda,\xi} \sum_{s,s'} P_{\lambda} \left\langle \lambda \middle| \hat{c}^{\dagger}_{\mathbf{k},n,\eta,s} \middle| \xi \right\rangle \langle\xi|\hat{c}_{\mathbf{k}',n',\eta',s'}|\lambda\rangle \delta_{s,s'} \delta\left(\omega + E_{\xi} - E_{\lambda}\right), \tag{C17}$$

respectively for the so called "electron" and "hole" contributions, and the spatial factor matrix $\mathcal{B}(\mathbf{r})$ whose elements are given by $\left[\mathcal{B}(\mathbf{r})\right]_{\mathbf{k}n\eta,\mathbf{k}'n'\eta'} = V^{*}_{\mathbf{r},\mathbf{k}'n'\eta'} V_{\mathbf{r},\mathbf{k}n\eta}$, or more precisely by

$$\left[\mathcal{B}(\mathbf{r})\right]_{\mathbf{k}n\eta,\mathbf{k}'n'\eta'} = \frac{1}{\Omega_{\mathrm{TBG}}\Omega_{\mathrm{SLG}}} \sum_{\substack{\alpha_1,l_1 \\ \alpha_2,l_2}} \sum_{\substack{\mathbf{Q}_1\in\mathcal{Q}_{\eta l_1} \\ \mathbf{Q}_2\in\mathcal{Q}_{\eta' l_2}}} \sum_{\substack{\mathbf{G}_1\in\mathcal{G}_{l_1} \\ \mathbf{G}_2\in\mathcal{G}_{l_2}}} \phi_{l_1}\left(\eta\mathbf{K}_{l_1} + \mathbf{k} - \mathbf{Q}_1 + \mathbf{G}_1\right) \phi^{*}_{l_2}\left(\eta'\mathbf{K}_{l_2} + \mathbf{k}' - \mathbf{Q}_2 + \mathbf{G}_2\right)$$
$$\times u^{*}_{\mathbf{Q}_1\alpha_1;n\eta}(\mathbf{k})\, u_{\mathbf{Q}_2\alpha_2;n'\eta'}(\mathbf{k}')\, e^{i\left(\mathbf{G}_1\cdot R_{\theta,l_1}\mathbf{t}_{\alpha_1} - \mathbf{G}_2\cdot R_{\theta,l_2}\mathbf{t}_{\alpha_2}\right)} e^{-i\left(\eta\mathbf{K}_{l_1} + \mathbf{k} - \mathbf{Q}_1 + \mathbf{G}_1\right)\cdot\mathbf{r}} e^{i\left(\eta'\mathbf{K}_{l_2} + \mathbf{k}' - \mathbf{Q}_2 + \mathbf{G}_2\right)\cdot\mathbf{r}}. \tag{C18}$$

It is important to note that neither the spectral function matrix elements, nor the spatial factor are separately gauge-invariant quantities. By fixing the gauge according to Appendix [A 1 d], we can however discuss their properties individually. We also note that provided that the moiré translation symmetry is not broken by the TBG ground state (which will always assume to be the case in this work), the spectral function matrix is diagonal in momentum space

$$\left[\mathcal{M}^{\pm}(\omega)\right]_{\mathbf{k}n\eta,\mathbf{k}'n'\eta'} = 0, \quad \text{if} \quad \mathbf{k}' \neq \mathbf{k}. \tag{C19}$$

Finally, the spectral function matrix elements can be used to determine the density of states $\rho(\omega)$ by tracing over all degrees of freedom

$$\rho(\omega) = \sum_{\mathbf{k}\in\mathrm{MBZ}} \sum_{n,\eta} \left[\mathcal{M}^{+}(\omega) + \mathcal{M}^{-}(\omega)\right]_{\mathbf{k}n\eta,\mathbf{k}n\eta} \tag{C20}$$

Alternatively, one can also adopt a momentum-space description and define the Fourier transformation of the spectral function and spatial factor

$$A(\mathbf{r},\omega) = \int \frac{d^2\mathbf{q}}{(2\pi)^2} A(\mathbf{q},\omega)\, e^{i\mathbf{q}\cdot\mathbf{r}}, \quad \mathcal{B}(\mathbf{r}) = \int \frac{d^2\mathbf{q}}{(2\pi)^2} \mathcal{B}(\mathbf{q})\, e^{i\mathbf{q}\cdot\mathbf{r}}. \tag{C21}$$

By analogy with Eq. (C15) $A(\mathbf{q},\omega)$ can also be expressed in terms of the spectral function matrix elements as

$$A(\mathbf{q},\omega) = \sum_{\mathbf{k}',\mathbf{k}\in\mathrm{MBZ}} \sum_{\substack{n,\eta \\ n',\eta'}} \left[\mathcal{M}^{+}(\omega) + \mathcal{M}^{-}(\omega)\right]_{\mathbf{k}n\eta,\mathbf{k}'n'\eta'} \left[\mathcal{B}(\mathbf{q})\right]_{\mathbf{k}n\eta,\mathbf{k}'n'\eta'}, \tag{C22}$$

where the Fourier-transformed spatial factor is given explicitly by

$$\left[\mathcal{B}(\mathbf{q})\right]_{\mathbf{k}n\eta,\mathbf{k}'n'\eta'} = \frac{(2\pi)^2}{\Omega_{\mathrm{TBG}}\Omega_{\mathrm{SLG}}} \sum_{\substack{\alpha_1,l_1 \\ \alpha_2,l_2}} \sum_{\substack{\mathbf{Q}_1\in\mathcal{Q}_{\eta l_1} \\ \mathbf{Q}_2\in\mathcal{Q}_{\eta' l_2}}} \sum_{\substack{\mathbf{G}_1\in\mathcal{G}_{l_1} \\ \mathbf{G}_2\in\mathcal{G}_{l_2}}} \phi_{l_1}\left(\eta\mathbf{K}_{l_1} + \mathbf{k} - \mathbf{Q}_1 + \mathbf{G}_1\right) \phi^{*}_{l_2}\left(\eta'\mathbf{K}_{l_2} + \mathbf{k}' - \mathbf{Q}_2 + \mathbf{G}_2\right)$$
$$\times u^{*}_{\mathbf{Q}_1\alpha_1;n\eta}(\mathbf{k})\, u_{\mathbf{Q}_2\alpha_2;n'\eta'}(\mathbf{k}')\, e^{i\left(\mathbf{G}_1\cdot R_{\theta,l_1}\mathbf{t}_{\alpha_1} - \mathbf{G}_2\cdot R_{\theta,l_2}\mathbf{t}_{\alpha_2}\right)} \delta\left(\eta\mathbf{K}_{l_1} + \mathbf{k} - \mathbf{Q}_1 + \mathbf{G}_1 - \eta'\mathbf{K}_{l_2} - \mathbf{k}' + \mathbf{Q}_2 - \mathbf{G}_2 + \mathbf{q}\right). \tag{C23}$$

From a computational standpoint, we evaluate and store the Fourier-transformed spatial factor. After contracting it with the spectral function matrix elements for a given insulator ground state, we employ the FINUFFT package [98, 99] for the efficient inverse (nonuniform) Fourier transformation back to real space. For the evaluation of the spectral function matrix elements, we approximate the δ-functions from Eqs. (C16) and (C17) by Lorentzians according to

$$\delta(\omega) \to \frac{1}{\pi} \frac{\varepsilon}{x^2 + \varepsilon^2}, \tag{C24}$$

where the broadening width ε is chosen adaptively throughout the MBZ, depending on the local gradient of the charge-one excitation dispersion [100].

2. Symmetries and the spatial factor

The discrete spatial symmetries of the single-particle TBG Hamiltonian summarized in Appendix [A 1 c] impose several constraints on the spatial factor, as a consequence of the gauge-fixing conventions from Appendix [A 1 d]. In this section, we discuss the consequences of the $C_{2z}T$ and T symmetries of single-particle TBG Hamiltonian on the spatial factor. The discussion of the particle-hole symmetry of $\hat{H}_0$ (in the $\lambda = 0$ case), which does not impose any further constraints on the spatial factor will be relegated to Appendix [C 3 b].

a. $C_{2z}T$ symmetry

Due to the $C_{2z}T$ symmetry implemented by Eqs. (A19) and (A22), as well as the gauge-fixing from Eq. (A27), we find that the single-particle TBG wave functions obey

$$u_{\mathbf{Q}\alpha;n\eta}\left(\mathbf{k}\right) = u^{*}_{\mathbf{Q}(-\alpha);n\eta}\left(\mathbf{k}\right), \tag{C25}$$

where $-\alpha = B, A$ for $\alpha = A, B$. Additionally, from Eq. (A3), we have that

$$e^{-i\mathbf{G}\cdot R_{\theta,l}\mathbf{t}_{\alpha}} = e^{i\mathbf{G}\cdot R_{\theta,l}\mathbf{t}_{-\alpha}}, \quad \text{for} \quad \mathbf{G} \in \mathcal{G}_{l}, \tag{C26}$$

where $\mathbf{t}_{\alpha}$ is the sublattice displacement vector for the graphene sublattice α. Using also the reality of the Fourier-transformed p_z orbital wave functions from Eq. (C10), one can show from Eq. (C23) that

$$\begin{aligned}
\left[\mathcal{B}\left(\mathbf{q}\right)\right]^{*}_{\mathbf{k}n\eta,\mathbf{k}'n'\eta'} &= \frac{\left(2\pi\right)^{2}}{\Omega_{\mathrm{TBG}}\Omega_{\mathrm{SLG}}} \sum_{\substack{\alpha_1,l_1\\ \alpha_2,l_2}} \sum_{\substack{\mathbf{Q}_1\in\mathcal{Q}_{\eta l_1}\\ \mathbf{Q}_2\in\mathcal{Q}_{\eta' l_2}}} \sum_{\substack{\mathbf{G}_1\in\mathcal{G}_{l_1}\\ \mathbf{G}_2\in\mathcal{G}_{l_2}}} \phi^{*}_{l_1}\left(\eta\mathbf{K}_{l_1} + \mathbf{k} - \mathbf{Q}_1 + \mathbf{G}_1\right)\phi_{l_2}\left(\eta'\mathbf{K}_{l_2} + \mathbf{k}' - \mathbf{Q}_2 + \mathbf{G}_2\right) \\
&\times u_{\mathbf{Q}_1\alpha_1;n\eta}\left(\mathbf{k}\right) u^{*}_{\mathbf{Q}_2\alpha_2;n'\eta'}\left(\mathbf{k}'\right) e^{-i\left(\mathbf{G}_1\cdot R_{\theta,l_1}\mathbf{t}_{\alpha_1} - \mathbf{G}_2\cdot R_{\theta,l_2}\mathbf{t}_{\alpha_2}\right)} \delta\left(\eta\mathbf{K}_{l_1} + \mathbf{k} - \mathbf{Q}_1 + \mathbf{G}_1 - \eta'\mathbf{K}_{l_2} - \mathbf{k}' + \mathbf{Q}_2 - \mathbf{G}_2 + \mathbf{q}\right) \\
&= \frac{\left(2\pi\right)^{2}}{\Omega_{\mathrm{TBG}}\Omega_{\mathrm{SLG}}} \sum_{\substack{\alpha_1,l_1\\ \alpha_2,l_2}} \sum_{\substack{\mathbf{Q}_1\in\mathcal{Q}_{\eta l_1}\\ \mathbf{Q}_2\in\mathcal{Q}_{\eta' l_2}}} \sum_{\substack{\mathbf{G}_1\in\mathcal{G}_{l_1}\\ \mathbf{G}_2\in\mathcal{G}_{l_2}}} \phi_{l_1}\left(\eta\mathbf{K}_{l_1} + \mathbf{k} - \mathbf{Q}_1 + \mathbf{G}_1\right)\phi^{*}_{l_2}\left(\eta'\mathbf{K}_{l_2} + \mathbf{k}' - \mathbf{Q}_2 + \mathbf{G}_2\right) \\
&\times u^{*}_{\mathbf{Q}_1-\alpha_1;n\eta}\left(\mathbf{k}\right) u_{\mathbf{Q}_2-\alpha_2;n'\eta'}\left(\mathbf{k}'\right) e^{i\left(\mathbf{G}_1\cdot R_{\theta,l_1}\mathbf{t}_{-\alpha_1} - \mathbf{G}_2\cdot R_{\theta,l_2}\mathbf{t}_{-\alpha_2}\right)} \delta\left(\eta\mathbf{K}_{l_1} + \mathbf{k} - \mathbf{Q}_1 + \mathbf{G}_1 - \eta'\mathbf{K}_{l_2} - \mathbf{k}' + \mathbf{Q}_2 - \mathbf{G}_2 + \mathbf{q}\right) \\
&= \frac{\left(2\pi\right)^{2}}{\Omega_{\mathrm{TBG}}\Omega_{\mathrm{SLG}}} \sum_{\substack{\alpha_1,l_1\\ \alpha_2,l_2}} \sum_{\substack{\mathbf{Q}_1\in\mathcal{Q}_{\eta l_1}\\ \mathbf{Q}_2\in\mathcal{Q}_{\eta' l_2}}} \sum_{\substack{\mathbf{G}_1\in\mathcal{G}_{l_1}\\ \mathbf{G}_2\in\mathcal{G}_{l_2}}} \phi_{l_1}\left(\eta\mathbf{K}_{l_1} + \mathbf{k} - \mathbf{Q}_1 + \mathbf{G}_1\right)\phi^{*}_{l_2}\left(\eta'\mathbf{K}_{l_2} + \mathbf{k}' - \mathbf{Q}_2 + \mathbf{G}_2\right) \\
&\times u^{*}_{\mathbf{Q}_1\alpha_1;n\eta}\left(\mathbf{k}\right) u_{\mathbf{Q}_2\alpha_2;n'\eta'}\left(\mathbf{k}'\right) e^{i\left(\mathbf{G}_1\cdot R_{\theta,l_1}\mathbf{t}_{\alpha_1} - \mathbf{G}_2\cdot R_{\theta,l_2}\mathbf{t}_{\alpha_2}\right)} \delta\left(\eta\mathbf{K}_{l_1} + \mathbf{k} - \mathbf{Q}_1 + \mathbf{G}_1 - \eta'\mathbf{K}_{l_2} - \mathbf{k}' + \mathbf{Q}_2 - \mathbf{G}_2 + \mathbf{q}\right).
\end{aligned} \tag{C27}$$

Otherwise stated, the spatial factor has a real Fourier transformation

$$\mathcal{B}\left(\mathbf{r}\right) = \mathcal{B}^{*}\left(-\mathbf{r}\right), \qquad \mathcal{B}\left(\mathbf{q}\right) = \mathcal{B}^{*}\left(\mathbf{q}\right), \tag{C28}$$

which greatly simplifies all numerical computations, by halving the memory usage and required processing power.

b. T symmetry

Another important property can be obtained by considering the T symmetry of TBG. Under the gauge-fixing conditions from Eq. (A27), Eq. (A22) implies that the single-particle TBG wave functions obey

$$u^{*}_{-\mathbf{Q}\alpha;n(-\eta)}\left(-\mathbf{k}\right) = \left[B^{T}\left(\mathbf{k}\right)\right]_{n\eta,n-\eta} u_{\mathbf{Q}\alpha,n\eta}\left(\mathbf{k}\right) = \left(-1\right)^{\mathbf{k}} u_{\mathbf{Q}\alpha;n\eta}\left(\mathbf{k}\right), \tag{C29}$$

where we have introduced the factor

$$\left(-1\right)^{\mathbf{k}} = \begin{cases} 1 & \mathbf{k} \neq \mathbf{k}_{M_M} \\ -1 & \mathbf{k} = \mathbf{k}_{M_M} \end{cases}, \tag{C30}$$

with $\mathbf{k}_{M_M}$ denoting any one of the three equivalent M_M points in the MBZ from Eq. (A29).

Additionally, using the rotational invariance, as well as the reality of the p_z orbital wave functions from Eqs. (C9) and (C10), respectively, one can show from Eq. (C23) that

$$\begin{aligned}
\left[\mathcal{B}\left(-\mathbf{q}\right)\right]^*_{\mathbf{k}n(-\eta),\mathbf{k}'n'(-\eta')} &= \frac{\left(2\pi\right)^2}{\Omega_{\mathrm{TBG}}\Omega_{\mathrm{SLG}}} \sum_{\substack{\alpha_1,l_1\\ \alpha_2,l_2}} \sum_{\substack{\mathbf{Q}_1\in\mathcal{Q}_{-\eta l_1}\\ \mathbf{Q}_2\in\mathcal{Q}_{-\eta' l_2}}} \sum_{\substack{\mathbf{G}_1\in\mathcal{G}_{l_1}\\ \mathbf{G}_2\in\mathcal{G}_{l_2}}} \phi^*_{l_1}\left(-\eta\mathbf{K}_{l_1}+\mathbf{k}-\mathbf{Q}_1+\mathbf{G}_1\right)\phi_{l_2}\left(-\eta'\mathbf{K}_{l_2}+\mathbf{k}'-\mathbf{Q}_2+\mathbf{G}_2\right) \\
&\times u_{\mathbf{Q}_1\alpha_1;n(-\eta)}\left(\mathbf{k}\right) u^*_{\mathbf{Q}_2\alpha_2;n'(-\eta')}\left(\mathbf{k}'\right) e^{-i\left(\mathbf{G}_1\cdot R_{\theta,l_1}\mathbf{t}_{\alpha_1}-\mathbf{G}_2\cdot R_{\theta,l_2}\mathbf{t}_{\alpha_2}\right)} \delta\left(\eta\mathbf{K}_{l_1}-\mathbf{k}+\mathbf{Q}_1-\mathbf{G}_1-\eta'\mathbf{K}_{l_2}+\mathbf{k}'-\mathbf{Q}_2+\mathbf{G}_2+\mathbf{q}\right) \\
&= \frac{\left(2\pi\right)^2}{\Omega_{\mathrm{TBG}}\Omega_{\mathrm{SLG}}} \sum_{\substack{\alpha_1,l_1\\ \alpha_2,l_2}} \sum_{\substack{\mathbf{Q}_1\in\mathcal{Q}_{\eta l_1}\\ \mathbf{Q}_2\in\mathcal{Q}_{\eta' l_2}}} \sum_{\substack{\mathbf{G}_1\in\mathcal{G}_{l_1}\\ \mathbf{G}_2\in\mathcal{G}_{l_2}}} \phi_{l_1}\left(-\eta\mathbf{K}_{l_1}+\mathbf{k}+\mathbf{Q}_1-\mathbf{G}_1\right)\phi^*_{l_2}\left(-\eta'\mathbf{K}_{l_2}+\mathbf{k}'+\mathbf{Q}_2-\mathbf{G}_2\right) \\
&\times(-1)^{\mathbf{k}}(-1)^{\mathbf{k}'} u^*_{\mathbf{Q}_1\alpha_1;n\eta}\left(-\mathbf{k}\right) u_{\mathbf{Q}_2\alpha_2;n'\eta'}\left(-\mathbf{k}'\right) e^{i\left(\mathbf{G}_1\cdot R_{\theta,l_1}\mathbf{t}_{\alpha_1}-\mathbf{G}_2\cdot R_{\theta,l_2}\mathbf{t}_{\alpha_2}\right)} \\
&\times\delta\left(\eta\mathbf{K}_{l_1}-\mathbf{k}-\mathbf{Q}_1+\mathbf{G}_1-\eta'\mathbf{K}_{l_2}+\mathbf{k}'+\mathbf{Q}_2-\mathbf{G}_2+\mathbf{q}\right).
\end{aligned} \tag{C31}$$

This implies using the definition from Eq. (C23) that

$$\left[\mathcal{B}\left(-\mathbf{q}\right)\right]^*_{\mathbf{k}n(-\eta),\mathbf{k}'n'(-\eta')} = (-1)^{\mathbf{k}}(-1)^{\mathbf{k}'}\left[\mathcal{B}\left(\mathbf{q}\right)\right]_{-\mathbf{k}n\eta,-\mathbf{k}'n'\eta'}. \tag{C32}$$

Additionally, the spectral function matrix obeys the trivial property

$$\left[\mathcal{B}\left(-\mathbf{q}\right)\right]^*_{\mathbf{k}n\eta,\mathbf{k}'n'\eta'} = \left[\mathcal{B}\left(\mathbf{q}\right)\right]_{\mathbf{k}'n'\eta',\mathbf{k}n\eta}, \tag{C33}$$

which can be readily verified using the definition from Eq. (C23). Combining Eqs. (C32) and (C33), we obtain

$$\left[\mathcal{B}\left(\mathbf{q}\right)\right]_{\mathbf{k}'n'(-\eta'),\mathbf{k}n(-\eta)} = (-1)^{\mathbf{k}}(-1)^{\mathbf{k}'}\left[\mathcal{B}\left(\mathbf{q}\right)\right]_{-\mathbf{k}n\eta,-\mathbf{k}'n'\eta'}. \tag{C34}$$

Eq. (C34) can be simplified for the case without translation symmetry breaking (for which the condition $\mathbf{k}=\mathbf{k}'$ is imposed from the spectral function matrix elements)

$$\left[\mathcal{B}\left(\mathbf{r}\right)\right]_{\mathbf{k}n'\eta',\mathbf{k}n\eta} = \left[\mathcal{B}\left(\mathbf{r}\right)\right]_{-\mathbf{k}n(-\eta),-\mathbf{k}n'(-\eta')}, \quad \left[\mathcal{B}\left(\mathbf{q}\right)\right]_{\mathbf{k}n'\eta',\mathbf{k}n\eta} = \left[\mathcal{B}\left(\mathbf{q}\right)\right]_{-\mathbf{k}n(-\eta),-\mathbf{k}n'(-\eta')}. \tag{C35}$$

Eq. (C35) will prove instrumental in providing a general understanding of the TBG spectral function. In anticipation of the results from Appendix [E], we briefly mention that because of Eq. (C35), the spectral function can be alternatively computed as

$$A\left(\mathbf{q},\omega\right) = \sum_{\substack{\mathbf{k}\in\mathrm{MBZ}\\ n,\eta,n',\eta'}} \left[\mathcal{M}^{S+}\left(\omega\right)+\mathcal{M}^{S-}\left(\omega\right)\right]_{\mathbf{k}n\eta,\mathbf{k}n'\eta'}\left[\mathcal{B}\left(\mathbf{q}\right)\right]_{\mathbf{k}n\eta,\mathbf{k}n'\eta'}, \tag{C36}$$

where we have introduced the *symmetrized* spectral function matrices

$$\left[\mathcal{M}^{S\pm}_{\varphi}\left(\omega\right)\right]_{\mathbf{k}n\eta,\mathbf{k}n'\eta'} = \frac{1}{2}\left(\left[\mathcal{M}^{\pm}_{\varphi}\left(\omega\right)\right]_{\mathbf{k}n\eta,\mathbf{k}n'\eta'} + \left[\mathcal{M}^{\pm}_{\varphi}\left(\omega\right)\right]_{-\mathbf{k}n'-\eta',-\mathbf{k}n-\eta}\right). \tag{C37}$$

Eq. (C36) implies that any components of $\mathcal{M}^{\pm}\left(\omega\right)$ which are anti-symmetric with respect to the transformation $[\mathbf{k}n\eta,\mathbf{k}n'\eta'] \to [-\mathbf{k}n'(-\eta'),-\mathbf{k}n(-\eta)]$ will necessarily vanish upon contracting with the spatial factor.

3. Approximations of the spatial factor

The goal of this section is to formulate a series of approximations to the spatial factor matrix for the purpose of obtaining some analytical intuition on the STM patterns. After deriving a general approximation to the spatial factor, we briefly review the consequences of the anti-commuting particle-hole symmetry of $\hat{H}_0$ on the approximations of the spatial factor. Finally, we compute the approximate spatial factor at key momenta at the SLG graphene scale.

a. General approximations

In deriving approximations to the spatial factor matrix, we will assume that the translation symmetry (at the level of the moiré lattice) is not broken and focus on the properties of $[\mathcal{B}(\mathbf{q})]_{\mathbf{k}n\eta,\mathbf{k}'n'\eta'}$. The generalization to the case when translation symmetry is broken is straightforward.

First, we note that $\mathbf{k} \in \text{MBZ}$ and therefore $|\mathbf{k}| \ll |\eta\mathbf{K}_l + \mathbf{G}|$ for any $\eta = \pm$, $l = \pm$, and $\mathbf{G} \in \mathcal{G}_l$. The Fourier transformations of p_z orbital wave functions do not change significantly on the scale of the MBZ, justifying the approximation $\phi_l(\eta\mathbf{K}_l + \mathbf{k} - \mathbf{Q} + \mathbf{G}) \approx \phi_l(\eta\mathbf{K}_l - \mathbf{Q} + \mathbf{G})$ for any $l = \pm$, $\mathbf{Q} \in \mathcal{Q}_\pm$, $\mathbf{k} \in \text{MBZ}$, and $\mathbf{G} \in \mathcal{G}_\mathbf{l}$. Thus a first simplification of the spatial factor matrix reads

$$\left[\mathcal{B}^{(1)}(\mathbf{q})\right]_{\mathbf{k}n\eta,\mathbf{k}'n'\eta'} = \frac{(2\pi)^2}{\Omega_{\text{TBG}}\Omega_{\text{SLG}}} \sum_{\substack{\alpha_1,l_1\\ \alpha_2,l_2}} \sum_{\substack{\mathbf{Q}_1\in\mathcal{Q}_{\eta l_1}\\ \mathbf{Q}_2\in\mathcal{Q}_{\eta' l_2}}} \sum_{\substack{\mathbf{G}_1\in\mathcal{G}_{l_1}\\ \mathbf{G}_2\in\mathcal{G}_{l_2}}} \phi_{l_1}(\eta\mathbf{K}_{l_1} - \mathbf{Q}_1 + \mathbf{G}_1)\,\phi^*_{l_2}(\eta'\mathbf{K}_{l_2} - \mathbf{Q}_2 + \mathbf{G}_2)$$

$$\times u^*_{\mathbf{Q}_1\alpha_1;n\eta}(\mathbf{k})\, u_{\mathbf{Q}_2\alpha_2;n'\eta'}(\mathbf{k}')\, e^{i\left(\mathbf{G}_1\cdot R_{\theta,l_1}\mathbf{t}_{\alpha_1} - \mathbf{G}_2\cdot R_{\theta,l_2}\mathbf{t}_{\alpha_2}\right)} \delta(\eta\mathbf{K}_{l_1} - \mathbf{Q}_1 + \mathbf{G}_1 - \eta'\mathbf{K}_{l_2} + \mathbf{Q}_2 - \mathbf{G}_2 + \mathbf{q}). \tag{C38}$$

Additionally, the TBG wave functions $u_{\mathbf{Q}\alpha;n\eta}(\mathbf{k})$ decay exponentially in magnitude for large values of $\mathbf{Q}$ as shown in Ref. [87]. As such, there is a natural cutoff $Q_{\max}$ for the magnitude of the vectors in $\mathcal{Q}_\pm$. More precisely, one has $|\mathbf{Q}| \leq Q_{\max}$ for any $\mathbf{Q} \in \mathcal{Q}_\pm$. Crucially, Ref. [87] found that $Q_{\max} \lesssim 2k_\theta$, implying that $|\mathbf{Q}| \ll |\eta\mathbf{K}_l + \mathbf{G}|$ for any $\eta = \pm$, $l = \pm$, $\mathbf{Q} \in \mathcal{Q}_\pm$, and $\mathbf{G} \in \mathcal{G}_l$. As the p_z orbital wave functions do not change significantly on the scale k_θ, we can approximate $\phi_l(\eta\mathbf{K}_l - \mathbf{Q} + \mathbf{G}) \approx \phi_l(\eta\mathbf{K}_l + \mathbf{G})$ for any $l = \pm$, $\mathbf{Q} \in \mathcal{Q}_\pm$, $\mathbf{G} \in \mathcal{G}_\mathbf{l}$. Thus, we can construct a second approximation to the spatial factor matrix

$$\left[\mathcal{B}^{(2)}(\mathbf{q})\right]_{\mathbf{k}n\eta,\mathbf{k}'n'\eta'} = \frac{(2\pi)^2}{\Omega_{\text{TBG}}\Omega_{\text{SLG}}} \sum_{\substack{\alpha_1,l_1\\ \alpha_2,l_2}} \sum_{\substack{\mathbf{Q}_1\in\mathcal{Q}_{\eta l_1}\\ \mathbf{Q}_2\in\mathcal{Q}_{\eta' l_2}}} \sum_{\substack{\mathbf{G}_1\in\mathcal{G}_{l_1}\\ \mathbf{G}_2\in\mathcal{G}_{l_2}}} \phi_{l_1}(\eta\mathbf{K}_{l_1} + \mathbf{G}_1)\,\phi^*_{l_2}(\eta'\mathbf{K}_{l_2} + \mathbf{G}_2)$$

$$\times u^*_{\mathbf{Q}_1\alpha_1;n\eta}(\mathbf{k})\, u_{\mathbf{Q}_2\alpha_2;n'\eta'}(\mathbf{k}')\, e^{i\left(\mathbf{G}_1\cdot R_{\theta,l_1}\mathbf{t}_{\alpha_1} - \mathbf{G}_2\cdot R_{\theta,l_2}\mathbf{t}_{\alpha_2}\right)} \delta(\eta\mathbf{K}_{l_1} - \mathbf{Q}_1 + \mathbf{G}_1 - \eta'\mathbf{K}_{l_2} + \mathbf{Q}_2 - \mathbf{G}_2 + \mathbf{q}). \tag{C39}$$

Although the p_z orbital wave functions are roughly constant at the MBZ scale, they do decay significantly at the graphene reciprocal lattice scale. In fact, it can be checked numerically that

$$\left|\frac{\phi_l(\eta\mathbf{K}_l + \mathbf{G})}{\phi_l(\eta\mathbf{K}_l)}\right| \lesssim 0.03, \text{ for any } \eta = \pm \text{ and } \mathbf{G} \in \mathcal{G}_l \text{ with } |\eta\mathbf{K}_l + \mathbf{G}| \neq |\eta\mathbf{K}_l|. \tag{C40}$$

This implies that in Eq. (C39), the only $\mathbf{G}_1$ and $\mathbf{G}_2$ vectors that contribute significantly to $\left[\mathcal{B}^2(\mathbf{q})\right]_{\mathbf{k}n\eta,\mathbf{k}'n'\eta'}$ are $\mathbf{G}_1 \in \mathcal{G}^*_{\eta,l_1}$ and $\mathbf{G}_2 \in \mathcal{G}^*_{\eta',l_2}$, where we have defined

$$\mathcal{G}^*_{\eta,l} = \{\mathbf{0}, -\eta\mathbf{g}_{l,1}, -\eta\mathbf{g}_{l,2}\}. \tag{C41}$$

Moreover, $|\eta\mathbf{K}_l + \mathbf{G}| = |\eta\mathbf{K}_l|$ for any $\mathbf{G} \in \mathcal{G}^*_{\eta,l}$, and as a consequence of Eq. (C9), we have that $\phi_l(\eta\mathbf{K}_l + \mathbf{G}) = \phi_l(\mathbf{K}_+)$ for any $l = \pm$, $\eta = \pm$, and $\mathbf{G} \in \mathcal{G}^*_{\eta,l}$. Therefore, we can write a third approximation for the spatial factor matrix as

$$\left[\mathcal{B}^{(3)}(\mathbf{q})\right]_{\mathbf{k}n\eta,\mathbf{k}'n'\eta'} = \frac{(2\pi)^2}{\Omega_{\text{TBG}}\Omega_{\text{SLG}}} \sum_{\substack{\alpha_1,l_1\\ \alpha_2,l_2}} \sum_{\substack{\mathbf{Q}_1\in\mathcal{Q}_{\eta l_1}\\ \mathbf{Q}_2\in\mathcal{Q}_{\eta' l_2}}} \sum_{\substack{\mathbf{G}_1\in\mathcal{G}_{l_1}\\ \mathbf{G}_2\in\mathcal{G}_{l_2}}} \phi_{l_1}(\mathbf{K}_+)\,\phi^*_{l_2}(\mathbf{K}_+)$$

$$\times u^*_{\mathbf{Q}_1\alpha_1;n\eta}(\mathbf{k})\, u_{\mathbf{Q}_2\alpha_2;n'\eta'}(\mathbf{k}')\, e^{i\left(\mathbf{G}_1\cdot R_{\theta,l_1}\mathbf{t}_{\alpha_1} - \mathbf{G}_2\cdot R_{\theta,l_2}\mathbf{t}_{\alpha_2}\right)} \delta(\eta\mathbf{K}_{l_1} - \mathbf{Q}_1 + \mathbf{G}_1 - \eta'\mathbf{K}_{l_2} + \mathbf{Q}_2 - \mathbf{G}_2 + \mathbf{q}). \tag{C42}$$

Finally, the bottom layer $l = -$ is about twice as far away from the STM tip than the top layer $l = +$ is ($z_p - z_+ \approx 3\,\text{Å}$ and $z_p - z_- \approx 6\,\text{Å}$). Mathematically, this implies that

$$\left|\frac{\phi_-(\mathbf{q})}{\phi_+(\mathbf{q})}\right| \lesssim 0.01, \tag{C43}$$

allowing us to further neglect the bottom layer contribution in Eq. (C42), and write a fourth approximation to the spatial factor matrix

$$\left[\mathcal{B}^{(4)}(\mathbf{q})\right]_{\mathbf{k}n\eta,\mathbf{k}'n'\eta'} = \frac{(2\pi)^2}{\Omega_{\text{TBG}}\Omega_{\text{SLG}}} |\phi_+(\mathbf{K}_+)|^2 \sum_{\substack{\alpha_1,\alpha_2\\ \mathbf{G}_1,\mathbf{G}_2\in\mathcal{G}^*_+}} \sum_{\substack{\mathbf{Q}_1\in\mathcal{Q}_\eta\\ \mathbf{Q}_2\in\mathcal{Q}_{\eta'}}} u^*_{\mathbf{Q}_1\alpha_1;n\eta}(\mathbf{k})\, u_{\mathbf{Q}_2\alpha_2;n'\eta'}(\mathbf{k}')$$

$$\times e^{i\left(\mathbf{G}_1\cdot R_{\theta,l_1}\mathbf{t}_{\alpha_1}-\mathbf{G}_2\cdot R_{\theta,l_2}\mathbf{t}_{\alpha_2}\right)}\delta\left[(\eta-\eta')\,\mathbf{K}_+-\mathbf{Q}_1+\mathbf{Q}_2+\mathbf{G}_1-\mathbf{G}_2+\mathbf{q}\right]. \tag{C44}$$

Defining the two order-three complex non-real roots of unity ω_α with $\alpha = A, B$ and

$$\omega_A = e^{i\frac{2\pi}{3}} \quad \text{and} \quad \omega_B = e^{-i\frac{2\pi}{3}}, \tag{C45}$$

one can rewrite the fourth approximation from Eq. (C44) as

$$\begin{aligned}\left[\mathcal{B}^{(4)}(\mathbf{q})\right]_{\mathbf{k}n\eta,\mathbf{k}n'\eta'} = \frac{(2\pi)^2}{\Omega_{\mathrm{TBG}}\Omega_{\mathrm{SLG}}}|\phi_+(\mathbf{K}_+)|^2 \sum_{\substack{\alpha_1,\alpha_2\\0\le j_1,j_2<3}}\sum_{\substack{\mathbf{Q}_1\in\mathcal{Q}_\eta\\\mathbf{Q}_2\in\mathcal{Q}_{\eta'}}} u^*_{\mathbf{Q}_1\alpha_1;n\eta}(\mathbf{k})\,u_{\mathbf{Q}_2\alpha_2;n'\eta'}(\mathbf{k})\\ \times\omega_{\alpha_2}^{\eta' j_2}\omega_{\alpha_1}^{-\eta j_1}\delta\left[C_{3z}^{j_2}\eta'\mathbf{K}_+ - C_{3z}^{j_1}\eta\mathbf{K}_+ - \mathbf{Q}_2+\mathbf{Q}_1-\mathbf{q}\right],\end{aligned} \tag{C46}$$

where C_{3z} denotes a three-fold rotation around the $\hat{\mathbf{z}}$ axis. It is important to note that *all* the approximations to the spatial factor matrix obey the properties derived in Appendix [C 2]. Specifically, as a consequence of the $C_{2z}T$ symmetry of the TBG single-particle Hamiltonian, the approximated spatial factor matrix has a real Fourier transformation, meaning that $\mathcal{B}^{(i)}(\mathbf{q})$ (for $1 \le i \le 4$) is real. Additionally, because of the T symmetry, the approximated spatial factor matrices obey

$$\left[\mathcal{B}^{(i)}(\mathbf{q})\right]_{\mathbf{k}n'-\eta',\mathbf{k}n-\eta} = \left[\mathcal{B}^{(i)}(\mathbf{q})\right]_{-\mathbf{k}n\eta,-\mathbf{k}n'\eta'}, \quad \text{for} \quad 1\le i\le 4. \tag{C47}$$

Finally, we note that the fourth approximation from Eq. (C44) agrees with the unappoximated spatial factor to a relative error smaller than 5%.

b. The particle-hole symmetry and the spatial factor

In Appendix [C 2], we have argued that the anti-commuting P symmetry of $\hat{H}_0$ in the $\lambda = 0$ does not provide any additional constraints on the spatial factors. Here, we show that the particle-hole symmetry allows us to relate the spatial factor in the fourth approximation to the TBG form factors defined in Eq. (A39). Under the gauge-fixing conditions from Eq. (A27), Eq. (A23) implies that the single-particle TBG wave functions obey

$$u_{-\mathbf{Q}\alpha,-n\eta}(-\mathbf{k}) = -\zeta_{\mathbf{Q}}\eta n(-1)^{\mathbf{k}}u_{\mathbf{Q}\alpha,n\eta}(\mathbf{k}), \tag{C48}$$

where the factor $(-1)^{\mathbf{k}}$ was defined in Eq. (C30). We now consider the fourth approximation of the spatial factor from Eq. (C46), where as a consequence of Eq. (C48), we have

$$\begin{aligned}\left[\mathcal{B}^{(4)}(\mathbf{q})\right]_{-\mathbf{k}-n\eta,-\mathbf{k}-n'\eta'} &= \frac{(2\pi)^2}{\Omega_{\mathrm{TBG}}\Omega_{\mathrm{SLG}}}|\phi_+(\mathbf{K}_+)|^2 \sum_{\substack{\alpha_1,\alpha_2\\0\le j_1,j_2<3}}\sum_{\substack{\mathbf{Q}_1\in\mathcal{Q}_{-\eta}\\\mathbf{Q}_2\in\mathcal{Q}_{-\eta'}}} u^*_{-\mathbf{Q}_1\alpha_1;-n\eta}(-\mathbf{k})\,u_{-\mathbf{Q}_2\alpha_2;-n'\eta'}(-\mathbf{k})\\ &\times\omega_{\alpha_2}^{\eta' j_2}\omega_{\alpha_1}^{-\eta j_1}\delta\left[C_{3z}^{j_2}\eta'\mathbf{K}_+ - C_{3z}^{j_1}\eta\mathbf{K}_+ + \mathbf{Q}_2-\mathbf{Q}_1-\mathbf{q}\right]\\ &= \frac{(2\pi)^2}{\Omega_{\mathrm{TBG}}\Omega_{\mathrm{SLG}}}|\phi_+(\mathbf{K}_+)|^2\eta\eta' nn' \sum_{\substack{\alpha_1,\alpha_2\\0\le j_1,j_2<3}}\sum_{\substack{\mathbf{Q}_1\in\mathcal{Q}_{-\eta}\\\mathbf{Q}_2\in\mathcal{Q}_{-\eta'}}} u^*_{\mathbf{Q}_1\alpha_1;n\eta}(\mathbf{k})\,u_{\mathbf{Q}_2\alpha_2;n'\eta'}(\mathbf{k})\\ &\times\omega_{\alpha_2}^{\eta' j_2}\omega_{\alpha_1}^{-\eta j_1}\delta\left[C_{3z}^{j_2}\eta'\mathbf{K}_+ - C_{3z}^{j_1}\eta\mathbf{K}_+ + \mathbf{Q}_2-\mathbf{Q}_1-\mathbf{q}\right].\end{aligned} \tag{C49}$$

In the neighborhood of $\mathbf{q}\approx\mathbf{G}\in\mathcal{Q}_0$, Eq. (C49) is dominated by $\mathbf{q}=\mathbf{G}$, leading to [4]

$$\left[\mathcal{B}^{(4)}(\mathbf{q})\right]_{-\mathbf{k}-n\eta,-\mathbf{k}-n'\eta'}\Big|_{\mathbf{q}\approx\mathbf{G}} = \frac{3(2\pi)^2\delta_{\eta,\eta'}}{\Omega_{\mathrm{TBG}}\Omega_{\mathrm{SLG}}}|\phi_+(\mathbf{K}_+)|^2 nn'\sum_\alpha\sum_{\mathbf{Q}_1,\mathbf{Q}_2\in\mathcal{Q}_{-\eta}} u^*_{\mathbf{Q}_1\alpha;n\eta}(\mathbf{k})\,u_{\mathbf{Q}_2\alpha;n'\eta}(\mathbf{k})$$

[4] Strictly speaking, the Fourier-transformed spatial factor matrix is not a function, but rather a distribution. Because of the Dirac δ-function located at $\mathbf{q}=\mathbf{G}$, $\left|\left[\mathcal{B}^{(4)}(\mathbf{G})\right]_{\mathbf{k}n\eta,\mathbf{k}n'\eta'}\right| = +\infty$. We therefore use the notation in Eq. (C50) to specify the amplitude of the Dirac δ-function at $\mathbf{q}=\mathbf{G}$.

$$\times \delta\left(\mathbf{Q}_2 - \mathbf{Q}_1 - \mathbf{q}\right)$$
$$= \frac{3\left(2\pi\right)^2 \delta_{\eta,\eta'}}{\Omega_{\mathrm{TBG}}\Omega_{\mathrm{SLG}}} |\phi_+\left(\mathbf{K}_+\right)|^2 nn' \sum_{\alpha} \sum_{\mathbf{Q}\in\mathcal{Q}_{-\eta}} u^*_{\mathbf{Q}\alpha;n\eta}\left(\mathbf{k}\right) u_{\mathbf{Q}+\mathbf{G}\alpha;n'\eta}\left(\mathbf{k}\right) \delta\left(\mathbf{q}-\mathbf{G}\right). \quad \text{(C50)}$$

At the same time, using the approximation from Eq. (C46) directly for $\mathbf{q} \approx \mathbf{G}$

$$\left[\mathcal{B}^{(4)}\left(\mathbf{q}\right)\right]_{\mathbf{k}n\eta,\mathbf{k}n'\eta'}\Big|_{\mathbf{q}\approx\mathbf{G}} = \frac{3\left(2\pi\right)^2 \delta_{\eta,\eta'}}{\Omega_{\mathrm{TBG}}\Omega_{\mathrm{SLG}}} |\phi_+\left(\mathbf{K}_+\right)|^2 \sum_{\alpha} \sum_{\mathbf{Q}_1,\mathbf{Q}_2\in\mathcal{Q}_{\eta}} u^*_{\mathbf{Q}_1\alpha;n\eta}\left(\mathbf{k}\right) u_{\mathbf{Q}_2\alpha;n'\eta}\left(\mathbf{k}\right)$$
$$\times \delta\left(-\mathbf{Q}_2 + \mathbf{Q}_1 - \mathbf{q}\right)$$
$$= \frac{3\left(2\pi\right)^2 \delta_{\eta,\eta'}}{\Omega_{\mathrm{TBG}}\Omega_{\mathrm{SLG}}} |\phi_+\left(\mathbf{K}_+\right)|^2 \sum_{\alpha} \sum_{\mathbf{Q}\in\mathcal{Q}_{\eta}} u^*_{\mathbf{Q}+\mathbf{G}\alpha;n\eta}\left(\mathbf{k}\right) u_{\mathbf{Q}\alpha;n'\eta}\left(\mathbf{k}\right) \delta\left(\mathbf{G}-\mathbf{q}\right). \quad \text{(C51)}$$

Combining Eqs. (C50) and (C51) with the definition of the TBG form factors from Eq. (A39), we find that

$$\left\{ nn' \left[\mathcal{B}^{(4)}\left(\mathbf{q}\right)\right]^*_{-\mathbf{k}-n'\eta,-\mathbf{k}-n\eta'} + \left[\mathcal{B}^{(4)}\left(\mathbf{q}\right)\right]_{\mathbf{k}n\eta,\mathbf{k}n'\eta'} \right\}\Big|_{\mathbf{q}\approx\mathbf{G}} = M^{\eta}_{nn'}\left(\mathbf{k},\mathbf{G}\right) \frac{3\left(2\pi\right)^2 \delta_{\eta,\eta'}}{\Omega_{\mathrm{TBG}}\Omega_{\mathrm{SLG}}} |\phi_+\left(\mathbf{K}_+\right)|^2 \delta\left(\mathbf{q}-\mathbf{G}\right). \quad \text{(C52)}$$

c. *Computing the spectral function at key momenta in the SLG BZ*

As discussed in Appendix [C 3 a], the active TBG wave functions $u_{\mathbf{Q}\alpha;n\eta}\left(\mathbf{k}\right)$ decay exponentially in magnitude for large values of $\mathbf{Q}$ [87]. As such, there is a natural cutoff $Q_{\max}$ for the magnitude of the vectors in $\mathcal{Q}_{\pm}$. More precisely, one has $|\mathbf{Q}| \leq Q_{\max} \lesssim 2k_\theta$ for any $\mathbf{Q} \in \mathcal{Q}_{\pm}$ [87], implying that $|\mathbf{Q}| \ll |\mathbf{K}_+|$ for any $\mathbf{Q} \in \mathcal{Q}_{\pm}$. Considering the fourth approximation from Eq. (C46), we find that the contributions to the spatial factor matrix are clustered around four types of momenta $\mathbf{q}$:

$$|\mathbf{q}| \approx 0, \quad |\mathbf{q}| \approx |\mathbf{K}_+|, \quad |\mathbf{q}| \approx 2|\mathbf{K}_+|, \quad |\mathbf{q}| \approx |\mathbf{g}_{+,1}|. \quad \text{(C53)}$$

For each of the four types of clusters, we will chose *one* relevant momentum $\mathbf{q}$ and explicitly work out the spatial factor matrix within the fourth approximation from Eq. (C46). It is also important to note that any non-vanishing amplitude of the spectral function with momenta $|\mathbf{q}| \approx |\mathbf{K}_+|$ or $|\mathbf{q}| \approx 2|\mathbf{K}_+|$ signals the presence of so-called $\sqrt{3}\times\sqrt{3}$ *ordering* at the level of the SLG. Without $\sqrt{3}\times\sqrt{3}$ ordering, the STM patterns of TBG display an apparent periodicity corresponding to the usual SLG lattice up to an additional modulation at the moiré scale. In the presence of $\sqrt{3}\times\sqrt{3}$ ordering, the apparent periodicity of the graphene mono-layer lattice is broken, with the SLG unit cell becoming enlarged from two to six carbon atoms per unit cell [78, 101, 102].

In fact, inspecting the (unapproximated) spatial factor from Eq. (C23) and remembering that $|\mathbf{Q}| \ll |\mathbf{K}_+|$ for any $\mathbf{Q} \in \mathcal{Q}_{\pm}$ as a consequence of the exponential decay of the TBG wave functions $u_{\mathbf{Q}\alpha,n\eta}\left(\mathbf{k}\right)$ with $|\mathbf{Q}|$ [87], we see that the contributions to the spatial factor $\left[\mathcal{B}\left(\mathbf{q}\right)\right]_{\mathbf{k}n\eta,\mathbf{k}'n'\eta'}$ cluster around three types of momenta, depending on the valley indices η and η':

$$\begin{aligned} \left[\mathcal{B}\left(\mathbf{q}\right)\right]_{\mathbf{k}n\eta,\mathbf{k}'n'\eta} \neq 0 \quad &\text{if and only if} \quad \mathbf{q} = \Delta\mathbf{q} + \mathbf{G}, \\ \left[\mathcal{B}\left(\mathbf{q}\right)\right]_{\mathbf{k}n\eta,\mathbf{k}'n'(-\eta)} \neq 0 \quad &\text{if and only if} \quad \mathbf{q} = \Delta\mathbf{q} + 2\eta\mathbf{K}_+ + \mathbf{G}, \end{aligned} \quad \text{(C54)}$$

where $\mathbf{G} \in \mathcal{G}_+$, and $|\Delta\mathbf{q}| \sim k_\theta \ll |\mathbf{K}_+|$. One important consequence of the second line in Eq. (C54) is that $\sqrt{3}\times\sqrt{3}$ ordering arises from the valley-off-diagonal elements of the spatial factor, a fact upon which we will rely heavily in Appendix [E] for understanding the real-space STM patterns of the various TBG insulators.

We will now consider each of the four types of momenta from Eq. (C53) individually and compute the spatial factor using the fourth approximation:

1. $\mathcal{B}\left(\mathbf{q}\right)$ *for* $|\mathbf{q}| \approx 0$.

   For the contributions with $|\mathbf{q}| \approx 0$, we choose to compute the spatial factor matrix at $\mathbf{q} = \mathbf{0}$, where we must have that $C^{j_2}_{3z}\eta'\mathbf{K}_+ - C^{j_1}_{3z}\eta\mathbf{K}_+ - \mathbf{Q}_2 + \mathbf{Q}_1 = \mathbf{0}$ in Eq. (C46). Since $|\mathbf{Q}_1|, |\mathbf{Q}_2| \ll |\mathbf{K}_+|$, this is only true if $j_1 = j_2$, $\mathbf{Q}_1 = \mathbf{Q}_2$ and $\eta = \eta'$. As such, we find that

$$\left[\mathcal{B}^{(4)}\left(\mathbf{q}\right)\right]_{\mathbf{k}n\eta,\mathbf{k}n'\eta'}\Big|_{\mathbf{q}\approx\mathbf{0}} = \frac{\left(2\pi\right)^2 \delta_{\eta,\eta'}}{\Omega_{\mathrm{TBG}}\Omega_{\mathrm{SLG}}} |\phi_+\left(\mathbf{K}_+\right)|^2 \sum_{\substack{\alpha_1,\alpha_2 \\ 0\leq j<3}} \sum_{\mathbf{Q}\in\mathcal{Q}_{\eta}} u^*_{\mathbf{Q}\alpha_1;n\eta}\left(\mathbf{k}\right) u_{\mathbf{Q}\alpha_2;n'\eta}\left(\mathbf{k}\right) \omega^{\eta j}_{\alpha_2}\omega^{-\eta j}_{\alpha_1} \delta\left(\mathbf{q}\right)$$

$$= \frac{3\left(2\pi\right)^2 \delta_{\eta,\eta'}}{\Omega_{\rm TBG}\Omega_{\rm SLG}} |\phi_+\left(\mathbf{K}_+\right)|^2 \sum_{\alpha} \sum_{\mathbf{Q}\in\mathcal{Q}_\eta} u^*_{\mathbf{Q}\alpha;n\eta}\left(\mathbf{k}\right) u_{\mathbf{Q}\alpha;n'\eta}\left(\mathbf{k}\right) \delta\left(\mathbf{q}\right). \tag{C55}$$

Notice that in Eq. (C55) the summation is only over the $\mathbf{Q} \in \mathcal{Q}_\eta$ and not over the entire $\mathcal{Q}_\pm$ lattice. Had Eq. (C55) included a summation over the entire $\mathcal{Q}_\pm$ lattice, this contribution would have been proportional to $\delta_{nn'}$. Nevertheless, we have checked numerically that to an error smaller than 1%,

$$\left[\mathcal{B}^{(4)}\left(\mathbf{q}\right)\right]_{\mathbf{k}n\eta,\mathbf{k}n'\eta'}\Big|_{\mathbf{q}\approx\mathbf{0}} \approx \frac{3\left(2\pi\right)^2 \delta_{\eta,\eta'}}{\Omega_{\rm TBG}\Omega_{\rm SLG}} |\phi_+\left(\mathbf{K}_+\right)|^2 \frac{\delta_{n,n'}}{2} \delta\left(\mathbf{q}\right). \tag{C56}$$

2. $\mathcal{B}\left(\mathbf{q}\right)$ *for* $|\mathbf{q}| \approx |\mathbf{K}_+|$.

When $|\mathbf{q}| \approx |\mathbf{K}_+|$, we choose to focus on the contribution at $\mathbf{q} \approx \mathbf{K}_+$. As such, we must have that $C_{3z}^{j_2}\eta'\mathbf{K}_+ - C_{3z}^{j_1}\eta\mathbf{K}_+ - \mathbf{Q}_2 + \mathbf{Q}_1 \approx \mathbf{K}_+$ in Eq. (C46). This necessarily means that $\eta = -\eta' = +$ and $j_1 = 1$, $j_2 = 2$, or $j_1 = 2$, $j_2 = 1$. Since this implies that $\mathbf{Q}_1 \in \mathcal{Q}_+$ and $\mathbf{Q}_2 \in \mathcal{Q}_-$, it follows that $\mathbf{Q}_1 \neq \mathbf{Q}_2$, meaning that we cannot chose $\mathbf{q}$ to be exactly at $\mathbf{K}_+$. However, we can still make $\mathbf{q}$ as close as possible to $\mathbf{K}_+$, by letting $|\mathbf{Q}_1 - \mathbf{Q}_2|$ be as small as possible. Here, we will consider $\mathbf{Q}_1 - \mathbf{Q}_2 = -\mathbf{q}_1$ to find that

$$\begin{aligned}
\left[\mathcal{B}^{(4)}\left(\mathbf{q}\right)\right]_{\mathbf{k}n\eta,\mathbf{k}n'\eta'}\Big|_{\mathbf{q}\approx\mathbf{K}_+-\mathbf{q}_1} =& \frac{\left(2\pi\right)^2 \delta_{\eta,+}\delta_{\eta',-}}{\Omega_{\rm TBG}\Omega_{\rm SLG}} |\phi_+\left(\mathbf{K}_+\right)|^2 \sum_{\alpha_1,\alpha_2} \sum_{\mathbf{Q}\in\mathcal{Q}_+} u^*_{\mathbf{Q}\alpha_1;n+}\left(\mathbf{k}\right) u_{\mathbf{Q}+\mathbf{q}_1\alpha_2;n'-}\left(\mathbf{k}\right) \\
& \times \left(\omega_{\alpha_2}^{-1}\omega_{\alpha_1}^{-2} + \omega_{\alpha_2}^{-2}\omega_{\alpha_1}^{-1}\right) \delta\left(\mathbf{K}_+ - \mathbf{q}_1 - \mathbf{q}\right) \\
=& \frac{\left(2\pi\right)^2 \delta_{\eta,+}\delta_{\eta',-}}{\Omega_{\rm TBG}\Omega_{\rm SLG}} |\phi_+\left(\mathbf{K}_+\right)|^2 \delta\left(\mathbf{K}_+ - \mathbf{q}_1 - \mathbf{q}\right) \\
& \times \sum_{\alpha} \sum_{\mathbf{Q}\in\mathcal{Q}_+} 2u^*_{\mathbf{Q}\alpha;n+}\left(\mathbf{k}\right) u_{\mathbf{Q}+\mathbf{q}_1\alpha;n'-}\left(\mathbf{k}\right) - u^*_{\mathbf{Q}\alpha;n+}\left(\mathbf{k}\right) u_{\mathbf{Q}+\mathbf{q}_1(-\alpha);n'-}\left(\mathbf{k}\right).
\end{aligned} \tag{C57}$$

3. $\mathcal{B}\left(\mathbf{q}\right)$ *for* $|\mathbf{q}| \approx 2|\mathbf{K}_+|$.

When $|\mathbf{q}| \approx 2|\mathbf{K}_+|$, we choose to focus on the contribution at $\mathbf{q} \approx 2\mathbf{K}_+$. As such, we must have that $C_{3z}^{j_2}\eta'\mathbf{K}_+ - C_{3z}^{j_1}\eta\mathbf{K}_+ - \mathbf{Q}_2 + \mathbf{Q}_1 \approx 2\mathbf{K}_+$ in Eq. (C46). This necessarily means that $\eta = -\eta' = +$ and $j_1 = j_2 = 0$. Since this implies that $\mathbf{Q}_1 \in \mathcal{Q}_+$ and $\mathbf{Q}_2 \in \mathcal{Q}_-$, it follows that $\mathbf{Q}_1 \neq \mathbf{Q}_2$, meaning that we cannot chose $\mathbf{q}$ to be exactly at $2\mathbf{K}_+$. However, we can still make $\mathbf{q}$ as close as possible to $2\mathbf{K}_+$, by letting $|\mathbf{Q}_1 - \mathbf{Q}_2|$ be as small as possible. Here, we will consider $\mathbf{Q}_1 - \mathbf{Q}_2 = -\mathbf{q}_1$ and find that

$$\begin{aligned}
\left[\mathcal{B}^{(4)}\left(\mathbf{q}\right)\right]_{\mathbf{k}n\eta,\mathbf{k}n'\eta'}\Big|_{\mathbf{q}\approx2\mathbf{K}_+-\mathbf{q}_1} =& \frac{\left(2\pi\right)^2 \delta_{\eta,+}\delta_{\eta',-}}{\Omega_{\rm TBG}\Omega_{\rm SLG}} |\phi_+\left(\mathbf{K}_+\right)|^2 \sum_{\alpha_1,\alpha_2} \sum_{\mathbf{Q}\in\mathcal{Q}_+} u^*_{\mathbf{Q}\alpha_1;n+}\left(\mathbf{k}\right) u_{\mathbf{Q}+\mathbf{q}_1\alpha_2;n'-}\left(\mathbf{k}\right) \delta\left(2\mathbf{K}_+ - \mathbf{q}_1 - \mathbf{q}\right) \\
=& \frac{\left(2\pi\right)^2 \delta_{\eta,+}\delta_{\eta',-}}{\Omega_{\rm TBG}\Omega_{\rm SLG}} |\phi_+\left(\mathbf{K}_+\right)|^2 \delta\left(2\mathbf{K}_+ - \mathbf{q}_1 - \mathbf{q}\right) \\
& \times \sum_{\alpha} \sum_{\mathbf{Q}\in\mathcal{Q}_+} u^*_{\mathbf{Q}\alpha;n+}\left(\mathbf{k}\right) u_{\mathbf{Q}+\mathbf{q}_1\alpha;n'-}\left(\mathbf{k}\right) + u^*_{\mathbf{Q}\alpha;n+}\left(\mathbf{k}\right) u_{\mathbf{Q}+\mathbf{q}_1(-\alpha);n'-}\left(\mathbf{k}\right).
\end{aligned} \tag{C58}$$

4. $\mathcal{B}\left(\mathbf{q}\right)$ *for* $|\mathbf{q}| \approx |\mathbf{g}_{+,1}|$.

Finally, for the contribution with $|\mathbf{q}| \approx |\mathbf{g}_{+,1}|$, we chose to focus on $\mathbf{q} = \mathbf{g}_{+,1}$. As such, we must have that $C_{3z}^{j_2}\eta'\mathbf{K}_+ - C_{3z}^{j_1}\eta\mathbf{K}_+ - \mathbf{Q}_2 + \mathbf{Q}_1 \approx \mathbf{g}_{+,1}$ in Eq. (C46). This necessarily means that $\eta = \eta' = +$, $j_1 = 0$ and $j_2 = 2$, or $\eta = \eta' = -$, and $j_1 = 2$ and $j_2 = 0$. Since $\mathbf{Q}_1, \mathbf{Q}_2 \in \mathcal{Q}_+$, it follows that we can chose $\mathbf{q}$ to be exactly at $\mathbf{g}_{+,1}$. We find that

$$\begin{aligned}
\left[\mathcal{B}^{(4)}\left(\mathbf{q}\right)\right]_{\mathbf{k}n\eta,\mathbf{k}n'\eta'}\Big|_{\mathbf{q}\approx\mathbf{g}_{+,1}} =& \frac{\left(2\pi\right)^2 \delta_{\eta,+}\delta_{\eta',+}}{\Omega_{\rm TBG}\Omega_{\rm SLG}} |\phi_+\left(\mathbf{K}_+\right)|^2 \sum_{\alpha_1,\alpha_2} \sum_{\mathbf{Q}\in\mathcal{Q}_+} u^*_{\mathbf{Q}\alpha_1;n+}\left(\mathbf{k}\right) u_{\mathbf{Q}\alpha_2;n'+}\left(\mathbf{k}\right) \omega_{\alpha_2}^2 \delta\left(\mathbf{g}_{+,1} - \mathbf{q}\right) \\
& + \frac{\left(2\pi\right)^2 \delta_{\eta,-}\delta_{\eta',-}}{\Omega_{\rm TBG}\Omega_{\rm SLG}} |\phi_+\left(\mathbf{K}_+\right)|^2 \sum_{\alpha_1,\alpha_2} \sum_{\mathbf{Q}\in\mathcal{Q}_-} u^*_{\mathbf{Q}\alpha_1;n-}\left(\mathbf{k}\right) u_{\mathbf{Q}\alpha_2;n'-}\left(\mathbf{k}\right) \omega_{\alpha_1}^2 \delta\left(\mathbf{g}_{+,1} - \mathbf{q}\right).
\end{aligned} \tag{C59}$$

Appendix D: The spectral function matrix elements

In Appendix [C], we have shown that the spectral function for TBG sample can be obtained by contracting two (gauge-dependent) tensors: the spatial factor – which depends on the TBG active band wave functions – and the spectral function matrices – which depend on the TBG ground state under consideration, as well as on the TBG Hamiltonian. With the properties of the spatial factor derived and discussed in Appendix [C], this appendix turns to the spectral function matrices $\mathcal{M}^{\pm}(\omega)$ and their evaluation. We start by focusing on the experimentally-relevant flat limit [74], in which the physics of the system is governed by the TBG interaction Hamiltonian H_I from Appendix [A 2]. We show how the charge-one excitations derived in Ref. [75] and reviewed in Appendix [B] can be used to compute the spectral function matrices for the TBG correlated insulators found in Ref. [68]. Under the assumption of rigidly filling the charge-one excitation bands, we additionally consider the effects of small doping away from integer filling on the TBG spectral function. Finally, the spectral function matrices are also computed in the non-interacting limit (*i.e.* when the electron-electron interactions are ignored). The direct comparison presented in the main paper between the computed spectral functions in both the non-interacting and interacting regimes and the STM experimental data at $\nu = \pm 4$ offers compelling evidence for the validity of the strongly-coupled limit in TBG at the magic angle.

1. Computing the spectral function matrices at integer fillings in the interacting limit

In this section, we derive the spectral function matrix $\mathcal{M}^{\pm}(\omega)$ using the exact charge-one excitations of TBG found by Ref. [75], and briefly reviewed in Appendix [B]. We will always assume to be in the so-called flat limit [74], and therefore ignore the projected single-particle Hamiltonian H_0 with respect to the interaction one H_I.

As in Appendix [B 4] (whose notation we will follow), we assume that the ground state is given by $|\varphi\rangle$ from Eq. (B34), which represents a certain $\mathrm{U}(4) \times \mathrm{U}(4)$ rotation $\hat{U}$ of the integer-filling ground state $\left|\Psi_{\nu}^{\nu_+,\nu_-}\right\rangle$ from Eq. (B8). Using Eqs. (C16) and (C17), we find the corresponding spectral function matrices $\mathcal{M}^{\pm}_{\varphi}(\omega)$ to be

$$\left[\mathcal{M}^{+}_{\varphi}(\omega)\right]_{\mathbf{k}n\eta,\mathbf{k}'n'\eta'} = \sum_{\xi}\sum_{s,s'} \langle\varphi|\hat{c}_{\mathbf{k}',n',\eta',s'}|\xi\rangle \left\langle \xi\middle|\hat{c}^{\dagger}_{\mathbf{k},n,\eta,s}\middle|\varphi\right\rangle \delta_{s,s'}\delta\left(\omega - E_{\xi} + E_{\varphi}\right), \tag{D1}$$

$$\left[\mathcal{M}^{-}_{\varphi}(\omega)\right]_{\mathbf{k}n\eta,\mathbf{k}'n'\eta'} = \sum_{\xi}\sum_{s,s'} \left\langle \varphi\middle|\hat{c}^{\dagger}_{\mathbf{k},n,\eta,s}\middle|\xi\right\rangle \langle\xi|\hat{c}_{\mathbf{k}',n',\eta',s'}|\varphi\rangle \delta_{s,s'}\delta\left(\omega + E_{\xi} - E_{\varphi}\right). \tag{D2}$$

Eqs. (D1) and (D2) include a summation over all the eigenstates of the TBG interaction Hamiltonian, $|\xi\rangle$. Nevertheless, one of the central results of the charge-commutation relations from Appendix [B 4] was that acting with the $\hat{c}^{\dagger}_{\mathbf{k},n,\eta,s}$ ($\hat{c}_{\mathbf{k},n,\eta,s}$) operators on the ground state $|\varphi\rangle$ leads to a superposition of electron (hole) excitations, which can be readily computed as a zero-body problem. Focusing on the electron excitations, we have shown in Appendix [B 4] that the eight fermionic operators $\hat{c}^{\dagger}_{\mathbf{k},n,\eta,s}|\varphi\rangle$ (for $s = \uparrow,\downarrow$, $\eta = \pm$, $n = \pm 1$) can be recombined into $\hat{\gamma}^{\dagger}_{\mathbf{k},p}$ (for $1 \leq p \leq 4-\nu$) and $\hat{\theta}^{\dagger}_{\mathbf{k},p}$ (for $1 \leq p \leq 4+\nu$), which were respectively defined in Eqs. (B57) and (B58). Thus, the Hillbert space of spanned by *all* states of the form $\hat{c}^{\dagger}_{\mathbf{k},n,\eta,s}|\varphi\rangle$ is identical to the space spanned by $\hat{\gamma}^{\dagger}_{\mathbf{k},p}|\varphi\rangle$ for $1 \leq p \leq 4-\nu$, *i.e.* the eigenstates of H_I corresponding to an electron excitation above the ground state $|\varphi\rangle$ [5]. Therefore, the *only* many-body eigenstates of H_I that have a non-vanishing overlap with $\hat{c}^{\dagger}_{\mathbf{k},n,\eta,s}|\varphi\rangle$ *are* the electron excitations $\hat{\gamma}^{\dagger}_{\mathbf{k},p}|\varphi\rangle$, for $1 \leq p \leq 4-\nu$ [6], whose properties were given in Appendix [B 4]. As shown in the text surrounding Eq. (B51), $\hat{\gamma}^{\dagger}_{\mathbf{k},p}|\varphi\rangle$ are eigenstates of the interaction Hamiltonian with eigenvalue $E_{\varphi} + E^{p}_{\mathbf{k}} + \mu$, for $1 \leq p \leq 4-\nu$, where E_{φ} is the ground state energy and the addition of the chemical potential μ reflects the fact that the excitation energies $E^{p}_{\mathbf{k}}$ were defined with respect to the grand canonical Hamiltonian $(H_I - \mu\hat{N})$, as opposed to microcanonical one, H_I. As a result, one can replace the summation over all excited states $|\xi\rangle$ in Eq. (D1), according to

$$\sum_{\xi} |\xi\rangle\,\delta\left(\omega - E_{\xi} + E_{\varphi}\right)\langle\xi| \rightarrow \sum_{\mathbf{k}}\sum_{p=1}^{4-\nu} \hat{\gamma}^{\dagger}_{\mathbf{k},p}|\varphi\rangle\,\delta\left(\omega - \mu - E^{p}_{\mathbf{k}}\right)\langle\varphi|\,\hat{\gamma}_{\mathbf{k},p}. \tag{D3}$$

---

[5] Note that $\hat{\theta}^{\dagger}_{\mathbf{k},p}$ (for $1 \leq p \leq 4+\nu$) are linear combinations of fermions corresponding to the occupied bands in $|\varphi\rangle$ and, therefore, $\hat{\theta}^{\dagger}_{\mathbf{k},p}|\varphi\rangle = 0$.

[6] Strictly speaking, this relies on $\hat{\gamma}^{\dagger}_{\mathbf{k},p}|\varphi\rangle$ being *exact* eigenstates of H_I. As argued in Appendix [B 1], this is only true in the chiral limit ($w_0 = 0$) for $|\varphi\rangle$ being any $\mathrm{U}(4) \times \mathrm{U}(4)$ rotation of the states from Eq. (B8), or away from the chiral limit in the particle-hole-symmetric case ($w_0 \neq 0$ and $\lambda = 0$) for $|\varphi\rangle$ being any $\mathrm{U}_{\mathrm{nc}}(4)$ rotation of the states in Eq. (B7). In the general case, we *approximate* the spectral function by treating both $|\varphi\rangle$ and $\hat{\gamma}^{\dagger}_{\mathbf{k},p}|\varphi\rangle$ as being *exact* eigenstates of H_I and ignore any further perturbative corrections to the spectral function matrix elements.

By analogy, the sum over $|\xi\rangle$ in Eq. (D2) can be changed to include only the hole excitations on top of $|\varphi\rangle$ from Eq. (B58) according to

$$\sum_{\xi} |\xi\rangle \, \delta\left(\omega + E_{\xi} - E_{\varphi}\right) \langle\xi| \rightarrow \sum_{\mathbf{k}} \sum_{p=1}^{4+\nu} \hat{\theta}_{\mathbf{k},p} \, |\varphi\rangle \, \delta\left(\omega - \mu + \tilde{E}^{p}_{\mathbf{k}}\right) \langle\varphi| \, \hat{\theta}^{\dagger}_{\mathbf{k},p}. \tag{D4}$$

Using Eqs. (D3) and (D4), as well as the wave functions of the charge-one excitations from Eqs. (B57) and (B58), we find that the spectral function matrices are given by

$$\left[\mathcal{M}^{+}_{\varphi}\left(\omega\right)\right]_{\mathbf{k}n\eta,\mathbf{k}'n'\eta'} = \delta_{\mathbf{k},\mathbf{k}'} \sum_{s,s'} \left[Y\left(\mathbf{k},\omega\right)\right]_{n\eta s,n'\eta's'} \delta_{s,s'}, \tag{D5}$$

$$\left[\mathcal{M}^{-}_{\varphi}\left(\omega\right)\right]_{\mathbf{k}n\eta,\mathbf{k}'n'\eta'} = \delta_{\mathbf{k},\mathbf{k}'} \sum_{s,s'} \left[\tilde{Y}\left(\mathbf{k},\omega\right)\right]_{n\eta s,n'\eta's'} \delta_{s,s'}. \tag{D6}$$

where, for simplicity, we have defined

$$\left[Y\left(\mathbf{k},\omega\right)\right]_{n\eta s,n'\eta's'} = \sum_{p=1}^{4-\nu} \delta\left(\omega - \mu - E^{p}_{\mathbf{k}}\right) Z^{*p}_{\mathbf{k},n\eta s} Z^{p}_{\mathbf{k},n'\eta's'}, \tag{D7}$$

$$\left[\tilde{Y}\left(\mathbf{k},\omega\right)\right]_{n\eta s,n'\eta's'} = \sum_{p=1}^{4+\nu} \delta\left(\omega - \mu + \tilde{E}^{p}_{\mathbf{k}}\right) \tilde{Z}^{p}_{\mathbf{k},n\eta s} \tilde{Z}^{*p}_{\mathbf{k},n'\eta's'}. \tag{D8}$$

Alternatively, the spectral function can also be defined in terms of charge-one excitation wave functions in the rotated fermion basis, $\Xi^{p}_{\mathbf{k},n\eta s}$ and $\tilde{\Xi}^{p}_{\mathbf{k},n\eta s}$, which were defined in Eqs. (B49) and (B50), respectively,

$$\left[\mathcal{M}^{+}_{\varphi}\left(\omega\right)\right]_{\mathbf{k}n\eta,\mathbf{k}'n'\eta'} = \delta_{\mathbf{k},\mathbf{k}'} \sum_{s,s'} \left[U^{\dagger} \Upsilon\left(\mathbf{k},\omega\right) U\right]_{n\eta s,n'\eta's'} \delta_{s,s'}, \tag{D9}$$

$$\left[\mathcal{M}^{-}_{\varphi}\left(\omega\right)\right]_{\mathbf{k}n\eta,\mathbf{k}'n'\eta'} = \delta_{\mathbf{k},\mathbf{k}'} \sum_{s,s'} \left[U^{\dagger} \tilde{\Upsilon}\left(\mathbf{k},\omega\right) U\right]_{n\eta s,n'\eta's'} \delta_{s,s'}, \tag{D10}$$

where U is the eight-dimensional unitary matrix defined in Eq. (B37) implementing the $\mathrm{U}\left(4\right) \times \mathrm{U}\left(4\right)$ rotation $\hat{U}$ from Eq. (B34) and

$$\left[\Upsilon\left(\mathbf{k},\omega\right)\right]_{n\eta s,n'\eta's'} = \sum_{p=1}^{4-\nu} \delta\left(\omega - \mu - E^{p}_{\mathbf{k}}\right) \Xi^{*p}_{\mathbf{k},n\eta s} \Xi^{p}_{\mathbf{k},n'\eta's'}, \tag{D11}$$

$$\left[\tilde{\Upsilon}\left(\mathbf{k},\omega\right)\right]_{n\eta s,n'\eta's'} = \sum_{p=1}^{4+\nu} \delta\left(\omega - \mu + \tilde{E}^{p}_{\mathbf{k}}\right) \tilde{\Xi}^{p}_{\mathbf{k},n\eta s} \tilde{\Xi}^{*p}_{\mathbf{k},n'\eta's'}. \tag{D12}$$

Finally, from Eqs. (B55) and (B56), we note that

$$U^{\dagger} \Upsilon\left(\mathbf{k},\omega\right) U = Y\left(\mathbf{k},\omega\right) \quad \text{and} \quad U^{\dagger} \tilde{\Upsilon}\left(\mathbf{k},\omega\right) U = \tilde{Y}\left(\mathbf{k},\omega\right), \tag{D13}$$

and therefore, the matrices $\Upsilon\left(\mathbf{k},\omega\right)$ and $\tilde{\Upsilon}\left(\mathbf{k},\omega\right)$ are related to $Y\left(\mathbf{k},\omega\right)$ and $\tilde{Y}\left(\mathbf{k},\omega\right)$ through a $\mathrm{U}\left(4\right) \times \mathrm{U}\left(4\right)$ rotation.

The advantage of using the notation from Eqs. (D5) and (D6) becomes apparent when comparing Eqs. (D7) and (D8) with Eqs. (B63) and (B64): up to a Dirac δ-function being applied on the (non-zero) eigenvalues, the matrices $Y\left(\mathbf{k},\omega\right)$ and $\tilde{Y}\left(\mathbf{k},\omega\right)$ share identical eigenspectra with the matrices $U^{\dagger}\Pi U \left(R\left(\mathbf{k}\right) \otimes s^{0}\right) U^{\dagger}\Pi U$ and $U^{\dagger}\Pi U \left(\tilde{R}\left(\mathbf{k}\right) \otimes s^{0}\right) U^{\dagger}\Pi U$, respectively. Similarly, the matrices $\Upsilon\left(\mathbf{k},\omega\right)$ and $\tilde{\Upsilon}\left(\mathbf{k},\omega\right)$ share identical eigenvectors with the matrices $\Pi U \left(R\left(\mathbf{k}\right) \otimes s^{0}\right) U^{\dagger}\Pi$ and $\Pi U \left(\tilde{R}\left(\mathbf{k}\right) \otimes s^{0}\right) U^{\dagger}\Pi$, respectively. In Appendix [E], we will leverage this connection extensively for deriving parameterizations for the $\mathcal{M}^{\pm}_{\varphi}\left(\omega\right)$ matrices and for obtaining an *analytical* understanding of the TBG spectral function patterns.

2. Influence of small doping away from integer fillings in the interacting limit

Having derived the spectral function matrix elements of the insulator $|\varphi\rangle$ (corresponding to an *exact* integer filling ν), we now investigate the influence of small doping *away* from integer filling. As a zeroth order approximation, we will assume that the ground state of the interacting Hamiltonian away from exact integer filling can be found by "rigidly" filling or depleting the charge-one excitation bands. In other words, we assume that for small doping away from integer fillings, the charge-one excitations can be approximated as non-interacting fermions and, as such, the charge-one excitation bands can be filled (or depleted) according to the Pauli exclusion principle. Such an approximation can be justified by noting that the steep dispersion of the charge-one excitations above $|\varphi\rangle$ is enough to stabilize a Fermi liquid for small doping away from integer filling [67].

To start with, we let $|\varphi_{\Delta\nu}\rangle$ be the ground state of the interaction TBG Hamiltonian at filling $\nu+\Delta\nu$, obtained by doping the insulator $|\varphi\rangle$

$$|\varphi_{\Delta\nu}\rangle = \left(\prod_{p=1}^{4-\nu}\prod_{\substack{\mathbf{k}\\(\mu_{\Delta\nu}-\mu-E^p_{\mathbf{k}})>0}}\hat{\gamma}^\dagger_{\mathbf{k},p}\right)\left(\prod_{p=1}^{4+\nu}\prod_{\substack{\mathbf{k}\\(\mu-\mu_{\Delta\nu}-\tilde{E}^p_{\mathbf{k}})>0}}\hat{\theta}_{\mathbf{k},p}\right)|\varphi\rangle\,, \tag{D14}$$

where $\mu_{\Delta\nu}$ (μ) is the chemical potential of the doped (un-doped) ground state. Because $|\varphi\rangle$ is a ground state of the TBG interaction Hamiltonian, the charge-one excitation energies are strictly positive. Therefore, Eq. (D14) is valid for both electron doping (where $\mu_{\Delta\nu}>\mu$ and the second product is identity) and hole doping (where $\mu_{\Delta\nu}<\mu$ and the first product is identity). The chemical potential of the doped ground state $\mu_{\Delta\nu}$ satisfies the self-consistent condition

$$\Delta\nu = \frac{1}{N_M}\begin{cases}\sum_{\mathbf{k}}\sum_{p=1}^{4-\nu}\Theta\left(\mu_{\Delta\nu}-\mu-E^p_{\mathbf{k}}\right), & \text{if}\quad \Delta\nu>0\\ -\sum_{\mathbf{k}}\sum_{p=1}^{4+\nu}\Theta\left(\mu-\mu_{\Delta\nu}-\tilde{E}^p_{\mathbf{k}}\right), & \text{if}\quad \Delta\nu<0\end{cases}, \tag{D15}$$

where N_M denotes the number of moiré unit cells in the system and $\Theta(x)$ is the Heaviside step function

$$\Theta(x)=\begin{cases}1, & x>0\\ 0, & x<0\end{cases}\quad. \tag{D16}$$

Eq. (D15) can also be written more succinctly as

$$\Delta\nu = \frac{1}{N_M}\left[\sum_{\mathbf{k}}\sum_{p=1}^{4-\nu}\Theta\left(\mu_{\Delta\nu}-\mu-E^p_{\mathbf{k}}\right)-\sum_{\mathbf{k}}\sum_{p=1}^{4+\nu}\Theta\left(\mu-\mu_{\Delta\nu}-\tilde{E}^p_{\mathbf{k}}\right)\right]. \tag{D17}$$

To obtain the spectral function matrix elements

$$\left[\mathcal{M}^+_{\varphi_{\Delta\nu}}(\omega)\right]_{\mathbf{k}n\eta,\mathbf{k}'n'\eta'} = \sum_{\xi}\sum_{s,s'}\langle\varphi_{\Delta\nu}|\hat{c}_{\mathbf{k}',n',\eta',s'}|\xi\rangle\left\langle\xi\middle|\hat{c}^\dagger_{\mathbf{k},n,\eta,s}\middle|\varphi_{\Delta\nu}\right\rangle\delta_{s,s'}\delta\left(\omega-E_\xi+E_{\varphi_{\Delta\nu}}\right), \tag{D18}$$

$$\left[\mathcal{M}^-_{\varphi_{\Delta\nu}}(\omega)\right]_{\mathbf{k}n\eta,\mathbf{k}'n'\eta'} = \sum_{\xi}\sum_{s,s'}\left\langle\varphi_{\Delta\nu}\middle|\hat{c}^\dagger_{\mathbf{k},n,\eta,s}\middle|\xi\right\rangle\langle\xi|\hat{c}_{\mathbf{k}',n',\eta',s'}|\varphi_{\Delta\nu}\rangle\,\delta_{s,s'}\delta\left(\omega+E_\xi-E_{\varphi_{\Delta\nu}}\right). \tag{D19}$$

we still need to compute the eigenstates of the interaction Hamiltonian that contain one additional electron or hole compared to $|\varphi_{\Delta\nu}\rangle$. Focusing on the electron contribution from Eq. (D18), we first note that the Hilbert space spanned by $\hat{c}^\dagger_{\mathbf{k},n,\eta,s}|\varphi_{\Delta\nu}\rangle$ for $s=\uparrow,\downarrow$, $\eta=\pm$, $n=\pm1$, is identical to the Hilbert space spanned by $\hat{\gamma}^\dagger_{\mathbf{k},p}|\varphi_{\Delta\nu}\rangle$, for $1\le p\le 4-\nu$, and $\hat{\theta}^\dagger_{\mathbf{k},p}|\varphi_{\Delta\nu}\rangle$, for $1\le p\le 4+\nu$, because the corresponding operators, $\hat{\gamma}^\dagger_{\mathbf{k},p}$ and $\hat{\theta}^\dagger_{\mathbf{k},p}$, are just linear combinations of the energy band operators $\hat{c}^\dagger_{\mathbf{k},n,\eta,s}$. Therefore, the *only* states containing one additional electron compared to $|\varphi_{\Delta\nu}\rangle$ that have a non-vanishing overlap with $\hat{c}^\dagger_{\mathbf{k},n,\eta,s}|\varphi_{\Delta\nu}\rangle$ are of the form $\hat{\gamma}^\dagger_{\mathbf{k},p}|\varphi_{\Delta\nu}\rangle$ or $\hat{\theta}^\dagger_{\mathbf{k},p}|\varphi_{\Delta\nu}\rangle$, provided that these states do themselves not vanish. Under the approximation that the charge-one excitations do not interact, these states are also *eigenstates* of the interaction Hamiltonian, and so we find that $|\xi\rangle$ from Eq. (D18) can be either $\hat{\gamma}^\dagger_{\mathbf{k},p}|\varphi_{\Delta\nu}\rangle$ (with energy $E_\xi=E_{\varphi_\Delta}+E^p_{\mathbf{k}}+\mu$) or $\hat{\theta}^\dagger_{\mathbf{k},p}|\varphi_{\Delta\nu}\rangle$ (with energy $E_\xi=E_{\varphi_\Delta}-\tilde{E}^p_{\mathbf{k}}+\mu$). As such, the summation over the states $|\xi\rangle$ in Eq. (D18) can be changed according to

$$\sum_\xi|\xi\rangle\,\delta\left(\omega-E_\xi+E_{\varphi_{\Delta\nu}}\right)\langle\xi| \to \sum_{\mathbf{k}}\left(\sum_{p=1}^{4-\nu}\hat{\gamma}^\dagger_{\mathbf{k},p}|\varphi_{\Delta\nu}\rangle\,\delta\left(\omega-\mu-E^p_{\mathbf{k}}\right)\langle\varphi_{\Delta\nu}|\,\hat{\gamma}_{\mathbf{k},p}\right.$$

$$+\sum_{p=1}^{4+\nu}\hat{\theta}^{\dagger}_{\mathbf{k},p}\left|\varphi_{\Delta\nu}\right\rangle\delta\left(\omega-\mu+\tilde{E}^{p}_{\mathbf{k}}\right)\left\langle\varphi_{\Delta\nu}\right|\hat{\theta}_{\mathbf{k},p}\Bigg). \tag{D20}$$

Using a similar argument for the hole contribution from Eq. (D19), we find that the summation over the states $|\xi\rangle$ in Eq. (D19) can also be replaced as

$$\begin{aligned}\sum_{\xi}\left|\xi\right\rangle\delta\left(\omega+E_{\xi}-E_{\varphi_{\Delta\nu}}\right)\left\langle\xi\right|\rightarrow\sum_{\mathbf{k}}\Bigg(&\sum_{p=1}^{4-\nu}\hat{\gamma}_{\mathbf{k},p}\left|\varphi_{\Delta\nu}\right\rangle\delta\left(\omega-\mu-E^{p}_{\mathbf{k}}\right)\left\langle\varphi_{\Delta\nu}\right|\hat{\gamma}^{\dagger}_{\mathbf{k},p}\\&+\sum_{p=1}^{4+\nu}\hat{\theta}_{\mathbf{k},p}\left|\varphi_{\Delta\nu}\right\rangle\delta\left(\omega-\mu+\tilde{E}^{p}_{\mathbf{k}}\right)\left\langle\varphi_{\Delta\nu}\right|\hat{\theta}^{\dagger}_{\mathbf{k},p}\Bigg).\end{aligned} \tag{D21}$$

By substituting Eqs. (D14), (D20) and (D21) in the expressions for the spectral function matrices from Eqs. (D18) and (D19), we find

$$\begin{aligned}\left[\mathcal{M}^{+}_{\varphi_{\Delta\nu}}(\omega)\right]_{\mathbf{k}n\eta,\mathbf{k}'n'\eta'}=&\delta_{\mathbf{k},\mathbf{k}'}\Bigg\{\sum_{p=1}^{4-\nu}\sum_{s,s'}Z^{*p}_{\mathbf{k},n\eta s}Z^{p}_{\mathbf{k},n'\eta's'}\delta_{s,s'}\delta\left(\omega-\mu-E^{p}_{\mathbf{k}}\right)\left[1-\Theta\left(\mu_{\Delta\nu}-\mu-E^{p}_{\mathbf{k}}\right)\right]\\&+\sum_{p=1}^{4+\nu}\sum_{s,s'}\tilde{Z}^{p}_{\mathbf{k},n\eta s}\tilde{Z}^{*p}_{\mathbf{k},n'\eta's'}\delta_{s,s'}\delta\left(\omega-\mu+\tilde{E}^{p}_{\mathbf{k}}\right)\Theta\left(\mu-\mu_{\Delta\nu}-\tilde{E}^{p}_{\mathbf{k}}\right)\Bigg\},\end{aligned} \tag{D22}$$

$$\begin{aligned}\left[\mathcal{M}^{-}_{\varphi_{\Delta\nu}}(\omega)\right]_{\mathbf{k}n\eta,\mathbf{k}'n'\eta'}=&\delta_{\mathbf{k},\mathbf{k}'}\Bigg\{\sum_{p=1}^{4+\nu}\sum_{s,s'}\tilde{Z}^{p}_{\mathbf{k},n\eta s}\tilde{Z}^{*p}_{\mathbf{k},n'\eta's'}\delta_{s,s'}\delta\left(\omega-\mu+\tilde{E}^{p}_{\mathbf{k}}\right)\left[1-\Theta\left(\mu-\mu_{\Delta\nu}-\tilde{E}^{p}_{\mathbf{k}}\right)\right]\\&+\sum_{p=1}^{4-\nu}\sum_{s,s'}Z^{*p}_{\mathbf{k},n\eta s}Z^{p}_{\mathbf{k},n'\eta's'}\delta_{s,s'}\delta\left(\omega-\mu-E^{p}_{\mathbf{k}}\right)\Theta\left(\mu_{\Delta\nu}-\mu-E^{p}_{\mathbf{k}}\right)\Bigg\}.\end{aligned} \tag{D23}$$

At first glance, since the spectral function matrix elements of the doped insulator from Eqs. (D22) and (D23) differ from the ones of the un-doped state $|\varphi\rangle$ from Eqs. (D5) and (D6), one might conclude that the spectral function itself also changes under small doping. However, as shown in Eq. (C15), the spectral function depends on the *sum* between the electron and hole contributions from Eqs. (D22) and (D23), which can be seen to obey

$$\mathcal{M}^{+}_{\varphi_{\Delta\nu}}(\omega)+\mathcal{M}^{-}_{\varphi_{\Delta\nu}}(\omega)=\mathcal{M}^{+}_{\varphi}(\omega)+\mathcal{M}^{-}_{\varphi}(\omega), \tag{D24}$$

implying that, under the assumption of rigidly filling the charge-one excitation bands, the spectral function does not change. This result is a direct consequence of treating the charge-one excitations as being non-interacting and represents a well-known result in non-interacting band theory [97]. For example, one can consider doping the insulator $|\varphi\rangle$ with electrons: there are fewer available electron excitations in $|\varphi_{\Delta\nu}\rangle$. However, the missing electron excitations from $|\varphi_{\Delta\nu}\rangle$ now appear as hole excitations, meaning that although the individual hole and electron contributions to the spectral function change, their sum does not.

3. Computing the spectral function matrices in the absence of interactions

For comparison purposes, it is instructive to compute the TBG spectral function in the non-interacting limit at a certain (not necessarily integer) filling factor ν. In this limit, the physics is governed by the single-particle TBG Hamiltonian from Eq. (A14), as electron-electron interactions are ignored. The corresponding ground state $|\phi_{\nu}\rangle$ at filling ν is found by populating the active TBG bands according the Pauli exclusion principle

$$\left|\phi_{\nu}\right\rangle=\prod_{n,\eta}\prod_{\substack{\mathbf{k}\\ \epsilon_{n,\eta}(\mathbf{k})<\mu}}\hat{c}^{\dagger}_{\mathbf{k},n,\eta,\uparrow}\hat{c}^{\dagger}_{\mathbf{k},n,\eta,\downarrow}\left|0\right\rangle. \tag{D25}$$

In Eq. (D25), $\epsilon_{n,\eta}(\mathbf{k})$ are the single-particle energies of the active TBG bands and μ is the chemical potential of $|\phi_{\nu}\rangle$ satisfying the self-consistent condition

$$\nu=-4+\frac{2}{N_{M}}\sum_{\mathbf{k}}\sum_{n,\eta}\Theta\big(\mu-\epsilon_{n,\eta}(\mathbf{k})\big). \tag{D26}$$

Since interactions are ignored completely, the state $\hat{c}^{\dagger}_{\mathbf{k},n,\eta,s}\left|\phi_{\nu}\right\rangle$ $[\hat{c}_{\mathbf{k},n,\eta,s}\left|\phi_{\nu}\right\rangle]$ is an exact eigenstate of the noninteracting TBG Hamiltonian with energy $E_{\phi_{\nu}}+\epsilon_{n,\eta}\left(\mathbf{k}\right)$ $[E_{\phi_{\nu}}-\epsilon_{n,\eta}\left(\mathbf{k}\right)]$, provided that the state itself does not vanish. As a result, one can replace the summation over all excited states $\left|\xi\right\rangle$ in the definition of the spectral function matrices from Eqs. (C16) and (C17) according to

$$\sum_{\xi}\left|\xi\right\rangle\delta\left(\omega-E_{\xi}+E_{\varphi_{\Delta\nu}}\right)\left\langle\xi\right|\rightarrow\sum_{\mathbf{k}}\sum_{n,\eta,s}\hat{c}^{\dagger}_{\mathbf{k},n,\eta,s}\left|\phi_{\nu}\right\rangle\delta\big(\omega-\epsilon_{n,\eta}\left(\mathbf{k}\right)\big)\left\langle\phi_{\nu}\right|\hat{c}_{\mathbf{k},n,\eta,s}, \tag{D27}$$

$$\sum_{\xi}\left|\xi\right\rangle\delta\left(\omega+E_{\xi}-E_{\varphi_{\Delta\nu}}\right)\left\langle\xi\right|\rightarrow\sum_{\mathbf{k}}\sum_{n,\eta,s}\hat{c}_{\mathbf{k},n,\eta,s}\left|\phi_{\nu}\right\rangle\delta\big(\omega-\epsilon_{n,\eta}\left(\mathbf{k}\right)\big)\left\langle\phi_{\nu}\right|\hat{c}^{\dagger}_{\mathbf{k},n,\eta,s}, \tag{D28}$$

respectively. The corresponding matrix elements can be readily computed to be

$$\Big[\mathcal{M}^{+}_{\phi_{\nu}}\left(\omega\right)\Big]_{\mathbf{k}n\eta,\mathbf{k}'n'\eta'}=\sum_{s,s'}\delta_{\mathbf{k},\mathbf{k}'}\delta_{n,n'}\delta_{\eta,\eta'}\delta_{s,s'}\delta\big(\omega-\epsilon_{n,\eta}\left(\mathbf{k}\right)\big)\left[1-\Theta\big(\mu-\epsilon_{n,\eta}\left(\mathbf{k}\right)\big)\right], \tag{D29}$$

$$\Big[\mathcal{M}^{-}_{\phi_{\nu}}\left(\omega\right)\Big]_{\mathbf{k}n\eta,\mathbf{k}'n'\eta'}=\sum_{s,s'}\delta_{\mathbf{k},\mathbf{k}'}\delta_{n,n'}\delta_{\eta,\eta'}\delta_{s,s'}\delta\big(\omega-\epsilon_{n,\eta}\left(\mathbf{k}\right)\big)\Theta\big(\mu-\epsilon_{n,\eta}\left(\mathbf{k}\right)\big). \tag{D30}$$

The TBG spectral function depends on the sum between the electron and hole contribution,

$$\Big[\mathcal{M}^{+}_{\phi_{\nu}}\left(\omega\right)\Big]_{\mathbf{k}n\eta,\mathbf{k}'n'\eta'}+\Big[\mathcal{M}^{-}_{\phi_{\nu}}\left(\omega\right)\Big]_{\mathbf{k}n\eta,\mathbf{k}'n'\eta'}=2\delta_{\mathbf{k},\mathbf{k}'}\delta_{n,n'}\delta_{\eta,\eta'}\delta\big(\omega-\epsilon_{n,\eta}\left(\mathbf{k}\right)\big), \tag{D31}$$

which is independent on the filling ν. Unlike the interacting spectral function matrices computed in Appendix [D 1], the spectral function matrices in the non-interacting case are necessarily diagonal in the band and valley subspaces.

Appendix E: Symmetry properties of the spectral function matrices in the interacting case

In Appendix [D 1], we showed how the exact charge-one excitations from Appendix [B 4] can be employed to compute the spectral function matrices for the correlated TBG insulating states found by Ref. [68]. Since evaluating the charge-one excitation spectrum for a given ground state $\left|\varphi\right\rangle$ in the interacting case is equivalent to a zero-body problem [75], the direct numerical calculation of the corresponding spectral function is computationally feasible even for relatively large system sizes (*i.e.* much higher than can be achieved with techniques such as exact diagonalization). Nevertheless, the various ways of populating the eight Chern bands in the unrotated state $\left|\Psi^{\nu_{+},\nu_{-}}_{\nu}\right\rangle$, coupled with the thermodynamically extensive number of possible $\mathrm{U}\left(4\right)\times\mathrm{U}\left(4\right)$ rotations thereof, results in a virtually infinite number of choices for the correlated TBG ground states $\left|\varphi\right\rangle$. As such, the numerical evaluation of the spectral functions for *all* possible insulating ground states found by Ref. [68] becomes neither feasible, nor useful.

With the goal of building a more complete understanding of the spectral functions for the various insulators found by Ref. [68], this appendix analytically derives the symmetry properties of the spectral functions matrices. To do so, we will leverage the connection outlined in Appendices [B 4 b] and [D 1] between the spectral function and charge-one excitation matrices. For a given ground state $\left|\varphi\right\rangle$ defined in Eq. (B34), comparing the spectral function matrices from Eqs. (D5) and (D6) with Eqs. (B63) and (B64) reveals that, up to a rescaling of the eigenvalues and a trace over the spin degrees of freedom, $\mathcal{M}^{+}_{\varphi}\left(\omega\right)$ and $\mathcal{M}^{-}_{\varphi}\left(\omega\right)$ have the same eigendecomposition as the matrices $U^{\dagger}\Pi U\left(R\left(\mathbf{k}\right)\otimes s^{0}\right)U^{\dagger}\Pi U$ and $U^{\dagger}\tilde{\Pi}U\left(\tilde{R}\left(\mathbf{k}\right)\otimes s^{0}\right)U^{\dagger}\tilde{\Pi}U$, respectively, where the unitary matrix U defined in Eq. (B37) specifies the $\mathrm{U}\left(4\right)\times\mathrm{U}\left(4\right)$ transformation defining $\left|\varphi\right\rangle$, and the projectors Π and $\tilde{\Pi}$ are related to the occupied bands of $\left|\varphi\right\rangle$ according to Eqs. (B59) and (B60). Since the charge-one excitation matrices $R\left(\mathbf{k}\right)$ and $\tilde{R}\left(\mathbf{k}\right)$ defined in Appendix [B 1] have been explicitly parameterized in Appendix [B 3], this connection allows us to derive parameterizations of the spectral function matrices, which take into consideration both the discrete and continuous symmetries of TBG. Coupled with the properties of the spatial factor derived in Appendix [C 2], these will enable us to obtain a general understanding of the real-space STM patterns of the integer-filled TBG insulators.

As argued in Appendix [C 3 c], the valley-off-diagonal elements of the spatial factor correspond to the emergence of $\sqrt{3}\times\sqrt{3}$ symmetry-breaking at the level of the SLG lattice. In turn, for intervalley-coherent TBG ground states, the spectral function matrices also contain valley-off-diagonal terms. As such, one might conclude that $\sqrt{3}\times\sqrt{3}$ ordering represents a generic feature of intervalley-coherent TBG ground states. In this appendix, we will show that this naive picture is, in fact, incorrect: $\sqrt{3}\times\sqrt{3}$ symmetry-breaking is *not* generic *even* in the presence of intervalley coherence, and therefore its presence or absence in the STM patterns can serve as a robust means of experimentally discriminating between the various theoretically-proposed TBG ground state at a given filling. Consequently, deriving

the conditions under which $\sqrt{3}\times\sqrt{3}$ ordering emerges within the TBG insulators found by Ref. [68] constitutes the main focus of this appendix.

We start by investigating the STM patterns of the insulators $|\Psi_\nu\rangle$, defined in Eq. (B7), together with their $\mathrm{U_{nc}}(4)$ rotations. The resulting states $|\varphi\rangle$ correspond to an even filling and zero Chern number, and were analytically shown [42, 58, 68] and numerically verified [58, 69] to be exact ground states of the projected interaction TBG Hamiltonian H_I (in the $\lambda=0$ case), thus making our analysis exact in the nonchiral-flat limit [74]. We show that the spectral function of these insulators is independent of the particular $\mathrm{U_{nc}}(4)$ rotation we consider, and prove that no $\sqrt{3}\times\sqrt{3}$ symmetry breaking is present in the corresponding STM patterns, *even* in the presence of intervalley coherence. We find that the counter-intuitive absence of $\sqrt{3}\times\sqrt{3}$ ordering stems from occupying both Chern bands of a given valley-spin flavor, considering only $\mathrm{U_{nc}}(4)$ rotations (as opposed to the more general $\mathrm{U}(4)\times\mathrm{U}(4)$ rotations), and the discrete symmetries of TBG – C_{2z}, T, and P.

We then consider the more general states $\left|\Psi_\nu^{\nu_+,\nu_-}\right\rangle$, alongside their $\mathrm{U}(4)\times\mathrm{U}(4)$ rotations, which were shown to be exact ground states of the interaction Hamiltonian in the chiral limit [68, 69]. Working similarly in the chiral limit, our analysis is also exact. We find that $\sqrt{3}\times\sqrt{3}$ ordering *can* arise for generic intervalley-coherent $\mathrm{U}(4)\times\mathrm{U}(4)$ rotations of the states $\left|\Psi_\nu^{\nu_+,\nu_-}\right\rangle$, provided that they are not $\mathrm{U_{nc}}(4)$ rotations of the insulators $|\Psi_\nu\rangle$, defined in Eq. (B7). The latter does not however constitute the only exception. Indeed, without being exhaustive, we show that there are possible choices (to be defined in Appendix [E 3]) for the states $\left|\Psi_\nu^{\nu_+,\nu_-}\right\rangle$ (different from $|\Psi_\nu\rangle$), which, when rotated according to a certain subgroup (to be defined in Appendix [E 3]) of $\mathrm{U}(4)\times\mathrm{U}(4)$ (different from the $\mathrm{U_{nc}}(4)$ group), give rise to intervalley-coherent insulators *without* any $\sqrt{3}\times\sqrt{3}$ ordering. On the other hand, we argue that such examples are fine-tuned, as there is no *a priori* reason for restricting to these $\mathrm{U}(4)\times\mathrm{U}(4)$ subgroups (unlike the $\mathrm{U_{nc}}(4)$ group which is obtained from $\mathrm{U}(4)\times\mathrm{U}(4)$ as a result of breaking the chiral symmetry). We end the discussion with an intuitive picture explaining the presence or absence of $\sqrt{3}\times\sqrt{3}$ ordering for the *maximally spin-polarized* TBG insulators.

Finally, we investigate the effects of breaking the exact particle-hole symmetry on the absence of $\sqrt{3}\times\sqrt{3}$ symmetry-breaking in the the STM patterns of the insulators $|\Psi_\nu\rangle$, defined in Eq. (B7), together with their $\mathrm{U_{nc}}(4)$ rotations.

In the forthcoming Appendix [G], we also provide a series of numerical results illustrating the main conclusions of this appendix.

1. The spectral function of $|\Psi_\nu\rangle$ and its $\mathrm{U_{nc}}(4)$ rotations

In this section we consider the spectral function of the even-integer-filled insulators $|\Psi_\nu\rangle$ defined in Eq. (B7), and their $\mathrm{U_{nc}}(4)$ rotations. We will assume that the single-particle TBG Hamiltonian has an exact particle-hole symmetry by focusing on the case $\lambda=0$ (the $\lambda=1$ case will be discussed in detail in Appendix [E 4]).

Following the notation in Appendix [B 4], we let

$$\hat{U}=\exp\left(i\sum_{a,b}\theta^{ab}S^{ab}\right)\quad\text{and}\quad U=\exp\left(i\sum_{a,b}\theta^{ab}\left(s^{ab}\right)^T\right)\tag{E1}$$

respectively denote a nonchiral-flat rotation operator and the corresponding eight-dimensional unitary matrix U implementing it in the energy band basis. In Eq. (E1), $\theta^{ab}\in\mathbb{R}$ (for $a,b=0,x,y,z$) denote the angles parameterizing the $\mathrm{U_{nc}}(4)$ rotation, S^{ab} are the $\mathrm{U_{nc}}(4)$ generators from Eq. (A52), while s^{ab} are the corresponding matrix generators given in Eq. (A53). The TBG ground state we consider can be written as

$$|\varphi\rangle=\hat{U}\,|\Psi_\nu\rangle\,,\tag{E2}$$

where the unrotated state $|\Psi_\nu\rangle$ was defined in Eq. (B7). Note that the states of the form in Eq. (E2) form a subset of the more general states considered in Eq. (B34). In what follows, we will employ $a_{\eta,s}$ to specify which valley-spin flavors of $|\Psi_\nu\rangle$ are occupied, such that

$$a_{\eta,s}=\begin{cases}1, & \text{if the valley-spin flavor } \{\eta,s\} \text{ is filled in } |\Psi_\nu\rangle\\ 0, & \text{if the valley-spin flavor } \{\eta,s\} \text{ is empty in } |\Psi_\nu\rangle\end{cases}.\tag{E3}$$

In the notation of Eq. (B35), this implies that $\rho_{+1,\eta,s}=\rho_{-1,\eta,s}=a_{\eta,s}$. The corresponding projectors in the empty and filled bands of $|\Psi_\nu\rangle$ defined in Eqs. (B59) and (B60), respectively read as

$$\Pi=\zeta^0\tau^0s^0-\frac{1}{4}\zeta^0\otimes\sum_\eta\left(\tau^0+\eta\tau^z\right)\otimes\left[a_{\eta,\uparrow}\left(s^0+s^z\right)+a_{\eta,\downarrow}\left(s^0-s^z\right)\right]\tag{E4}$$

$$\tilde{\Pi} = \frac{1}{4}\zeta^0 \otimes \sum_{\eta} \left(\tau^0 + \eta\tau^z\right) \otimes \left[a_{\eta,\uparrow}\left(s^0 + s^z\right) + a_{\eta,\downarrow}\left(s^0 - s^z\right)\right] \tag{E5}$$

Our goal is to obtain parameterizations of the spectral function matrix elements of the insulator $|\varphi\rangle$. To do so, we note that the spectral function matrices are obtained by tracing over the spin degrees of freedom of the matrices $\Upsilon(\mathbf{k},\omega)$ and $\tilde{\Upsilon}(\mathbf{k},\omega)$, defined in Eqs. (D11) and (D12). By comparing Eqs. (D11) and (D12) with Eqs. (B61) and (B62), respectively, we find that, up to a Dirac δ-function being applied on the (non-zero) eigenvalues, the matrices $\Upsilon(\mathbf{k},\omega)$ and $\tilde{\Upsilon}(\mathbf{k},\omega)$ share identical eigenspectra with the matrices $\Pi U\left(R(\mathbf{k})\otimes s^0\right)U^\dagger\Pi$ and $\Pi U\left(\tilde{R}(\mathbf{k})\otimes s^0\right)U^\dagger\Pi$, respectively. Therefore, parameterized forms of the former can be inferred from the parameterizations of the latter. In what follows, we will focus on the electron excitations, and obtain the parameterization of $\Upsilon(\mathbf{k},\omega)$, which we then use to parameterize $\mathcal{M}^+(\omega)$. The hole contribution can be computed analogously, which allows us to discuss the spectral function of the insulator $|\varphi\rangle$.

a. *Parameterized form of* $\Upsilon(\mathbf{k},\omega)$

To obtain $\Pi U\left(R(\mathbf{k})\otimes s^0\right)U^\dagger\Pi$, we first note that Eq. (B25) implies for the $\lambda = 0$ case that

$$R(\mathbf{k})\otimes s^0 = \zeta^0\tau^0 s^0 d_2(\mathbf{k}) + \zeta^x\tau^z s^0 d_3(\mathbf{k}) + \zeta^z\tau^z s^0 d_5(\mathbf{k}), \tag{E6}$$

and, because $\zeta^0\tau^0 s^0$, $\zeta^x\tau^z s^0$, and $\zeta^z\tau^z s^0$ commute with *all* the $\mathrm{U_{nc}}(4)$ generators s^{ab} from Eq. (A53),

$$U\left(R(\mathbf{k})\otimes s^0\right)U^\dagger = R(\mathbf{k})\otimes s^0. \tag{E7}$$

We then project Eq. (E7) using the projector Π defined in Eq. (E4) to obtain

$$\begin{aligned}
&\Pi U\left(R(\mathbf{k})\otimes s^0\right)U^\dagger\Pi = \Pi\left(R(\mathbf{k})\otimes s^0\right)\Pi = \\
&\frac{1}{4}\zeta^0\tau^0 s^0\left(4 - a_{-,\downarrow} - a_{-,\uparrow} - a_{+,\downarrow} - a_{+,\uparrow}\right)d_2(\mathbf{k}) + \frac{1}{4}\zeta^0\tau^0 s^z\left(-a_{-,\downarrow} + a_{-,\uparrow} - a_{+,\downarrow} + a_{+,\uparrow}\right)d_2(\mathbf{k}) \\
+&\frac{1}{4}\zeta^0\tau^z s^0\left(-a_{-,\downarrow} - a_{-,\uparrow} + a_{+,\downarrow} + a_{+,\uparrow}\right)d_2(\mathbf{k}) + \frac{1}{4}\zeta^0\tau^z s^z\left(-a_{-,\downarrow} + a_{-,\uparrow} + a_{+,\downarrow} - a_{+,\uparrow}\right)d_2(\mathbf{k}) \\
+&\frac{1}{4}\zeta^x\tau^0 s^0\left(-a_{-,\downarrow} - a_{-,\uparrow} + a_{+,\downarrow} + a_{+,\uparrow}\right)d_3(\mathbf{k}) + \frac{1}{4}\zeta^x\tau^0 s^z\left(-a_{-,\downarrow} + a_{-,\uparrow} + a_{+,\downarrow} - a_{+,\uparrow}\right)d_3(\mathbf{k}) \\
+&\frac{1}{4}\zeta^x\tau^z s^0\left(4 - a_{-,\downarrow} - a_{-,\uparrow} - a_{+,\downarrow} - a_{+,\uparrow}\right)d_3(\mathbf{k}) + \frac{1}{4}\zeta^x\tau^z s^z\left(-a_{-,\downarrow} + a_{-,\uparrow} - a_{+,\downarrow} + a_{+,\uparrow}\right)d_3(\mathbf{k}) \\
+&\frac{1}{4}\zeta^z\tau^0 s^0\left(-a_{-,\downarrow} - a_{-,\uparrow} + a_{+,\downarrow} + a_{+,\uparrow}\right)d_5(\mathbf{k}) + \frac{1}{4}\zeta^z\tau^0 s^z\left(-a_{-,\downarrow} + a_{-,\uparrow} + a_{+,\downarrow} - a_{+,\uparrow}\right)d_5(\mathbf{k}) \\
+&\frac{1}{4}\zeta^z\tau^z s^0\left(4 - a_{-,\downarrow} - a_{-,\uparrow} - a_{+,\downarrow} - a_{+,\uparrow}\right)d_5(\mathbf{k}) + \frac{1}{4}\zeta^z\tau^z s^z\left(-a_{-,\downarrow} + a_{-,\uparrow} - a_{+,\downarrow} + a_{+,\uparrow}\right)d_5(\mathbf{k}),
\end{aligned} \tag{E8}$$

where we have employed $a_{\eta,s}^2 = a_{\eta,s}$. Using Eq. (E8), as well as the parity of the function d_i $(i = 2,3,5)$ from Eq. (B23), we can find *all* the symmetries of the matrix $\Pi U\left(R(\mathbf{k})\otimes s^0\right)U^\dagger\Pi$

$$\begin{aligned}
\left[\zeta^0\tau^0 s^z, \Pi U\left(R(\mathbf{k})\otimes s^0\right)U^\dagger\Pi\right] &= \left[\zeta^0\tau^z s^0, \Pi U\left(R(\mathbf{k})\otimes s^0\right)U^\dagger\Pi\right] = 0, \\
\left(\zeta^y\tau^0 s^0\right)\Pi U\left(R(\mathbf{k})\otimes s^0\right)U^\dagger\Pi\left(\zeta^y\tau^0 s^0\right) &= \Pi U\left(R(-\mathbf{k})\otimes s^0\right)U^\dagger\Pi.
\end{aligned} \tag{E9}$$

Because $\Pi U\left(R(\mathbf{k})\otimes s^0\right)U^\dagger\Pi$ and $\Upsilon(\mathbf{k},\omega)$ share the same eigenvectors, as can be seen from Eqs. (B61) and (D11), the symmetries of the former also represent symmetries of the latter, thus implying that

$$\begin{aligned}
\left[\zeta^0\tau^0 s^z, \Upsilon(\mathbf{k},\omega)\right] &= \left[\zeta^0\tau^z s^0, \Upsilon(\mathbf{k},\omega)\right] = 0, \\
\left(\zeta^y\tau^0 s^0\right)\Upsilon(\mathbf{k},\omega)\left(\zeta^y\tau^0 s^0\right) &= \Upsilon(-\mathbf{k},\omega).
\end{aligned} \tag{E10}$$

Additionally, since $\Pi U\left(R(\mathbf{k})\otimes s^0\right)U^\dagger\Pi$ is real, its eigenstate are real, implying that $\Upsilon(\mathbf{k},\omega)$ is also real. Moreover, from its definition in Eq. (D11), $\Upsilon(\mathbf{k},\omega)$ is manifestly Hermitian. Coupled with the symmetries from Eq. (E10), we obtain the decomposition of $\Upsilon(\mathbf{k},\omega)$ in the energy band, valley, and spin subspaces as

$$\Upsilon(\mathbf{k},\omega) = \sum_{\substack{a\in\{0,x,z\}\\ b,c\in\{0,z\}}} \zeta^a\tau^b s^c \beta_{abc}(\mathbf{k},\omega), \tag{E11}$$

where $\beta_{abc}(\mathbf{k},\omega)$ are real functions whose parity with respect to momentum inversion is given by

$$\beta_{abc}(\mathbf{k},\omega)=\begin{cases}\beta_{abc}(-\mathbf{k},\omega), & \text{if } a=0\\ -\beta_{abc}(-\mathbf{k},\omega), & \text{if } a=x,z\end{cases}, \quad \text{for} \quad a\in\{0,x,z\} \text{ and } b,c\in\{0,z\}, \tag{E12}$$

and which only depend on the occupation of the valley-spin flavors $a_{\eta,s}$ defined in Eq. (E3), but *not* on the $\hat{U}$ rotation.

b. *Parameterized form of* $\mathcal{M}^{+}_{\varphi}(\omega)$

As shown in Eq. (D9), to obtain the electron spectral function matrix from Eq. (E12), we need to perform one final $\mathrm{U_{nc}}(4)$ transformation on $\Upsilon(\mathbf{k},\omega)$, which results in

$$Y(\mathbf{k},\omega)=U^{\dagger}\Upsilon(\mathbf{k},\omega)U=\zeta^{0}\tau^{0}s^{0}\beta_{000}(\mathbf{k},\omega)+\zeta^{x}\tau^{z}s^{0}\beta_{xz0}(\mathbf{k},\omega)+\zeta^{z}\tau^{z}s^{0}\beta_{zz0}(\mathbf{k},\omega)+\sum_{j=1}^{3}N^{j}\beta_{j}(\mathbf{k},\omega), \tag{E13}$$

where $\beta_{i}(\mathbf{k},\omega)$ are real functions $(i=1,2,3)$ obeying

$$\beta_{1}(\mathbf{k},\omega)=\beta_{1}(-\mathbf{k},\omega), \quad \beta_{2}(\mathbf{k},\omega)=-\beta_{2}(-\mathbf{k},\omega), \quad \beta_{3}(\mathbf{k},\omega)=-\beta_{3}(-\mathbf{k},\omega), \tag{E14}$$

but which we otherwise leave unspecified. In Eq. (E13), we have also introduced the matrices N^{i} for $i=1,2,3$, which depend on the specific $\mathrm{U_{nc}}(4)$ rotation $\hat{U}$ and belong to the sets $N^{i}\in\mathcal{N}^{i}$, with

$$\begin{aligned}
&\mathcal{N}^{1}=\mathcal{N}_{\mathrm{U_{nc}}(4)},\\
&\mathcal{N}^{2}=\left\{\sum_{a,b\in\{0,x,y,z\}}\phi^{ab}t^{ab}\;\middle|\;\phi^{ab}\in\mathbb{C},\phi^{00}=0,t^{0b}=\zeta^{x}\tau^{z}s^{b},t^{xb}=\zeta^{z}\tau^{x}s^{b},t^{yb}=\zeta^{z}\tau^{y}s^{b},t^{zb}=\zeta^{x}\tau^{0}s^{b}\right\},\\
&\mathcal{N}^{3}=\left\{\sum_{a,b\in\{0,x,y,z\}}\phi^{ab}t^{ab}\;\middle|\;\phi^{ab}\in\mathbb{C},\phi^{00}=0,t^{0b}=\zeta^{z}\tau^{z}s^{b},t^{xb}=\zeta^{x}\tau^{x}s^{b},t^{yb}=\zeta^{x}\tau^{y}s^{b},t^{zb}=\zeta^{z}\tau^{0}s^{b}\right\},
\end{aligned} \tag{E15}$$

where $\mathcal{N}_{\mathrm{U_{nc}}(4)}$ was defined in Eq. (A54). To see how Eq. (E13) was obtained from Eq. (E11), we start by observing that the sets from Eq. (E15) share one important property: they form invariant spaces under the $\mathrm{U_{nc}}(4)$ group. This can be seen by remarking that for any matrix $T\in\mathcal{N}^{i}$, $\left[T,s^{ab}\right]\in\mathcal{N}^{i}$, and so, from Eq. (E1), $U^{\dagger}TU\in\mathcal{N}^{i}$, for any $i=1,2,3$. We then group all the matrices in the expansion from Eq. (E11) according to how they transform under a $\mathrm{U_{nc}}(4)$ rotation. The first three terms of Eq. (E13) are obtained by noting that the matrices $\zeta^{0}\tau^{0}s^{0}$, $\zeta^{x}\tau^{z}s^{0}$, $\zeta^{z}\tau^{z}s^{0}$ are invariant under any transformation U, as they commute with all the nonchrial-flat $\mathrm{U_{nc}}(4)$ generators s^{ab}. The other matrices from Eq. (E11) can be grouped as follows

$$\begin{aligned}
&\zeta^{0}\tau^{0}s^{z},\zeta^{0}\tau^{z}s^{0},\zeta^{0}\tau^{z}s^{z}\in\mathcal{N}^{1},\\
&\zeta^{x}\tau^{0}s^{0},\zeta^{x}\tau^{x}s^{z},\zeta^{x}\tau^{z}s^{z}\in\mathcal{N}^{2},\\
&\zeta^{z}\tau^{0}s^{0},\zeta^{z}\tau^{0}s^{z},\zeta^{z}\tau^{z}s^{z}\in\mathcal{N}^{3}.
\end{aligned} \tag{E16}$$

Within each one of the three groups, the parity with respect to momentum inversion of the real functions $\beta_{abc}(\mathbf{k},\omega)$ multiplying each matrix is the same, thus leading to the expansion from Eq. (E13).

The parameterization of the electron spectral function matrix is obtained from Eq. (E13), by employing Eq. (D9)

$$\left[\mathcal{M}^{+}_{\varphi}(\omega)\right]_{\mathbf{k}n\eta,\mathbf{k}'n'\eta'}=\delta_{\mathbf{k},\mathbf{k}'}\left[\zeta^{0}\tau^{0}\beta_{000}(\mathbf{k},\omega)+\zeta^{x}\tau^{z}\beta_{xz0}(\mathbf{k},\omega)+\zeta^{z}\tau^{z}\beta_{zz0}(\mathbf{k},\omega)+\sum_{j=1}^{3}\left(\mathrm{tr}_{s}\,N^{j}\right)\beta_{j}(\mathbf{k},\omega)\right]_{n\eta,n'\eta'}, \tag{E17}$$

where tr_{s} denotes the trace over the spin degrees of freedom, and the spin-traced matrices obey

$$\begin{aligned}
&\mathrm{tr}_{s}\,N^{1}\in\left\{\,\phi_{x}\zeta^{y}\tau^{x}+\phi_{y}\zeta^{y}\tau^{y}+\phi_{z}\zeta^{0}\tau^{z}\;\middle|\;\phi_{x},\phi_{y},\phi_{z}\in\mathbb{C}\,\right\},\\
&\mathrm{tr}_{s}\,N^{2}\in\left\{\,\phi_{x}\zeta^{z}\tau^{x}+\phi_{y}\zeta^{z}\tau^{y}+\phi_{z}\zeta^{x}\tau^{0}\;\middle|\;\phi_{x},\phi_{y},\phi_{z}\in\mathbb{C}\,\right\},\\
&\mathrm{tr}_{s}\,N^{3}\in\left\{\,\phi_{x}\zeta^{x}\tau^{x}+\phi_{y}\zeta^{x}\tau^{y}+\phi_{z}\zeta^{z}\tau^{0}\;\middle|\;\phi_{x},\phi_{y},\phi_{z}\in\mathbb{C}\,\right\}.
\end{aligned} \tag{E18}$$

c. Parameterized form of $\mathcal{M}_{\varphi}^{S\pm}$

As seen in Eq. (E17), for general non-chiral flat $\mathrm{U_{nc}}(4)$ rotations, $\mathcal{M}_{\varphi}^{+}(\omega)$ contains off-diagonal elements in the valley subspace. Following the discussion surrounding Eq. (C54), one might conclude that this signals the presence of $\sqrt{3}\times\sqrt{3}$ ordering at the level of the SLG lattice. In fact, introducing intervalley coherence by means of a $\mathrm{U_{nc}}(4)$ rotation in the ground state $|\varphi\rangle$ results to intervalley-coherent charge-one excitations, according to the discussion from Appendix [B 4]. In turn, intervalley-coherent charge-one excitations lead to scattering between the two K points of the SLG Brillouin Zone and generically give rise to $\sqrt{3}\times\sqrt{3}$ ordering at the level of the SLG lattice [78, 101, 102].

However, the above reasoning neglects the discrete symmetries of TBG, which impose several restrictions on both the spatial factor and the spectral function matrices. It was shown in Appendix [C 2 b] that owing to the time-reversal symmetry of $\hat{H}_0$, the components of $[\mathcal{M}^{\pm}(\omega)]_{\mathbf{k}n\eta,\mathbf{k}n'\eta'}$ which are anti-symmetric with respect to the transformation $[\mathbf{k}n\eta,\mathbf{k}n'\eta']\to[-\mathbf{k}n'(-\eta'),-\mathbf{k}n(-\eta)]$ vanish upon contracting with the spatial factor tensor. Following Eq. (C36), we find that instead of studying $\mathcal{M}_{\varphi}^{\pm}(\omega)$ directly, one should instead focus on the symmetrized tensors $\mathcal{M}_{\varphi}^{S\pm}(\omega)$ defined in Eq. (C37).

To compute $\mathcal{M}_{\varphi}^{S+}$, we first note that in Eq. (E17),

$$\begin{aligned}
\left[\zeta^0\tau^0\right]_{n\eta,n'\eta'} &= \left[\zeta^0\tau^0\right]_{n'(-\eta'),n(-\eta)}, & \left[\mathrm{tr}_s\, N^1\right]_{n\eta,n'\eta'} &= -\left[\mathrm{tr}_s\, N^1\right]_{n'(-\eta'),n(-\eta)},\\
\left[\zeta^x\tau^z\right]_{n\eta,n'\eta'} &= -\left[\zeta^x\tau^z\right]_{n'(-\eta'),n(-\eta)}, & \left[\mathrm{tr}_s\, N^2\right]_{n\eta,n'\eta'} &= \left[\mathrm{tr}_s\, N^2\right]_{n'(-\eta'),n(-\eta)},\\
\left[\zeta^z\tau^z\right]_{n\eta,n'\eta'} &= -\left[\zeta^z\tau^z\right]_{n'(-\eta'),n(-\eta)}, & \left[\mathrm{tr}_s\, N^3\right]_{n\eta,n'\eta'} &= \left[\mathrm{tr}_s\, N^3\right]_{n'(-\eta'),n(-\eta)},
\end{aligned} \tag{E19}$$

which coupled with Eqs. (C37), (E12) and (E14) leads to

$$\left[\mathcal{M}_{\varphi}^{S+}(\omega)\right]_{\mathbf{k}n\eta,\mathbf{k}n'\eta'} = \delta_{\mathbf{k},\mathbf{k}'}\left[\zeta^0\tau^0\beta_{000}(\mathbf{k},\omega)+\zeta^x\tau^z\beta_{xz0}(\mathbf{k},\omega)+\zeta^z\tau^z\beta_{zz0}(\mathbf{k},\omega)\right]_{n\eta,n'\eta'}. \tag{E20}$$

In an analogous fashion, it can be shown that the hole contribution to the spectral function matrix elements is

$$\left[\mathcal{M}_{\varphi}^{S-}(\omega)\right]_{\mathbf{k}n\eta,\mathbf{k}n'\eta'} = \delta_{\mathbf{k},\mathbf{k}'}\left[\zeta^0\tau^0\tilde{\beta}_{000}(\mathbf{k},\omega)+\zeta^x\tau^z\tilde{\beta}_{xz0}(\mathbf{k},\omega)+\zeta^z\tau^z\tilde{\beta}_{zz0}(\mathbf{k},\omega)\right]_{n\eta,n'\eta'}, \tag{E21}$$

where the real functions $\tilde{\beta}_{abc}(\mathbf{k},\omega)$ have the same parity as the functions $\beta_{abc}(\mathbf{k},\omega)$ (for $abc=000,xz0,zz0$) with respect to momentum inversion and, similarly, only depend on the occupation of the valley-spin flavors, $a_{\eta,s}$, but *not* on the exact $\mathrm{U_{nc}}(4)$ rotation.

The parameterizations in Eqs. (E20) and (E21) imply that the spectral function matrices are diagonal in the valley-subspace. As a result of this and of Eq. (C36), for the insulators $|\Psi_\nu\rangle$ defined in Eq. (B7), and their $\mathrm{U_{nc}}(4)$ rotations, there is no $\sqrt{3}\times\sqrt{3}$ ordering, *despite* the possible presence of intervalley coherence. Equally surprising is the fact that the spectral function of the insulators of the form $\hat{U}|\Psi_\nu\rangle$ is *independent* on the particular $\mathrm{U_{nc}}(4)$ rotation considered.

The counter-intuitive absence of $\sqrt{3}\times\sqrt{3}$ ordering even in the presence of intervalley coherence in *any* $\mathrm{U_{nc}}(4)$ rotation of the states $|\Psi_\nu\rangle$ warrants a more careful explanation. At the level of the spatial factor, the presence of T symmetry imposes Eq. (C35), which requires that we consider only the symmetrized spectral function matrices defined Eq. (C37). For the spectral function matrices themselves, the vanishing of the valley-off-diagonal terms in the parameterizations from Eqs. (E20) and (E21) *even* in the case of valley-coherent insulators $\hat{U}|\Psi_\nu\rangle$ relies on three main peculiarities of this specific ground state and the TBG Hamiltonian:

1. Occupying *both* Chern bands in each of the filled spin-valley sector of the unrotated state $|\Psi_\nu\rangle$.

2. Restricting to the non-chiral flat $\mathrm{U_{nc}}(4)$ rotations of the $|\Psi_\nu\rangle$ state, as opposed to the more general $\mathrm{U}(4)\times\mathrm{U}(4)$ rotations.

3. The presence of C_{2z}, T, and P symmetries of the TBG single-particle Hamiltonian which constrain the forms of the charge-one excitation matrices, as derived in Eqs. (B25) and (B26). In turn, the parameterizations of the charge-one excitation matrices directly determine the parameterization of the spectral function matrices.

In Appendix [E 2], we will investigate the effects of relaxing the first two assumptions in the first chiral-flat limit [74, 86]. Additionally, in Appendix [E 4] we will relax the third assumption and explore the spectral function of $|\Psi_\nu\rangle$ as defined in Eq. (B7) and some of its $\mathrm{U_{nc}}(4)$ rotations using the full-fledged TBG interaction Hamiltonian away from the first chiral-flat limit and without assuming *exact* particle-hole symmetry (*i.e.* focusing on the $\lambda=1$ case).

2. The spectral function of $\left|\Psi_{\nu}^{\nu_+,\nu_-}\right\rangle$ and its $\mathrm{U}(4)\times\mathrm{U}(4)$ rotations

In Appendix [E 1], we discussed the spectral function of the integer-filled states $|\Psi_\nu\rangle$ and their nonchiral-flat $\mathrm{U}_{\mathrm{nc}}(4)$ rotations. The corresponding spectral function is independent on the $\mathrm{U}_{\mathrm{nc}}(4)$ rotation in question and no $\sqrt{3}\times\sqrt{3}$ ordering emerges at the level of the SLG lattice, even in the presence of intervalley coherence. To better understand the reasons behind the *exact* cancellation from Appendix [E 1] leading to the absence of $\sqrt{3}\times\sqrt{3}$ ordering, we here derive the minimal set of conditions necessary (but not sufficient) for the *emergence* of $\sqrt{3}\times\sqrt{3}$ ordering in the STM signal in a given TBG insulator.

For simplicity, we will focus on the chiral limit [74, 86]. This is because any $\sqrt{3}\times\sqrt{3}$ ordering emerging in the chiral limit for a given TBG insulator will necessarily persist when the chiral symmetry is broken. In other words, the absence of $\sqrt{3}\times\sqrt{3}$ ordering for a given insulator is reliant on the *presence* rather than the *absence* of certain symmetries, so breaking chiral symmetry in itself cannot remove the $\sqrt{3}\times\sqrt{3}$ ordering. On the other hand, as shown in Eqs. (B28) and (B29), in the chiral limit, the charge-one excitation matrices are proportional to identity, which vastly simplifies all algebraic manipulations.

We consider the general ground state $|\varphi\rangle$ defined in Eq. (B34) for a generic $\mathrm{U}(4)\times\mathrm{U}(4)$ rotation $\hat{U}$, where

$$\hat{U}=\exp\left(i\sum_{a,b}\theta_{+}^{ab}S_{+}^{ab}+\theta_{-}^{ab}S_{-}^{ab}\right)\quad\text{and}\quad U=\exp\left(i\sum_{a,b}\theta_{+}^{ab}\left(s_{+}^{ab}\right)^{T}+\theta_{-}^{ab}\left(s_{-}^{ab}\right)^{T}\right)\tag{E22}$$

respectively denote the rotation operator and the corresponding eight-dimensional unitary matrix U implementing it in the energy band basis. In Eq. (E22), $\theta_{\pm}^{ab}\in\mathbb{R}$ (for $a,b=0,x,y,z$) denote the angles parameterizing the $\mathrm{U}(4)\times\mathrm{U}(4)$ rotation, while $S_{\pm}^{ab}$ and $s_{\pm}^{ab}$ are the corresponding generators in the operator and matrix form, as given in Eqs. (A55) and (A56), respectively. In order to specify the filled Chern-band, valley, and spin flavors in the unrotated ground state $\left|\Psi_{\nu}^{\nu_+,\nu_-}\right\rangle$, we will find it useful to define

$$a_{\eta,s}=\frac{1}{2}\sum_{e_Y}\rho_{e_Y,\eta,s},\qquad b_{\eta,s}=\frac{1}{2}\sum_{e_Y}e_Y\rho_{e_Y,\eta,s},\tag{E23}$$

where $\rho_{e_Y,\eta,s}=1,0$ was introduced in Eq. (B35). In Eq. (E23), $a_{\eta,s}$ specifies whether the valley-spin flavor $\{\eta,s\}$ has zero ($a_{\eta,s}=0$), one ($a_{\eta,s}=1/2$), or two ($a_{\eta,s}=1$) filled Chern bands in $\left|\Psi_{\nu}^{\nu_+,\nu_-}\right\rangle$. In addition, $2b_{\eta,s}=-1,0,1$ denotes the total Chern number of the occupied bands in the valley-spin flavor $\{\eta,s\}$. As an example, the insulator $\left|\Psi_{-1}^{1,2}\right\rangle=\prod_{\mathbf{k}}\left(\hat{d}_{\mathbf{k},-1,-,\uparrow}^{\dagger}\hat{d}_{\mathbf{k},+1,-,\uparrow}^{\dagger}\hat{d}_{\mathbf{k},-1,-,\downarrow}^{\dagger}\right)|0\rangle$ (also depicted in Fig. 6 of Appendix [B 4]) corresponds to $a_{-,\uparrow}=1$, $a_{-,\downarrow}=1/2$, $a_{+,\uparrow/\downarrow}=0$, and $b_{-,\downarrow}=-1/2$, $b_{-,\uparrow}=b_{+,\uparrow/\downarrow}=0$. This notation is consistent with the one introduced in Eq. (E3): the states considered in Appendix [E 2] correspond to $a_{\eta,s}=0,1$ and $b_{\eta,s}=0$.

a. *Parameterized forms of* $\Upsilon(\mathbf{k},\omega)$ *and* $\tilde{\Upsilon}(\mathbf{k},\omega)$

We are interested in obtaining parameterizatizations of the spectral function matrices $\mathcal{M}_{\varphi}^{\pm}(\omega)$. Focusing on the electron contribution, $\mathcal{M}_{\varphi}^{+}(\omega)$ can be written in terms of the matrix $\Upsilon(\mathbf{k},\omega)$ introduced in Eq. (D9), according to Eq. (D11). In turn, we have argued in Appendix [E 1] that $\Upsilon(\mathbf{k},\omega)$ shares identical eigenvectors with the matrix $\Pi U\left(R(\mathbf{k})\otimes s^{0}\right)U^{\dagger}\Pi$, as can be seen by comparing Eqs. (B61) and (D11). However, in the first chiral limit, the charge-one excitation matrices are proportional to identity, implying from Eq. (B28) that the electron excitations are degenerate, having energies given by $E_{\mathbf{k}}^{p}=d_2(\mathbf{k})$, for any $1\leq p\leq 4-\nu$, which allows us derive an even stronger relation

$$\Upsilon(\mathbf{k},\omega)=\frac{\delta\left[\omega-d_2(\mathbf{k})\right]}{d_2(\mathbf{k})}\Pi U\left(R(\mathbf{k})\otimes s^{0}\right)U^{\dagger}\Pi=\Pi\beta(\mathbf{k},\omega),\tag{E24}$$

where $\beta(\mathbf{k},\omega)=\delta\left[\omega-d_2(\mathbf{k})\right]$ is a real function which is even with respect to momentum inversion. In the last equality of Eq. (E24), we have used the fact that $R(\mathbf{k})\otimes s^{0}$ is proportional to the identity matrix and that the projector Π is idempotent (*i.e.* $\Pi^2=\Pi$). A similar relation can be written for hole contribution

$$\tilde{\Upsilon}(\mathbf{k},\omega)=\frac{\delta\left[\omega-\tilde{d}_2(\mathbf{k})\right]}{\tilde{d}_2(\mathbf{k})}\tilde{\Pi}U\left(\tilde{R}(\mathbf{k})\otimes s^{0}\right)U^{\dagger}\tilde{\Pi}=\tilde{\Pi}\tilde{\beta}(\mathbf{k},\omega),\tag{E25}$$

where $\tilde{\beta}(\mathbf{k},\omega)=\delta\left[\omega-\tilde{d}_2(\mathbf{k})\right]$ is also a real function which is even with respect to momentum inversion.

Using the notation in Eq. (E23), we find that the two projector matrices are given by

$$\begin{aligned}\Pi=&\frac{1}{4}\zeta^0\tau^0 s^0\left(4-a_{-,\downarrow}-a_{-,\uparrow}-a_{+,\downarrow}-a_{+,\uparrow}\right)+\frac{1}{4}\zeta^0\tau^0 s^z\left(a_{-,\downarrow}-a_{-,\uparrow}+a_{+,\downarrow}-a_{+,\uparrow}\right)\\&+\frac{1}{4}\zeta^0\tau^z s^0\left(a_{-,\downarrow}+a_{-,\uparrow}-a_{+,\downarrow}-a_{+,\uparrow}\right)+\frac{1}{4}\zeta^0\tau^z s^z\left(-a_{-,\downarrow}+a_{-,\uparrow}+a_{+,\downarrow}-a_{+,\uparrow}\right)\\&+\frac{1}{4}\zeta^y\tau^0 s^0\left(b_{-,\downarrow}+b_{-,\uparrow}+b_{+,\downarrow}+b_{+,\uparrow}\right)+\frac{1}{4}\zeta^y\tau^0 s^z\left(-b_{-,\downarrow}+b_{-,\uparrow}-b_{+,\downarrow}+b_{+,\uparrow}\right)\\&+\frac{1}{4}\zeta^y\tau^z s^0\left(-b_{-,\downarrow}-b_{-,\uparrow}+b_{+,\downarrow}+b_{+,\uparrow}\right)+\frac{1}{4}\zeta^y\tau^z s^z\left(b_{-,\downarrow}-b_{-,\uparrow}-b_{+,\downarrow}+b_{+,\uparrow}\right),\end{aligned}\tag{E26}$$

$$\tilde{\Pi}=\zeta^0\tau^0 s^0-\Pi,\tag{E27}$$

or, equivalently, in index notation by

$$\Pi_{n\eta s,n'\eta's'}=\delta_{\eta,\eta'}\delta_{s,s'}\left\{\left[\zeta^0\right]_{nn'}\left(1-a_{\eta,s}\right)-\left[\zeta^y\right]_{nn'}b_{\eta,s}\right\},\tag{E28}$$

$$\tilde{\Pi}_{n\eta s,n'\eta's'}=\delta_{\eta,\eta'}\delta_{s,s'}\left\{\left[\zeta^0\right]_{nn'}a_{\eta,s}+\left[\zeta^y\right]_{nn'}b_{\eta,s}\right\}.\tag{E29}$$

b. *Parameterized form of* $\mathcal{M}_\varphi^{S\pm}$

To obtain the spectral function matrices, we perform one additional $\mathrm{U}(4)\times\mathrm{U}(4)$ rotation on Eqs. (E24) and (E25), which affords

$$Y(\mathbf{k},\omega)=U^\dagger\Upsilon(\mathbf{k},\omega)U=\beta(\mathbf{k},\omega)U^\dagger\Pi U=\beta(\mathbf{k},\omega)\left[\frac{1}{4}\zeta^0\tau^0 s^0\left(4-\sum_{\eta,s}a_{\eta,s}\right)+\frac{1}{4}\zeta^y\tau^0 s^0\left(\sum_{\eta,s}b_{\eta,s}\right)+N\right],\tag{E30}$$

$$\tilde{Y}(\mathbf{k},\omega)=U^\dagger\tilde{\Upsilon}(\mathbf{k},\omega)U=\tilde{\beta}(\mathbf{k},\omega)U^\dagger\tilde{\Pi}U=\tilde{\beta}(\mathbf{k},\omega)\left[\frac{1}{4}\zeta^0\tau^0 s^0\left(\sum_{\eta,s}a_{\eta,s}\right)-\frac{1}{4}\zeta^y\tau^0 s^0\left(\sum_{\eta,s}b_{\eta,s}\right)+\tilde{N}\right],\tag{E31}$$

where the matrices N and $\tilde{N}$ depend on the exact rotation $\hat{U}$, as well as on the parameters $a_{\eta,s}$ and $b_{\eta,s}$. In what follows, we will work out the parameterization of N and $\tilde{N}$ in different cases and derive properties of the corresponding spectral function matrices.

Eqs. (E30) and (E31) were derived in analogy with Eq. (E13). Focusing on the electron contribution (the hole contribution follows in exactly the same manner), the matrices $\zeta^0\tau^0 s^0$ and $\zeta^y\tau^0 s^0$ commute with all the generators of the $\mathrm{U}(4)\times\mathrm{U}(4)$ group from Eq. (A56): the corresponding terms in the expansion in Eq. (E26) remain invariant under the transformation U. The remaining matrices in the expansion of Π are *not* invariant under general $\mathrm{U}(4)\times\mathrm{U}(4)$ transformations, but belong to the set $\mathcal{N}_{\mathrm{U}(4)\times\mathrm{U}(4)}$ defined in Eq. (A57). Since $\mathcal{N}_{\mathrm{U}(4)\times\mathrm{U}(4)}$ *is* invariant (as a set) under $\mathrm{U}(4)\times\mathrm{U}(4)$ rotations (*i.e.* for any $T\in\mathcal{N}_{\mathrm{U}(4)\times\mathrm{U}(4)}$, $U^\dagger TU\in\mathcal{N}_{\mathrm{U}(4)\times\mathrm{U}(4)}$), it follows that $N,\tilde{N}\in\mathcal{N}_{\mathrm{U}(4)\times\mathrm{U}(4)}$.

Remembering that the functions $\beta(\mathbf{k},\omega)$ and $\tilde{\beta}(\mathbf{k},\omega)$ are even with respect to momentum inversion, we can derive the parameterized form of the symmetrized spectral function from Eqs. (C37), (E30) and (E31)

$$\left[\mathcal{M}_\varphi^{S+}(\omega)\right]_{\mathbf{k}n\eta,\mathbf{k}n'\eta'}=\delta_{\mathbf{k},\mathbf{k}'}\frac{1}{2}\left(\frac{4-\nu}{2}\delta_{n,n'}\delta_{\eta,\eta'}+\left[\mathrm{tr}_s\,N\right]_{n\eta,n'\eta'}+\left[\mathrm{tr}_s\,N\right]_{n'(-\eta'),n(-\eta)}\right)\beta(\mathbf{k},\omega),\tag{E32}$$

$$\left[\mathcal{M}_\varphi^{S-}(\omega)\right]_{\mathbf{k}n\eta,\mathbf{k}n'\eta'}=\delta_{\mathbf{k},\mathbf{k}'}\frac{1}{2}\left(\frac{4+\nu}{2}\delta_{n,n'}\delta_{\eta,\eta'}+\left[\mathrm{tr}_s\,\tilde{N}\right]_{n\eta,n'\eta'}+\left[\mathrm{tr}_s\,\tilde{N}\right]_{n'(-\eta'),n(-\eta)}\right)\tilde{\beta}(\mathbf{k},\omega),\tag{E33}$$

where, as in Eq. (E17), tr_s denotes the trace over the spin degree of freedom. Depending on the rotation $\hat{U}$ and the parameters $a_{\eta,s}$ and $b_{\eta,s}$, more restrictive statements can be made about the matrices N and $\tilde{N}$. Without being exhaustive, we can identify two distinct cases with particular relevance to the existence of $\sqrt{3}\times\sqrt{3}$ ordering:

1. $\hat{U}\in\mathrm{U}_{\mathrm{nc}}(4)$ and $b_{\eta,s}=0$ for all $\eta=\pm$ and $s=\uparrow,\downarrow$, where $\mathrm{U}_{\mathrm{nc}}(4)$ denotes the nonchiral-flat subgroup of $\mathrm{U}(4)\times\mathrm{U}(4)$ whose generators are given in Eq. (A52).

   If all $b_{\eta,s}$ are zero, then all matrices from Eqs. (E26) and (E27) which are not proportional to $\zeta^0\tau^0 s^0$ or $\zeta^y\tau^0 s^0$ belong to the set $\mathcal{N}_{\mathrm{U}_{\mathrm{nc}}(4)}$, defined in Eq. (A54). Because $\mathcal{N}_{\mathrm{U}_{\mathrm{nc}}(4)}$ (as a set) is invariant under any $\mathrm{U}_{\mathrm{nc}}(4)$

rotations, it follows that $N, \tilde{N} \in \mathcal{N}_{\mathrm{U_{nc}}(4)}$, implying that $\mathrm{tr}_s\, N, \mathrm{tr}_s\, \tilde{N} \in \mathrm{tr}_s\, \mathcal{N}_{\mathrm{U_{nc}}(4)}$, where

$$\mathrm{tr}_s\, \mathcal{N}_{\mathrm{U_{nc}}(4)} = \left\{ \sum_{i=1}^{3} \phi_i t_i \;\middle|\; \phi_i \in \mathbb{C}, t_1 = \zeta^y \tau^x, t_2 = \zeta^y \tau^y, t_3 = \zeta^0 \tau^z \right\}. \tag{E34}$$

In this case, one obtains that

$$[\mathrm{tr}_s\, N]_{n\eta,n'\eta'} + [\mathrm{tr}_s\, N]_{n'(-\eta'),n(-\eta)} = \left[\mathrm{tr}_s\, \tilde{N}\right]_{n\eta,n'\eta'} + \left[\mathrm{tr}_s\, \tilde{N}\right]_{n'(-\eta'),n(-\eta)} = 0, \tag{E35}$$

which implies from Eqs. (E32) and (E33) that the spectral function matrices are diagonal in the valley and band indices and independent on the rotation $\hat{U}$. Therefore, no $\sqrt{3} \times \sqrt{3}$ ordering emerges in this case and the corresponding spectral functions are independent on the particular rotation $\hat{U}$. This result can also be seen as a consequence of the general case away from the chiral limit, derived in Appendix [E 1].

2. Generic $\hat{U} \in [\mathrm{U}(4) \times \mathrm{U}(4)] \setminus \mathrm{U_{nc}}(4)$ rotations and/or $b_{\eta,s} \neq 0$ for some η and s.

   For any choices of $|\varphi\rangle$, which do not otherwise belong to Case 1, we have $N, \tilde{N} \in \mathcal{N}_{\mathrm{U}(4)\times\mathrm{U}(4)}$. Therefore, we find that $\mathrm{tr}_s\, N, \mathrm{tr}_s\, \tilde{N} \in \mathrm{tr}_s\, \mathcal{N}_{\mathrm{U}(4)\times\mathrm{U}(4)}$, where

$$\mathrm{tr}_s\, \mathcal{N}_{\mathrm{U}(4)\times\mathrm{U}(4)} = \left\{ \sum_{i=1}^{7} \phi_i t_i \;\middle|\; \phi_i \in \mathbb{C}, t_1 = \zeta^y \tau^x, t_2 = \zeta^y \tau^y, t_3 = \zeta^0 \tau^z, t_4 = \zeta^y \tau^0, t_5 = \zeta^0 \tau^x, t_6 = \zeta^0 \tau^y, t_7 = \zeta^y \tau^z \right\}, \tag{E36}$$

   implying that for generic rotations $\hat{U}$ we expect to have

$$[\mathrm{tr}_s\, N]_{n\eta,n'\eta'} + [\mathrm{tr}_s\, N]_{n'(-\eta'),n(-\eta)} \neq 0 \quad \text{and} \quad \left[\mathrm{tr}_s\, \tilde{N}\right]_{n\eta,n'\eta'} + \left[\mathrm{tr}_s\, \tilde{N}\right]_{n'(-\eta'),n(-\eta)} \neq 0. \tag{E37}$$

   A simple example illustrating this case corresponds to an intervalley-coherent $\mathcal{C} = 1$ insulator at $\nu = -3$

$$|\varphi\rangle = \prod_{\mathbf{k}} \left(\hat{d}^\dagger_{\mathbf{k},+1,+,\uparrow} \cos\alpha - \hat{d}^\dagger_{\mathbf{k},+1,-,\uparrow} \sin\alpha \right) |0\rangle\,, \tag{E38}$$

   which can be obtained by setting $\theta^{y0}_{+} = \alpha$ and all other angles $\theta^{ab}_{\pm} = 0$ in Eq. (E22), as well as $b_{+,\uparrow} = a_{+,\uparrow} = 1/2$ and all other $b_{\eta,s} = a_{\eta,s} = 0$. From Eqs. (E30) and (E31), we find that

$$\begin{aligned} \frac{1}{2}\left([\mathrm{tr}_s\, N]_{n\eta,n'\eta'} + [\mathrm{tr}_s\, N]_{n'(-\eta'),n(-\eta)} \right) &= \frac{1}{4}\left[\left(\zeta^0\tau^x\right) \sin 2\alpha + \left(\zeta^y\tau^z\right) \cos 2\alpha \right]_{n\eta,n'\eta'} \\ \frac{1}{2}\left(\left[\mathrm{tr}_s\, \tilde{N}\right]_{n\eta,n'\eta'} + \left[\mathrm{tr}_s\, \tilde{N}\right]_{n'(-\eta'),n(-\eta)} \right) &= -\frac{1}{4}\left[\left(\zeta^0\tau^x\right) \sin 2\alpha + \left(\zeta^y\tau^z\right) \cos 2\alpha \right]_{n\eta,n'\eta'} \end{aligned} \tag{E39}$$

   which manifestly obeys Eq. (E37).

   In this case, the symmetrized spectral function matrices from Eqs. (E32) and (E33) *can* generically have non-vanishing off-diagonal valley components (as can be seen in the above example for general values of α), leading to the emergence of $\sqrt{3} \times \sqrt{3}$ ordering in the corresponding STM patterns. This does *not* however imply that for any intervalley-coherent insulator not contained in Case 1, $\sqrt{3} \times \sqrt{3}$ ordering emerges, but rather that there is no symmetry precluding it. In the following Appendix [E 3], we present one additional example of intervalley-coherent insulators *without* $\sqrt{3} \times \sqrt{3}$ ordering, which do not belong to Case 1.

The analysis from this section complements the conclusions of Appendix [E 1]: for an intervalley-coherent $\mathrm{U}(4) \times \mathrm{U}(4)$ rotation of the state $\left|\Psi_\nu^{\nu_+,\nu_-}\right\rangle$ defined in Eq. (B8), which is not part of the set of insulators discussed in Appendix [E 1], an $\sqrt{3} \times \sqrt{3}$ pattern *can* generically arise in the STM signal. Moreover, as $\sqrt{3} \times \sqrt{3}$ ordering is a symmetry-breaking effect, we expect the conditions for its emergence to hold even as we move away from the chiral limit (*i.e.* the vanishing of $\sqrt{3} \times \sqrt{3}$ ordering relies on the *presence* rather than the *absence* of certain symmetries).

On the other hand, the insulators discussed in Appendix [E 1] are *not* the only example of intervalley-coherent insulators $|\varphi\rangle$ of the form in Eq. (B34) without $\sqrt{3} \times \sqrt{3}$ symmetry-breaking. Far from being exhaustive, in Appendix [E 3], we will show by direct construction that a different submanifold of intervalley-coherent TBG ground states without $\sqrt{3} \times \sqrt{3}$ ordering exists. While deriving all the necessary *and sufficient* conditions for the emergence of $\sqrt{3} \times \sqrt{3}$ symmetry-breaking is beyond the scope of this work, we will nevertheless build a complete picture describing the presence or absence of $\sqrt{3} \times \sqrt{3}$ ordering in the case of *maximally spin-polarized* TBG ground states of the form in Eq. (B34).

3. Additional examples of intervalley-coherent ground states without $\sqrt{3}\times\sqrt{3}$ ordering

In Appendix [E 2], we argued that an intervalley-coherent $\mathrm{U}(4)\times\mathrm{U}(4)$ rotation of the state $\left|\Psi_{\nu}^{\nu_+,\nu_-}\right\rangle$ defined in Eq. (B8) does *generically* show $\sqrt{3}\times\sqrt{3}$ ordering, unless the rotation is part of the $\mathrm{U}_{\mathrm{nc}}(4)$ group, and the state $\left|\Psi_{\nu}^{\nu_+,\nu_-}\right\rangle$ has only fully-filled and fully-empty valley-spin flavors. In this section, we construct a different submanifold of TBG ground states of the form in Eq. (B34) that are intervalley-coherent, but do not exhibit $\sqrt{3}\times\sqrt{3}$ symmetry breaking. Coupled with the analysis in Appendix [E 1], this will enable us discuss the $\sqrt{3}\times\sqrt{3}$ symmetry-breaking in the *maximally spin-polarized* insulators of the form in Eq. (B34).

a. $\mathcal{C}=0$ *intervalley-coherent insulators with opposite valley polarization per Chern sector*

We start by defining $\mathrm{SU_S}(2)\times\mathrm{SU_V}(2)$ to be a subgroup of $\mathrm{U}(4)\times\mathrm{U}(4)$ corresponding to independent $\mathrm{SU}(2)$ rotations in both the valley (V) and spin (S) subspaces. The $\mathrm{SU_S}(2)\times\mathrm{SU_V}(2)$ group is generated by the six operators

$$\begin{aligned} S_{\mathrm{V}}^{a} &= \sum_{\mathbf{k}}\sum_{\eta,s,\eta',s',n}\left[\tau^{0}s^{a}\right]_{\eta s,\eta' s'}\hat{c}^{\dagger}_{\mathbf{k},n,\eta,s}\hat{c}_{\mathbf{k},n,\eta',s'}, \quad \text{for} \quad a=x,y,z,\\ S_{\mathrm{S}}^{a} &= \sum_{\mathbf{k}}\sum_{\eta,s,\eta',s',n}\left[\tau^{a}s^{0}\right]_{\eta s,\eta' s'}\hat{c}^{\dagger}_{\mathbf{k},n,\eta,s}\hat{c}_{\mathbf{k},n,\eta',s'}, \quad \text{for} \quad a=x,y,z, \end{aligned} \tag{E40}$$

which are diagonal in the band subspace, and therefore act *identically* within the two Chern sectors. Unlike the $\mathrm{U}_{\mathrm{nc}}(4)$ group, within the $\mathrm{SU_S}(2)\times\mathrm{SU_V}(2)$ group, the valley rotations generated by S_{V}^{a} rotate the two Chern-band operators in the same direction.

Using the notation from Eq. (E23), we now focus on the case

$$b_{\eta,s}=-\sum_{s'}M_{ss'}b_{-\eta,s'}, \quad \text{for all } \eta=\pm \text{ and } s=\uparrow,\downarrow \tag{E41}$$

where we take either $M=s^{0}$ or $M=s^{x}$. Depending on the matrix M, this case corresponds to occupying the Chern bands of the unrotated state $\left|\Psi_{\nu}^{\nu_+,\nu_-}\right\rangle$ two at a time, with *opposite* Chern numbers, *opposite* valley indices and *identical* ($M=s^{0}$) or *opposite* ($M=s^{x}$) spin projections along the $\hat{\mathbf{z}}$ axis. To obtain the rotated state $|\varphi\rangle$ defined in Eq. (B34), we perform two successive $\mathrm{SU}(2)$ rotations in the valley (V) and spin (S) subspaces by letting $\hat{U}=\hat{U}_{\mathrm{S}}\hat{U}_{\mathrm{V}}=\hat{U}_{\mathrm{V}}\hat{U}_{\mathrm{S}}$, where

$$\hat{U}_{\mathrm{V}}=\exp\left(i\sum_{a\in\{x,y,z\}}\theta_{\mathrm{V}}^{a}S_{\mathrm{V}}^{a}\right), \quad \text{and} \quad \hat{U}_{\mathrm{S}}=\exp\left(i\sum_{a\in\{x,y,z\}}\theta_{\mathrm{S}}^{a}S_{\mathrm{S}}^{a}\right), \tag{E42}$$

with $\theta_{\mathrm{V}}^{a},\theta_{\mathrm{S}}^{a}\in\mathbb{R}$ denoting the angles parameterizing the two $\mathrm{SU}(2)$ rotations, and S_{V} and S_{S} being the $\mathrm{SU_S}(2)\times\mathrm{SU_V}(2)$ generators introduced in Eq. (E40). Within the energy-band basis, the transformation $\hat{U}$ is implemented by the eight-dimensional unitary matrix $U=U_{\mathrm{S}}U_{\mathrm{V}}=U_{\mathrm{V}}U_{\mathrm{S}}$, with

$$U_{\mathrm{V}}^{T}=\exp\left(i\sum_{a\in\{x,y,z\}}\theta_{\mathrm{V}}^{a}\zeta^{0}\tau^{a}s^{0}\right), \quad \text{and} \quad U_{\mathrm{S}}^{T}=\exp\left(i\sum_{a\in\{x,y,z\}}\theta_{\mathrm{S}}^{a}\zeta^{0}\tau^{0}s^{a}\right), \tag{E43}$$

corresponding to the two individual $\mathrm{SU}(2)$ rotations in the valley and spin subspaces. As the transformation $\hat{U}_{\mathrm{V}}$ rotates the two Chern sectors identically and the bands of the *unrotated* state $\left|\Psi_{\nu}^{\nu_+,\nu_-}\right\rangle$ are occupied two at a time within opposite Chern sectors and opposite valleys, it follows that in the state $|\varphi\rangle$, any bands with opposite Chern numbers have exactly opposite valley polarizations.

We will now prove that no $\sqrt{3}\times\sqrt{3}$ ordering emerges in the STM signal of $|\varphi\rangle$, despite it being generically intervalley coherent. We first note that for the particular choice of occupying the bands of $\left|\Psi_{\nu}^{\nu_+,\nu_-}\right\rangle$, the projectors from Eqs. (E26) and (E27) obey

$$\left(\zeta^{0}\tau^{x}M\right)\Pi^{*}\left(\zeta^{0}\tau^{x}M\right)^{\dagger}=\Pi \quad \text{and} \quad \left(\zeta^{0}\tau^{x}M\right)\tilde{\Pi}^{*}\left(\zeta^{0}\tau^{x}M\right)^{\dagger}=\tilde{\Pi}, \tag{E44}$$

where the matrix M was defined in the text surrounding Eq. (E41). In addition, it can checked that for any $\mathrm{SU_S}(2)\times\mathrm{SU_V}(2)$ rotation as defined in Eq. (E42), we have that

$$\left(\zeta^0\tau^z s^0\right)U_{\mathrm{V}}\left(\zeta^0\tau^z s^0\right)^\dagger=\left(\zeta^0\tau^x M\right)U_{\mathrm{V}}^*\left(\zeta^0\tau^x M\right)^\dagger. \tag{E45}$$

Focusing on the electron contribution to the spectral function matrix and letting $Q\equiv\left(\zeta^0\tau^0 M\right)U_{\mathrm{S}}\left(\zeta^0\tau^0 M\right)$, we can show from Eqs. (E44) and (E45) that the projector matrix from Eq. (E26) obeys

$$\begin{aligned}\left(\zeta^0\tau^x M\right)\left(U^\dagger\Pi U\right)^*\left(\zeta^0\tau^x M\right)^\dagger&=Q^T\left(\zeta^0\tau^x M\right)U_{\mathrm{V}}^T\Pi^* U_{\mathrm{V}}^*\left(\zeta^0\tau^x M\right)^\dagger Q^*\\&=Q^T\left(\zeta^0\tau^x M\right)U_{\mathrm{V}}^T\left(\zeta^0\tau^x M\right)^\dagger\Pi\left(\zeta^0\tau^x M\right)U_{\mathrm{V}}^*\left(\zeta^0\tau^x M\right)^\dagger Q^*\\&=Q^T\left(\zeta^0\tau^z s^0\right)U_{\mathrm{V}}^\dagger\left(\zeta^0\tau^z s^0\right)^\dagger\Pi\left(\zeta^0\tau^z s^0\right)U_{\mathrm{V}}\left(\zeta^0\tau^z s^0\right)^\dagger Q^*\\&=\left(\zeta^0\tau^z s^0\right)Q^T U_{\mathrm{S}}\left(U^\dagger\Pi U\right)U_{\mathrm{S}}^\dagger Q^*\left(\zeta^0\tau^z s^0\right)^\dagger.\end{aligned} \tag{E46}$$

In deriving Eq. (E46), we have also used $M^2=s^0$, $[\tau^x,Q]=[U_{\mathrm{S}},U_{\mathrm{V}}]=0$. Additionally, using the parametrization of the electron excitation matrix from Eq. (B21), it is straightforward to show that

$$\left(\zeta^0\tau^x M\right)\left(R(\mathbf{k})\otimes s^0\right)^*\left(\zeta^0\tau^x M\right)^\dagger=\left(R(-\mathbf{k})\otimes s^0\right). \tag{E47}$$

Combining Eqs. (E46) and (E47), we can derive a relation for the electron excitations wave functions

$$\left(\zeta^0\tau^x M\right)\left[U^\dagger\Pi U\left(R(\mathbf{k})\otimes s^0\right)U^\dagger\Pi U\right]^*\left(\zeta^0\tau^x M\right)^\dagger=\left(\zeta^0\tau^z s^0\right)Q^T U_{\mathrm{S}}\left[U^\dagger\Pi U\left(R(-\mathbf{k})\otimes s^0\right)U^\dagger\Pi U\right]U_{\mathrm{S}}^\dagger Q^*\left(\zeta^0\tau^z s^0\right)^\dagger. \tag{E48}$$

As discussed at the end of Appendix [D 1], the matrix $Y(\mathbf{k},\omega)$ defined in Eq. (D7) and $U^\dagger\Pi U\left(R(\mathbf{k})\otimes s^0\right)U^\dagger\Pi U$, whose spectral decomposition was given in Eq. (B63), share identical eigendecompositions, up to a rescaling of the eigenvalues. As such, $Y(\mathbf{k},\omega)$ satisfies a similar relation to Eq. (E48), namely

$$\left(\zeta^0\tau^x M\right)\left[Y(\mathbf{k},\omega)\right]^*\left(\zeta^0\tau^x M\right)^\dagger=\left(\zeta^0\tau^z s^0\right)Q^T U_{\mathrm{S}}\left[Y(-\mathbf{k},\omega)\right]U_{\mathrm{S}}^\dagger Q^*\left(\zeta^0\tau^z s^0\right)^\dagger \tag{E49}$$

Tracing over the spin degree of freedom in Eq. (E49) and using the Hermiticity of $Y(\mathbf{k},\omega)$, we find that

$$\left[\mathrm{tr}_s\, Y(-\mathbf{k},\omega)\right]_{n'(-\eta'),n(-\eta)}=\left[\left(\zeta^0\tau^z\right)\mathrm{tr}_s\, Y(\mathbf{k},\omega)\left(\zeta^0\tau^z\right)^\dagger\right]_{n\eta,n'\eta'}=\eta\eta'\left[\mathrm{tr}_s\, Y(\mathbf{k},\omega)\right]_{n\eta,n'\eta'}. \tag{E50}$$

At the same time, using Eqs. (C37) and (D5), we can find the symmetrized spectral function matrix corresponding to electron excitations to be

$$\left[\mathcal{M}_\varphi^{S+}(\omega)\right]_{\mathbf{k}n\eta,\mathbf{k}'n'\eta'}=\frac{1}{2}\delta_{\mathbf{k},\mathbf{k}'}\left(1+\eta\eta'\right)\left[\mathrm{tr}_s\, Y(\mathbf{k},\omega)\right]_{n\eta,n'\eta'}. \tag{E51}$$

In analogous manner, the hole symmetrized spectral function matrix is given by

$$\left[\mathcal{M}_\varphi^{S-}(\omega)\right]_{\mathbf{k}n\eta,\mathbf{k}'n'\eta'}=\frac{1}{2}\delta_{\mathbf{k},\mathbf{k}'}\left(1+\eta\eta'\right)\left[\mathrm{tr}_s\,\tilde{Y}(\mathbf{k},\omega)\right]_{n\eta,n'\eta'}. \tag{E52}$$

Inspecting Eqs. (E51) and (E52) reveals that the symmetrized spectral function matrices are diagonal in valley subspace, thus proving that no $\sqrt{3}\times\sqrt{3}$ ordering emerges for the insulator $|\varphi\rangle$.

The insulators $\hat{U}\left|\Psi_\nu^{\nu_+,\nu_-}\right\rangle$ with $\hat{U}$ restricted to $\mathrm{SU_S}(2)\times\mathrm{SU_V}(2)$ and the occupancy of the Chern bands of $\left|\Psi_\nu^{\nu_+,\nu_-}\right\rangle$ given in Eq. (E42) constitute another example of intervalley-coherent states without $\sqrt{3}\times\sqrt{3}$ ordering, in addition to the set of ground states discussed already in Appendix [E 1]. The key difference between the two cases lies in the symmetries enforcing the absence of $\sqrt{3}\times\sqrt{3}$ ordering. In Appendix [E 1], we proved that the vanishing of $\sqrt{3}\times\sqrt{3}$ ordering is a direct consequence of restricting to the insulators with fully-occupied or fully-empty spin-valley flavors and only considering nonchiral $\mathrm{U_{nc}}(4)$ rotations thereof, rather than the more general $\mathrm{U}(4)\times\mathrm{U}(4)$ transformations. This particular submanifold of ground states over the more general states given by Eq. (B8) becomes energetically favored - in the absence of chiral symmetry - in comparison to the latter at even fillings [68, 69]. On the other hand, the absence of $\sqrt{3}\times\sqrt{3}$ ordering for the insulators discussed in this section is *fine tuned*: there is no *a priori* reason for restricting to the $\mathrm{SU_S}(2)\times\mathrm{SU_V}(2)$ subgroup of $\mathrm{U}(4)\times\mathrm{U}(4)$ or to the unrotated states described by Eq. (E41). Nevertheless, coupled with the conclusions of Appendix [E 1], this example allows us to provide an intuitive picture explaining the vanishing of $\sqrt{3}\times\sqrt{3}$ ordering in *maximally spin-polarized* TBG insulators of the form in Eq. (B8).

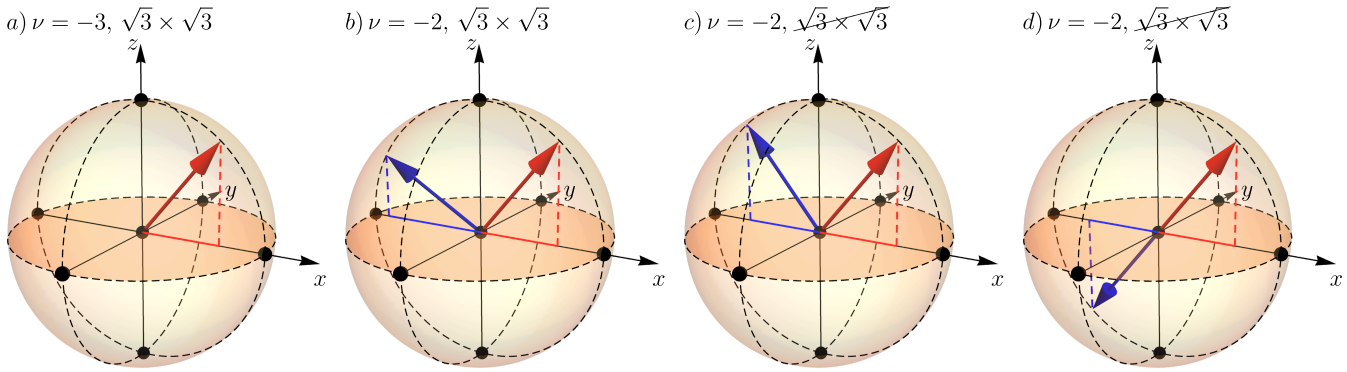

FIG. 7. The presence of $\sqrt{3} \times \sqrt{3}$ symmetry-breaking and the valley polarization Bloch sphere for the maximally spin-polarized TBG ground states. We show how the valley polarization of the $\mathcal{C} = +1$ (red) and $\mathcal{C} = -1$ (blue) bands for the maximally spin-polarized TBG insulators at $\nu = -3, -2$ determines the presence of $\sqrt{3} \times \sqrt{3}$ ordering. With only one Chern band filled [panel a)], the intervalley coherent, maximally spin-polarized $\nu = -3$ ground state will harbor $\sqrt{3} \times \sqrt{3}$ symmetry breaking. For the $\nu = -2$ and $\mathcal{C} = 0$ insulators [panels b)-d)], intervalley coherence does lead to the emergence of $\sqrt{3} \times \sqrt{3}$ ordering [panel b)], unless the polarization vectors of the two Chern bands have opposite projections in the xy plane [panels c) and d)]. The insulator in panel c) corresponds to a $\mathrm{U_{nc}}(4)$ rotation of a TBG ground state with a single fully-filled valley-spin flavor, and thus, as shown in Appendix [E 1], does not display $\sqrt{3} \times \sqrt{3}$ ordering. The absence of $\sqrt{3} \times \sqrt{3}$ ordering in the insulator from panel d) is due to the opposite valley polarizations of the two Chern bands, as shown in Appendix [E 3 a]. The vanishing of $\sqrt{3} \times \sqrt{3}$ ordering in panels c) and d) can be understood by noting that in both cases the xy-projections of the valley polarizations of the two Chern band exactly cancel.

b. *An intuitive picture for the maximally spin-polarized insulators*

Intervalley-coherence is a necessary, but insufficient condition for the emergence of $\sqrt{3} \times \sqrt{3}$ patterns in the STM signals of the TBG insulators constructed in Ref. [68]. This was illustrated in Appendices [E 1] and [E 3 a], where we identified two distinct ground-state submanifolds that are manifestly intervalley-coherent, but do not harbor any $\sqrt{3} \times \sqrt{3}$ ordering. Due to the nature of the $\mathrm{U}(4) \times \mathrm{U}(4)$ group, whose rotations mix the valley and spin degrees of freedom, deriving *all* the necessary *and* sufficient conditions for the absence of $\sqrt{3} \times \sqrt{3}$ symmetry-breaking for the valley-coherent TBG insulators from Eq. (B34) is beyond the scope of the current work. Nevertheless, an intuitive explanation for the absence of $\sqrt{3} \times \sqrt{3}$ ordering in some valley-coherent TBG insulators can be obtained by restricting to the subset of TBG ground states from Eq. (B34), which are *maximally spin-polarized*.

The complete set of maximally spin-polarized (along the $\hat{\mathbf{z}}$ direction, without loss of generality) states $|\varphi\rangle$, as defined in Eq. (B34), can be obtained by letting $\hat{U}$ be a product of $\mathrm{SU}(2)$ valley transformations in each of the two Chern sectors [*i.e.* letting $\theta_{\pm}^{x0}$, $\theta_{\pm}^{y0}$, $\theta_{\pm}^{z0}$ be the only nonzero angles in Eq. (E22)], and occupying the spin-$\uparrow$ bands of the unrotated state $\left|\Psi_{\nu}^{\nu_+,\nu_-}\right\rangle$ first. For $\nu = -4$, TBG ground state is not intervalley-coherent, so no $\sqrt{3} \times \sqrt{3}$ ordering is expected. At $\nu = -3$, the only possibility is to occupy a single Chern band, and it was already shown in Case 2 of Appendix [E 2 b] that the resulting insulator does show $\sqrt{3} \times \sqrt{3}$ symmetry-breaking if it is intervalley-coherent (see Fig. 7a). For $\nu = -2$, there are two choices. Filling two Chern bands with the same Chern number leads to a valley-polarized state, which does not display any $\sqrt{3} \times \sqrt{3}$ ordering. On the other hand filling two Chern bands with opposite Chern numbers will generically lead to the emergence of $\sqrt{3} \times \sqrt{3}$ ordering, unless $|\varphi\rangle = \hat{U}\,|\Psi_{\nu}\rangle$, with $\hat{U} \in \mathrm{U_{nc}}(4)$ (*i.e.* $|\varphi\rangle$ is one of the insulators discussed in Appendix [E 1]), or $|\varphi\rangle$ has opposite valley polarizations per Chern sector (as discussed in Appendix [E 3 a]). As shown in Figs. 7b to 7d, the maximally spin-polarized $\nu = -2$ and $\mathcal{C} = 0$ insulators $|\varphi\rangle$ generally harbor $\sqrt{3} \times \sqrt{3}$ symmetry-breaking, unless valley polarization projections of the two Chern bands in the xy plane exactly cancel.

At $\nu = -1$, the situation is similar to that at $\nu = -3$ for the maximally spin-polarized insulators. As both valleys are filled, one Chern sector will be valley-polarized. Assuming that the other Chern band is intervalley-coherent, $\sqrt{3} \times \sqrt{3}$ ordering will generally emerge for the insulator $|\varphi\rangle$. For $\nu = 0$, both valleys are fully filled for a given spin sector, thus precluding any $\sqrt{3} \times \sqrt{3}$ symmetry breaking. For any positive filling ν, the conditions for the presence or absence of $\sqrt{3} \times \sqrt{3}$ ordering are identical to the ones at $-\nu$, as a consequence of the many-body charge-conjugation symmetry of TBG [74].

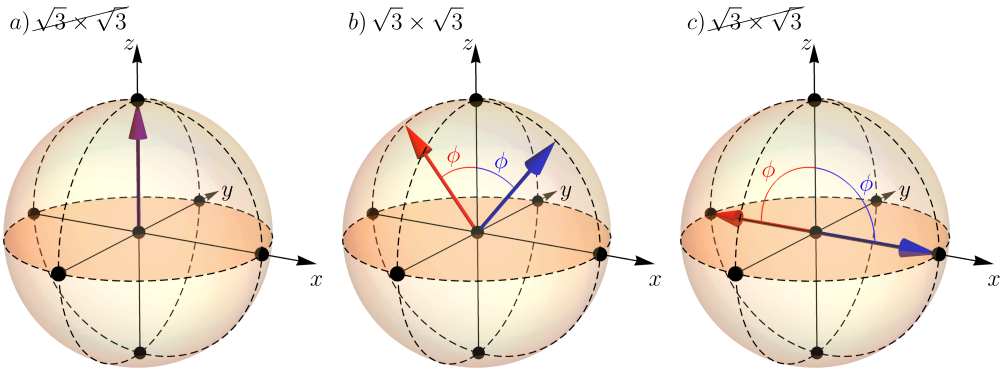

FIG. 8. Emergence of $\sqrt{3}\times\sqrt{3}$ ordering in the absence of exact particle-hole symmetry ($\lambda = 1$). We consider the $\nu = -2$ insulator from Eq. (E53) for different rotation $\hat{U}$ given by Eq. (E54), and show how the valley polarization of the $\mathcal{C} = +1$ (red) and $\mathcal{C} = -1$ (blue) bands determines the presence of $\sqrt{3}\times\sqrt{3}$ symmetry-breaking. The $\mathrm{U_{nc}}\,(4)$ rotation from Eq. (E54) rotates the polarizations of the two Chern bands by an angle ϕ in opposite directions within the xz plane. As expected, the valley polarized case [panel a)] does not exhibit $\sqrt{3}\times\sqrt{3}$ ordering. Unlike the case with exact particle-hole symmetry ($\lambda = 0$), a general values of ϕ leads to the emergence of $\sqrt{3}\times\sqrt{3}$ ordering, unless the Chern bands are polarized in the xy plane [panel c)], when the $\sqrt{3}\times\sqrt{3}$ ordering vanishes even without *exact* particle-hole symmetry.

4. Breaking the particle-hole symmetry

In Appendix [E 1], we showed that the states $\hat{U}\,|\Psi_\nu\rangle$, where $\hat{U}\in \mathrm{U_{nc}}\,(4)$ and the unrotated state $|\Psi_\nu\rangle$ defined in Eq. (B7) contains only fully-filled or fully-empty valley-spin flavors, do not harbor any $\sqrt{3}\times\sqrt{3}$ ordering *even* in the presence of intervalley-coherence. Among other reasons, we argued that the absence of $\sqrt{3}\times\sqrt{3}$ symmetry breaking is a direct result of the discrete symmetries of TBG: C_{2z}, T, and P. While the particle-hole symmetry is an excellent *approximate* symmetry of TBG [82, 84], it is nevertheless not *exact*. In this section, we investigate the effects of relaxing the assumption of *exact* particle-hole symmetry by considering the unapproximated case $\lambda = 1$.

For simplicity, we will focus on the insulator

$$|\varphi\rangle = \hat{U}\,|\Psi_{-2}\rangle = \hat{U}\left(\prod_{\mathbf{k}}\hat{c}^\dagger_{\mathbf{k},+1,+,\uparrow}\hat{c}^\dagger_{\mathbf{k},-1,+,\uparrow}\right)|0\rangle \tag{E53}$$

where the rotation $\hat{U}$ is given in terms of the $\mathrm{U_{nc}}\,(4)$ generators from Eq. (A52) by

$$\hat{U} = \exp\left(\frac{i\phi S^{y0}}{2}\right). \tag{E54}$$

The transformation $\hat{U}$ rotates the valley polarization of the Chern sector e_Y, by an angle $e_Y\phi$ within the xz plane (see Fig. 8). Although $\hat{U}$ is not the most general $\mathrm{U_{nc}}\,(4)$ rotation, it is nevertheless sufficient for understanding the implications of breaking the exact particle-hole symmetry on the conclusions of Appendix [E 1].

As in Appendix [E 2], to parameterize the spectral function matrix, we can leverage the fact that the matrix $Y\,(\mathbf{k},\omega)$ defined in Eq. (D7) and $U^\dagger\Pi U\left(R\,(\mathbf{k})\otimes s^0\right)U^\dagger\Pi U$, whose spectral decomposition was given in Eq. (B63), share identical eigendecompositions, up to a rescaling of the eigenvalues (and similarly for the hole contribution). The matrices $U^\dagger\Pi U\left(R\,(\mathbf{k})\otimes s^0\right)U^\dagger\Pi U$ and $U^\dagger\tilde{\Pi}U\left(\tilde{R}\,(\mathbf{k})\otimes s^0\right)U^\dagger\tilde{\Pi}U$ can be obtained directly for $|\varphi\rangle$, by using the parameterizations of the charge-one excitation matrices in the $\lambda = 1$ case from Eqs. (B21) and (B22)

$$\begin{aligned}
&U^\dagger\Pi U\left(R\,(\mathbf{k})\otimes s^0\right)U^\dagger\Pi U- = \frac{1}{4}\zeta^0\tau^0 s^0\left(-\cos(\phi)d_1\,(\mathbf{k})+3d_2\,(\mathbf{k})\right)\\
&-\frac{1}{4}\zeta^0\tau^0 s^z\left(-\cos(\phi)d_1\,(\mathbf{k})-d_2\,(\mathbf{k})\right)-\frac{1}{8}\zeta^0\tau^z s^0\left((5+\cos(2\phi))d_1\,(\mathbf{k})-2\cos(\phi)d_2\,(\mathbf{k})\right)\\
&-\frac{1}{8}\zeta^0\tau^z s^z\left((-3+\cos(2\phi))d_1\,(\mathbf{k})-2\cos(\phi)d_2\,(\mathbf{k})\right)\\
&-\frac{1}{8}\zeta^x\tau^0 s^0\left(-2\cos(\phi)d_3\,(\mathbf{k})+(5+\cos(2\phi))d_4\,(\mathbf{k})\right)
\end{aligned}$$

$$
\begin{aligned}
&-\frac{1}{8}\zeta^{x}\tau^{0}s^{z}\left(-2\cos(\phi)d_{3}\left(\mathbf{k}\right)+\left(-3+\cos(2\phi)\right)d_{4}\left(\mathbf{k}\right)\right)-\frac{1}{4}\zeta^{x}\tau^{y}s^{0}\sin(\phi)\left(d_{5}\left(\mathbf{k}\right)-\cos(\phi)d_{6}\left(\mathbf{k}\right)\right)\\
&-\frac{1}{4}\zeta^{x}\tau^{y}s^{z}\sin(\phi)\left(d_{5}\left(\mathbf{k}\right)-\cos(\phi)d_{6}\left(\mathbf{k}\right)\right)-\frac{1}{4}\zeta^{x}\tau^{z}s^{0}\left(3d_{3}\left(\mathbf{k}\right)-\cos(\phi)d_{4}\left(\mathbf{k}\right)\right)\\
&-\frac{1}{4}\zeta^{x}\tau^{z}s^{z}\left(-d_{3}\left(\mathbf{k}\right)-\cos(\phi)d_{4}\left(\mathbf{k}\right)\right)-\frac{1}{4}\zeta^{y}\tau^{x}s^{0}\sin(\phi)\left(-\cos(\phi)d_{1}\left(\mathbf{k}\right)+d_{2}\left(\mathbf{k}\right)\right)\\
&-\frac{1}{4}\zeta^{y}\tau^{x}s^{z}\sin(\phi)\left(-\cos(\phi)d_{1}\left(\mathbf{k}\right)+d_{2}\left(\mathbf{k}\right)\right)-\frac{1}{8}\zeta^{z}\tau^{0}s^{0}\left(-2\cos(\phi)d_{5}\left(\mathbf{k}\right)+\left(5+\cos(2\phi)\right)d_{6}\left(\mathbf{k}\right)\right)\\
&-\frac{1}{8}\zeta^{z}\tau^{0}s^{z}\left(-2\cos(\phi)d_{5}\left(\mathbf{k}\right)+\left(-3+\cos(2\phi)\right)d_{6}\left(\mathbf{k}\right)\right)-\frac{1}{4}\zeta^{z}\tau^{y}s^{0}\sin(\phi)\left(-d_{3}\left(\mathbf{k}\right)+\cos(\phi)d_{4}\left(\mathbf{k}\right)\right)\\
&-\frac{1}{4}\zeta^{z}\tau^{y}s^{z}\sin(\phi)\left(-d_{3}\left(\mathbf{k}\right)+\cos(\phi)d_{4}\left(\mathbf{k}\right)\right)-\frac{1}{4}\zeta^{z}\tau^{z}s^{0}\left(3d_{5}\left(\mathbf{k}\right)-\cos(\phi)d_{6}\left(\mathbf{k}\right)\right)\\
&-\frac{1}{4}\zeta^{z}\tau^{z}s^{z}\left(-d_{5}\left(\mathbf{k}\right)-\cos(\phi)d_{6}\left(\mathbf{k}\right)\right),
\end{aligned}
\tag{E55}
$$

$$
\begin{aligned}
&U^{\dagger}\tilde{\Pi}U\left(\tilde{R}\left(\mathbf{k}\right)\otimes s^{0}\right)U^{\dagger}\tilde{\Pi}U-=\frac{1}{4}\zeta^{0}\tau^{0}s^{0}\left(\cos(\phi)\tilde{d}_{1}\left(\mathbf{k}\right)+\tilde{d}_{2}\left(\mathbf{k}\right)\right)-\frac{1}{4}\zeta^{0}\tau^{0}s^{z}\left(\cos(\phi)\tilde{d}_{1}\left(\mathbf{k}\right)+\tilde{d}_{2}\left(\mathbf{k}\right)\right)\\
&-\frac{1}{4}\zeta^{0}\tau^{z}s^{0}\cos(\phi)\left(\cos(\phi)\tilde{d}_{1}\left(\mathbf{k}\right)+\tilde{d}_{2}\left(\mathbf{k}\right)\right)-\frac{1}{4}\zeta^{0}\tau^{z}s^{z}\cos(\phi)\left(\cos(\phi)\tilde{d}_{1}\left(\mathbf{k}\right)+\tilde{d}_{2}\left(\mathbf{k}\right)\right)\\
&-\frac{1}{4}\zeta^{x}\tau^{0}s^{0}\cos(\phi)\left(\tilde{d}_{3}\left(\mathbf{k}\right)+\cos(\phi)\tilde{d}_{4}\left(\mathbf{k}\right)\right)-\frac{1}{4}\zeta^{x}\tau^{0}s^{z}\cos(\phi)\left(\tilde{d}_{3}\left(\mathbf{k}\right)+\cos(\phi)\tilde{d}_{4}\left(\mathbf{k}\right)\right)\\
&-\frac{1}{4}\zeta^{x}\tau^{y}s^{0}\sin(\phi)\left(\tilde{d}_{5}\left(\mathbf{k}\right)+\cos(\phi)\tilde{d}_{6}\left(\mathbf{k}\right)\right)-\frac{1}{4}\zeta^{x}\tau^{y}s^{z}\sin(\phi)\left(\tilde{d}_{5}\left(\mathbf{k}\right)+\cos(\phi)\tilde{d}_{6}\left(\mathbf{k}\right)\right)\\
&-\frac{1}{4}\zeta^{x}\tau^{z}s^{0}\left(\tilde{d}_{3}\left(\mathbf{k}\right)+\cos(\phi)\tilde{d}_{4}\left(\mathbf{k}\right)\right)-\frac{1}{4}\zeta^{x}\tau^{z}s^{z}\left(\tilde{d}_{3}\left(\mathbf{k}\right)+\cos(\phi)\tilde{d}_{4}\left(\mathbf{k}\right)\right)\\
&-\frac{1}{4}\zeta^{y}\tau^{x}s^{0}\sin(\phi)\left(\cos(\phi)\tilde{d}_{1}\left(\mathbf{k}\right)+\tilde{d}_{2}\left(\mathbf{k}\right)\right)-\frac{1}{4}\zeta^{y}\tau^{x}s^{z}\sin(\phi)\left(\cos(\phi)\tilde{d}_{1}\left(\mathbf{k}\right)+\tilde{d}_{2}\left(\mathbf{k}\right)\right)\\
&-\frac{1}{4}\zeta^{z}\tau^{0}s^{0}\cos(\phi)\left(\tilde{d}_{5}\left(\mathbf{k}\right)+\cos(\phi)\tilde{d}_{6}\left(\mathbf{k}\right)\right)-\frac{1}{4}\zeta^{z}\tau^{0}s^{z}\cos(\phi)\left(\tilde{d}_{5}\left(\mathbf{k}\right)+\cos(\phi)\tilde{d}_{6}\left(\mathbf{k}\right)\right)\\
&-\frac{1}{4}\zeta^{z}\tau^{y}s^{0}\sin(\phi)\left(\tilde{d}_{3}\left(\mathbf{k}\right)+\cos(\phi)\tilde{d}_{4}\left(\mathbf{k}\right)\right)-\frac{1}{4}\zeta^{z}\tau^{y}s^{z}\sin(\phi)\left(\tilde{d}_{3}\left(\mathbf{k}\right)+\cos(\phi)\tilde{d}_{4}\left(\mathbf{k}\right)\right)\\
&-\frac{1}{4}\zeta^{z}\tau^{z}s^{0}\left(\tilde{d}_{5}\left(\mathbf{k}\right)+\cos(\phi)\tilde{d}_{6}\left(\mathbf{k}\right)\right)-\frac{1}{4}\zeta^{z}\tau^{z}s^{z}\left(\tilde{d}_{5}\left(\mathbf{k}\right)+\cos(\phi)\tilde{d}_{6}\left(\mathbf{k}\right)\right),
\end{aligned}
\tag{E56}
$$

with the parity of the functions $d_i\left(\mathbf{k}\right)$ and $\tilde{d}_i\left(\mathbf{k}\right)$ (for $1\leq i\leq 6$) being given in Eq. (B23). For general values of ϕ, none of the terms in the matrix expansions from Eqs. (E55) and (E56) has definite momentum parity, implying that the matrices $U^{\dagger}\Pi U\left(R\left(\mathbf{k}\right)\otimes s^{0}\right)U^{\dagger}\Pi U$ and $U^{\dagger}\tilde{\Pi}U\left(\tilde{R}\left(\mathbf{k}\right)\otimes s^{0}\right)U^{\dagger}\tilde{\Pi}U$ at opposite momenta cannot be related through a similarity transformation. As a result, $Y\left(\mathbf{k},\omega\right)$ and $\tilde{Y}\left(\mathbf{k},\omega\right)$ defined in Eqs. (D7) and (D8), which share identical eigenvectors with the matrices from Eqs. (E55) and (E56), are not similar with the matrices $Y\left(-\mathbf{k},\omega\right)$ and $\tilde{Y}\left(-\mathbf{k},\omega\right)$, respectively. At the same time, for general values of ϕ, the matrices $U^{\dagger}\Pi U\left(R\left(\mathbf{k}\right)\otimes s^{0}\right)U^{\dagger}\Pi U$ and $U^{\dagger}\tilde{\Pi}U\left(\tilde{R}\left(\mathbf{k}\right)\otimes s^{0}\right)U^{\dagger}\tilde{\Pi}U$ have non-vanishing valley-off-diagonal terms, implying that $Y\left(\mathbf{k},\omega\right)$ and $\tilde{Y}\left(\mathbf{k},\omega\right)$ are not necessarily diagonal in the valley subspace. Since $Y\left(\mathbf{k},\omega\right)$ and $\tilde{Y}\left(\mathbf{k},\omega\right)$ have different eigenvalues at opposite momenta, no *exact* cancellation of the valley-off-diagonal matrix elements can occur when computing the symmetrized spectral function matrices. As a result, $\sqrt{3}\times\sqrt{3}$ ordering generally emerges in the STM signal of $|\varphi\rangle$.

In addition to the cases $\phi=0,\pi$, which correspond to valley-polarized insulators, there is one other notable exception for which $\sqrt{3}\times\sqrt{3}$ ordering vanishes *exactly* even in the $\lambda=1$ case: $\phi=\pi/2$. For $\phi=\pi/2$ the valley polarizations of the two Chern bands lie in the xy plane, a configuration which was shown by Ref. [58, 68] to be energetically favored when the effects of kinetic energy are considered (*i.e.* the K-IVC state discussed in the main paper). To show that $\sqrt{3}\times\sqrt{3}$ order vanishes in this case, despite $|\varphi\rangle$ being valley-coherent, we note that for $\phi=\pi/2$, the matrices from Eqs. (E55) and (E56) are given by

$$
\begin{aligned}
&U^{\dagger}\Pi U\left(R\left(\mathbf{k}\right)\otimes s^{0}\right)U^{\dagger}\Pi U=\\
&\zeta^{0}\tau^{0}s^{0}\frac{3d_{2}\left(\mathbf{k}\right)}{4}-\frac{1}{4}\zeta^{0}\tau^{0}s^{z}d_{2}\left(\mathbf{k}\right)-\zeta^{0}\tau^{z}s^{0}\frac{d_{1}\left(\mathbf{k}\right)}{2}-\frac{1}{2}\zeta^{0}\tau^{z}s^{z}d_{1}\left(\mathbf{k}\right)-\zeta^{x}\tau^{0}s^{0}\frac{d_{4}\left(\mathbf{k}\right)}{2}-\frac{1}{2}\zeta^{x}\tau^{0}s^{z}d_{4}\left(\mathbf{k}\right)\\
&-\zeta^{x}\tau^{y}s^{0}\frac{d_{5}\left(\mathbf{k}\right)}{4}-\zeta^{x}\tau^{y}s^{z}\frac{d_{5}\left(\mathbf{k}\right)}{4}-\zeta^{x}\tau^{z}s^{0}\frac{3d_{3}\left(\mathbf{k}\right)}{4}-\frac{1}{4}\zeta^{x}\tau^{z}s^{z}d_{3}\left(\mathbf{k}\right)-\zeta^{y}\tau^{x}s^{0}\frac{d_{2}\left(\mathbf{k}\right)}{4}-\zeta^{y}\tau^{x}s^{z}\frac{d_{2}\left(\mathbf{k}\right)}{4}
\end{aligned}
$$

$$-\zeta^z\tau^0 s^0\frac{d_6\left(\mathbf{k}\right)}{2}-\frac{1}{2}\zeta^z\tau^0 s^z d_6\left(\mathbf{k}\right)-\frac{1}{4}\zeta^z\tau^y s^0 d_3\left(\mathbf{k}\right)-\frac{1}{4}\zeta^z\tau^y s^z d_3\left(\mathbf{k}\right)-\zeta^z\tau^z s^0\frac{3d_5\left(\mathbf{k}\right)}{4}-\frac{1}{4}\zeta^z\tau^z s^z d_5\left(\mathbf{k}\right), \tag{E57}$$

$$\begin{aligned}&U^\dagger\tilde{\Pi}U\left(\tilde{R}\left(\mathbf{k}\right)\otimes s^0\right)U^\dagger\tilde{\Pi}U=\\&\frac{1}{4}\zeta^0\tau^0 s^0\tilde{d}_2\left(\mathbf{k}\right)-\frac{1}{4}\zeta^0\tau^0 s^z\tilde{d}_2\left(\mathbf{k}\right)-\frac{1}{4}\zeta^x\tau^y s^0\tilde{d}_5\left(\mathbf{k}\right)-\frac{1}{4}\zeta^x\tau^y s^z\tilde{d}_5\left(\mathbf{k}\right)-\frac{1}{4}\zeta^x\tau^z s^0\tilde{d}_3\left(\mathbf{k}\right)-\frac{1}{4}\zeta^x\tau^z s^z\tilde{d}_3\left(\mathbf{k}\right)\\&-\frac{1}{4}\zeta^y\tau^x s^0\tilde{d}_2\left(\mathbf{k}\right)-\frac{1}{4}\zeta^y\tau^x s^z\tilde{d}_2\left(\mathbf{k}\right)-\frac{1}{4}\zeta^z\tau^y s^0\tilde{d}_3\left(\mathbf{k}\right)-\frac{1}{4}\zeta^z\tau^y s^z\tilde{d}_3\left(\mathbf{k}\right)-\frac{1}{4}\zeta^z\tau^z s^0\tilde{d}_5\left(\mathbf{k}\right)\\&-\frac{1}{4}\zeta^z\tau^z s^z\tilde{d}_5\left(\mathbf{k}\right).\end{aligned} \tag{E58}$$

Using the parity and the reality of the functions $d_i\left(\mathbf{k}\right)$ and $\tilde{d}_i\left(\mathbf{k}\right)$ (for $1\leq i\leq 6$) from Eq. (B23), we find that

$$\left(\zeta^0\tau^y s^0\right)U^\dagger\Pi U\left(R\left(\mathbf{k}\right)\otimes s^0\right)U^\dagger\Pi U\left(\zeta^0\tau^y s^0\right)^\dagger=U^\dagger\Pi U\left(R\left(-\mathbf{k}\right)\otimes s^0\right)^* U^\dagger\Pi U, \tag{E59}$$

$$\left(\zeta^0\tau^y s^0\right)U^\dagger\tilde{\Pi}U\left(\tilde{R}\left(\mathbf{k}\right)\otimes s^0\right)U^\dagger\tilde{\Pi}U\left(\zeta^0\tau^y s^0\right)^\dagger=U^\dagger\tilde{\Pi}U\left(\tilde{R}\left(-\mathbf{k}\right)\otimes s^0\right)^* U^\dagger\tilde{\Pi}U, \tag{E60}$$

which implies (as a result of sharing identical eigenvectors) that the $Y\left(\mathbf{k},\omega\right)$ and $\tilde{Y}\left(\mathbf{k},\omega\right)$ matrices defined in Eqs. (D7) and (D8) obey an identical property

$$\left(\zeta^0\tau^y s^0\right)Y\left(\mathbf{k},\omega\right)\left(\zeta^0\tau^y s^0\right)^\dagger=Y^*\left(-\mathbf{k},\omega\right), \tag{E61}$$

$$\left(\zeta^0\tau^y s^0\right)\tilde{Y}\left(\mathbf{k},\omega\right)\left(\zeta^0\tau^y s^0\right)^\dagger=\tilde{Y}^*\left(-\mathbf{k},\omega\right). \tag{E62}$$

Focusing on the electron contribution, tracing over the spin degree of freedom of $Y\left(\mathbf{k},\omega\right)$ and using its Hermiticity, we obtain that

$$\eta\eta'\left[\mathrm{tr}_s\, Y\left(-\mathbf{k},\omega\right)\right]_{n'(-\eta'),n(-\eta)}=\left[\mathrm{tr}_s\, Y\left(\mathbf{k},\omega\right)\right]_{n\eta,n'\eta'}. \tag{E63}$$

At the same time, using Eqs. (C37) and (D5), we can find the symmetrized spectral function matrix corresponding to electron excitations to be

$$\left[\mathcal{M}_\varphi^{S+}\left(\omega\right)\right]_{\mathbf{k}n\eta,\mathbf{k}n'\eta'}=\frac{1}{2}\delta_{\mathbf{k},\mathbf{k}'}\left(1+\eta\eta'\right)\left[\mathrm{tr}_s\, Y\left(\mathbf{k},\omega\right)\right]_{n\eta,n'\eta'}. \tag{E64}$$

In analogous manner, the hole symmetrized spectral function matrix is given by

$$\left[\mathcal{M}_\varphi^{S-}\left(\omega\right)\right]_{\mathbf{k}n\eta,\mathbf{k}n'\eta'}=\frac{1}{2}\delta_{\mathbf{k},\mathbf{k}'}\left(1+\eta\eta'\right)\left[\mathrm{tr}_s\,\tilde{Y}\left(\mathbf{k},\omega\right)\right]_{n\eta,n'\eta'}. \tag{E65}$$

Inspecting Eqs. (E64) and (E65) reveals that the symmetrized spectral function matrices are and are manifestly valley-diagonal, thus proving that no $\sqrt{3}\times\sqrt{3}$ ordering emerges for the insulator $|\varphi\rangle$ for $\phi=\pi/2$.

In conclusion, breaking the exact particle-hole symmetry generally leads to the emergence of $\sqrt{3}\times\sqrt{3}$ ordering in $\mathrm{U_{nc}}\left(4\right)$ rotations of the insulators $|\Psi_\nu\rangle$. Nevertheless, because the particle-hole symmetry-breaking terms in Eqs. (E55) and (E56) (*i.e.* $d_i\left(\mathbf{k}\right)$ and $\tilde{d}_i\left(\mathbf{k}\right)$ for $i=1,4,6$) are relatively small, as shown in Eq. (B27), we expect the amplitude of the $\sqrt{3}\times\sqrt{3}$ ordering signal to be small in an STM measurement, implying that the conclusions of Appendix [E 1] hold *approximately* even in the $\lambda=1$ case. Nevertheless, we note that when the valley polarizations of the two Chern bands of $|\varphi\rangle$ are in the xy plane, a configuration which was shown to be energetically favorable when kinetic energy effects are included [68], the $\sqrt{3}\times\sqrt{3}$ ordering vanishes *exactly*, even in the absence of *exact* particle-hole symmetry.

Appendix F: Experimental method

In this appendix, we provide additional information about the experimental data discussed in the article. Tunneling measurements were performed on a homebuilt, ultra-high vacuum (UHV) STM [103] using tungsten tips calibrated against the Cu(111) Shockley surface state. Tungsten and copper were chosen to match the work function of graphene. TBG devices, which consist of TBG/hexagonal boron nitride (hBN)/SiO_2/Si, were electrically contacted through pre-patterned gold electrodes. The TBG was biased relative to the tip, which was referenced to ground, and a gate voltage was applied to Si to tune the carrier density to $\nu=\pm 4$. Differential conductance was obtained via lock-in detection of the AC tunnel current induced by an AC modulation voltage added to the sample bias.

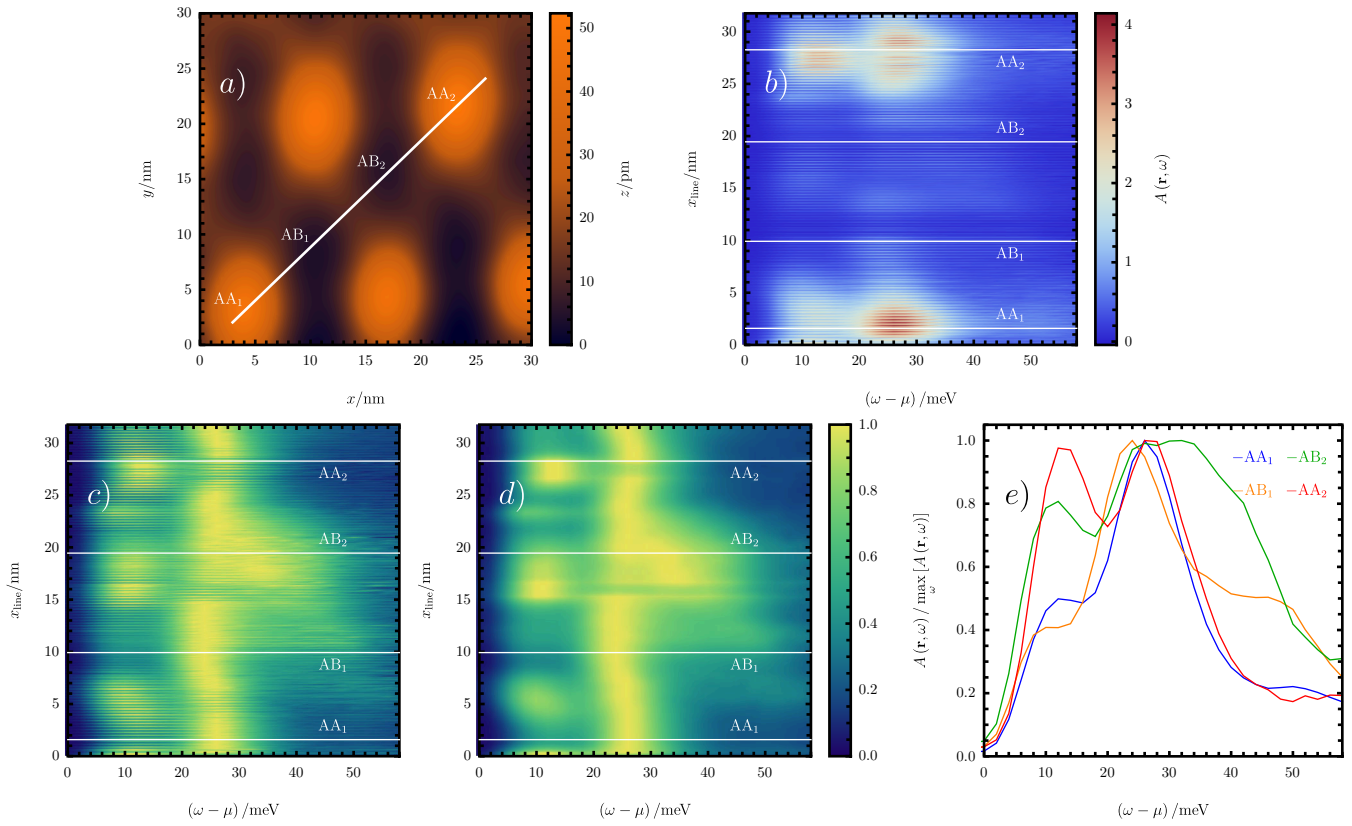

FIG. 9. STM signal along a line connecting two AA stacking sites of TBG for the $\nu = -4$ band insulator with a gate voltage $V_g = -43\,\mathrm{V}$. In panel a), we show the topography map of the sample together with the line connecting the two AA regions, passing through one AB and one BA regions. Because the AB and BA regions of TBG are equivalent, we label the centers of the staking regions along the line by AA_1, AB_1, AB_2, and AA_2. The (unnormalized) differential conductance is measured along the line and shown in panel b) as a function of the bias $(\omega - \mu)$, as well as the distance along the line x_{line}, with the four stacking regions marked by vertical lines. As explained in Appendix [C], for each value of x_{line}, we normalize the differential conductance such that the maximum value is 1 and show the resulting data in panel c). There is significant variability in the differential conductance on the atomic graphene scale. For that reason, we convolve the signals *along* the line with a Gaussian with standard deviation $\sigma = 0.8\,\mathrm{nm}$, resulting in the data shown in panel d). In panel e) we show the resulting four STM signals at AA_1, AB_1, AB_2, and AA_2, of which the AA_2 and AB_1 are showcased in Fig. 1 of the main text.

TBG devices were fabricated through a "tear-and-stack" method [104] whereby monolayer graphene was torn into two pieces via pickup on a sacrificial polyvinyl alcohol (PVA) structure. One monolayer was rotated relative to the other and was stacked on top of the other. As explained in greater detail in Ref. [103], the PVA structure was dissolved through water injection, and the subsequent heterostructure was annealed at 400°C.

In the main paper, we present STM data at $\nu = \pm 4$ which fits with the overall features of the TBG spectral function in the strong-coupling picture. We now give a broader overview of the data at $\nu = -4$ in Figs. 9 and 10. The two figures are obtained from the same sample but at two different locations, and we will detail Fig. 9 knowing that a similar analysis can be done for Fig. 10. We measure the STM signal along a line connecting two AA regions and passing through an AB and a BA region: as depicted in Fig. 9a, the measurement starts at the lower-left endpoint and ends approximately at the upper-right corner (with a small amount of drift). The resulting differential conductance from Fig. 9b is then normalized with respect to its maximum in Fig. 9c. The data shows a significant degree of variability in the STM signal on the atomic graphene scale. We circumvent this issue by applying a Gaussian filter with standard deviation $\sigma = 0.8\,\mathrm{nm}$ *before normalization*, resulting in Fig. 9d. Finally, we extract the normalized STM signals corresponding to the two AA and two AB regions and illustrated them in Fig. 9e. Note that the normalized STM signals shown in Fig. 1a are the AA_2 and AB_1 plots of Fig. 9e.

The results shown in both Fig. 9e and Fig. 10e indicate a fair amount of variability between different AA and AB sites of the same sample, primarily in how the ratio between the two peaks changes upon moving from the AA to the AB site. Nevertheless, as explained in the main paper, the signal broadening is consistent with the interaction energy scale as opposed to the bandwidth of the TBG bands. Thus, it validates the strong coupling approach in describing

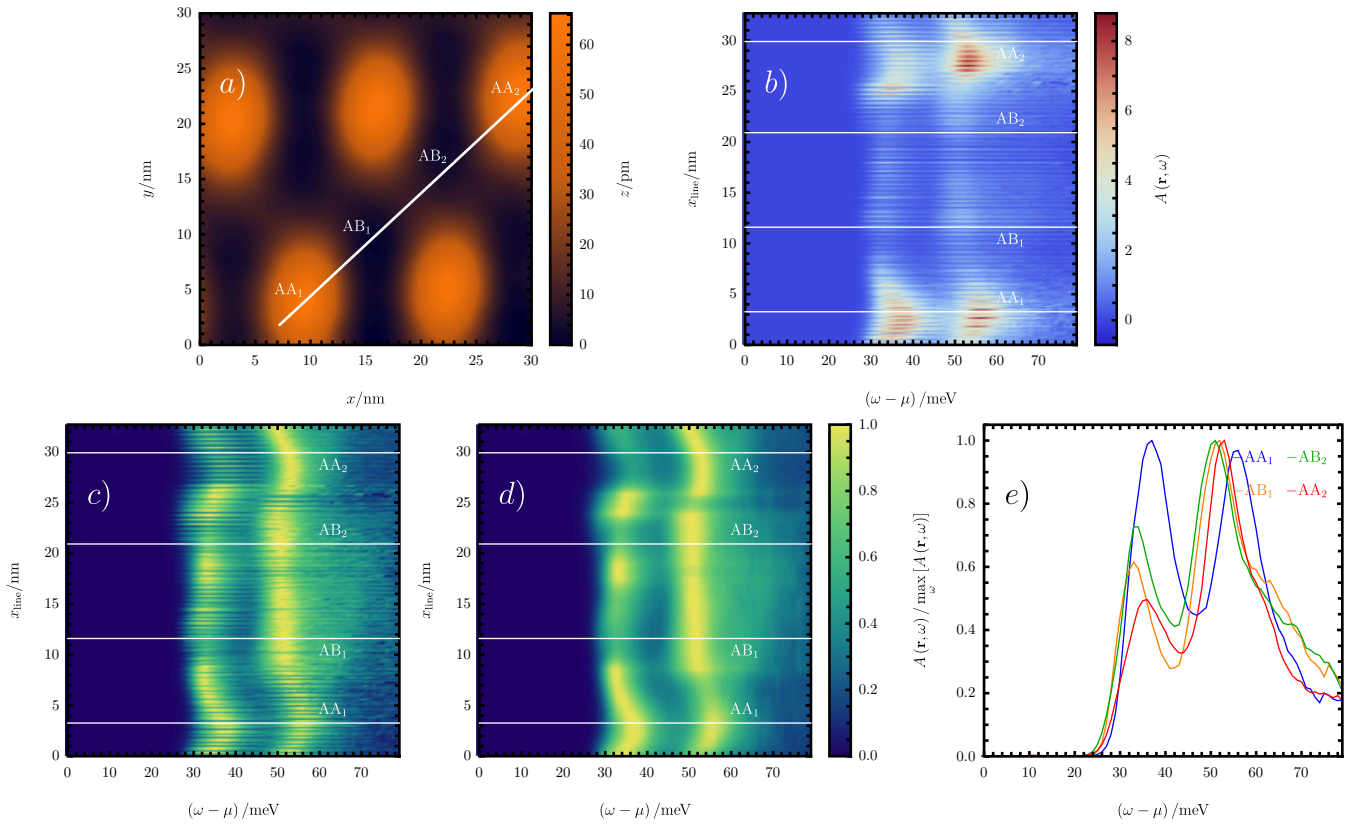

FIG. 10. STM signal along a line connecting two AA sites of TBG for the $\nu = -4$ band insulator with a gate voltage $V_g = -45\,\mathrm{V}$ at a different location than Fig. 9 (but the same sample). The panels have the same meaning as in Fig. 9.

the physics of TBG.

Appendix G: Additional numerical results

In this appendix we provide numerical results for 14 TBG insulator states listed in Table II. For each insulator we consider four parameter values $(w_0/w_1, \lambda) = (0.0, 0)$, $(w_0/w_1, \lambda) = (0.4, 0)$, $(w_0/w_1, \lambda) = (0.8, 0)$, $(w_0/w_1, \lambda) = (0.8, 1)$. In each case, we show the spectral function at the AA and AB stacking centers, together with the charge-one excitation dispersion plotted along the high-symmetry lines of the MBZ. For each insulator and parameter choice, we also plot the spatial structure of the TBG spectral function in both real and momentum spaces for two values of $\omega - \mu$ (corresponding roughly to the maxima of the AA STM signal for hole or electron tunneling, respectively).

ν	$\|\phi\rangle$	Appendix	Description	w_0/w_1 0.0	0.4	0.8
-4	$\left\|\phi^{(0)}\right\rangle = \|0\rangle$	Appendix [G 1]	Insulator with all TBG active bands empty	✓	✓	✓
-3	$\left\|\phi^{(1)}\right\rangle = \prod_{\mathbf{k}} \hat{d}^\dagger_{\mathbf{k},+1,+,\uparrow} \|0\rangle$	Appendix [G 2]	$C = 1$, valley polarized	✓	✓	✗
-3	$\left\|\phi^{(2)}\right\rangle = \prod_{\mathbf{k}} \frac{\hat{d}^\dagger_{\mathbf{k},+1,+,\uparrow} + \hat{d}^\dagger_{\mathbf{k},+1,-,\uparrow}}{\sqrt{2}} \|0\rangle$	Appendix [G 3]	$C = 1$, valley coherent	✓	✓	✗
-2	$\left\|\phi^{(3)}\right\rangle = \prod_{\mathbf{k}} \prod_{e_Y=\pm1} \frac{\hat{d}^\dagger_{\mathbf{k},e_Y,+,\uparrow} + e_Y \hat{d}^\dagger_{\mathbf{k},e_Y,-,\uparrow}}{\sqrt{2}} \|0\rangle$	Appendix [G 4]	$C = 0$, KIVC	✓	✓	✓
-2	$\left\|\phi^{(4)}\right\rangle = \prod_{\mathbf{k}} \prod_{e_Y=\pm1} \frac{\hat{d}^\dagger_{\mathbf{k},e_Y,+,\uparrow} + \hat{d}^\dagger_{\mathbf{k},e_Y,-,\uparrow}}{\sqrt{2}} \|0\rangle$	Appendix [G 5]	$C = 0$, TIVC	✓	✓	✓
-2	$\left\|\phi^{(5)}\right\rangle = \prod_{\mathbf{k}} \hat{d}^\dagger_{\mathbf{k},+1,+,\uparrow} \hat{d}^\dagger_{\mathbf{k},-1,+,\uparrow} \|0\rangle$	Appendix [G 6]	$C = 0$, valley polarized	✓	✓	✓
-2	$\left\|\phi^{(6)}\right\rangle = \prod_{\mathbf{k}} \hat{d}^\dagger_{\mathbf{k},+1,+,\uparrow} \hat{d}^\dagger_{\mathbf{k},+1,+,\downarrow} \|0\rangle$	Appendix [G 7]	$C = 2$, valley polarized	✓	✓	✓
-2	$\left\|\phi^{(7)}\right\rangle = \prod_{\mathbf{k}} \prod_{s=\uparrow,\downarrow} \frac{\hat{d}^\dagger_{\mathbf{k},+1,+,s} + \hat{d}^\dagger_{\mathbf{k},+1,-,s}}{\sqrt{2}} \|0\rangle$	Appendix [G 8]	$C = 2$, valley coherent	✓	✓	✓
-1	$\left\|\phi^{(8)}\right\rangle = \prod_{\mathbf{k}} \hat{d}^\dagger_{\mathbf{k},+1,+,\uparrow} \hat{d}^\dagger_{\mathbf{k},+1,+,\downarrow} \hat{d}^\dagger_{\mathbf{k},+1,-,\downarrow} \|0\rangle$	Appendix [G 9]	$C = 3$, valley polarized	✓	✓	✓
-1	$\left\|\phi^{(9)}\right\rangle = \prod_{\mathbf{k}} \hat{d}^\dagger_{\mathbf{k},+1,-,\downarrow} \prod_{e_Y=\pm1} \frac{\hat{d}^\dagger_{\mathbf{k},e_Y,+,\uparrow} + e_Y \hat{d}^\dagger_{\mathbf{k},e_Y,-,\uparrow}}{\sqrt{2}} \|0\rangle$	Appendix [G 10]	$C = 1$, two occupied KIVC bands and a valley polarized band	✓	✓	✓
0	$\left\|\phi^{(10)}\right\rangle = \prod_{\mathbf{k}} \prod_{e_Y=\pm1} \prod_{s=\uparrow,\downarrow} \frac{\hat{d}^\dagger_{\mathbf{k},e_Y,+,s} + e_Y \hat{d}^\dagger_{\mathbf{k},e_Y,-,s}}{\sqrt{2}} \|0\rangle$	Appendix [G 11]	$C = 0$, KIVC	✓	✓	✓
0	$\left\|\phi^{(11)}\right\rangle = \prod_{\mathbf{k}} \prod_{e_Y=\pm1} \prod_{s=\uparrow,\downarrow} \hat{d}^\dagger_{\mathbf{k},e_Y,+,s} \|0\rangle$	Appendix [G 12]	$C = 0$, valley polarized	✓	✓	✓
0	$\left\|\phi^{(12)}\right\rangle = \prod_{\mathbf{k}} \prod_{\eta=\pm} \prod_{s=\uparrow,\downarrow} \hat{d}^\dagger_{\mathbf{k},+1,\eta,s} \|0\rangle$	Appendix [G 13]	$C = 4$, valley polarized	✓	✓	✓
$+4$	$\left\|\phi^{(13)}\right\rangle = \prod_{\mathbf{k}} \prod_{\eta=\pm} \prod_{s=\uparrow,\downarrow} \prod_{e_Y=\pm1} \hat{d}^\dagger_{\mathbf{k},e_Y,\eta,s} \|0\rangle$	Appendix [G 14]	Insulator with all TBG active bands filled	✓	✓	✓

TABLE II. Model insulator states of TBG, for which we study the spectral function. Each model insulator is investigated for multiple values of the w_0/w_1. For each value of w_0/w_1 and type of potential, we indicate whether the insulator shows only positive-energy charge-one and charge neutral excitations (✓) or not (✗). If an insulator has negative-energy excitations, then we do not compute the spectral function (as this implies the insulators is not a ground state of H_I).

1. $\nu = -4$, insulator with all TBG active bands empty: $|0\rangle$

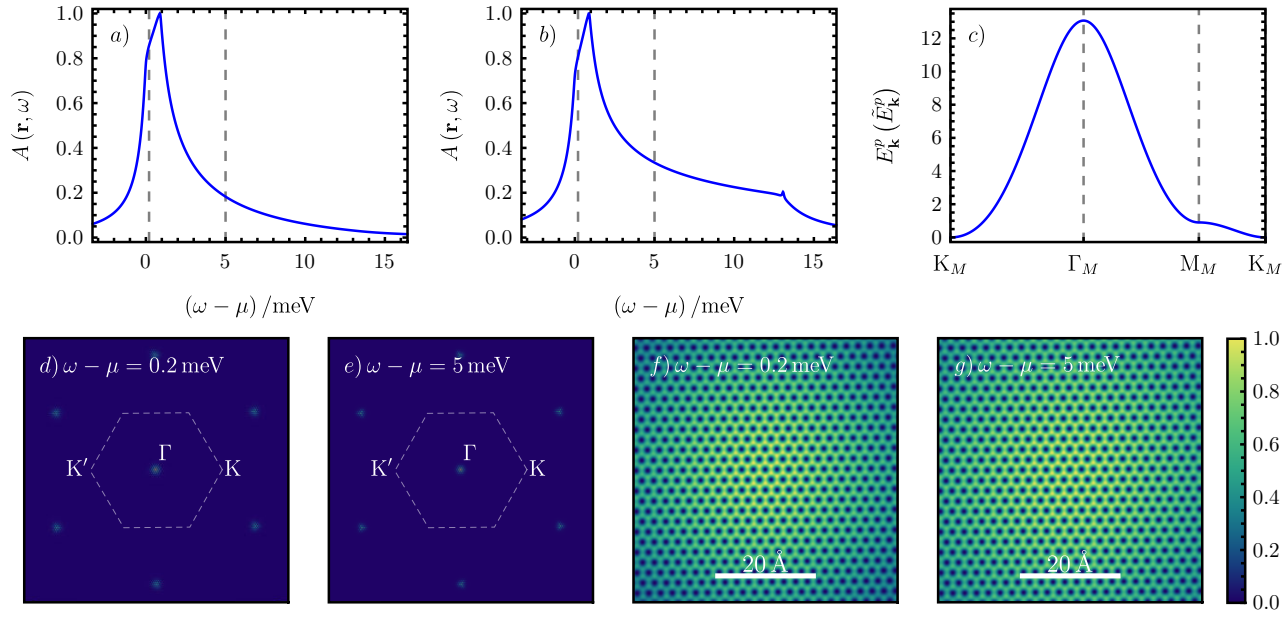

FIG. 11. $\nu = -4$, *insulator with all TBG active bands empty*: The real-space spectral function averaged over three graphene unit cells at the AA site [panel a)] and at the AB site [panel b)]. The electron (blue) and hole (orange) dispersion is shown in panel c). In panels d)-g), we illustrate the spatial variation of the spectral function in momentum space [d) and e)], as well as real space [f) and g)] for the two energy choices depicted by dashed gray lines in panels a) and b). Here, we focus on $(w_0/w_1, \lambda) = (0.0, 0)$.

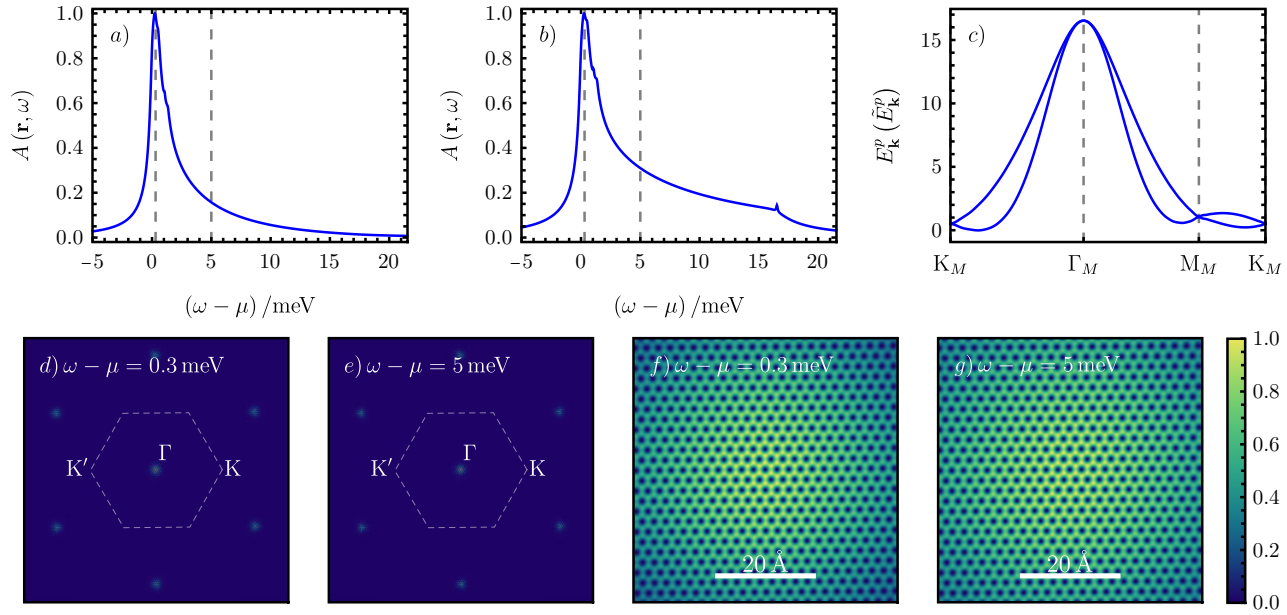

FIG. 12. $\nu = -4$, *insulator with all TBG active bands empty*: The real-space spectral function averaged over three graphene unit cells at the AA site [panel a)] and at the AB site [panel b)]. The electron (blue) and hole (orange) dispersion is shown in panel c). In panels d)-g), we illustrate the spatial variation of the spectral function in momentum space [d) and e)], as well as real space [f) and g)] for the two energy choices depicted by dashed gray lines in panels a) and b). Here, we focus on $(w_0/w_1, \lambda) = (0.4, 0)$.

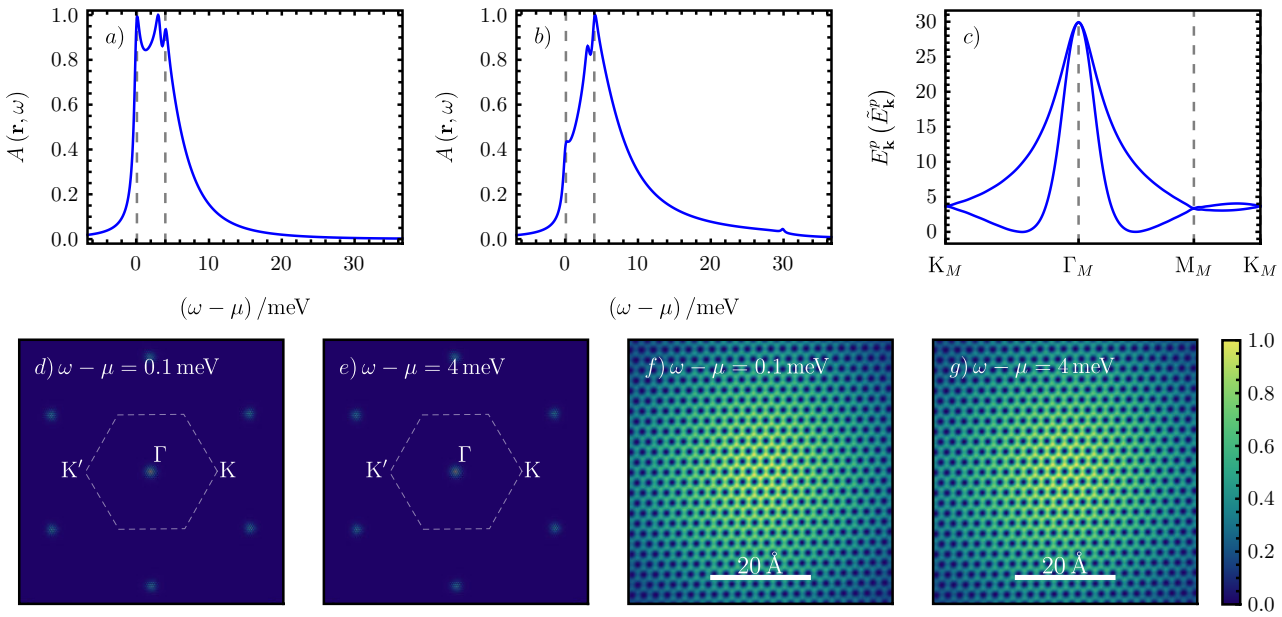

FIG. 13. $\nu=-4$, *insulator with all TBG active bands empty*: The real-space spectral function averaged over three graphene unit cells at the AA site [panel a)] and at the AB site [panel b)]. The electron (blue) and hole (orange) dispersion is shown in panel c). In panels d)-g), we illustrate the spatial variation of the spectral function in momentum space [d) and e)], as well as real space [f) and g)] for the two energy choices depicted by dashed gray lines in panels a) and b). Here, we focus on $(w_0/w_1,\lambda)=(0.8,0)$.

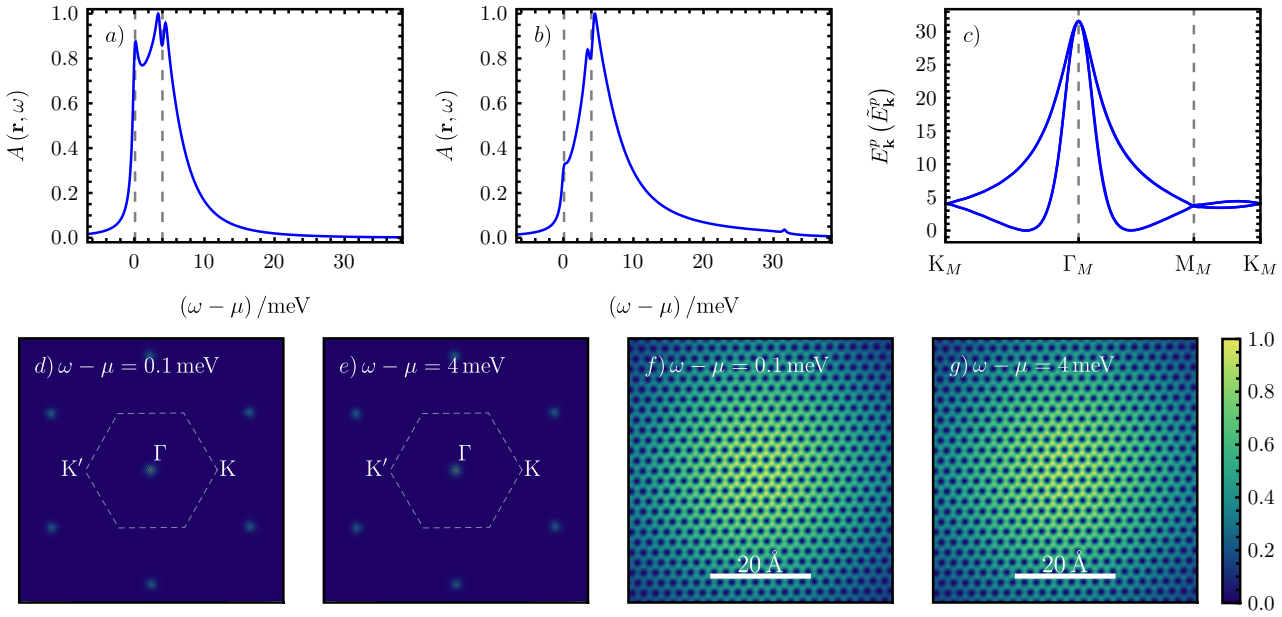

FIG. 14. $\nu=-4$, *insulator with all TBG active bands empty*: The real-space spectral function averaged over three graphene unit cells at the AA site [panel a)] and at the AB site [panel b)]. The electron (blue) and hole (orange) dispersion is shown in panel c). In panels d)-g), we illustrate the spatial variation of the spectral function in momentum space [d) and e)], as well as real space [f) and g)] for the two energy choices depicted by dashed gray lines in panels a) and b). Here, we focus on $(w_0/w_1,\lambda)=(0.8,1)$.

2. $\nu = -3$, $C = 1$, valley polarized: $\prod_{\mathbf{k}} \hat{d}^{\dagger}_{\mathbf{k},+1,+,\uparrow} |0\rangle$

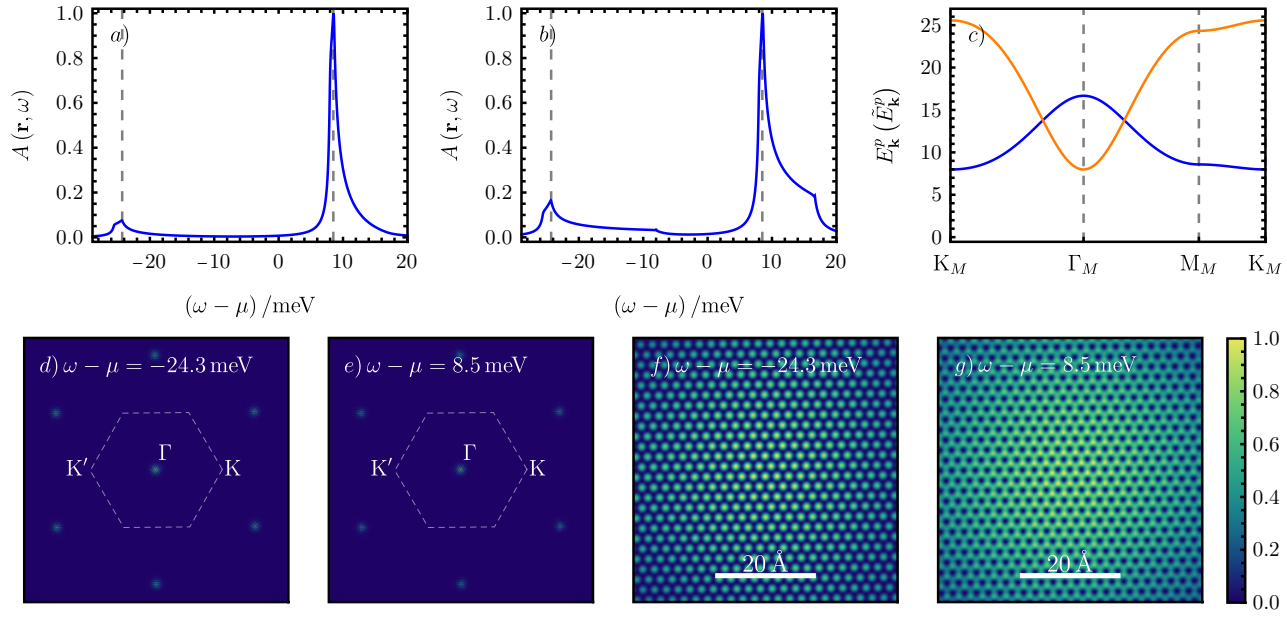

FIG. 15. $\nu = -3$, $C = 1$, *valley polarized*: The real-space spectral function averaged over three graphene unit cells at the AA site [panel a)] and at the AB site [panel b)]. The electron (blue) and hole (orange) dispersion is shown in panel c). In panels d)-g), we illustrate the spatial variation of the spectral function in momentum space [d) and e)], as well as real space [f) and g)] for the two energy choices depicted by dashed gray lines in panels a) and b). Here, we focus on $(w_0/w_1, \lambda) = (0.0, 0)$.

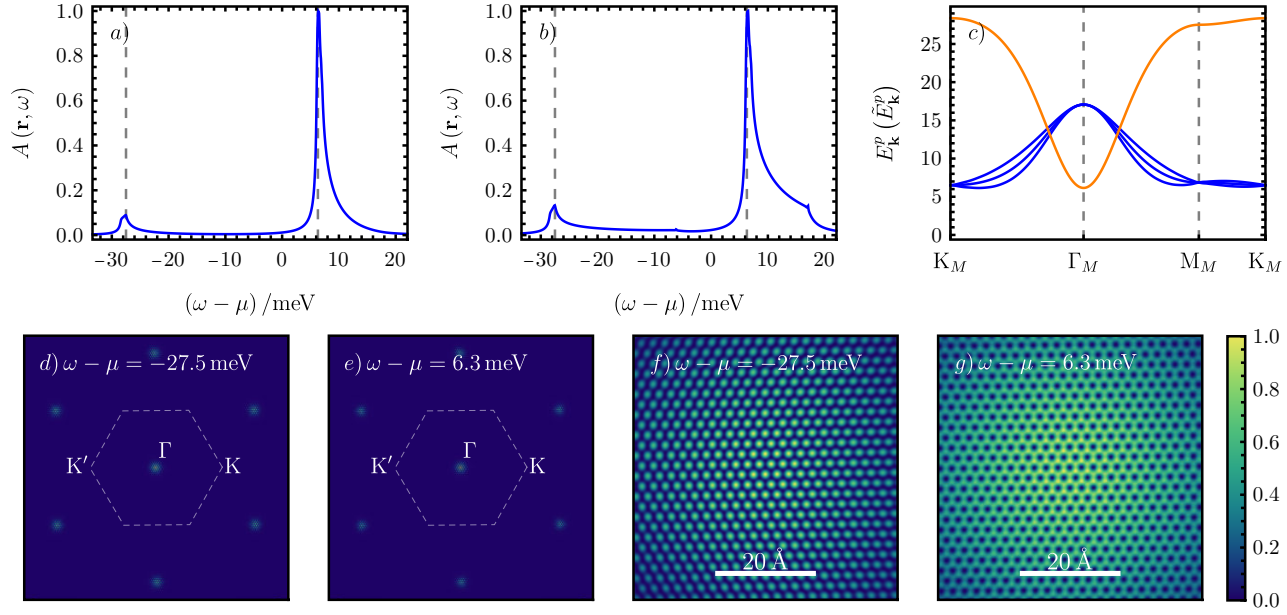

FIG. 16. $\nu = -3$, $C = 1$, *valley polarized*: The real-space spectral function averaged over three graphene unit cells at the AA site [panel a)] and at the AB site [panel b)]. The electron (blue) and hole (orange) dispersion is shown in panel c). In panels d)-g), we illustrate the spatial variation of the spectral function in momentum space [d) and e)], as well as real space [f) and g)] for the two energy choices depicted by dashed gray lines in panels a) and b). Here, we focus on $(w_0/w_1, \lambda) = (0.4, 0)$.

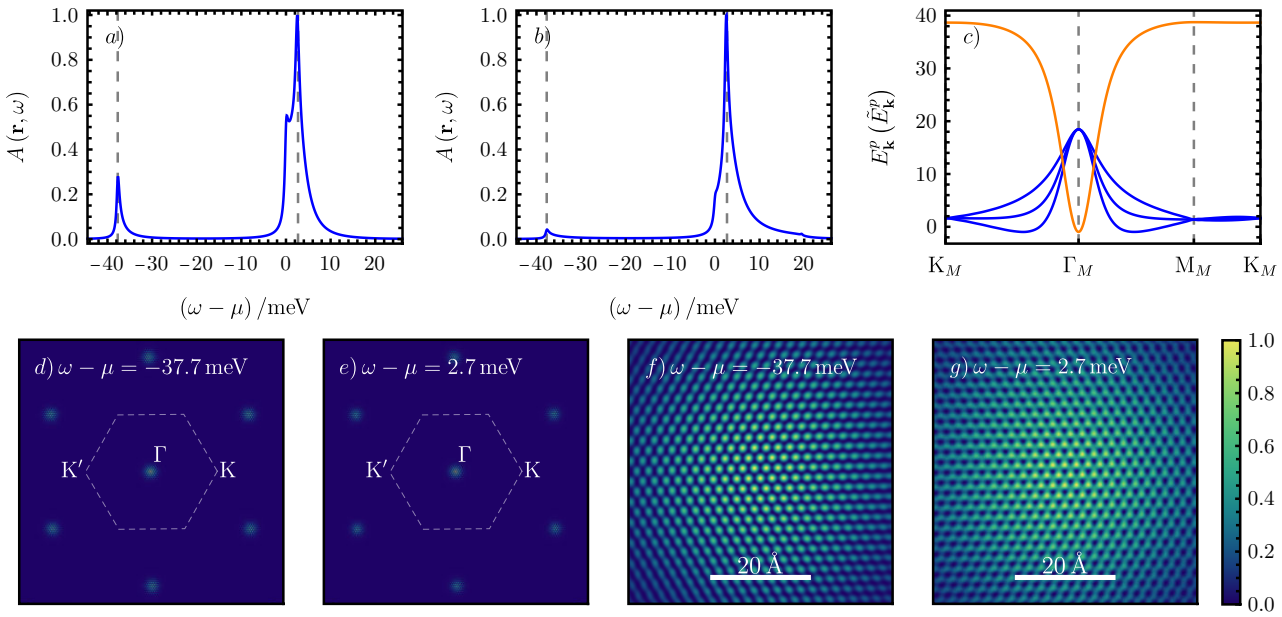

FIG. 17. $\nu=-3$, $C=1$, *valley polarized*: The real-space spectral function averaged over three graphene unit cells at the AA site [panel a)] and at the AB site [panel b)]. The electron (blue) and hole (orange) dispersion is shown in panel c). In panels d)-g), we illustrate the spatial variation of the spectral function in momentum space [d) and e)], as well as real space [f) and g)] for the two energy choices depicted by dashed gray lines in panels a) and b). Here, we focus on $(w_0/w_1,\lambda)=(0.8,0)$.

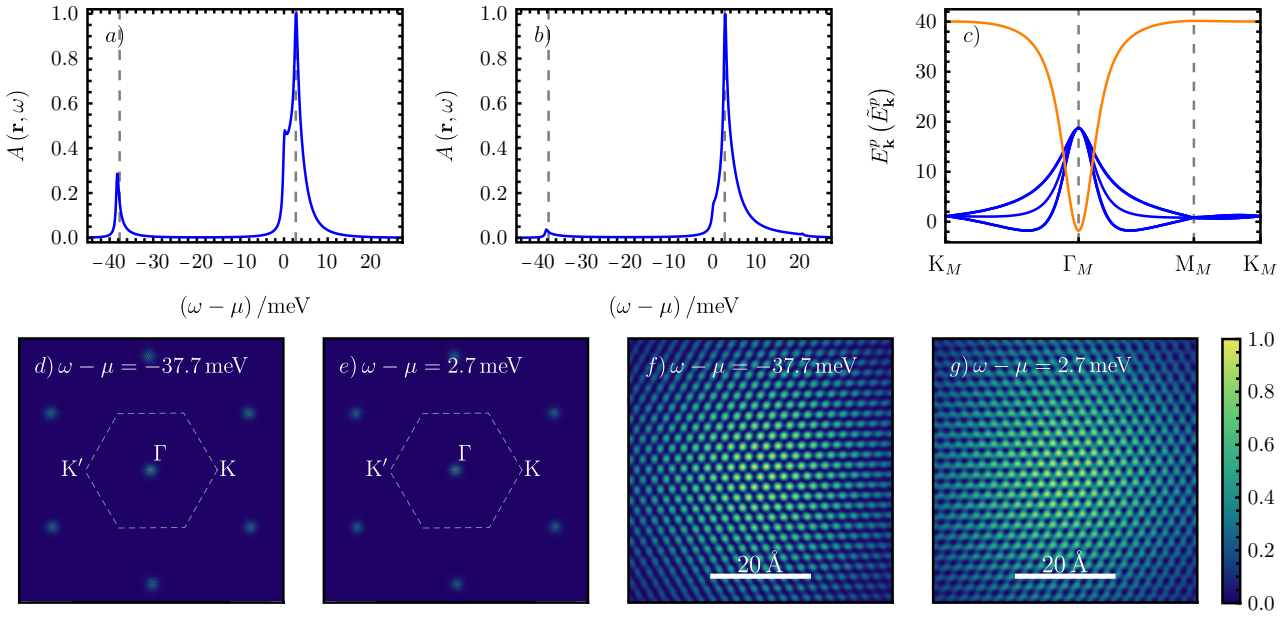

FIG. 18. $\nu=-3$, $C=1$, *valley polarized*: The real-space spectral function averaged over three graphene unit cells at the AA site [panel a)] and at the AB site [panel b)]. The electron (blue) and hole (orange) dispersion is shown in panel c). In panels d)-g), we illustrate the spatial variation of the spectral function in momentum space [d) and e)], as well as real space [f) and g)] for the two energy choices depicted by dashed gray lines in panels a) and b). Here, we focus on $(w_0/w_1,\lambda)=(0.8,1)$.

3. $\nu = -3$, $C = 1$, valley coherent: $\prod_{\mathbf{k}} \frac{\hat{d}^\dagger_{\mathbf{k},+1,+,\uparrow} + \hat{d}^\dagger_{\mathbf{k},+1,-,\uparrow}}{\sqrt{2}} |0\rangle$

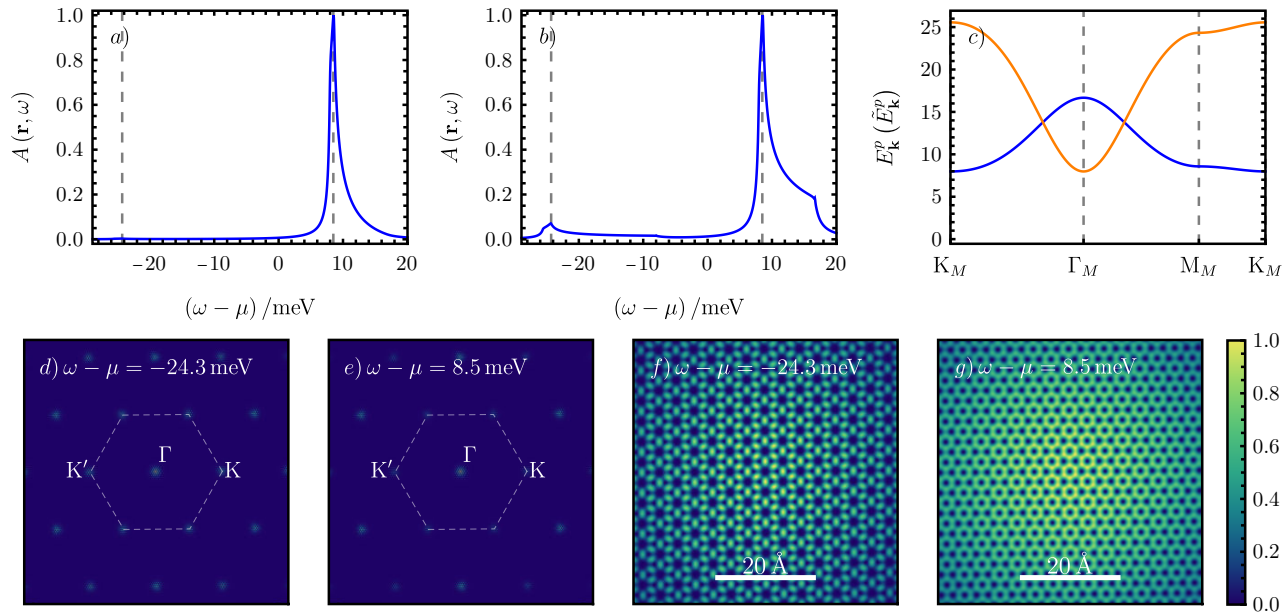

FIG. 19. $\nu = -3$, $C = 1$, *valley coherent*: The real-space spectral function averaged over three graphene unit cells at the AA site [panel a)] and at the AB site [panel b)]. The electron (blue) and hole (orange) dispersion is shown in panel c). In panels d)-g), we illustrate the spatial variation of the spectral function in momentum space [d) and e)], as well as real space [f) and g)] for the two energy choices depicted by dashed gray lines in panels a) and b). Here, we focus on $(w_0/w_1, \lambda) = (0.0, 0)$.

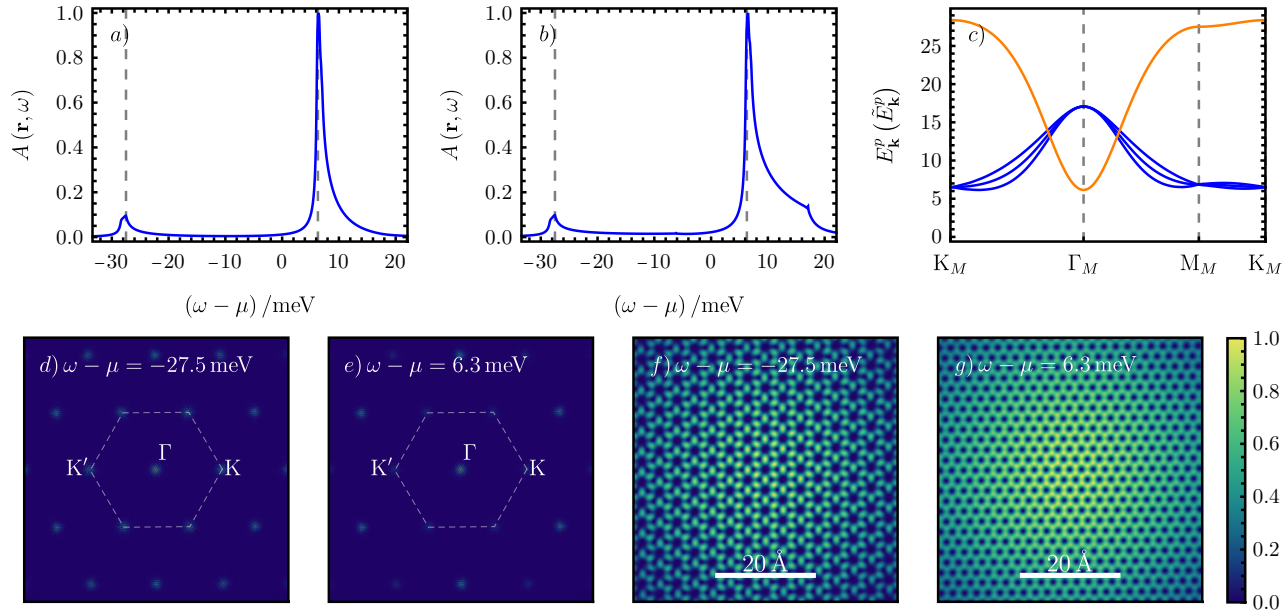

FIG. 20. $\nu = -3$, $C = 1$, *valley coherent*: The real-space spectral function averaged over three graphene unit cells at the AA site [panel a)] and at the AB site [panel b)]. The electron (blue) and hole (orange) dispersion is shown in panel c). In panels d)-g), we illustrate the spatial variation of the spectral function in momentum space [d) and e)], as well as real space [f) and g)] for the two energy choices depicted by dashed gray lines in panels a) and b). Here, we focus on $(w_0/w_1, \lambda) = (0.4, 0)$.

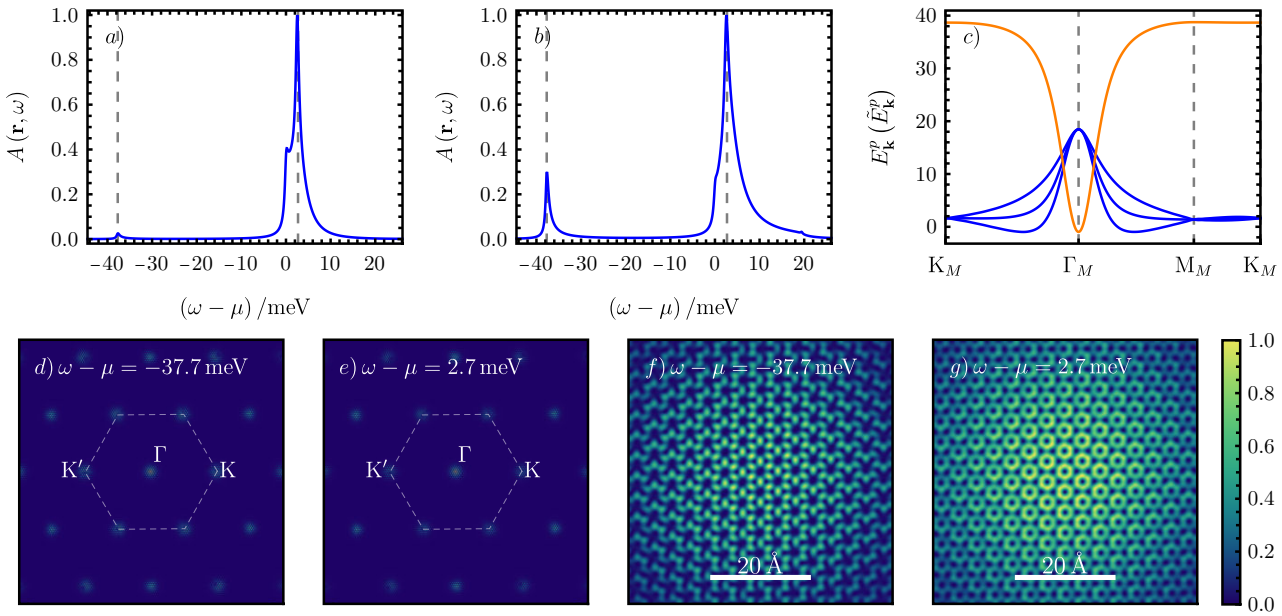

FIG. 21. $\nu=-3$, $C=1$, *valley coherent*: The real-space spectral function averaged over three graphene unit cells at the AA site [panel a)] and at the AB site [panel b)]. The electron (blue) and hole (orange) dispersion is shown in panel c). In panels d)-g), we illustrate the spatial variation of the spectral function in momentum space [d) and e)], as well as real space [f) and g)] for the two energy choices depicted by dashed gray lines in panels a) and b). Here, we focus on $(w_0/w_1,\lambda)=(0.8,0)$.

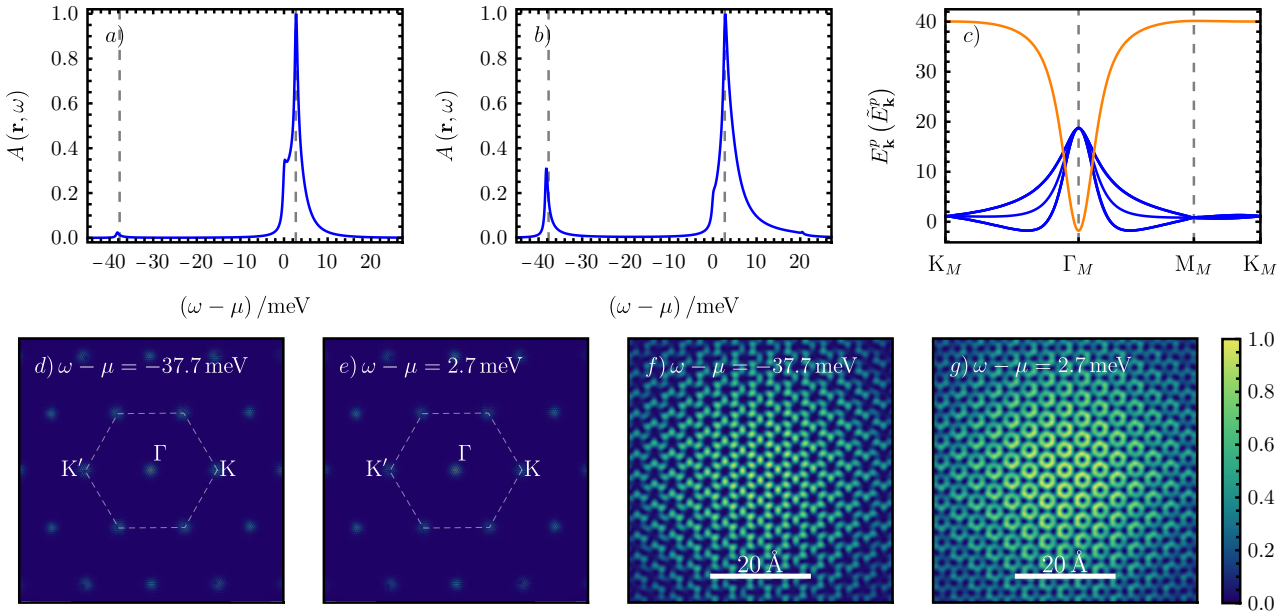

FIG. 22. $\nu=-3$, $C=1$, *valley coherent*: The real-space spectral function averaged over three graphene unit cells at the AA site [panel a)] and at the AB site [panel b)]. The electron (blue) and hole (orange) dispersion is shown in panel c). In panels d)-g), we illustrate the spatial variation of the spectral function in momentum space [d) and e)], as well as real space [f) and g)] for the two energy choices depicted by dashed gray lines in panels a) and b). Here, we focus on $(w_0/w_1,\lambda)=(0.8,1)$.

4. $\nu = -2$, $C = 0$, **KIVC:** $\prod_{\mathbf{k}} \prod_{e_Y=\pm 1} \frac{\hat{d}^\dagger_{\mathbf{k},e_Y,+,\uparrow} + e_Y \hat{d}^\dagger_{\mathbf{k},e_Y,-,\uparrow}}{\sqrt{2}} |0\rangle$

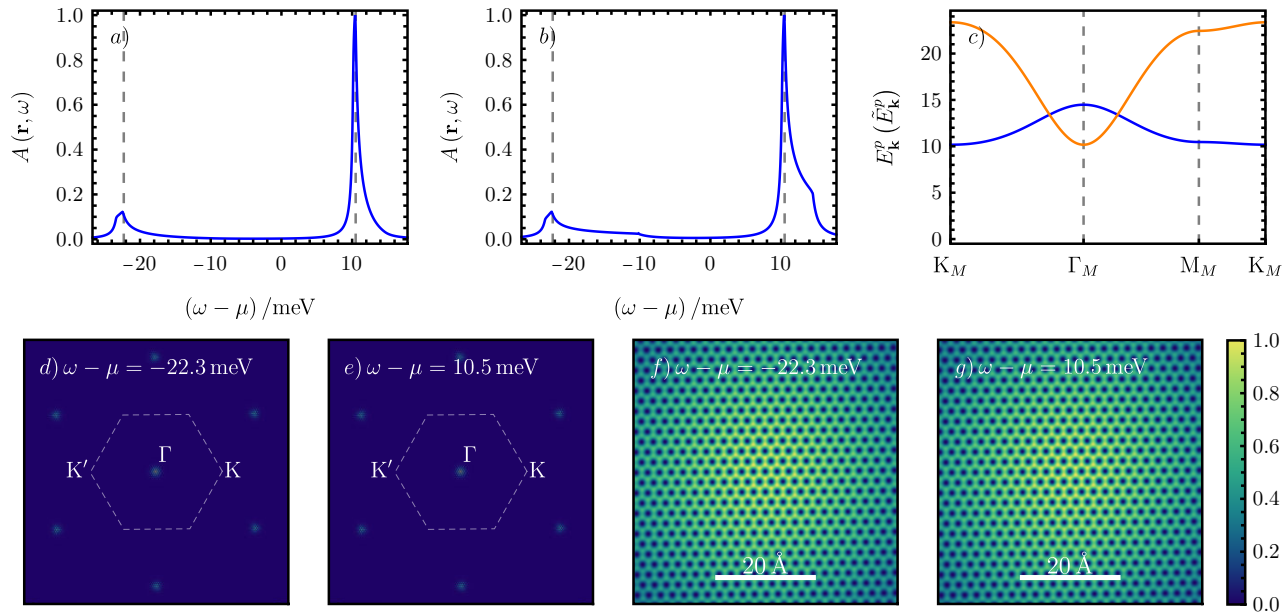

FIG. 23. $\nu = -2$, $C = 0$, *KIVC*: The real-space spectral function averaged over three graphene unit cells at the AA site [panel a)] and at the AB site [panel b)]. The electron (blue) and hole (orange) dispersion is shown in panel c). In panels d)-g), we illustrate the spatial variation of the spectral function in momentum space [d) and e)], as well as real space [f) and g)] for the two energy choices depicted by dashed gray lines in panels a) and b). Here, we focus on $(w_0/w_1, \lambda) = (0.0, 0)$.

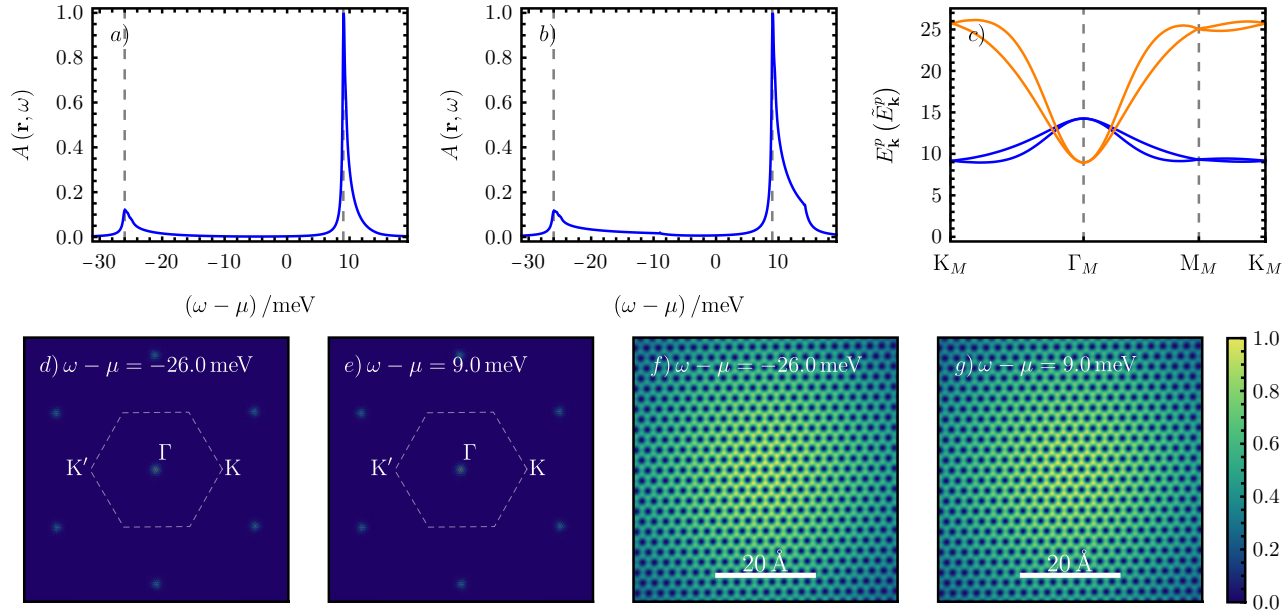

FIG. 24. $\nu = -2$, $C = 0$, *KIVC*: The real-space spectral function averaged over three graphene unit cells at the AA site [panel a)] and at the AB site [panel b)]. The electron (blue) and hole (orange) dispersion is shown in panel c). In panels d)-g), we illustrate the spatial variation of the spectral function in momentum space [d) and e)], as well as real space [f) and g)] for the two energy choices depicted by dashed gray lines in panels a) and b). Here, we focus on $(w_0/w_1, \lambda) = (0.4, 0)$.

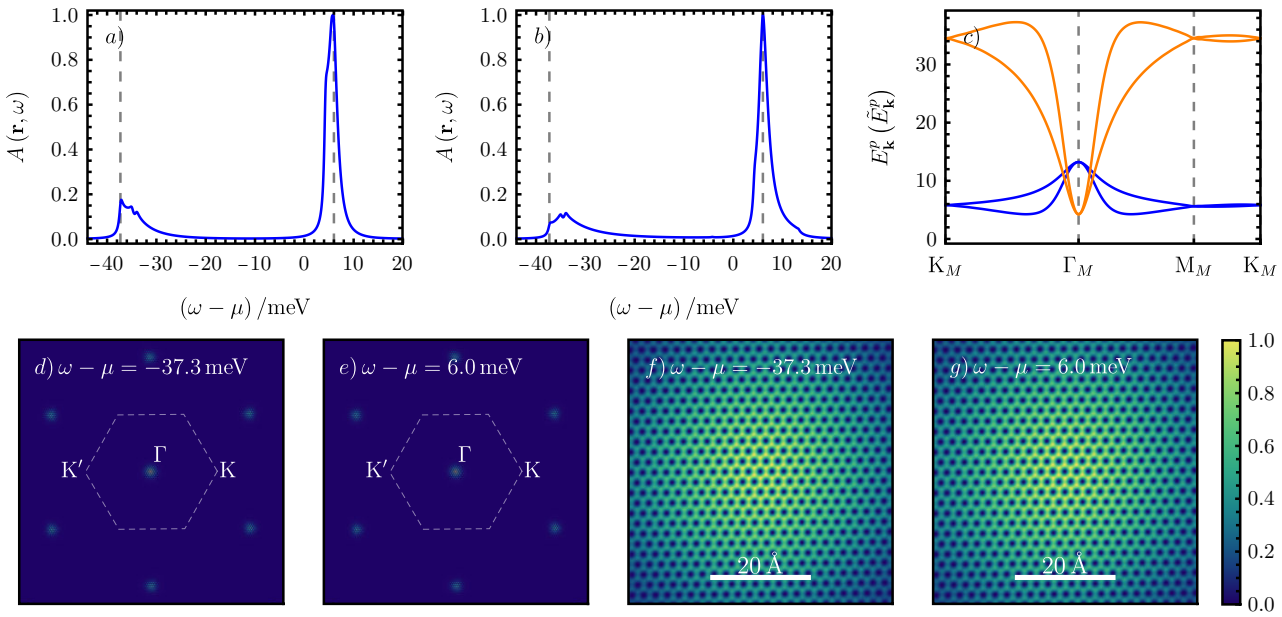

FIG. 25. $\nu=-2$, $C=0$, *KIVC*: The real-space spectral function averaged over three graphene unit cells at the AA site [panel a)] and at the AB site [panel b)]. The electron (blue) and hole (orange) dispersion is shown in panel c). In panels d)-g), we illustrate the spatial variation of the spectral function in momentum space [d) and e)], as well as real space [f) and g)] for the two energy choices depicted by dashed gray lines in panels a) and b). Here, we focus on $(w_0/w_1,\lambda)=(0.8,0)$.

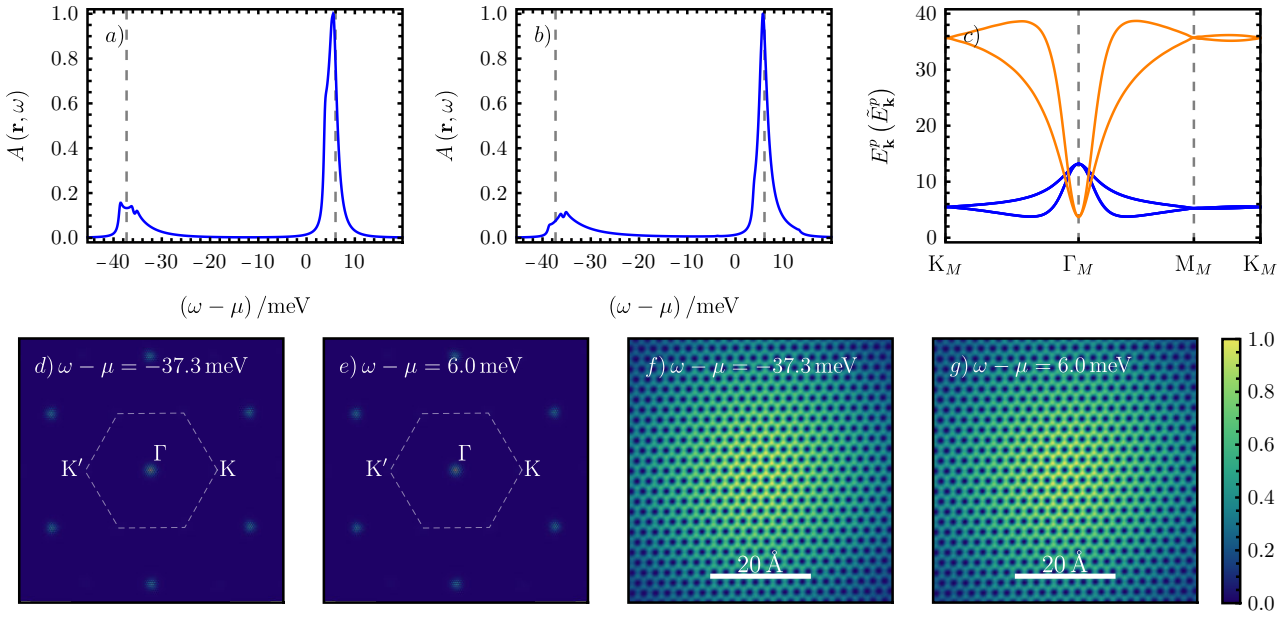

FIG. 26. $\nu=-2$, $C=0$, *KIVC*: The real-space spectral function averaged over three graphene unit cells at the AA site [panel a)] and at the AB site [panel b)]. The electron (blue) and hole (orange) dispersion is shown in panel c). In panels d)-g), we illustrate the spatial variation of the spectral function in momentum space [d) and e)], as well as real space [f) and g)] for the two energy choices depicted by dashed gray lines in panels a) and b). Here, we focus on $(w_0/w_1,\lambda)=(0.8,1)$.

5. $\nu = -2$, $C = 0$, **TIVC:** $\prod_{\mathbf{k}} \prod_{e_Y=\pm 1} \frac{\hat{d}^\dagger_{\mathbf{k},e_Y,+,\uparrow} + \hat{d}^\dagger_{\mathbf{k},e_Y,-,\uparrow}}{\sqrt{2}} |0\rangle$

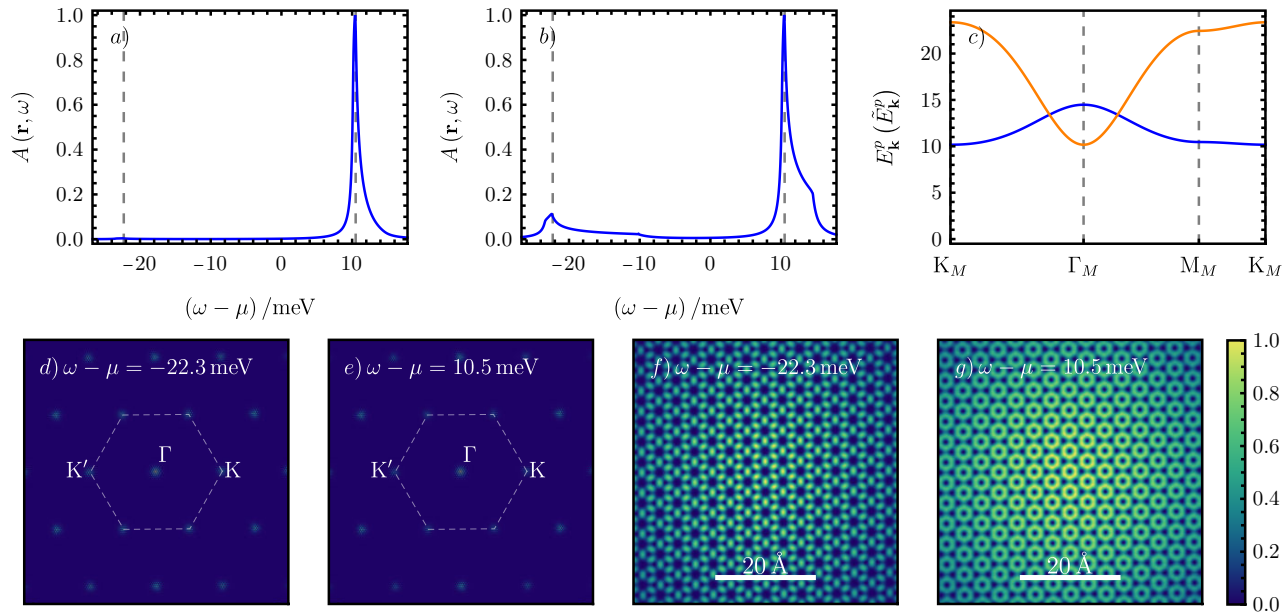

FIG. 27. $\nu = -2$, $C = 0$, *TIVC*: The real-space spectral function averaged over three graphene unit cells at the AA site [panel a)] and at the AB site [panel b)]. The electron (blue) and hole (orange) dispersion is shown in panel c). In panels d)-g), we illustrate the spatial variation of the spectral function in momentum space [d) and e)], as well as real space [f) and g)] for the two energy choices depicted by dashed gray lines in panels a) and b). Here, we focus on $(w_0/w_1, \lambda) = (0.0, 0)$.

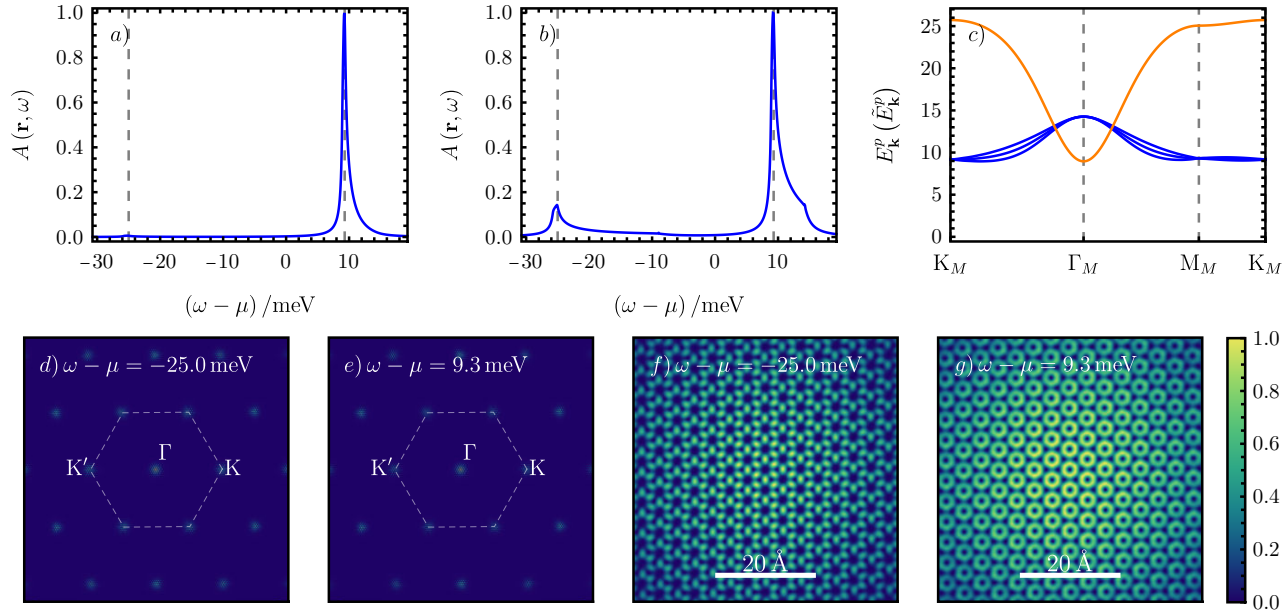

FIG. 28. $\nu = -2$, $C = 0$, *TIVC*: The real-space spectral function averaged over three graphene unit cells at the AA site [panel a)] and at the AB site [panel b)]. The electron (blue) and hole (orange) dispersion is shown in panel c). In panels d)-g), we illustrate the spatial variation of the spectral function in momentum space [d) and e)], as well as real space [f) and g)] for the two energy choices depicted by dashed gray lines in panels a) and b). Here, we focus on $(w_0/w_1, \lambda) = (0.4, 0)$.

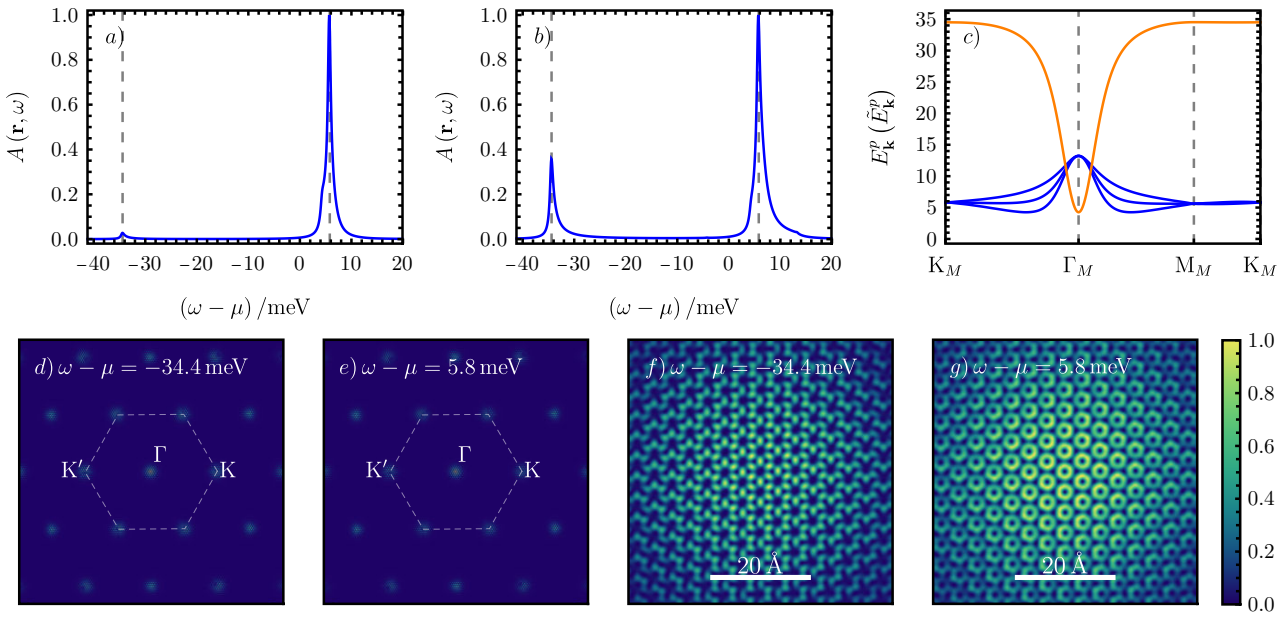

FIG. 29. $\nu=-2$, $C=0$, *TIVC*: The real-space spectral function averaged over three graphene unit cells at the AA site [panel a)] and at the AB site [panel b)]. The electron (blue) and hole (orange) dispersion is shown in panel c). In panels d)-g), we illustrate the spatial variation of the spectral function in momentum space [d) and e)], as well as real space [f) and g)] for the two energy choices depicted by dashed gray lines in panels a) and b). Here, we focus on $(w_0/w_1,\lambda)=(0.8,0)$.

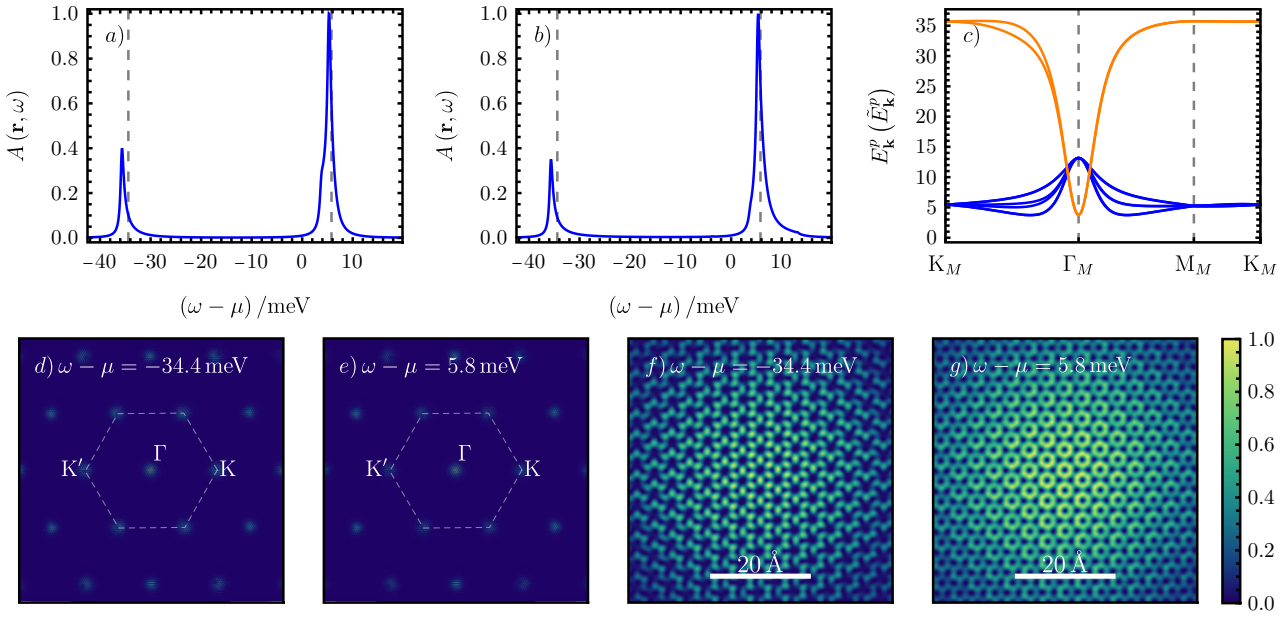

FIG. 30. $\nu=-2$, $C=0$, *TIVC*: The real-space spectral function averaged over three graphene unit cells at the AA site [panel a)] and at the AB site [panel b)]. The electron (blue) and hole (orange) dispersion is shown in panel c). In panels d)-g), we illustrate the spatial variation of the spectral function in momentum space [d) and e)], as well as real space [f) and g)] for the two energy choices depicted by dashed gray lines in panels a) and b). Here, we focus on $(w_0/w_1,\lambda)=(0.8,1)$.

6. $\nu = -2$, $C = 0$, valley polarized: $\prod_{\mathbf{k}} \hat{d}^{\dagger}_{\mathbf{k},+1,+,\uparrow} \hat{d}^{\dagger}_{\mathbf{k},-1,+,\uparrow} |0\rangle$

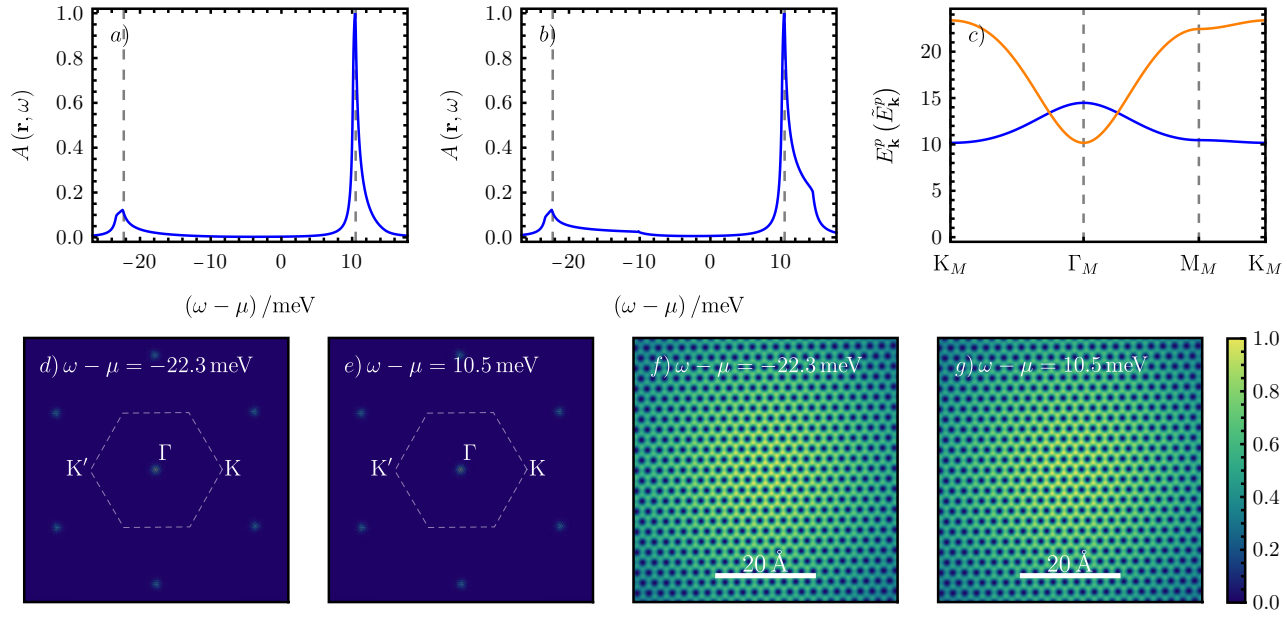

FIG. 31. $\nu = -2$, $C = 0$, *valley polarized*: The real-space spectral function averaged over three graphene unit cells at the AA site [panel a)] and at the AB site [panel b)]. The electron (blue) and hole (orange) dispersion is shown in panel c). In panels d)-g), we illustrate the spatial variation of the spectral function in momentum space [d) and e)], as well as real space [f) and g)] for the two energy choices depicted by dashed gray lines in panels a) and b). Here, we focus on $(w_0/w_1, \lambda) = (0.0, 0)$.

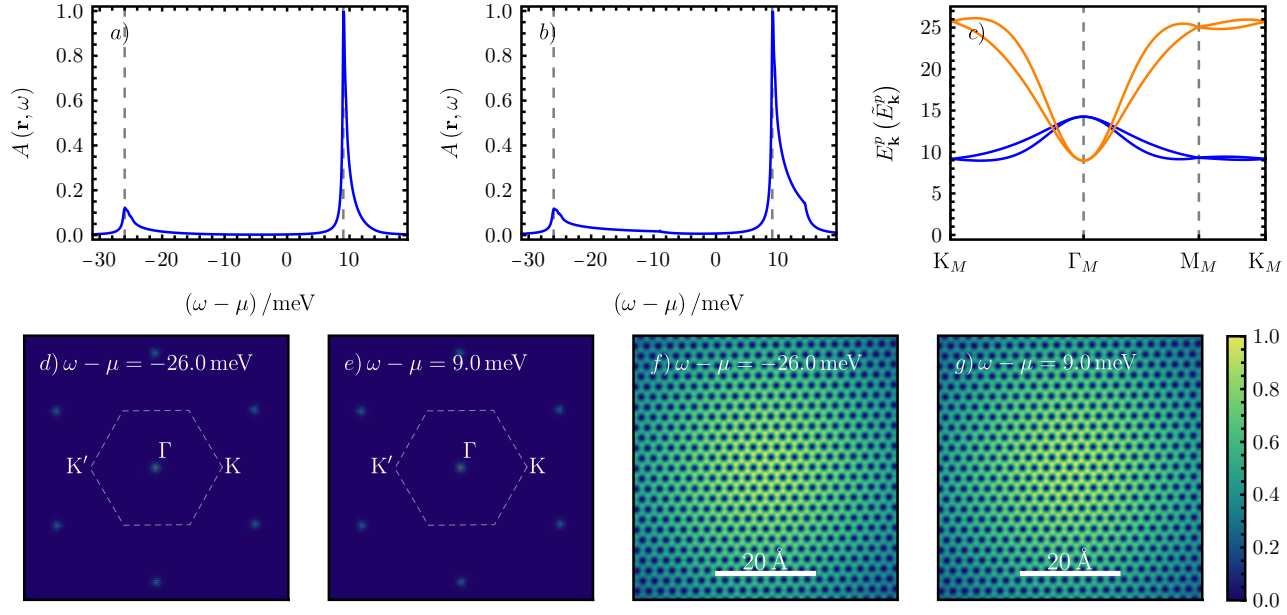

FIG. 32. $\nu = -2$, $C = 0$, *valley polarized*: The real-space spectral function averaged over three graphene unit cells at the AA site [panel a)] and at the AB site [panel b)]. The electron (blue) and hole (orange) dispersion is shown in panel c). In panels d)-g), we illustrate the spatial variation of the spectral function in momentum space [d) and e)], as well as real space [f) and g)] for the two energy choices depicted by dashed gray lines in panels a) and b). Here, we focus on $(w_0/w_1, \lambda) = (0.4, 0)$.

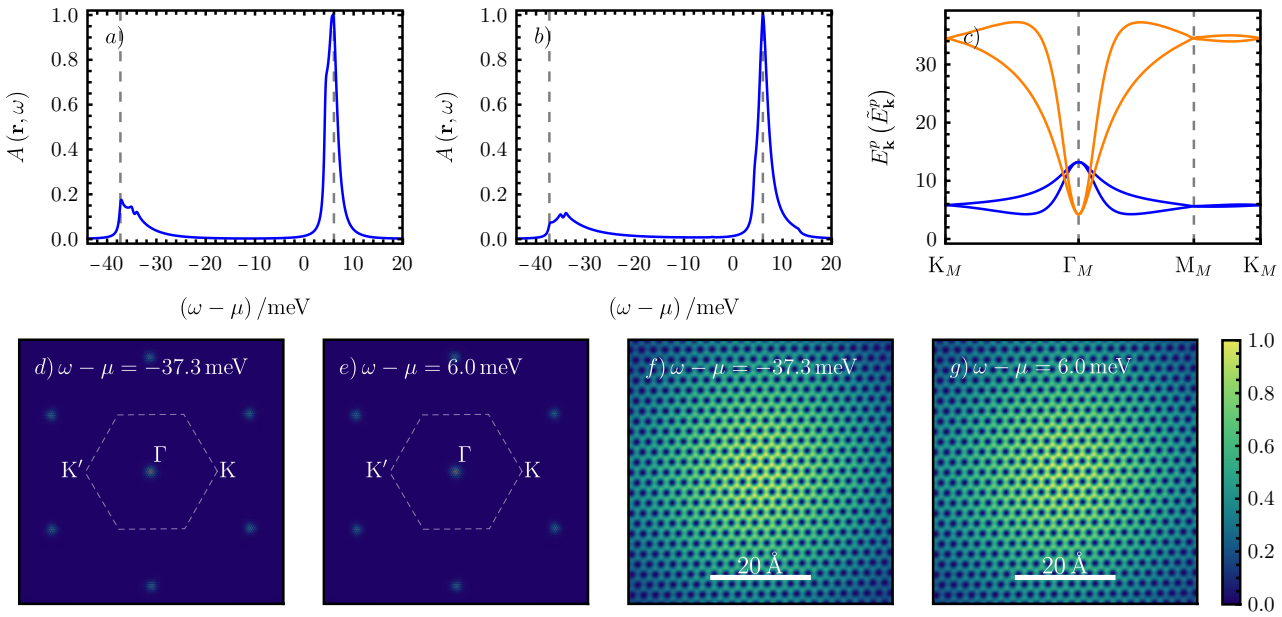

FIG. 33. $\nu=-2$, $C=0$, *valley polarized*: The real-space spectral function averaged over three graphene unit cells at the AA site [panel a)] and at the AB site [panel b)]. The electron (blue) and hole (orange) dispersion is shown in panel c). In panels d)-g), we illustrate the spatial variation of the spectral function in momentum space [d) and e)], as well as real space [f) and g)] for the two energy choices depicted by dashed gray lines in panels a) and b). Here, we focus on $(w_0/w_1,\lambda)=(0.8,0)$.

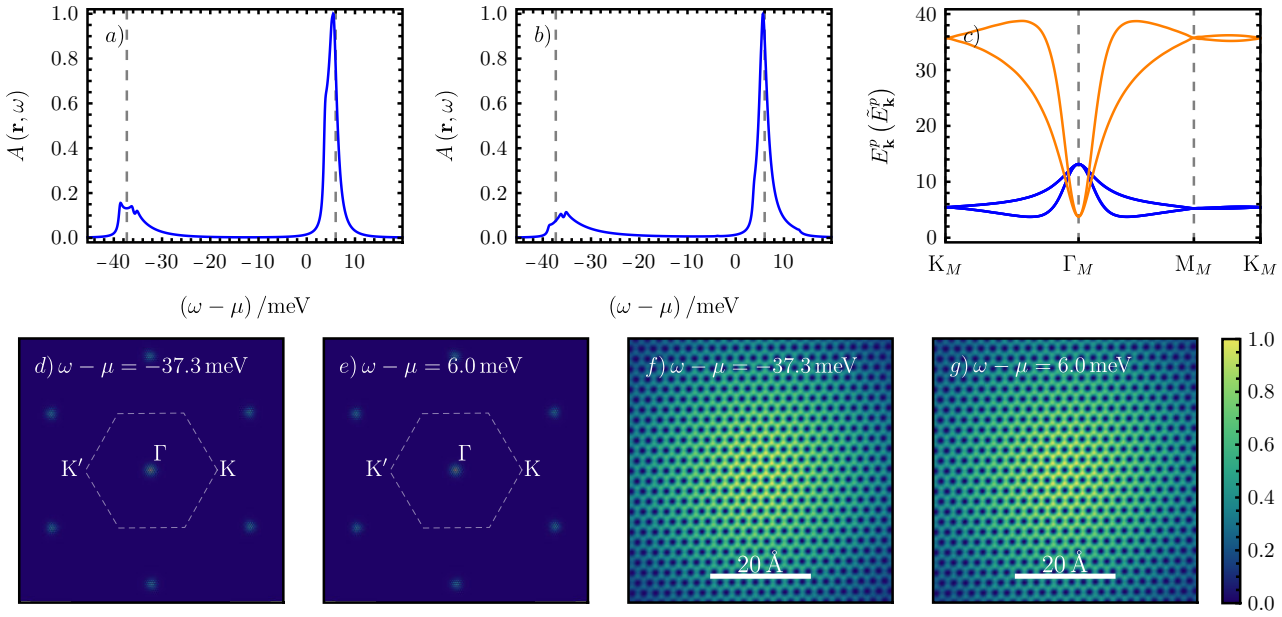

FIG. 34. $\nu=-2$, $C=0$, *valley polarized*: The real-space spectral function averaged over three graphene unit cells at the AA site [panel a)] and at the AB site [panel b)]. The electron (blue) and hole (orange) dispersion is shown in panel c). In panels d)-g), we illustrate the spatial variation of the spectral function in momentum space [d) and e)], as well as real space [f) and g)] for the two energy choices depicted by dashed gray lines in panels a) and b). Here, we focus on $(w_0/w_1,\lambda)=(0.8,1)$.

7. $\nu = -2$, $C = 2$, valley polarized: $\prod_{\mathbf{k}} \hat{d}^\dagger_{\mathbf{k},+1,+,\uparrow} \hat{d}^\dagger_{\mathbf{k},+1,+,\downarrow} |0\rangle$

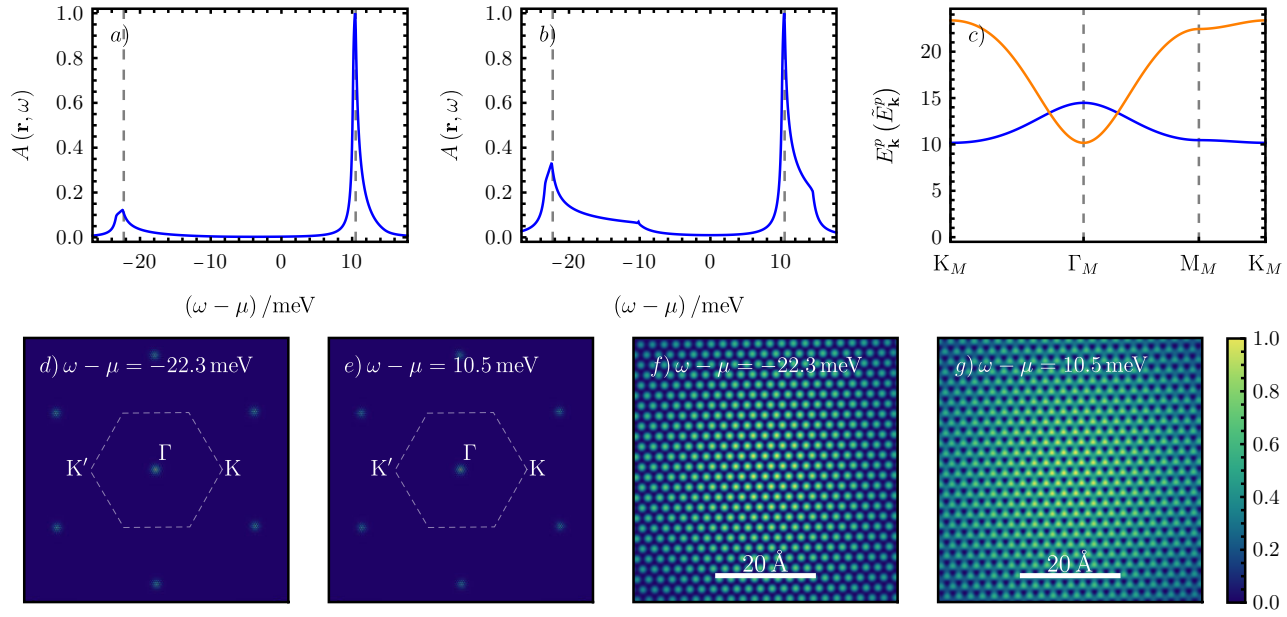

FIG. 35. $\nu = -2$, $C = 2$, *valley polarized*: The real-space spectral function averaged over three graphene unit cells at the AA site [panel a)] and at the AB site [panel b)]. The electron (blue) and hole (orange) dispersion is shown in panel c). In panels d)-g), we illustrate the spatial variation of the spectral function in momentum space [d) and e)], as well as real space [f) and g)] for the two energy choices depicted by dashed gray lines in panels a) and b). Here, we focus on $(w_0/w_1, \lambda) = (0.0, 0)$.

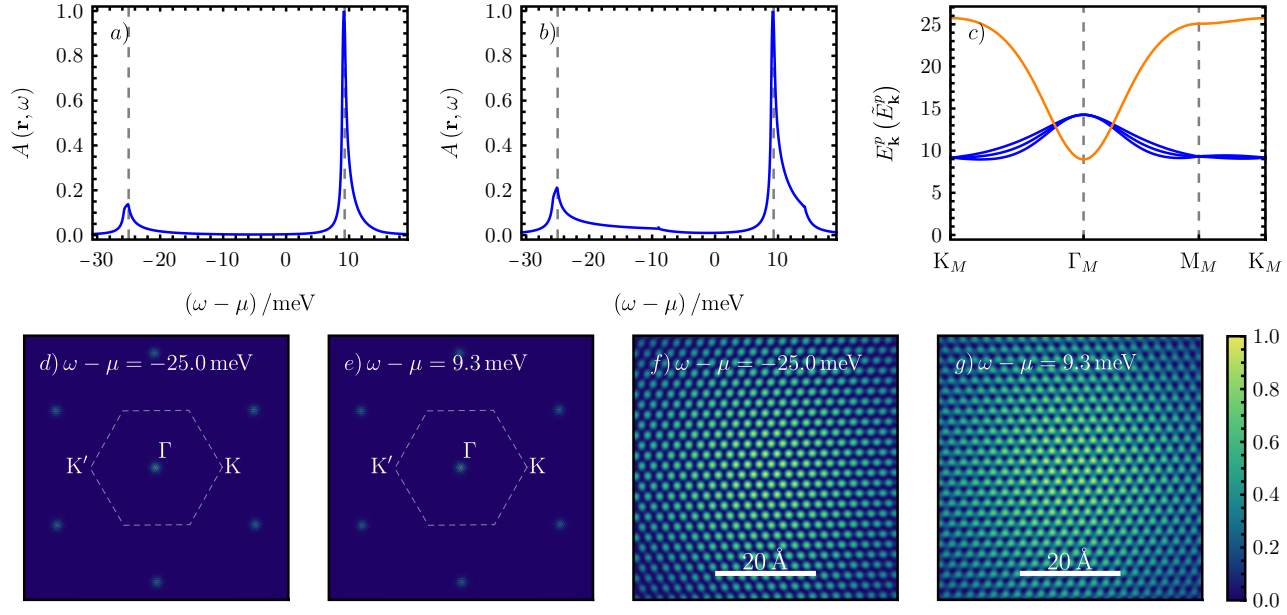

FIG. 36. $\nu = -2$, $C = 2$, *valley polarized*: The real-space spectral function averaged over three graphene unit cells at the AA site [panel a)] and at the AB site [panel b)]. The electron (blue) and hole (orange) dispersion is shown in panel c). In panels d)-g), we illustrate the spatial variation of the spectral function in momentum space [d) and e)], as well as real space [f) and g)] for the two energy choices depicted by dashed gray lines in panels a) and b). Here, we focus on $(w_0/w_1, \lambda) = (0.4, 0)$.

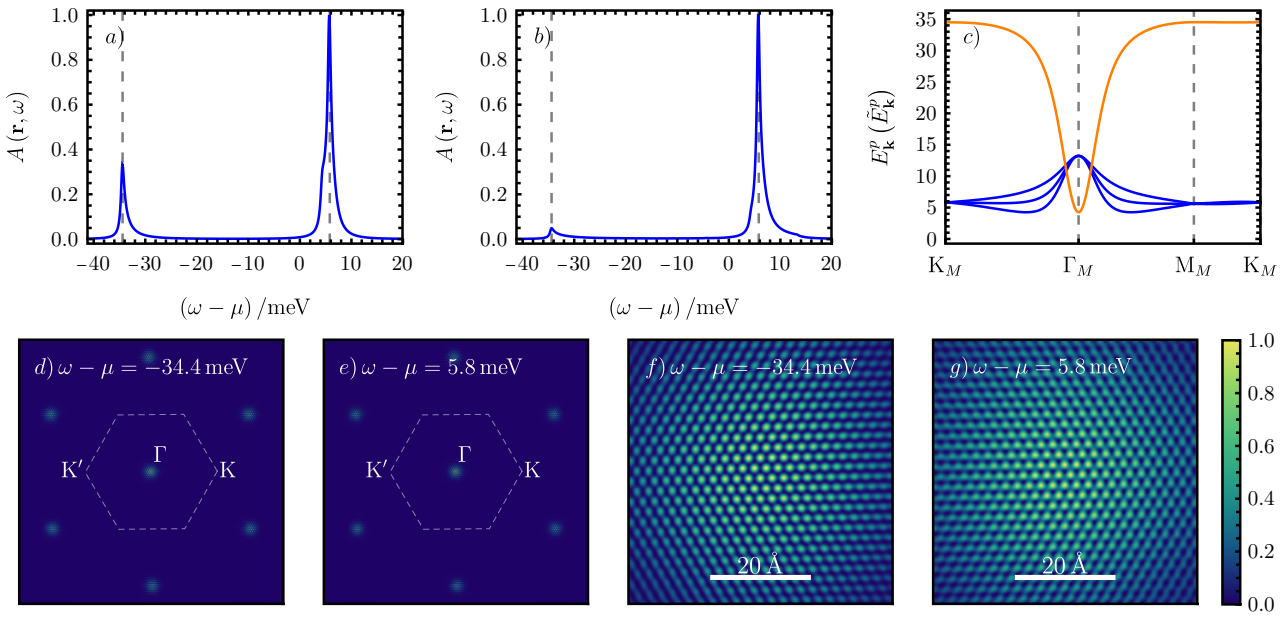

FIG. 37. $\nu=-2$, $C=2$, *valley polarized*: The real-space spectral function averaged over three graphene unit cells at the AA site [panel a)] and at the AB site [panel b)]. The electron (blue) and hole (orange) dispersion is shown in panel c). In panels d)-g), we illustrate the spatial variation of the spectral function in momentum space [d) and e)], as well as real space [f) and g)] for the two energy choices depicted by dashed gray lines in panels a) and b). Here, we focus on $(w_0/w_1,\lambda)=(0.8,0)$.

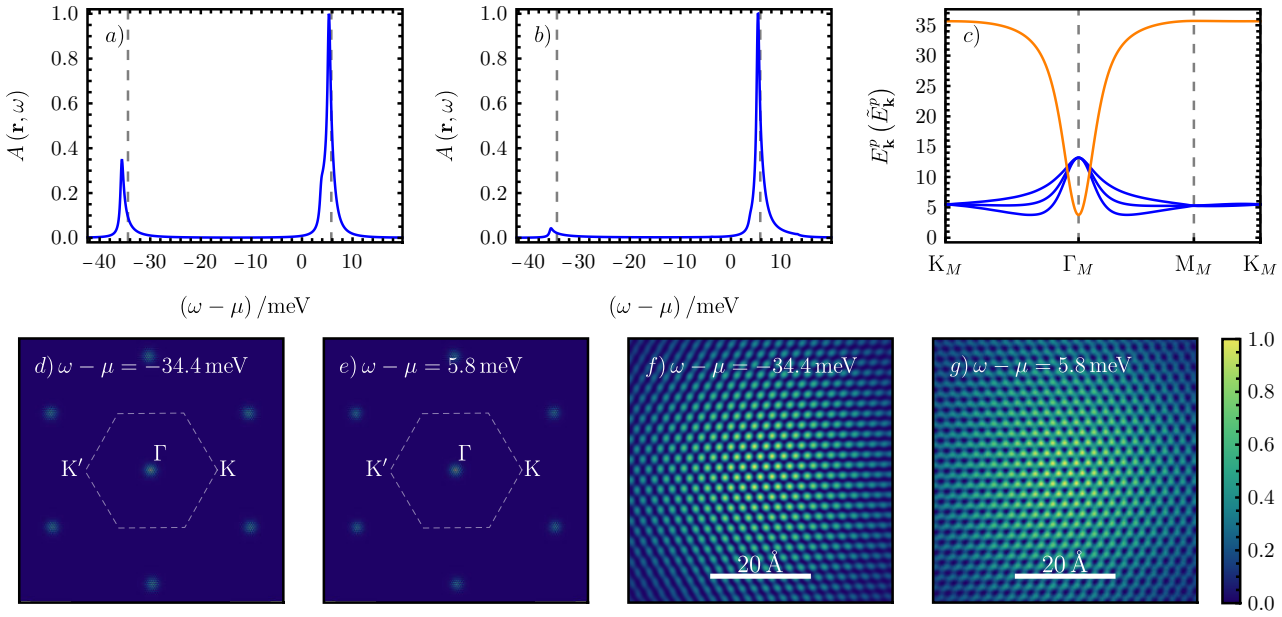

FIG. 38. $\nu=-2$, $C=2$, *valley polarized*: The real-space spectral function averaged over three graphene unit cells at the AA site [panel a)] and at the AB site [panel b)]. The electron (blue) and hole (orange) dispersion is shown in panel c). In panels d)-g), we illustrate the spatial variation of the spectral function in momentum space [d) and e)], as well as real space [f) and g)] for the two energy choices depicted by dashed gray lines in panels a) and b). Here, we focus on $(w_0/w_1,\lambda)=(0.8,1)$.

8. $\nu = -2$, $C = 2$, **valley coherent:** $\prod_{\mathbf{k}} \prod_{s=\uparrow,\downarrow} \frac{\hat{d}^\dagger_{\mathbf{k},+1,+,s} + \hat{d}^\dagger_{\mathbf{k},+1,-,s}}{\sqrt{2}} |0\rangle$

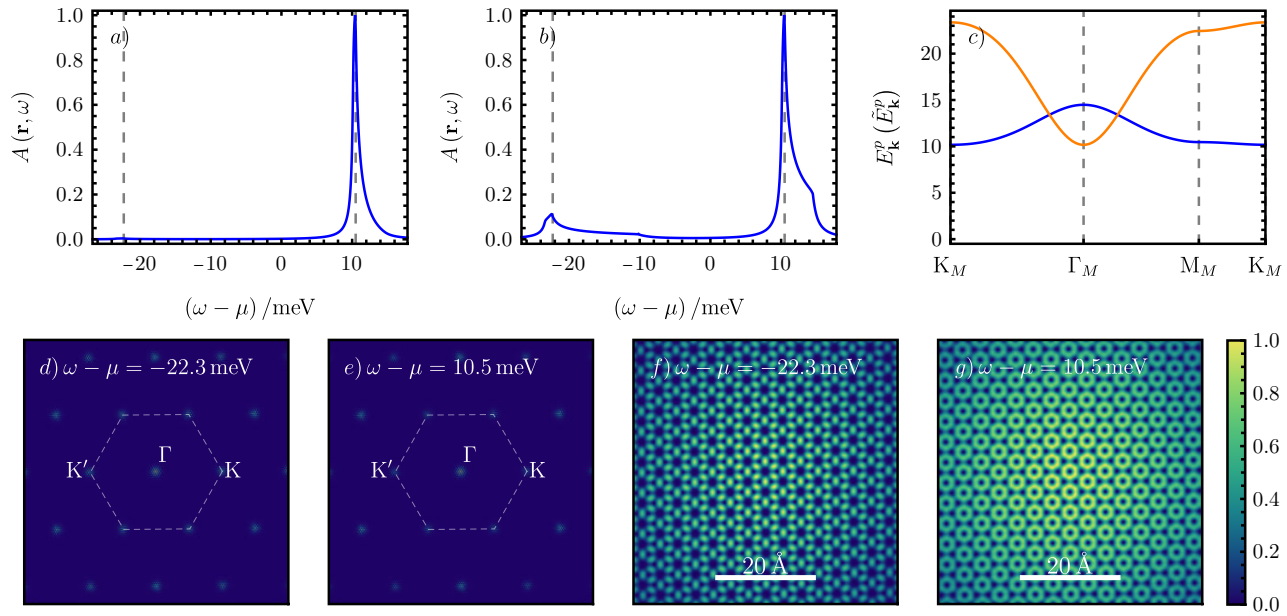

FIG. 39. $\nu = -2$, $C = 2$, *valley coherent*: The real-space spectral function averaged over three graphene unit cells at the AA site [panel a)] and at the AB site [panel b)]. The electron (blue) and hole (orange) dispersion is shown in panel c). In panels d)-g), we illustrate the spatial variation of the spectral function in momentum space [d) and e)], as well as real space [f) and g)] for the two energy choices depicted by dashed gray lines in panels a) and b). Here, we focus on $(w_0/w_1, \lambda) = (0.0, 0)$.

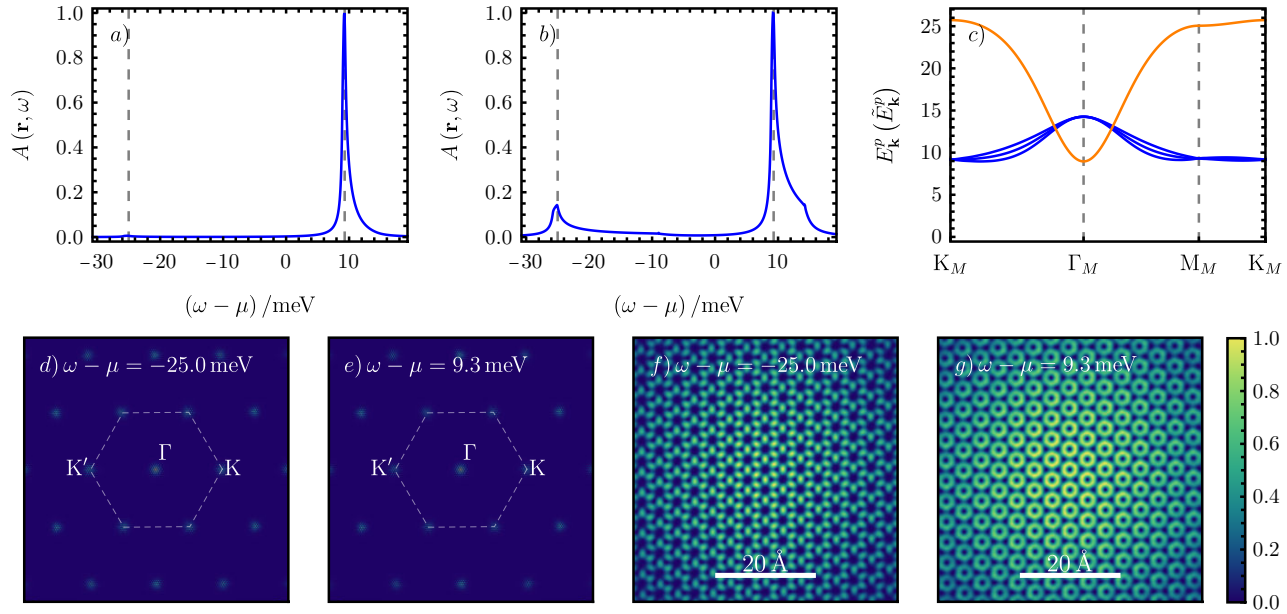

FIG. 40. $\nu = -2$, $C = 2$, *valley coherent*: The real-space spectral function averaged over three graphene unit cells at the AA site [panel a)] and at the AB site [panel b)]. The electron (blue) and hole (orange) dispersion is shown in panel c). In panels d)-g), we illustrate the spatial variation of the spectral function in momentum space [d) and e)], as well as real space [f) and g)] for the two energy choices depicted by dashed gray lines in panels a) and b). Here, we focus on $(w_0/w_1, \lambda) = (0.4, 0)$.

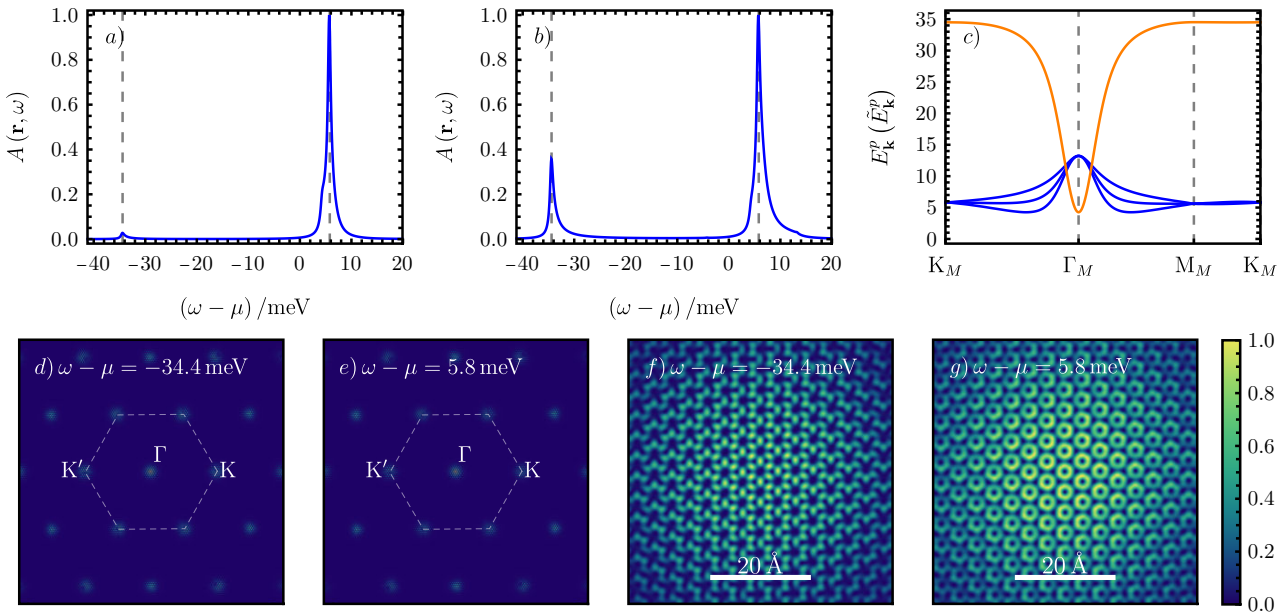

FIG. 41. $\nu=-2$, $C=2$, *valley coherent*: The real-space spectral function averaged over three graphene unit cells at the AA site [panel a)] and at the AB site [panel b)]. The electron (blue) and hole (orange) dispersion is shown in panel c). In panels d)-g), we illustrate the spatial variation of the spectral function in momentum space [d) and e)], as well as real space [f) and g)] for the two energy choices depicted by dashed gray lines in panels a) and b). Here, we focus on $(w_0/w_1,\lambda)=(0.8,0)$.

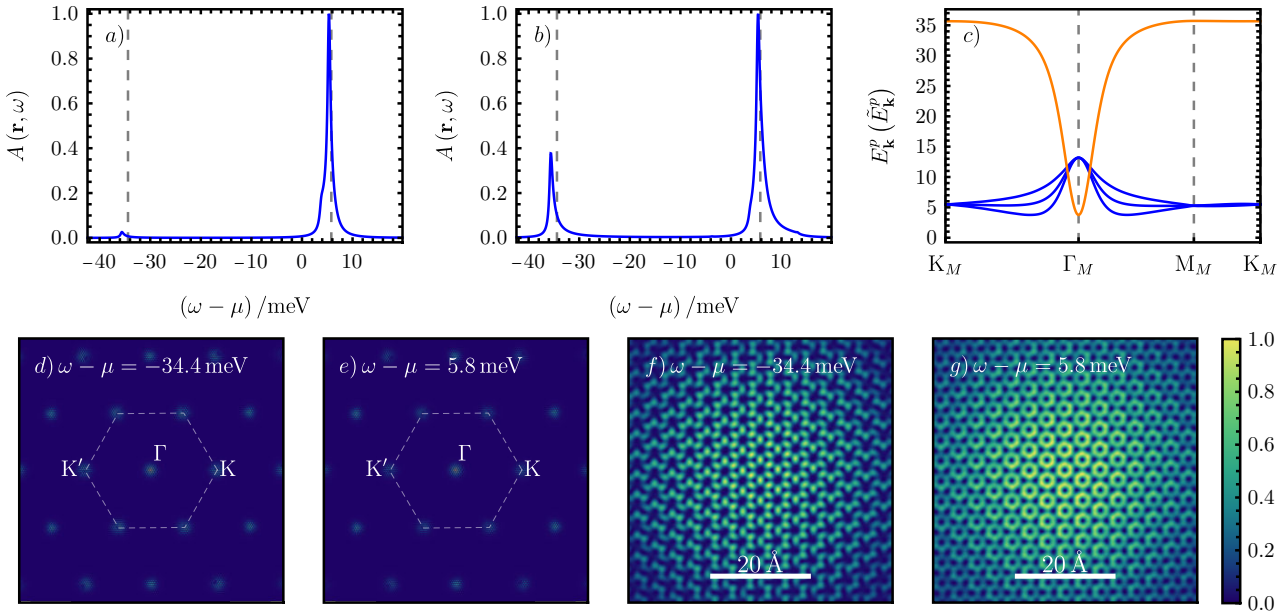

FIG. 42. $\nu=-2$, $C=2$, *valley coherent*: The real-space spectral function averaged over three graphene unit cells at the AA site [panel a)] and at the AB site [panel b)]. The electron (blue) and hole (orange) dispersion is shown in panel c). In panels d)-g), we illustrate the spatial variation of the spectral function in momentum space [d) and e)], as well as real space [f) and g)] for the two energy choices depicted by dashed gray lines in panels a) and b). Here, we focus on $(w_0/w_1,\lambda)=(0.8,1)$.

9. $\nu = -1$, $C = 3$, valley polarized: $\prod_{\mathbf{k}} \hat{d}^\dagger_{\mathbf{k},+1,+,\uparrow} \hat{d}^\dagger_{\mathbf{k},+1,+,\downarrow} \hat{d}^\dagger_{\mathbf{k},+1,-,\downarrow} |0\rangle$

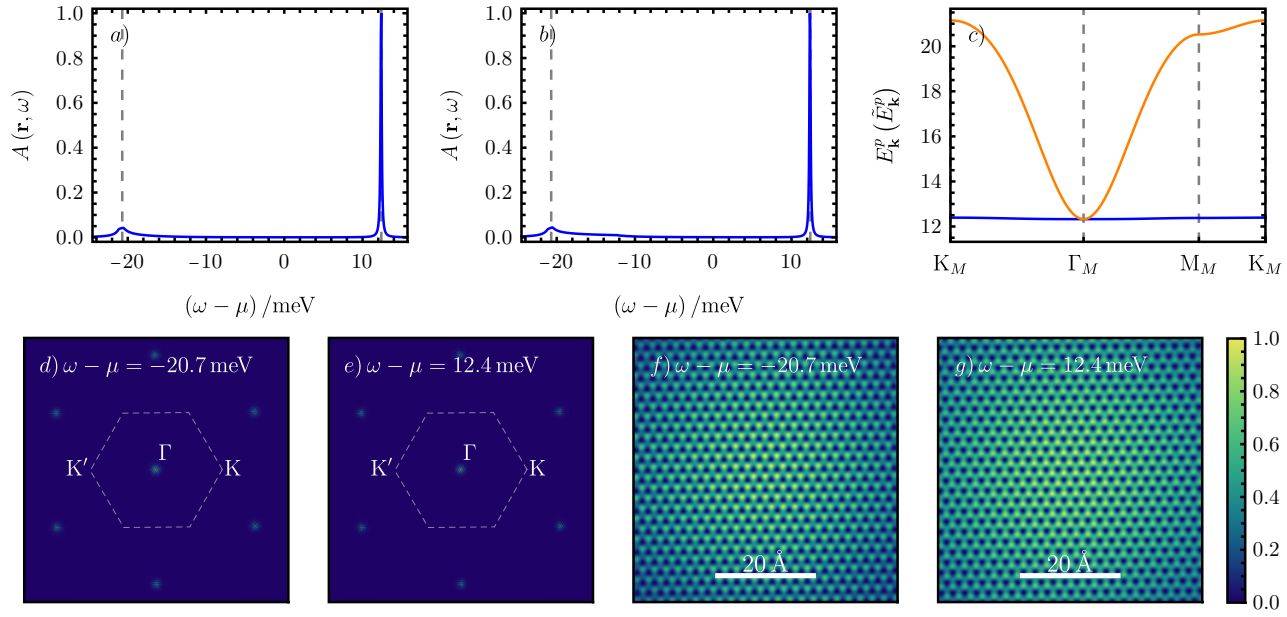

FIG. 43. $\nu = -1$, $C = 3$, *valley polarized*: The real-space spectral function averaged over three graphene unit cells at the AA site [panel a)] and at the AB site [panel b)]. The electron (blue) and hole (orange) dispersion is shown in panel c). In panels d)-g), we illustrate the spatial variation of the spectral function in momentum space [d) and e)], as well as real space [f) and g)] for the two energy choices depicted by dashed gray lines in panels a) and b). Here, we focus on $(w_0/w_1, \lambda) = (0.0, 0)$.

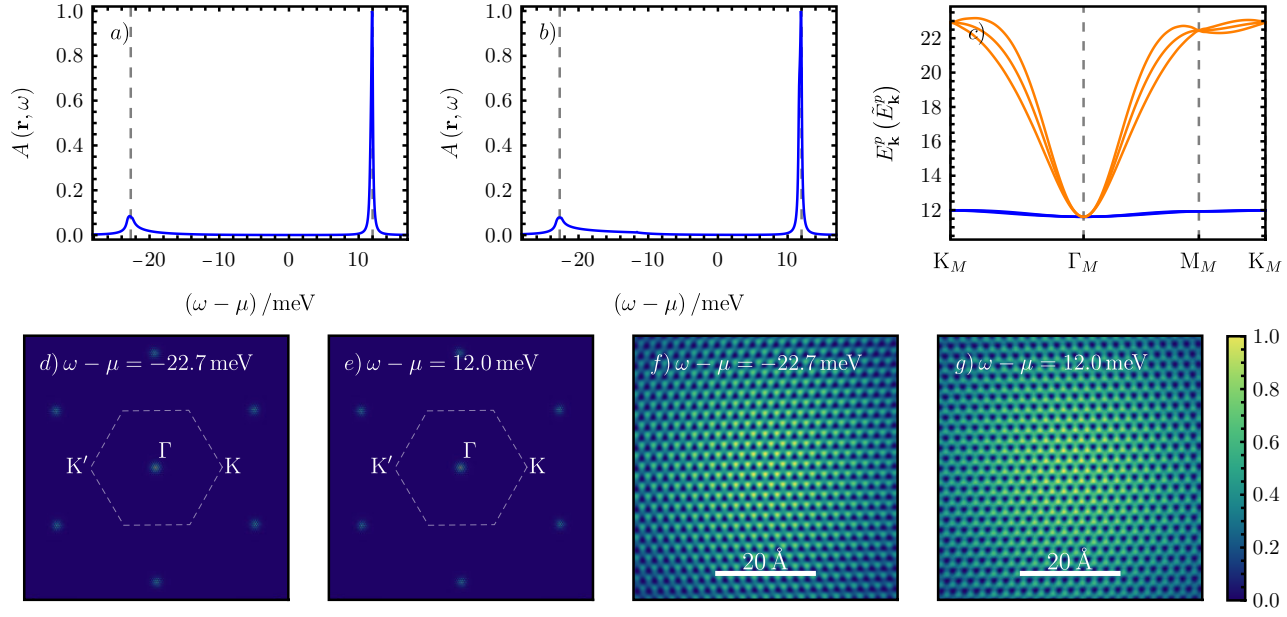

FIG. 44. $\nu = -1$, $C = 3$, *valley polarized*: The real-space spectral function averaged over three graphene unit cells at the AA site [panel a)] and at the AB site [panel b)]. The electron (blue) and hole (orange) dispersion is shown in panel c). In panels d)-g), we illustrate the spatial variation of the spectral function in momentum space [d) and e)], as well as real space [f) and g)] for the two energy choices depicted by dashed gray lines in panels a) and b). Here, we focus on $(w_0/w_1, \lambda) = (0.4, 0)$.

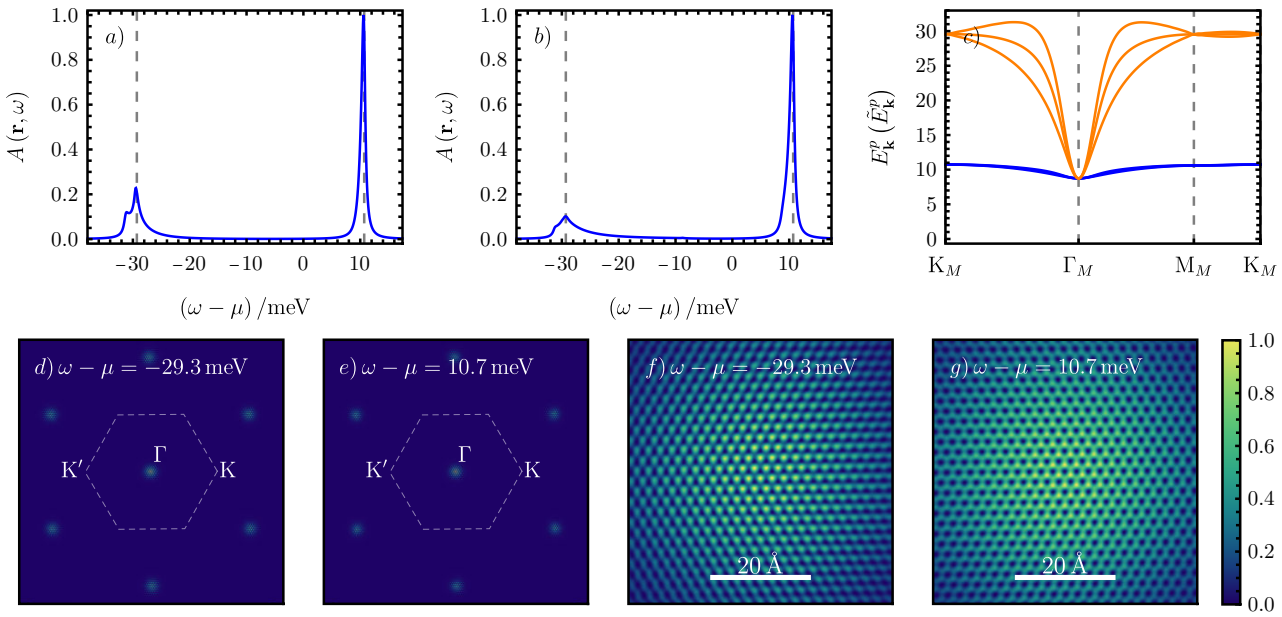

FIG. 45. $\nu=-1$, $C=3$, *valley polarized*: The real-space spectral function averaged over three graphene unit cells at the AA site [panel a)] and at the AB site [panel b)]. The electron (blue) and hole (orange) dispersion is shown in panel c). In panels d)-g), we illustrate the spatial variation of the spectral function in momentum space [d) and e)], as well as real space [f) and g)] for the two energy choices depicted by dashed gray lines in panels a) and b). Here, we focus on $(w_0/w_1,\lambda)=(0.8,0)$.

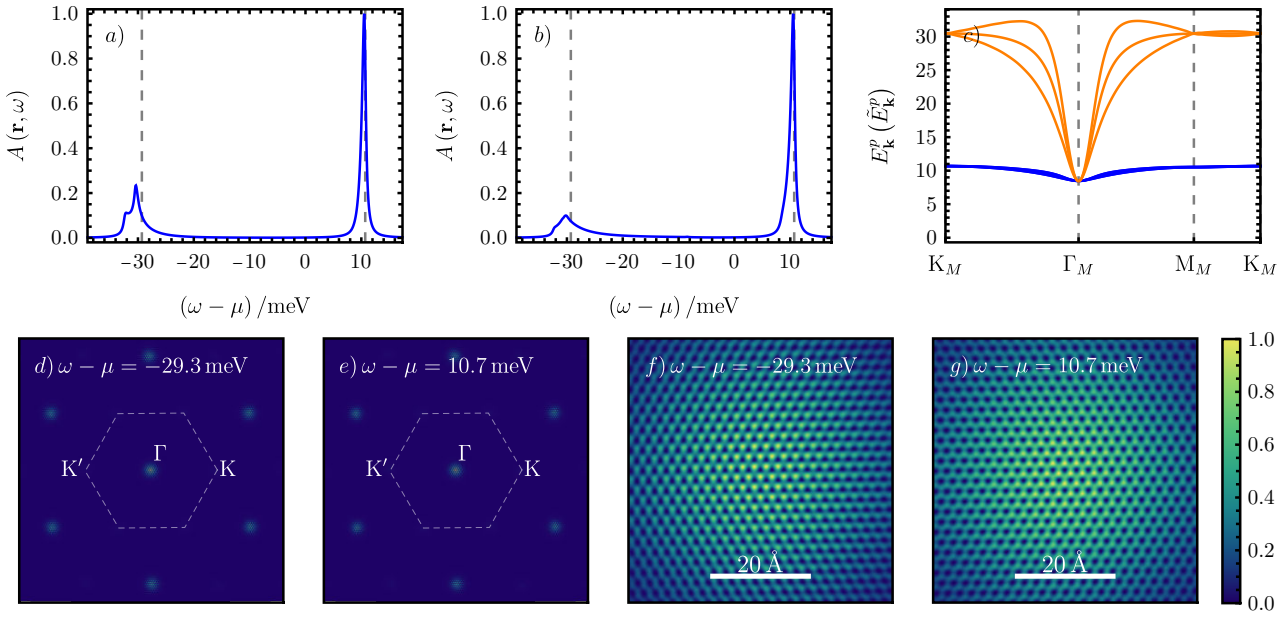

FIG. 46. $\nu=-1$, $C=3$, *valley polarized*: The real-space spectral function averaged over three graphene unit cells at the AA site [panel a)] and at the AB site [panel b)]. The electron (blue) and hole (orange) dispersion is shown in panel c). In panels d)-g), we illustrate the spatial variation of the spectral function in momentum space [d) and e)], as well as real space [f) and g)] for the two energy choices depicted by dashed gray lines in panels a) and b). Here, we focus on $(w_0/w_1,\lambda)=(0.8,1)$.

10. $\nu = -1$, $C = 1$, two occupied KIVC bands and a valley polarized band:

$$\prod_{\mathbf{k}} \hat{d}^{\dagger}_{\mathbf{k},+1,-,\downarrow} \prod_{e_Y=\pm 1} \frac{\hat{d}^{\dagger}_{\mathbf{k},e_Y,+,\uparrow} + e_Y \hat{d}^{\dagger}_{\mathbf{k},e_Y,-,\uparrow}}{\sqrt{2}} |0\rangle$$

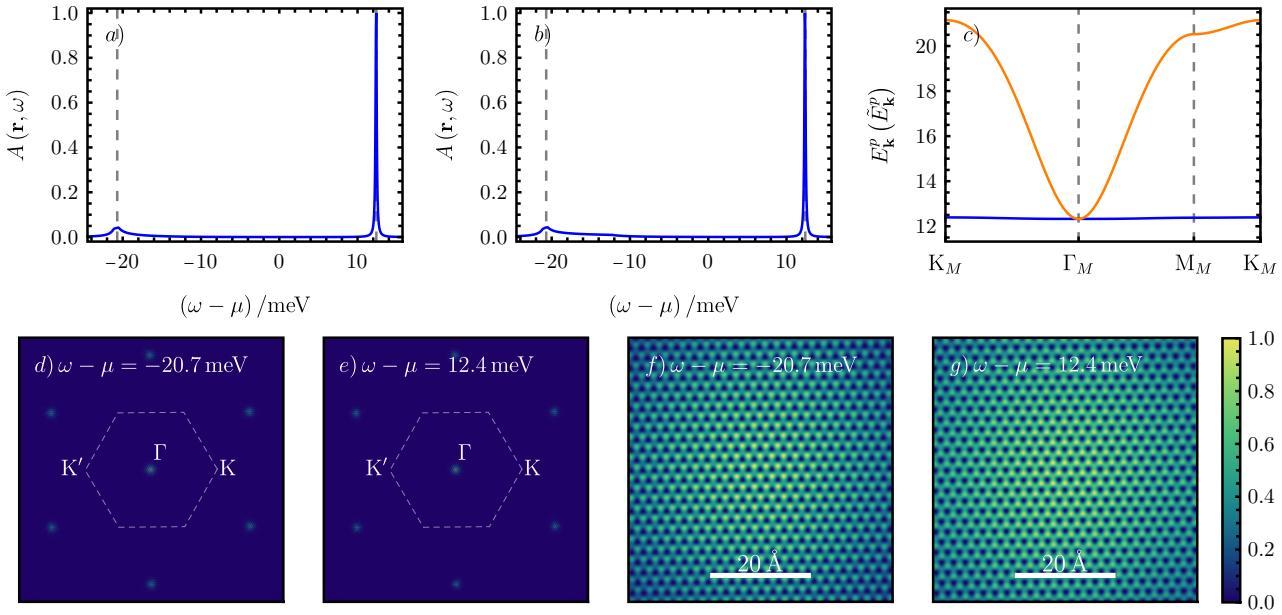

FIG. 47. $\nu = -1$, $C = 1$, *two occupied KIVC bands and a valley polarized band*: The real-space spectral function averaged over three graphene unit cells at the AA site [panel a)] and at the AB site [panel b)]. The electron (blue) and hole (orange) dispersion is shown in panel c). In panels d)-g), we illustrate the spatial variation of the spectral function in momentum space [d) and e)], as well as real space [f) and g)] for the two energy choices depicted by dashed gray lines in panels a) and b). Here, we focus on $(w_0/w_1, \lambda) = (0.0, 0)$.

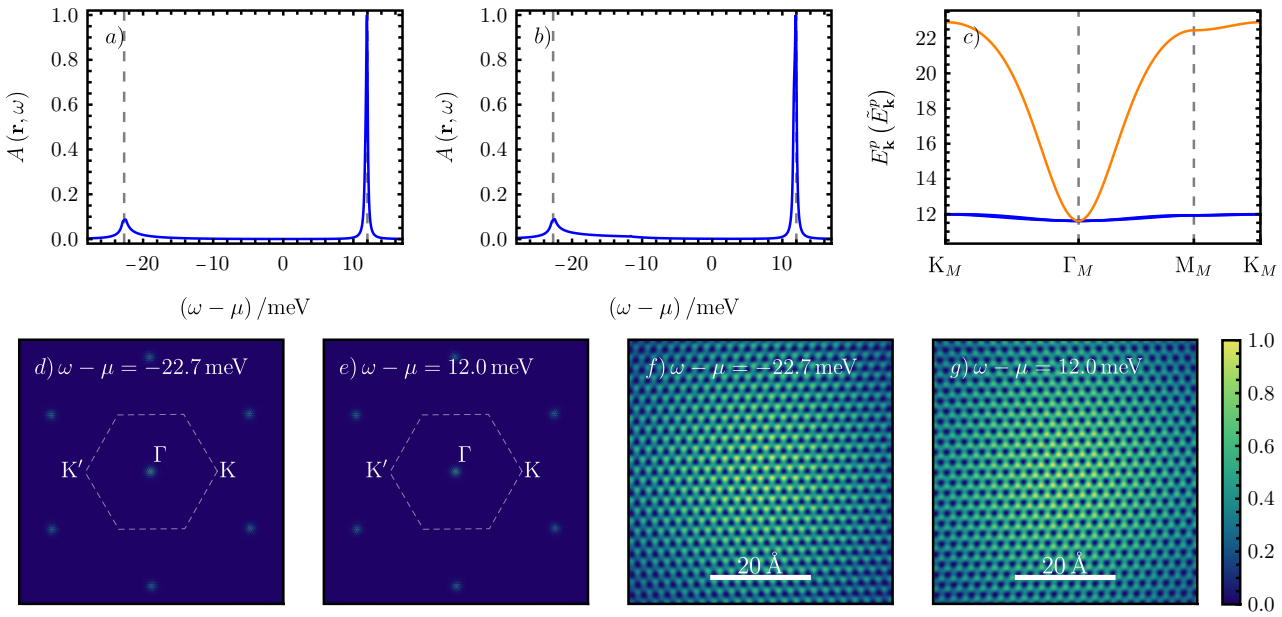

FIG. 48. $\nu=-1$, $C=1$, *two occupied KIVC bands and a valley polarized band*: The real-space spectral function averaged over three graphene unit cells at the AA site [panel a)] and at the AB site [panel b)]. The electron (blue) and hole (orange) dispersion is shown in panel c). In panels d)-g), we illustrate the spatial variation of the spectral function in momentum space [d) and e)], as well as real space [f) and g)] for the two energy choices depicted by dashed gray lines in panels a) and b). Here, we focus on $(w_0/w_1,\lambda)=(0.4,0)$.

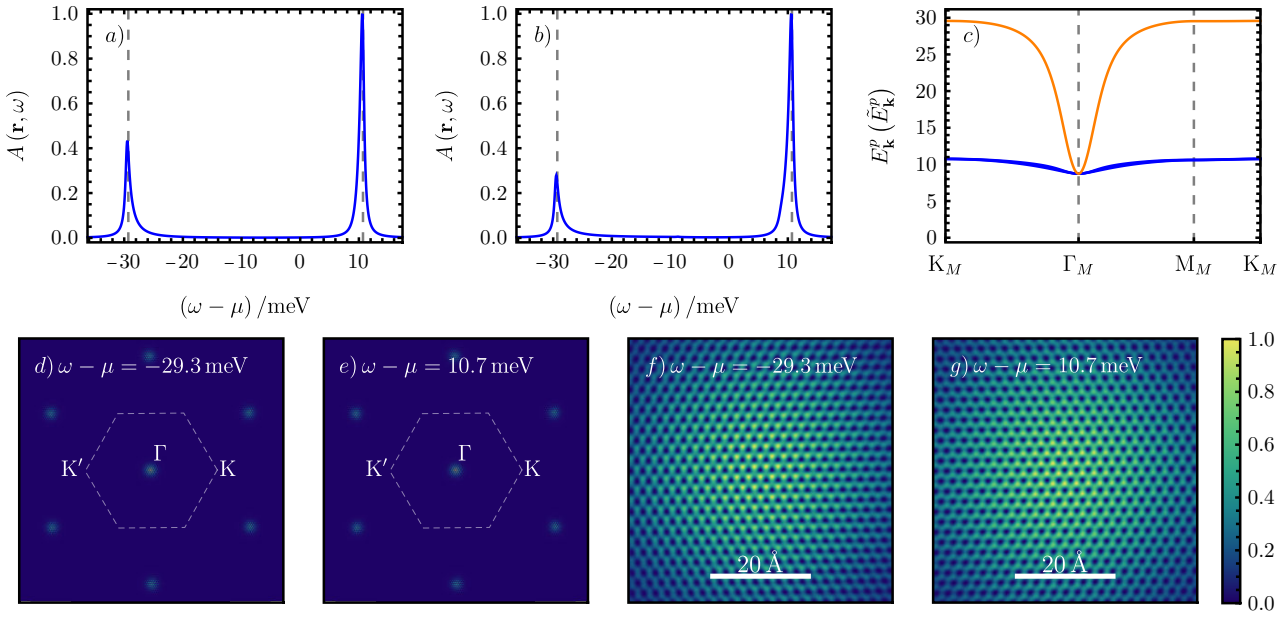

FIG. 49. $\nu=-1$, $C=1$, *two occupied KIVC bands and a valley polarized band*: The real-space spectral function averaged over three graphene unit cells at the AA site [panel a)] and at the AB site [panel b)]. The electron (blue) and hole (orange) dispersion is shown in panel c). In panels d)-g), we illustrate the spatial variation of the spectral function in momentum space [d) and e)], as well as real space [f) and g)] for the two energy choices depicted by dashed gray lines in panels a) and b). Here, we focus on $(w_0/w_1,\lambda)=(0.8,0)$.

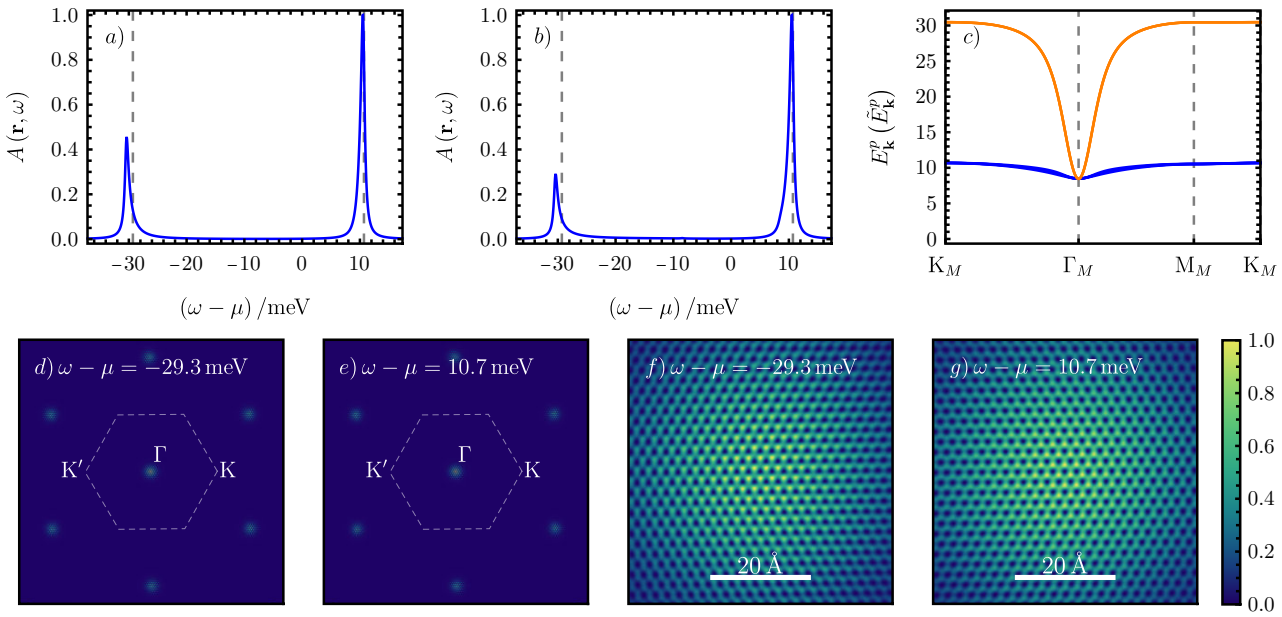

FIG. 50. $\nu=-1$, $C=1$, *two occupied KIVC bands and a valley polarized band*: The real-space spectral function averaged over three graphene unit cells at the AA site [panel a)] and at the AB site [panel b)]. The electron (blue) and hole (orange) dispersion is shown in panel c). In panels d)-g), we illustrate the spatial variation of the spectral function in momentum space [d) and e)], as well as real space [f) and g)] for the two energy choices depicted by dashed gray lines in panels a) and b). Here, we focus on $(w_0/w_1,\lambda)=(0.8,1)$.

11. $\nu = 0$, $C = 0$, **KIVC:** $\prod_{\mathbf{k}} \prod_{e_Y=\pm 1} \prod_{s=\uparrow,\downarrow} \frac{\hat{d}^\dagger_{\mathbf{k},e_Y,+,s} + e_Y \hat{d}^\dagger_{\mathbf{k},e_Y,-,s}}{\sqrt{2}} |0\rangle$

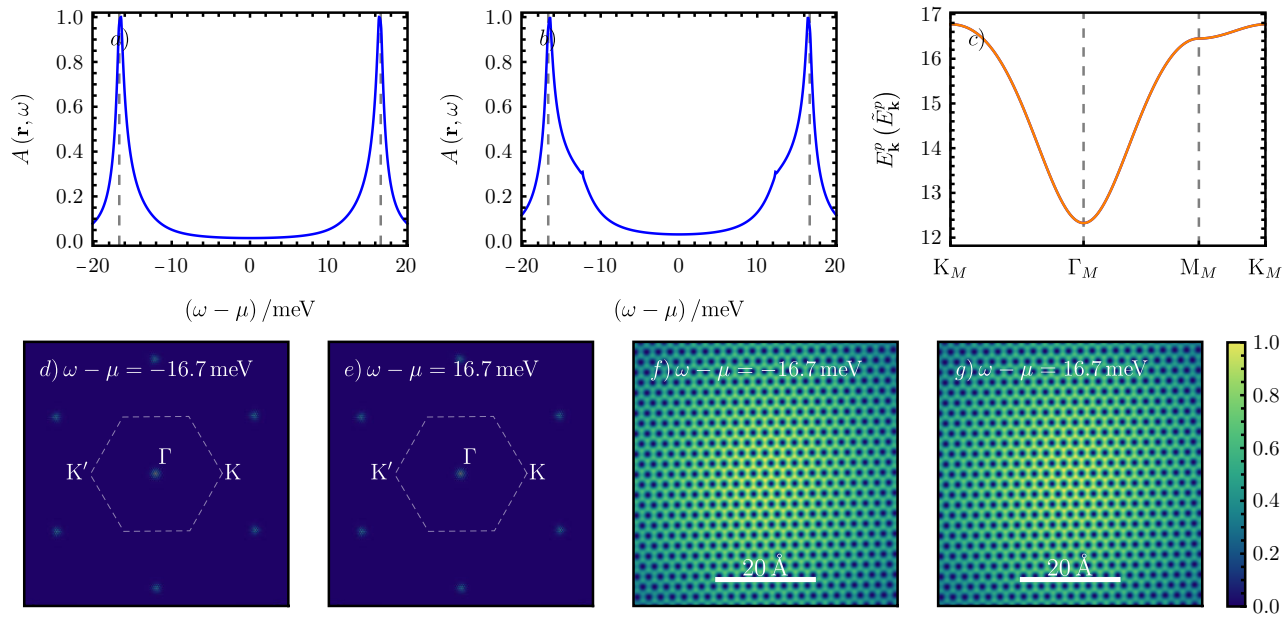

FIG. 51. $\nu = 0$, $C = 0$, *KIVC*: The real-space spectral function averaged over three graphene unit cells at the AA site [panel a)] and at the AB site [panel b)]. The electron (blue) and hole (orange) dispersion is shown in panel c). In panels d)-g), we illustrate the spatial variation of the spectral function in momentum space [d) and e)], as well as real space [f) and g)] for the two energy choices depicted by dashed gray lines in panels a) and b). Here, we focus on $(w_0/w_1, \lambda) = (0.0, 0)$.

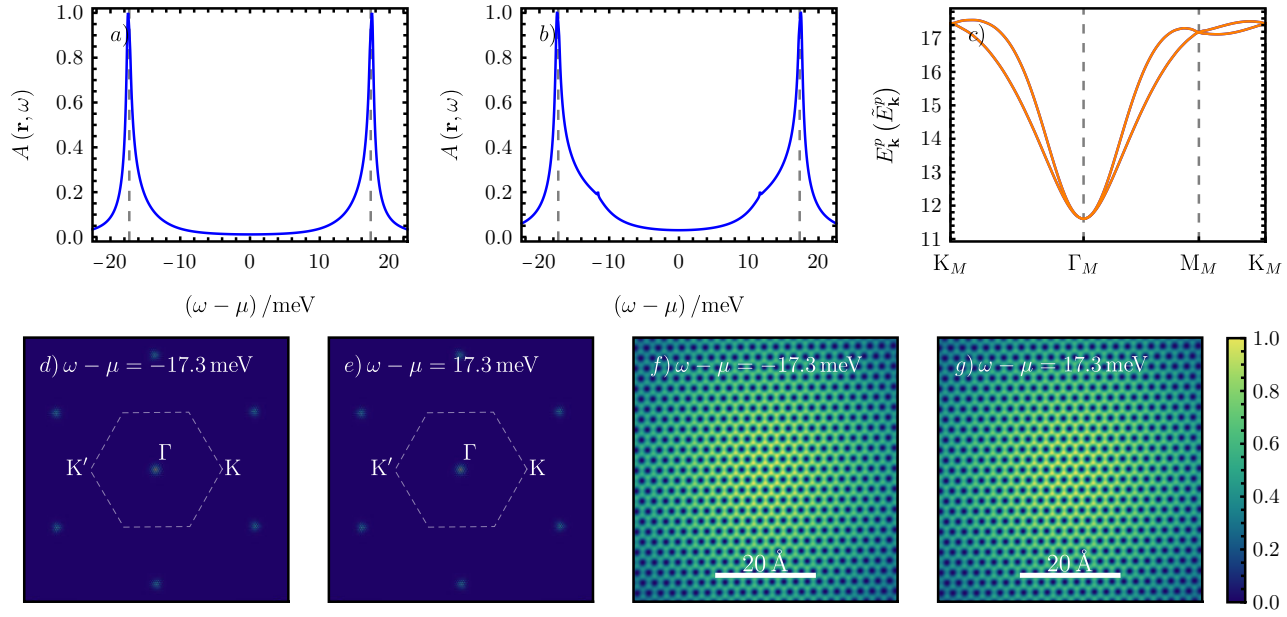

FIG. 52. $\nu = 0$, $C = 0$, *KIVC*: The real-space spectral function averaged over three graphene unit cells at the AA site [panel a)] and at the AB site [panel b)]. The electron (blue) and hole (orange) dispersion is shown in panel c). In panels d)-g), we illustrate the spatial variation of the spectral function in momentum space [d) and e)], as well as real space [f) and g)] for the two energy choices depicted by dashed gray lines in panels a) and b). Here, we focus on $(w_0/w_1, \lambda) = (0.4, 0)$.

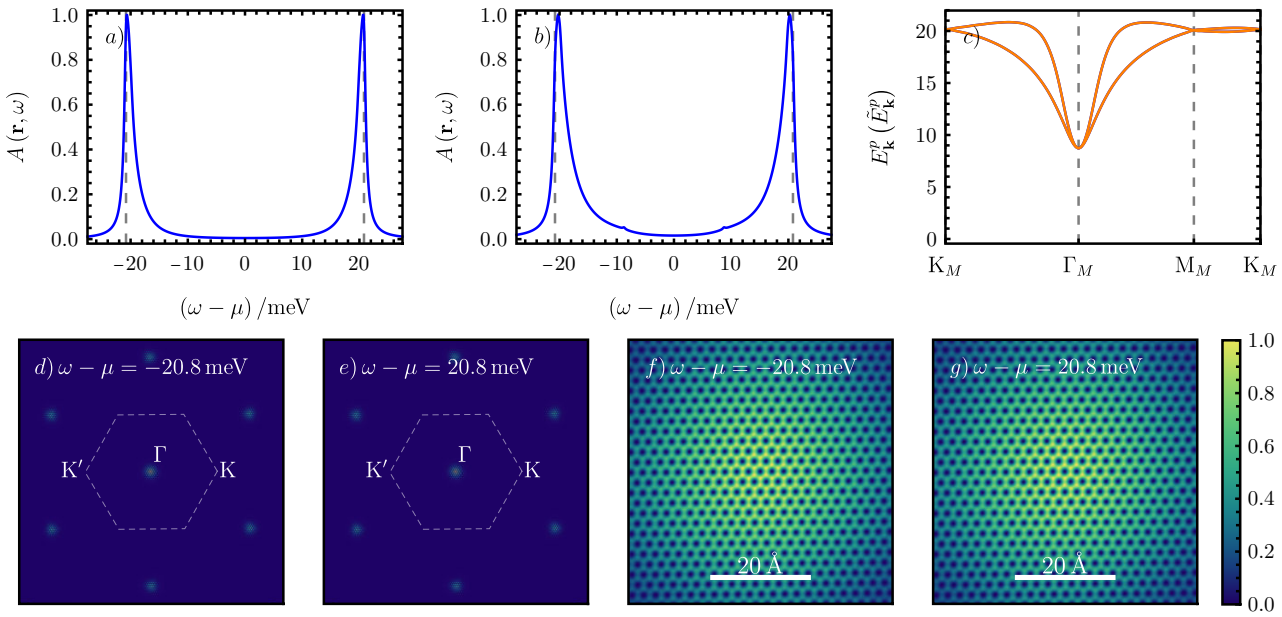

FIG. 53. $\nu = 0$, $C = 0$, *KIVC*: The real-space spectral function averaged over three graphene unit cells at the AA site [panel a)] and at the AB site [panel b)]. The electron (blue) and hole (orange) dispersion is shown in panel c). In panels d)-g), we illustrate the spatial variation of the spectral function in momentum space [d) and e)], as well as real space [f) and g)] for the two energy choices depicted by dashed gray lines in panels a) and b). Here, we focus on $(w_0/w_1, \lambda) = (0.8, 0)$.

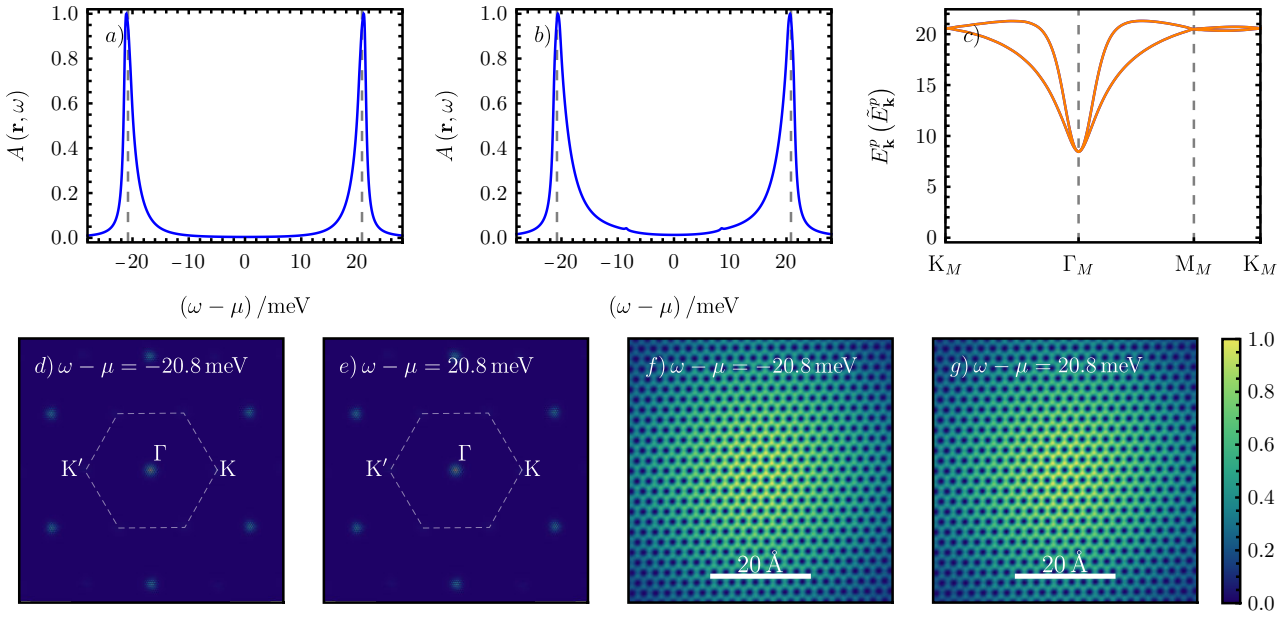

FIG. 54. $\nu = 0$, $C = 0$, *KIVC*: The real-space spectral function averaged over three graphene unit cells at the AA site [panel a)] and at the AB site [panel b)]. The electron (blue) and hole (orange) dispersion is shown in panel c). In panels d)-g), we illustrate the spatial variation of the spectral function in momentum space [d) and e)], as well as real space [f) and g)] for the two energy choices depicted by dashed gray lines in panels a) and b). Here, we focus on $(w_0/w_1, \lambda) = (0.8, 1)$.

12. $\nu = 0$, $C = 0$, **valley polarized:** $\prod_{\mathbf{k}} \prod_{e_Y=\pm 1} \prod_{s=\uparrow,\downarrow} \hat{d}^{\dagger}_{\mathbf{k},e_Y,+,s} |0\rangle$

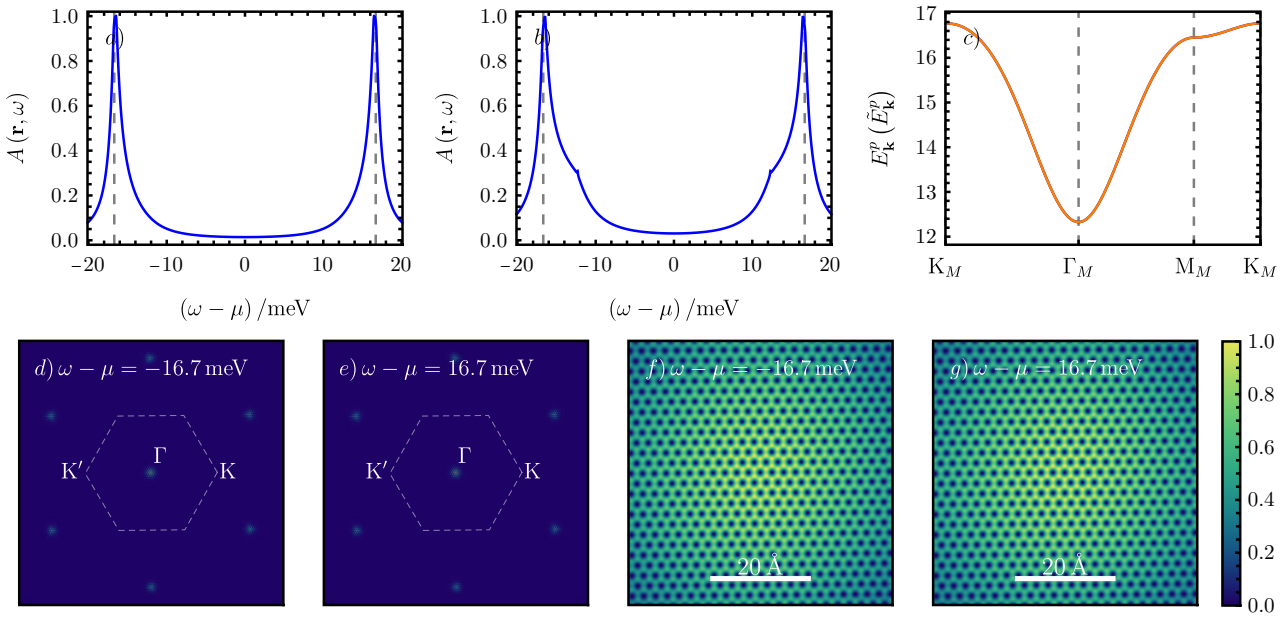

FIG. 55. $\nu = 0$, $C = 0$, *valley polarized*: The real-space spectral function averaged over three graphene unit cells at the AA site [panel a)] and at the AB site [panel b)]. The electron (blue) and hole (orange) dispersion is shown in panel c). In panels d)-g), we illustrate the spatial variation of the spectral function in momentum space [d) and e)], as well as real space [f) and g)] for the two energy choices depicted by dashed gray lines in panels a) and b). Here, we focus on $(w_0/w_1, \lambda) = (0.0, 0)$.

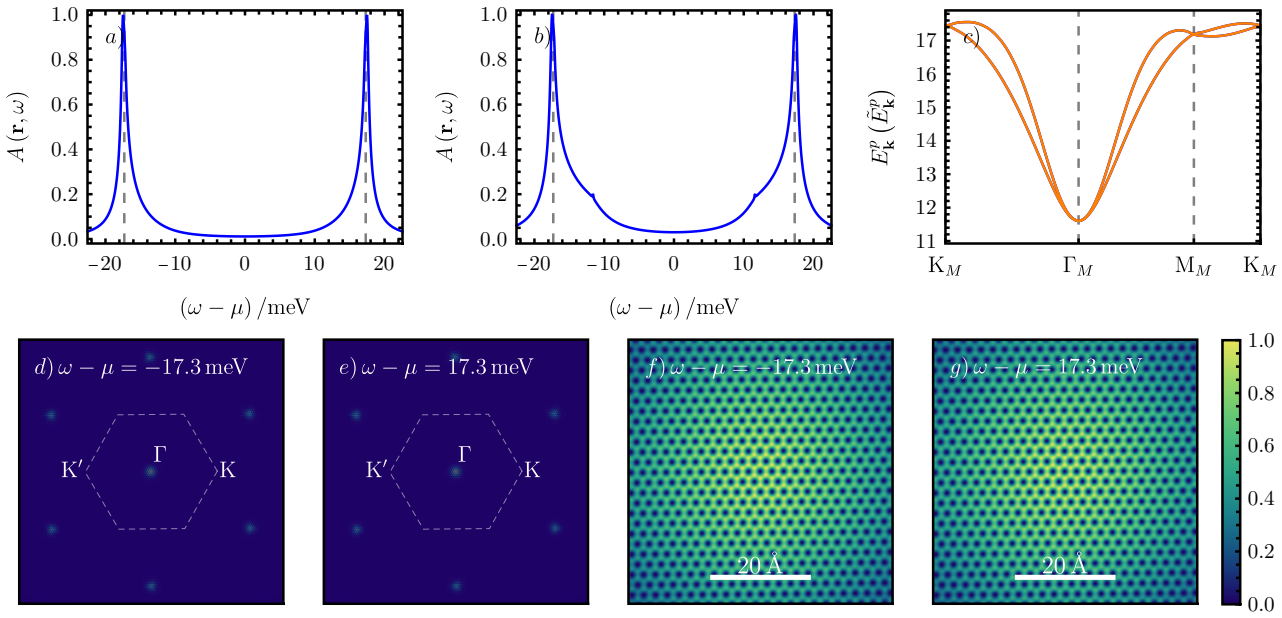

FIG. 56. $\nu = 0$, $C = 0$, *valley polarized*: The real-space spectral function averaged over three graphene unit cells at the AA site [panel a)] and at the AB site [panel b)]. The electron (blue) and hole (orange) dispersion is shown in panel c). In panels d)-g), we illustrate the spatial variation of the spectral function in momentum space [d) and e)], as well as real space [f) and g)] for the two energy choices depicted by dashed gray lines in panels a) and b). Here, we focus on $(w_0/w_1, \lambda) = (0.4, 0)$.

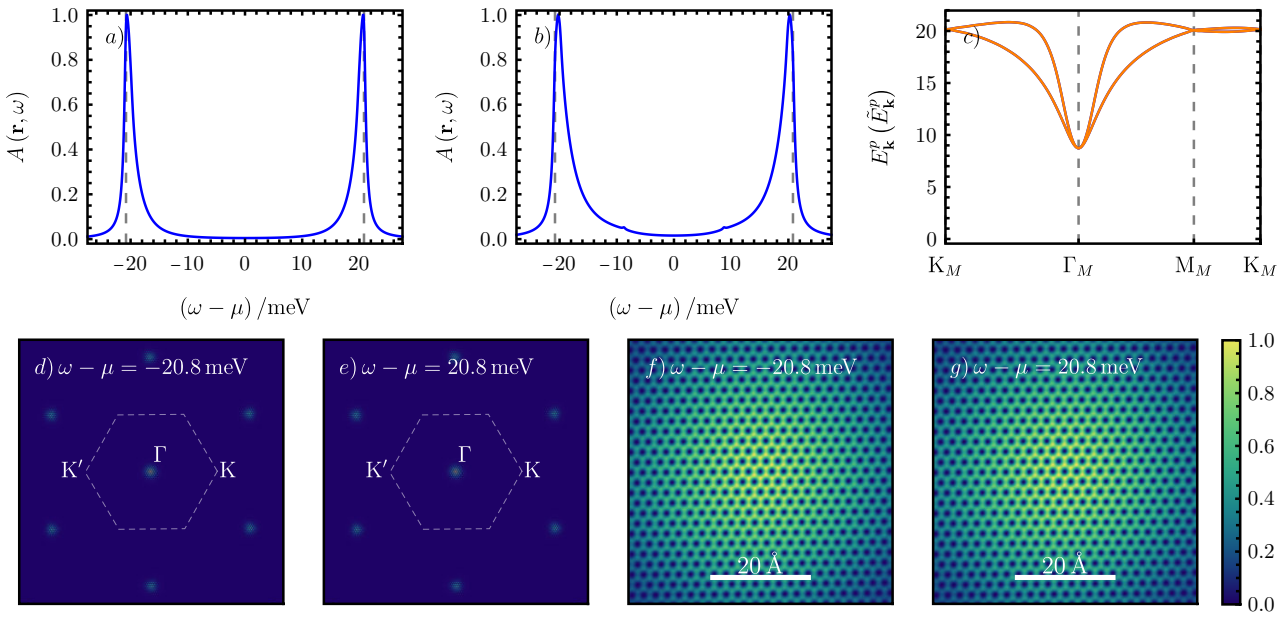

FIG. 57. $\nu = 0$, $C = 0$, *valley polarized*: The real-space spectral function averaged over three graphene unit cells at the AA site [panel a)] and at the AB site [panel b)]. The electron (blue) and hole (orange) dispersion is shown in panel c). In panels d)-g), we illustrate the spatial variation of the spectral function in momentum space [d) and e)], as well as real space [f) and g)] for the two energy choices depicted by dashed gray lines in panels a) and b). Here, we focus on $(w_0/w_1, \lambda) = (0.8, 0)$.

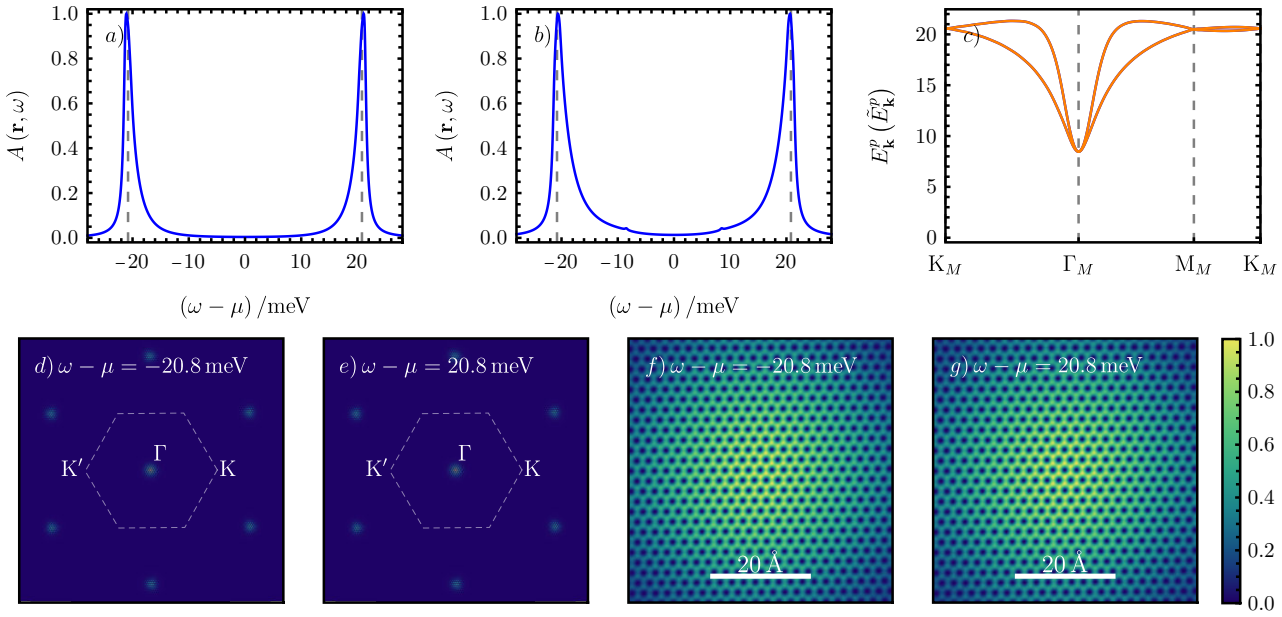

FIG. 58. $\nu = 0$, $C = 0$, *valley polarized*: The real-space spectral function averaged over three graphene unit cells at the AA site [panel a)] and at the AB site [panel b)]. The electron (blue) and hole (orange) dispersion is shown in panel c). In panels d)-g), we illustrate the spatial variation of the spectral function in momentum space [d) and e)], as well as real space [f) and g)] for the two energy choices depicted by dashed gray lines in panels a) and b). Here, we focus on $(w_0/w_1, \lambda) = (0.8, 1)$.

13. $\nu = 0$, $C = 4$, **valley polarized:** $\prod_{\mathbf{k}} \prod_{\eta=\pm} \prod_{s=\uparrow,\downarrow} \hat{d}^{\dagger}_{\mathbf{k},+1,\eta,s} |0\rangle$

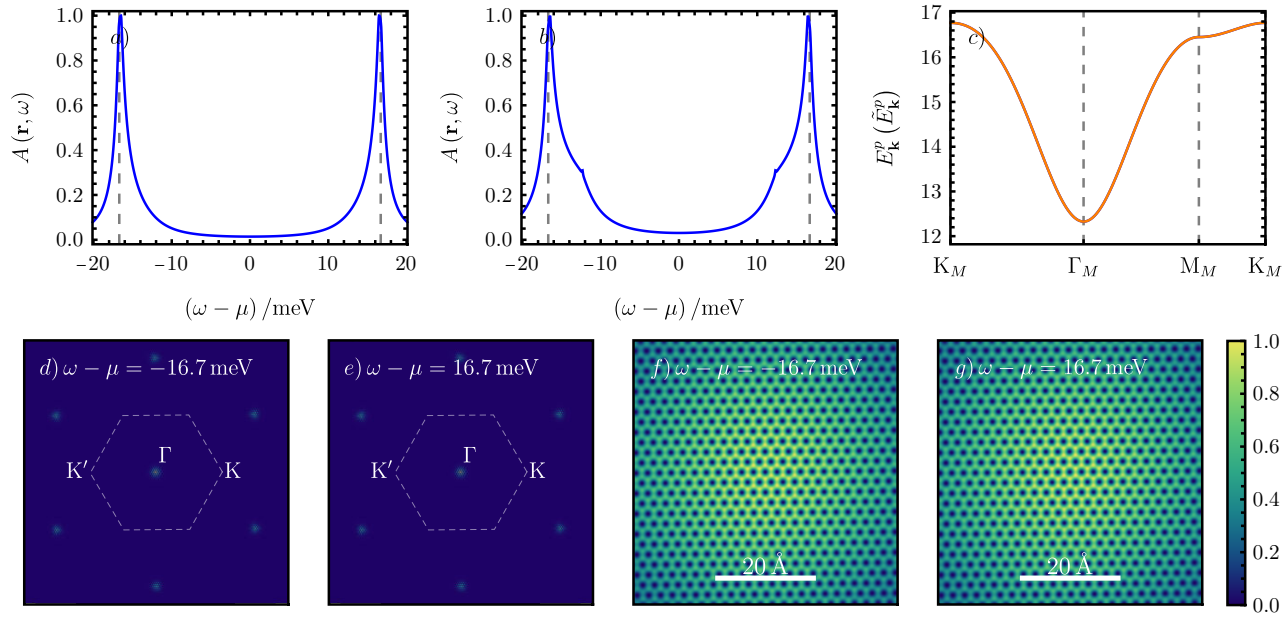

FIG. 59. $\nu = 0$, $C = 4$, *valley polarized*: The real-space spectral function averaged over three graphene unit cells at the AA site [panel a)] and at the AB site [panel b)]. The electron (blue) and hole (orange) dispersion is shown in panel c). In panels d)-g), we illustrate the spatial variation of the spectral function in momentum space [d) and e)], as well as real space [f) and g)] for the two energy choices depicted by dashed gray lines in panels a) and b). Here, we focus on $(w_0/w_1, \lambda) = (0.0, 0)$.

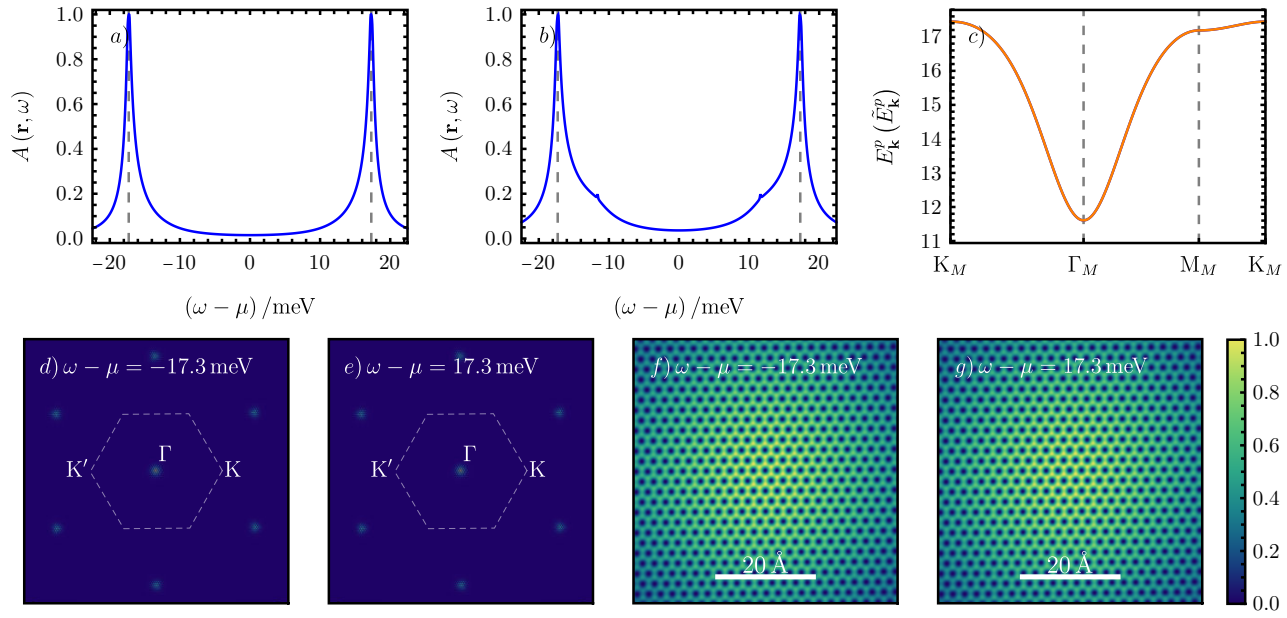

FIG. 60. $\nu = 0$, $C = 4$, *valley polarized*: The real-space spectral function averaged over three graphene unit cells at the AA site [panel a)] and at the AB site [panel b)]. The electron (blue) and hole (orange) dispersion is shown in panel c). In panels d)-g), we illustrate the spatial variation of the spectral function in momentum space [d) and e)], as well as real space [f) and g)] for the two energy choices depicted by dashed gray lines in panels a) and b). Here, we focus on $(w_0/w_1, \lambda) = (0.4, 0)$.

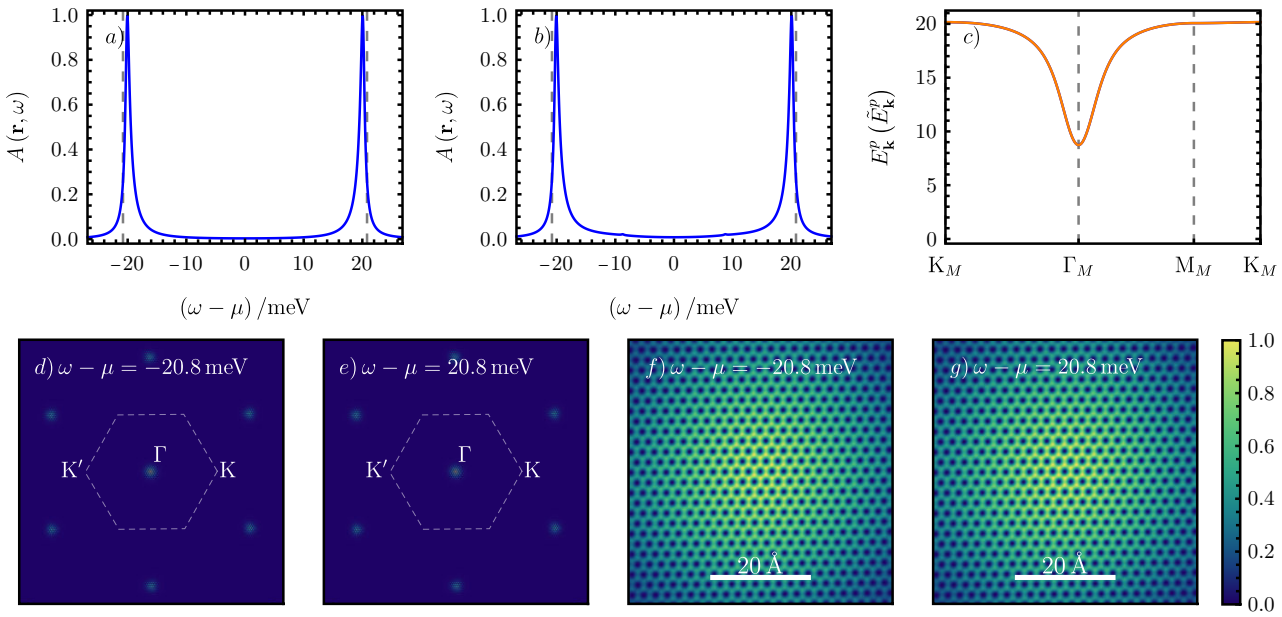

FIG. 61. $\nu = 0$, $C = 4$, *valley polarized*: The real-space spectral function averaged over three graphene unit cells at the AA site [panel a)] and at the AB site [panel b)]. The electron (blue) and hole (orange) dispersion is shown in panel c). In panels d)-g), we illustrate the spatial variation of the spectral function in momentum space [d) and e)], as well as real space [f) and g)] for the two energy choices depicted by dashed gray lines in panels a) and b). Here, we focus on $(w_0/w_1, \lambda) = (0.8, 0)$.

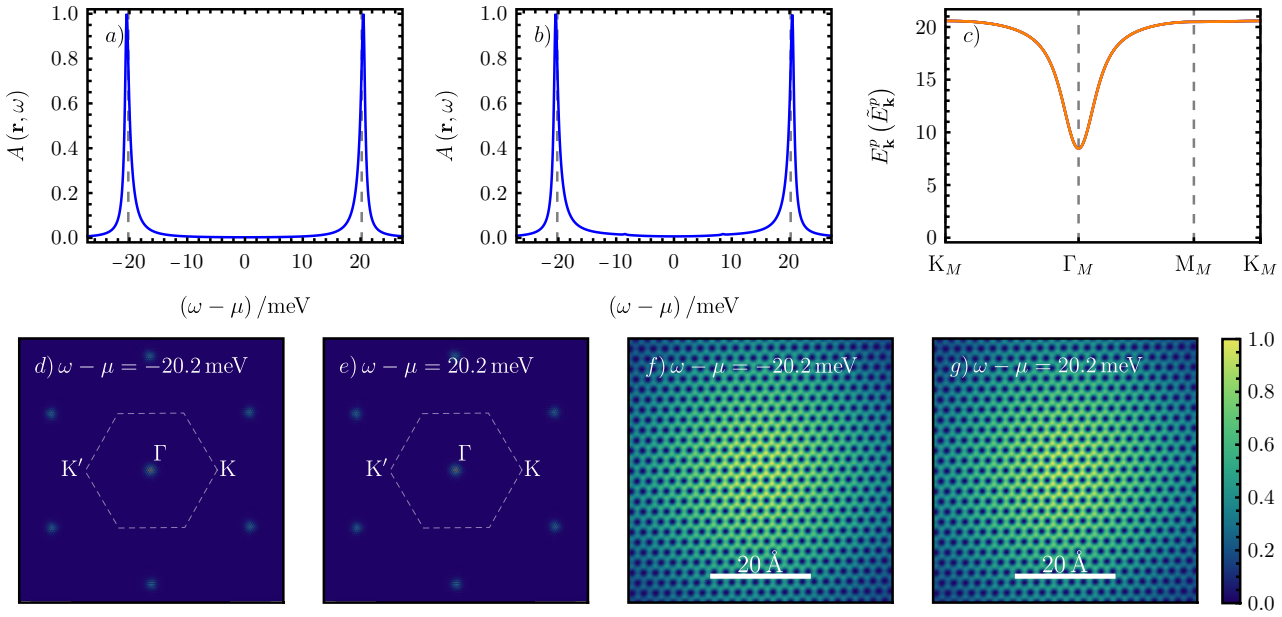

FIG. 62. $\nu = 0$, $C = 4$, *valley polarized*: The real-space spectral function averaged over three graphene unit cells at the AA site [panel a)] and at the AB site [panel b)]. The electron (blue) and hole (orange) dispersion is shown in panel c). In panels d)-g), we illustrate the spatial variation of the spectral function in momentum space [d) and e)], as well as real space [f) and g)] for the two energy choices depicted by dashed gray lines in panels a) and b). Here, we focus on $(w_0/w_1, \lambda) = (0.8, 1)$.

14. $\nu = +4$, insulator with all TBG active bands filled: $\prod_{\mathbf{k}} \prod_{\eta=\pm} \prod_{s=\uparrow,\downarrow} \prod_{e_Y=\pm 1} \hat{d}^{\dagger}_{\mathbf{k},e_Y,\eta,s} |0\rangle$

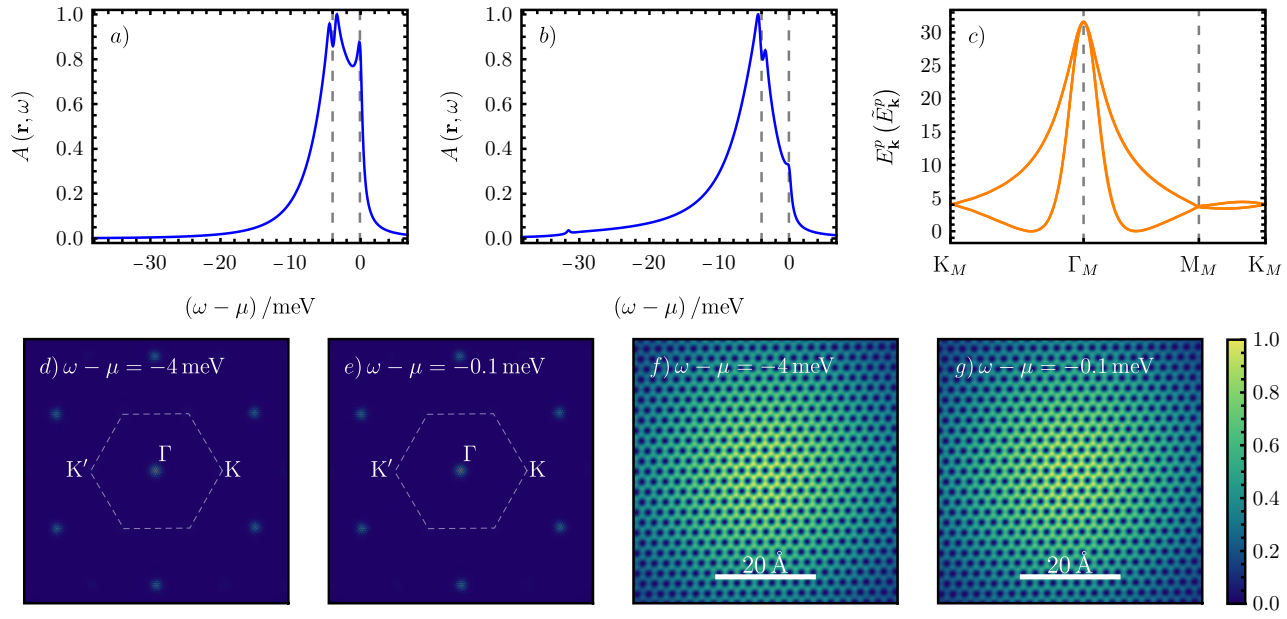

FIG. 63. $\nu = +4$, *insulator with all TBG active bands filled*: The real-space spectral function averaged over three graphene unit cells at the AA site [panel a)] and at the AB site [panel b)]. The electron (blue) and hole (orange) dispersion is shown in panel c). In panels d)-g), we illustrate the spatial variation of the spectral function in momentum space [d) and e)], as well as real space [f) and g)] for the two energy choices depicted by dashed gray lines in panels a) and b). Here, we focus on $(w_0/w_1, \lambda) = (0.0, 0)$.

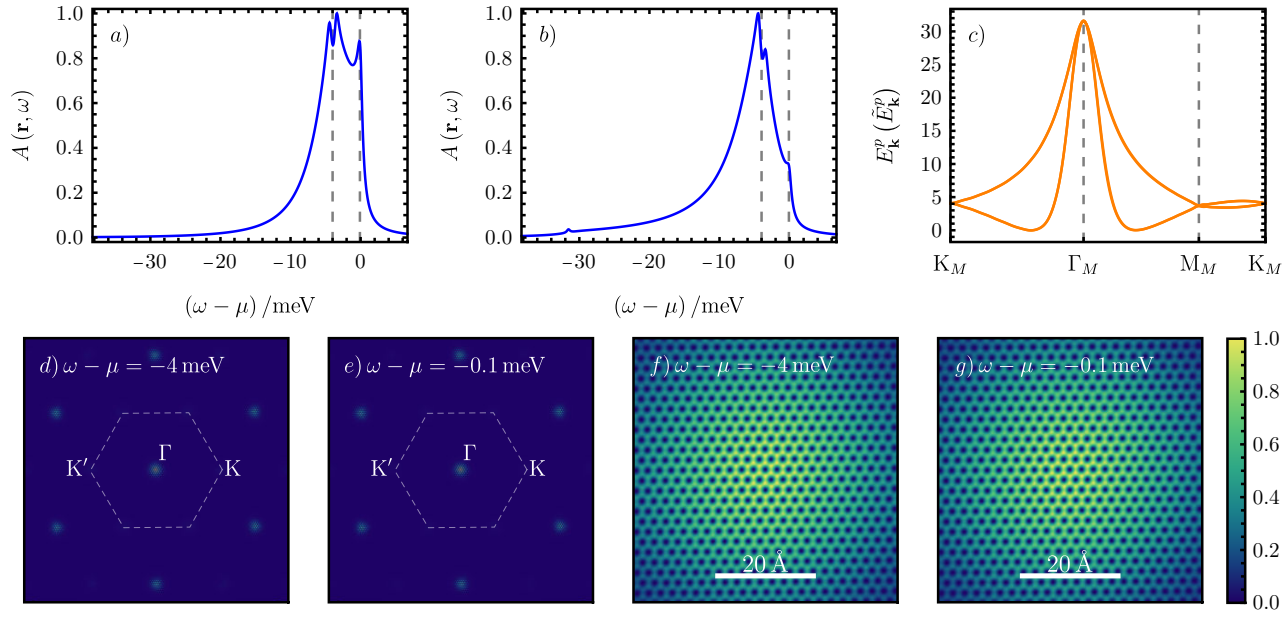

FIG. 64. $\nu = +4$, *insulator with all TBG active bands filled*: The real-space spectral function averaged over three graphene unit cells at the AA site [panel a)] and at the AB site [panel b)]. The electron (blue) and hole (orange) dispersion is shown in panel c). In panels d)-g), we illustrate the spatial variation of the spectral function in momentum space [d) and e)], as well as real space [f) and g)] for the two energy choices depicted by dashed gray lines in panels a) and b). Here, we focus on $(w_0/w_1, \lambda) = (0.4, 0)$.

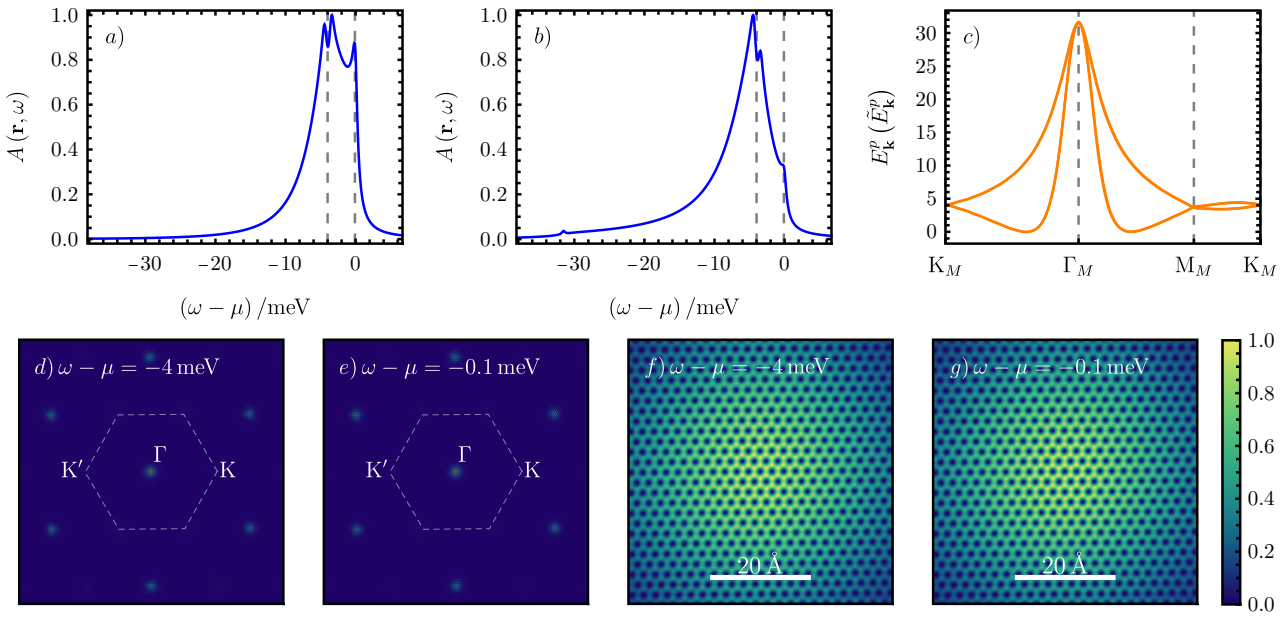

FIG. 65. $\nu = +4$, *insulator with all TBG active bands filled*: The real-space spectral function averaged over three graphene unit cells at the AA site [panel a)] and at the AB site [panel b)]. The electron (blue) and hole (orange) dispersion is shown in panel c). In panels d)-g), we illustrate the spatial variation of the spectral function in momentum space [d) and e)], as well as real space [f) and g)] for the two energy choices depicted by dashed gray lines in panels a) and b). Here, we focus on $(w_0/w_1, \lambda) = (0.8, 0)$.

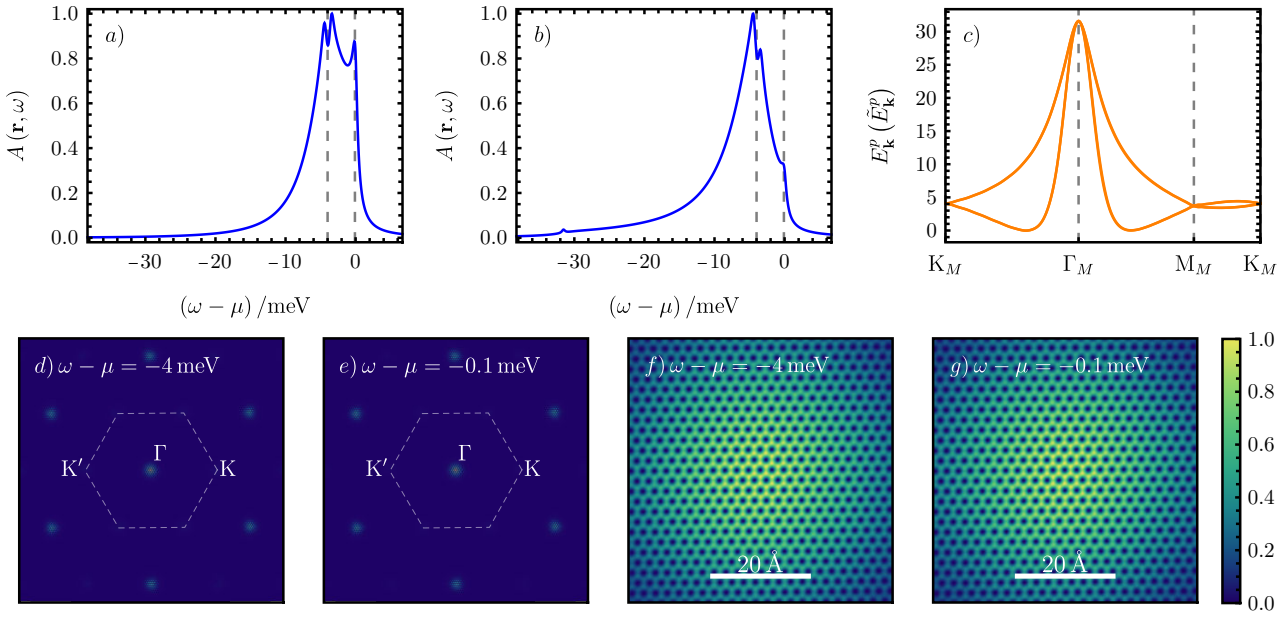

FIG. 66. $\nu = +4$, *insulator with all TBG active bands filled*: The real-space spectral function averaged over three graphene unit cells at the AA site [panel a)] and at the AB site [panel b)]. The electron (blue) and hole (orange) dispersion is shown in panel c). In panels d)-g), we illustrate the spatial variation of the spectral function in momentum space [d) and e)], as well as real space [f) and g)] for the two energy choices depicted by dashed gray lines in panels a) and b). Here, we focus on $(w_0/w_1, \lambda) = (0.8, 1)$.